Understanding phase behaviour in the geological storage of carbon dioxide

A thesis submitted to the University of Manchester for the degree of
Doctor of Philosophy in the Faculty of Engineering and Physical
Sciences

By

Oliver William Peter Warr

School of Earth, Atmospheric & Environmental Sciences
The University of Manchester

2013

Contents

Chapter One: Background and literature

Chapter Two: Developing and commissioning of experimental system

Chapter 3: Development of Modelling

Chapter Four: Measured partition coefficients

Chapter Five: Simulated Henry's constants

Chapter Six: Future work

Full Word Count 75,918

(Word Count excl. appendices & references 64,198)

List of Figures

Chapter One: Background and literature

Chapter Two: Developing and commissioning of experimental system

Chapter Three: Development of Modelling

Chapter Four: Measured partition coefficients

Chapter Five: Simulated Henry's constants

List of Tables

Chapter One: Background and literature

Chapter Two: Developing and commissioning of experimental system

Chapter Three: Development of Modelling

Chapter Four: Measured partition coefficients

Chapter Five: Simulated Henry's constants

Appendix I: Worked partition coefficient examples

Appendix II: Pure noble gas-water simulation data tables

Appendix III: Low pressure CO_2-water simulation data table

Appendix IV: High pressure CO_2-water simulation data table

Acronyms, Abbreviations and Symbols

Acronyms and Abbreviations

AC	Alternating Current
AMU	Atomic Mass Unit
AVC	Aliquot Volume Correction
BGS	British Geological Survey
BSE	Bulk Silicate Earth
CCS	Carbon Capture and Storage
CSF	Computational Shared Facility
DC	Direct Current
DCO	Density Correction
GEMC	Gibbs Ensemble Monte Carlo
EOR	Enhanced Oil Recovery
HAL	Hiden Analytical
HPLC	High Performance Liquid Chromatography
IPCC	Intergovernmental Panel on Climate Change
MORB	Mid Ocean Ridge Basalts
MD	Molecular Dynamics
MC	Monte Carlo
NIST	National Institute Standards Technology
OIB	Oceanic Island Basalts
RF	Radio Frequency
Rs	Relative sensitivity
RSC	Relative Sensitivity Correction
σ	Standard Deviation
S.E.	Standard Error
SGE	Sun Grid Engine
SSH	Secure Shell client
STP	Standard temperature
UHV	Ultra High Vacuum
VLE	Vapour-Liquid Equilibrium

Symbols

Chapter One

P	Pressure
V	Volume
T	Temperature
X	Phase Composition
R_A	Atmospheric ratio of ^{3}He/^{4}He
i	Molecular species '*i*'
F_{Ar}	Remaining fraction of argon in the water phase
α	Gas/liquid fractionation coefficient
P_i	Partial pressure of '*i*'
K_i	Henry's constant for species '*i*'
x_i	Molar fraction of '*i*'
Φ_i	Fugacity of species '*i*'
V_m	Real molar volume occupied by gas

R	Ideal gas constant
f_i	Actual gas fugacity of species ‘*i*’
f_i^θ	Gas fugacity of pure ‘*i*’
γ_i	Liquid phase activity coefficient of species ‘*i*’
S_i^o	Non-electrolyte *i* solubility in pure water
S_i^o	Non-electrolyte *i* solubility in pure water
S_i	Non-electrolyte *i* solubility in salt solution
C	Molar concentration of salt
k_i	Setschenow coefficient
$\overline{V}_{mi}$	Partial molar volume of *i* at infinite dilution
μ_i	Chemical potential of species *i* in an ideal dilute solution
μ_i^0	Excess chemical potential of i at infinite dilution
P^0	Reference pressure
$K_{i_i}^0$	Henry’s constant at the reference pressure

Chapter Two

E	Kinetic energy of the ion
eV	Ionic charge
m	Mass
z	Charge
v	Velocity
e	Elementary positive charge
I	Current
t	Time
N	Absolute quantity of a given ion
m/z	Mass to charge ratio
D_i	Unitless partitioning ratio of noble gas ‘*i*’ between each phase
C_i	Partial pressure of noble gas ‘*i*’ in the CO_2 phase
W_i	Partial pressure of noble gas ‘*i*’ in the water phase
C_{Raw}	Raw partial pressure of noble gas ‘*i*’ in the CO_2 phase
W_{Raw}	Raw partial pressure of noble gas ‘*i*’ in the water phase
C_A	Volume of CO_2 sampler
W_A	Volume of water sampler
F	Aliquot Correction Factor (37.73)
ρ_c	CO_2 density correction factor
ρ_w	Water density correction factor
$\rho_{sampling(c)}$	CO_2 density during sampling
$\rho_{sampling(w)}$	Water density during sampling
$\rho_{experimental(c)}$	Experimental CO_2 density
$\rho_{experimental(w)}$	Experimental water density
n	Number of moles
$P_{i(absolute)}$	Absolute partial pressure of noble gas ‘*i*’
$P_{i(measured)}$	Measured partial pressure of noble gas ‘*i*’
$\Delta C_{i(P,T)}$	Measurement uncertainty for noble gas ‘*i*’ in the CO_2 phase
$\Delta W_{i(P,T)}$	Measurement uncertainty for noble gas ‘*i*’ in the water phase
ΔC_A	Volume uncertainty for CO_2 sampler
ΔW_A	Volume uncertainty for water sampler
ΔF	Uncertainty in Aliquot Correction Factor
$\Delta\rho_C$	Density correction for CO_2 phase
$\Delta\rho_W$	Density correction for water phase
ΔP	Uncertainty in pressure
P_{Samp}	Sampling pressure
P_{Exp}	Experimental pressure

ΔT	Uncertainty in temperature
ΔT_{Samp}	Sampling temperature
ΔT_{Exp}	Experimental temperature
$\overline{D}_i$	mean partition coefficient for noble gas
$n_{(P,T)}$	Number of samples at a given pressure and temperature
n_{tot}	Total number of samples

Chapter Three

$V(r)$	Lennard-Jones 12 – 6 potential
r	Intermolecular distance
r_m	Distance at which attractive and repulsive interactions are balanced
ε	Depth of the potential well
i	Molecular species ‘*i*’
j	Molecular species ‘*j*’
ε_{ij}	Depth of the potential well between molecular species ‘*i*’ and ‘*j*’
q_α	Point charge on particle α
q_β	Point charge on particle β
ε_0	Vacuum permittivity
$r_{\alpha\beta}$	Distance between particle α and particle β
N	Number of molecules within a simulation
μ	Chemical potential
T	Temperature
P	Pressure
V	Volume
E	Entropy
I	Referring to box I
II	Referring to box II
U_{tot}	Total potential energy of the system
U_{Intra}	Potential energy from intra-molecular forces
U_{Inter}	Potential energy from inter-molecular forces
ΔW	Change to potential energy
ΔU	Change to the system energy
k	Boltzmann constant
ΔV	Change in volume
P_{acc}	Probability of accepting a less favourable new configuration
P_{rand}	System-generated random number between 0 and 1
$\mu_i^{E}{}_{CO_2}$	Excess chemical potential of species ‘*i*’ in the CO_2 phase
$\mu_i^{E}{}_{H_2O}$	Excess chemical potential of species ‘*i*’ in the water phase
μ^{I}_i	Chemical potential of species ‘*i*’ in isolation
μ^{FI}_i	Chemical potential of species ‘*i*’ resulting from a full insertion
W	Rosenbluth weighting
W^I	Full Rosenbluth weight

Chapter Four

κ_i	Deviation coefficient
$D_{i(exp)}$	Experimentally defined partition coefficient for species ‘*i*’
$D_{i(pub)}$	Published partition coefficients for species ‘*i*’
y_{H_2O}	Molar fraction of water in the CO_2 phase
x_{CO_2}	Molar fraction of CO_2 in the water phase

Abstract

Understanding phase behaviour in the geological storage of carbon dioxide

A thesis submitted to the University of Manchester for the degree of Doctor of Philosophy
by Oliver William Peter Warr, September 2013

Noble gas partitioning between supercritical CO_2-H_2O phases can be used to monitor Carbon Capture and Storage (CCS) sites and their natural analogues. However, in order for viable application, noble gas partitioning within these environments must be well constrained. Present estimates of partition coefficient for these systems are taken from the low pressure pure noble gas-water experiments of Crovetto *et al*. and Smith (Crovetto *et al.*, 1982; Smith, 1985). The effect a supercritical CO_2 phase may have on noble gas partitioning is assumed negligible, although this has not been empirically verified. In this work this assumption of noble gas behaviour within a supercritical CO_2-H_2O binary phase system is evaluated using a combined approach of experiment and simulation.

Using a specially commissioned high pressure system at the British Geological Survey paired CO_2 and H_2O samples were collected from noble gas-enriched systems at pressures and temperatures ranging between 90 – 140 bar and 323.15 – 373.15 K. These were analysed for their noble gas content using a quadrupole mass spectrometer system developed specifically for this project. By comparing the relative concentrations of noble gases in each phase partition coefficients were defined for the experimental conditions. These were compared to their low pressure analogues. At higher CO_2 densities all noble gases expressed a significant deviation from predicted partition coefficients. At the highest density (656 kg/m^3) helium values decreased by -54% (i.e. reduced solubility within CO_2) while argon, krypton and xenon values increased by 76%, 106% and 291% respectively. These deviations are due to supercritical CO_2 acting as a polar solvent, the solvation power of which increases as a function of density. Polarisation is induced in each noble gas within this solvent based on their respective polarisabilities. Hence xenon, krypton and argon become more easily solvated as a function of CO_2 density while solvating helium becomes harder. These deviation trends are well described using a second order polynomial. This fit defines a deviation coefficient which can be used to adapt low pressure partition coefficients to allow accurate predictions of partitioning within highly dense CO_2 phases.

Concurrently a Gibbs Ensemble Monte Carlo (GEMC) molecular model was iteratively developed to reproduce noble gas behaviour within these experimental systems. By optimising noble gas-water interactions a pure noble gas-water system was constructed for each noble gas at low pressure which replicated published partition coefficients. These optimised interactions were subsequently applied to low pressure CO_2-H_2O systems where partition coefficients were derived by calculating excess chemical potentials of noble gases in each phase. Again a good agreement was observed with published values. When the model was applied to the experimental conditions however, a poor agreement with the experimental values was observed. Instead simulated values replicated the low pressure Crovetto *et al*. and Smith datasets (Crovetto *et al.*, 1982; Smith, 1985). This was due to no CO_2-noble gas polarisation terms being included in the current iteration of the model. By including this within the model in the future a full reconciliation between the datasets is expected.

Declaration

No portion of the work referred to in the thesis has been submitted in support of an application for another degree or qualification of this or any other university or other institute of learning.

Copyright statement

i. The author of this thesis (including any appendices and/or schedules to this thesis) owns certain copyright or related rights in it (the "Copyright") and s/he has given The University of Manchester certain rights to use such Copyright, including for administrative purposes.

ii. Copies of this thesis, either in full or in extracts and whether in hard or electronic copy, may be made **only** in accordance with the Copyright, Designs and Patents Act 1988 (as amended) and regulations issued under it or, where appropriate, in accordance with licensing agreements which the University has from time to time. This page must form part of any such copies made.

iii. The ownership of certain Copyright, patents, designs, trade marks and other intellectual property (the "Intellectual Property") and any reproductions of copyright works in the thesis, for example graphs and tables ("Reproductions"), which may be described in this thesis, may not be owned by the author and may be owned by third parties. Such Intellectual Property and Reproductions cannot and must not be made available for use without the prior written permission of the owner(s) of the relevant Intellectual Property and/or Reproductions.

iv. Further information on the conditions under which disclosure, publication and commercialisation of this thesis, the Copyright and any Intellectual Property and/or Reproductions described in it may take place is available in the University IP Policy (see http://documents.manchester.ac.uk/DocuInfo.aspx?DocID=487), in any relevant Thesis restriction declarations deposited in the University Library, The University Library's regulations (see http://www.manchester.ac.uk/library/aboutus/regulations) and in The University's policy on Presentation of Theses.

About the Author

The author graduated from the University of Leicester in 2008 with an undergraduate master's degree in Earth Sciences (MGeol). In September 2009 the author joined the School of Earth, Atmospheric and Environmental Sciences within the University of Manchester to take up a Ph.D. studentship under the co-supervision of Professor Chris Ballentine and Professor Andrew Masters (School of Chemical Engineering and Analytical Science). Since then the author has been engaged in the research presented within this thesis.

Acknowledgements

First and foremost I would like to thank my supervisors Professor Chris Ballentine and Professor Andrew Masters for their support, guidance and encouragement throughout this project. Additionally I would like to extend my sincerest gratitude to Dr. Chris Rochelle at the British Geological Survey who not only provided great assistance with the construction and maintenance of the high pressure experimental rig, but also whose unwavering optimism and enthusiasm was a great source of inspiration.

Similarly sincere thanks are also given to John Cowpe, Bevist Clementson, Cath Davies and Dave Blagburn for all their assistance in developing the analytical aspect of the project (as well as their patience when faced with an inexorable tide of questions!). I'd like to thank NERC for funding the project. Thanks are also given to all those I have had the opportunity to work with and learn from; this especially includes my fellow CRIUS members, the Isotope group at Manchester and the people of the Mill who have witnessed the development of my project and helped make my project what it is today. Special thanks go to Drs. Zheng Zhou, Ray Burgess, Jon Fellowes and Benoit Dubacq. A particular mention is made for Dr. Róisín Moriarty who's valued friendship managed to keep nearly everything in perspective throughout the Ph.D. (even G54!); Thanks Dr. M! In the same vein Rob Sargant is equally as appreciated for all his help in keeping me on the straight and narrow wherever the subtle nuances of modelling raised their unfortunate heads!

Additionally my fellow office friends and Ph.D. students, both past and present, are thanked for enriching the experience. Although I can't name everybody this especially includes; James Byrne, Richard Kimber, Abigail Hackston, Mike Lawson, Greg Holland, Chris Boothman, Ashley Brown, Mat Watts, Rich Newport, Annalaura Del Regno, Niel Williams, Lisa Jepson, Jo Foulkes, Victoria Evans, Jonathan Lavi and Sarah Smith.

Unfortunately it cannot be said that work always stayed at work; for that my housemates, Nic and Laura, along those of Tara and 'Channel Commander' Tony have my eternal gratitude for their enduring friendships.

Last but by no means least, my parents are thanked for their love and support both during this Ph.D., and for all time.

I met a traveller from an antique land
Who said: `Two vast and trunkless legs of stone
Stand in the desert. Near them, on the sand,
Half sunk, a shattered visage lies, whose frown,
And wrinkled lip, and sneer of cold command,
Tell that its sculptor well those passions read
Which yet survive, stamped on these lifeless things,
The hand that mocked them and the heart that fed.
And on the pedestal these words appear --
"My name is Ozymandias, king of kings:
Look on my works, ye Mighty, and despair!"
Nothing beside remains. Round the decay
Of that colossal wreck, boundless and bare
The lone and level sands stretch far away.'

Ozymandias
(Percy Bysshe Shelley)

Chapter One

Background and literature

1.1 Introduction

Global warming has been widely accepted by the scientific community as a serious, imminent problem faced by present-day society. The overwhelming evidence indicates that anthropogenic CO_2 is the main causal agent for the enhanced global warming effect (IPCC, 2007). As the global need for energy is currently met by combustion of fossil fuels it is imperative that the CO_2 being produced needs to be disposed of in a viable, efficient and safe way. One potential method of disposing of CO_2 is by storing it securely underground where it is expected to remain secure on a timescale of at least 10^5 years (Bachu, 2003). This process is known as Carbon Capture and Storage (CCS) and is seen as a viable way to resolve the issue while still allowing global energy requirements to be met (IPCC, 2005; Katzer, 2007). Although small-scale sequestration operations are currently underway (Bickle *et al.*, 2007), the focus now must be on implementing large scale CCS projects, as over 25 GT of anthropogenic CO_2 is released annually (Friedmann, 2007). Current estimates indicate that there are at least 2000 GT of storage space suitable for CO_2 storage at depths of 800 m or more (IPCC, 2005).

Under CCS conditions CO_2 is expected to occupy a dense supercritical phase which most efficiently utilises the storage space available (Holloway & Savage, 1993; IPCC, 2005). This will form a separate phase to the existing water-rich pore fluid. However, these two phases are not entirely immiscible and there will be significant phase interactions between the two. It is therefore essential that these interactions be well understood and quantitatively assessed for any large scale project to be considered viable. Unfortunately many key characteristics of CO_2-bearing geological systems are impossible to determine directly. Consequentially proxies are frequently employed to fully document systems of interest. The noble gases are perfect candidates for this role and are ubiquitous within all geological systems. It is their geochemical inertness coupled with a dynamic responsiveness to changing thermodynamic conditions which make them ideal for defining the physical properties of relevant systems (Ballentine *et al.*, 1991; Ballentine *et al.*, 2002; Stalker *et al.*, 2009; Holland & Gilfillan, 2012). In addition the major terrestrial geological reservoirs (i.e. crustal, magmatic or atmospheric) have unique and readily identifiable noble gas isotopic signatures which allow for a quantitative determination of sources and processes operating on the fluids for a given system (Ballentine *et al.*, 2002).

For a CO_2-water system the noble gases are expected to partition into the CO_2 phase. However a quantifiable fraction will also enter the water phase as defined by a Henry's constant and the CO_2/water ratio. This partitioning is dependent on system-specific variables such as pressure (P), temperature (T), volume (V) and phase composition (X). Any perturbations to the $PVTX$ of a system will result in a period of re-equilibration due to a change in the Henry's constant. By determining the noble gas content of each phase and assessing how the perturbation has modified the partition coefficients a method is provided for quantifying how the system has been affected and to what extent. Such an approach is valid for both natural and man-made CO_2-rich systems.

As a result the potential future role that noble gas geochemistry has within CCS projects is unparalleled. Careful sampling and analysis of the noble gas content from CO_2 and water at an injection site will provide a straightforward technique for quantifying key dynamic and static system variables. These include CO_2 dissolution rates, groundwater volumes, and the degree and lateral variation of CO_2-water phase interactions. By determining these factors other site-specific geological considerations for CCS projects can be constrained. These include crustal fluid migration, CO_2 reaction kinetics and porosity (Zhou *et al.*, 2011). Quantifying these variables to an appropriate extent will provide a well-understood system. This is required for sequestration projects whilst providing geochemists with innovative techniques which can be applied to enhancing the understanding of all injection sites. Currently CCS research is focussed on small-scale injection projects designed to assess the stability, feasibility and safety associated with storing CO_2 underground (Stenhouse *et al.*, 2006; Bickle *et al.*, 2007; Kharaka *et al.*, 2007; Duxbury *et al.*, 2012). Parallel research is also ongoing into natural geological analogues containing significant volumes of trapped CO_2. These systems definitively highlight the effectiveness of noble gases in enhancing our understanding of CO_2 system processes. This knowledge can be applied directly to future CCS projects. Recent studies have emphasised that by noble gas analysis alone, the origin of trapped CO_2 can be unequivocally established (Ballentine *et al.*, 2001; Gilfillan *et al.*, 2008), CO_2 migration into geological trapping structures can be traced (Battani *et al.*, 2000; Ballentine *et al.*, 2001; Zhou *et al.*, 2012), the very mechanisms of trapping can be identified and quantified (Gilfillan *et al.*, 2008; Gilfillan *et al.*, 2009; Zhou *et al.*, 2012) and the age of the system can be determined (Ballentine *et al.*, 2001; Zhou *et al.*, 2012).

Frequently one or more of these processes are thought to have occurred sporadically during the development of the system (Zhou *et al.*, 2012). This provides an additional degree of complexity when determining how a system evolved over time. This increased level of complication can be resolved via a combined approach utilising stable carbon isotopes coupled with the noble gases. Each process can then be isolated, defined and quantified to accurately define the evolution of a system over time (Ballentine *et al.*, 2001; Gilfillan *et al.*, 2008). This ability to identify, separate and accurately define the ongoing processes throughout the maturation of CCS natural analogues is unrivalled. This application of noble gas geochemistry to natural examples has therefore afforded a unique insight to subsurface systems which is perfect for application to current and future man-made storage sites.

For their application into studying CCS, artificial noble gas tracers can be injected alongside CO_2. This will not only enhance natural levels of noble gases to aid detection but they will also serve as a marker to track initial migration from the injection point (Stalker *et al.*, 2009; Zhou *et al.*, 2011). As the technology for injection is currently available and only trace quantities of noble gases are required the added cost of including some noble gas isotopes at injection point may be favourable (Nimz & Hudson, 2005). This stage can be easily incorporated into current and future injection projects (Klusman, 2011). All sampling and analytical procedures from a CCS site would be the same as when investigating natural analogues. Once analysed, isotopic deviations from initial noble gas values will be indicative of CO_2 migration from the injection site and interactions with the surrounding media, which can subsequently be quantified using previously discussed approaches. Localised noble gas depletion can also be used to locate and quantify any unanticipated CO_2 migration from the storage site (i.e. leakage). Therefore the addition of noble gases also allows effective monitoring of the overall safety and stability of the site (Marty *et al.*, 2003; Nimz & Hudson, 2005; Mackintosh & Ballentine, 2012).

Currently all noble gas-based research into geological systems at high pressures and temperatures uses Henry’s constants derived from the benchmark studies of Crovetto *et al.*, Smith & Kennedy and Smith (Crovetto *et al.*, 1982; Smith & Kennedy, 1983; Smith, 1985). These experimental studies investigated noble gas solubility in water/brines over a range of temperatures and pressures. This was achieved using interactions of pure phases with one another to generate partition coefficients. By applying these partition coefficients to geological systems identical noble gas behaviour is assumed for both system types. However the initial studies were at much lower pressures and temperatures than the geological systems where they are typically applied. Additionally they did not incorporate a supercritical CO_2 phase. The assumption being made therefore is that none of these changes affect the behaviour of noble gases. Thus noble gases are expected to maintain near ideal behaviour with all water-CO_2-noble gas interactions considered negligible, even at high pressures and temperatures. Such supposition requires valid justification; however, no corroborating published studies exist (Ballentine *et al.*, 2002). Therefore the legitimacy of applying these studies to geological systems must be questioned and tested.

Once the behaviour of noble gases within CO_2-water systems is known applicability to CCS programs and their natural analogues will have a greater legitimate basis. Additionally, depending on the outcome of such studies, the potential exists for justifying research into other sympathetic geological systems/processes where noble gas behaviour is equally less well constrained. Examples of this are magma degassing and melt partitioning which are also based on low pressure noble gas experiments (Jambon *et al.*, 1986; Aubry *et al.*, 2013).

1.2 Aims

The primary focus of this study is to accurately define noble gas partition coefficients between a supercritical CO_2 phase and a water-rich phase. To realise this goal a combined approach of experimental and simulation-based techniques are employed. The objectives of the project are thus:

1. To generate experimental noble gas partitioning data over a range of temperatures and pressures for a supercritical CO_2-water binary phase system and relevant to CO_2 sequestration targets.

2. Using these data, to build and test a robust modelling technique which accurately predicts noble gas behaviour over a range of thermodynamic and environmental conditions.

The ranges of primary interest are 323.15 – 373.15 K and pressures between 90 – 140 bar as these are reasonable ranges for the P,T conditions to be found within shallow aquifers suitable for CCS. Under these conditions CO_2 is comfortably in the supercritical regime (Bachu, 2003). By formulating a simulation technique, able to accurately predict partition values for any given system, the future role of noble gases as tracers within CCS environments can be assumed with much greater confidence. Additionally such a model can be used to investigate current conceptions of noble gases behaviour in natural analogues. Such systems are discussed in greater detail in section 1.3. Any discrepancies can subsequently be quantified via this model which will also provide a sound basis for reinterpretation of any affected system.

1.3 Review of current literature

1.3.1 Introduction

There are six noble gases: helium, neon, argon, krypton, xenon and radon. Each of these has different stable isotopes associated with them, with the exception of radon. They all occupy group VIII in the periodic table and are considered, for all intents and purposes, to be completely chemically inert due to their complete electron shells. As no stable isotopes of radon exist and given their short half-lives their usefulness as geological tracers in the context of CCS is restricted. So radon will not be considered further. The other five all exist only in trace amounts in any given natural system and this coupled with their volatile nature make them highly susceptible to any chemical or physical change affecting the system. As each of the five major noble gases possesses different physical properties due to their mass, induced polarisation potential and sizes, they all possess a unique response to any change affecting a system. It is possible therefore to utilise noble gases to investigate natural processes which occur both cosmogenically and terrestrially.

The inherent potential application of noble gases was first explored with the investigation of helium and argon isotopes in natural gas samples (Zartman *et al.*, 1961). Since this pioneering work their usefulness as tracers of crustal fluid processes has rapidly come to the fore with applications to a wide range of geologically important systems. For example they can be used to determine water recharge temperatures and rates in natural aquifers (Cey *et al.*, 2009; Thoma *et al.*, 2011; Heilweil *et al.*, 2012), understanding fluid origin, migration and evolution within gold mineralisation zones (Burnard *et al.*, 1999; Hu *et al.*, 2004; Kendrick *et al.*, 2007) documenting flow processes at work within oil reservoirs (Pinti & Marty, 1995; Kennedy *et al.*, 2002; Prinzhofer *et al.*, 2007) or constraining temperatures for palaeoclimate reconstructions (Kluge *et al.*, 2008; Klump *et al.*, 2008; Castro *et al.*, 2012).

The remainder of this chapter gives a concise overview of the current level of terrestrial noble gas research. Specific examples of key applications are defined and discussed where appropriate. Supplementary information is provided in the relevant references and in the following publications (Ballentine *et al.*, 2002; Ballentine & Burnard, 2002; Graham, 2002; Porcelli *et al.*, 2002; Holland & Gilfillan, 2012; Sano *et al.*, 2012).

1.3.2 Isotopes and origins of noble gases

The isotopes of all terrestrial noble gases have two major primary sources: those produced via nucleosysnthesis (and subsequently captured during the accretion of the Earth) and isotopes created via nuclear decay processes in the post accretion phase (Pepin & Porcelli, 2002). These post accretion nuclear interactions can be further sub-divided: radiogenic, nucleogenic and fissiogenic (Ballentine & Burnard, 2002). Radiogenic refers to daughter products produced as a result of radioactive decay of the parent nucleus. Nucleogenic-derived noble gases are the product of nuclear interactions between a nucleus and subatomic particles, for example neutron capture, while fissiogenic is the term given to noble gases formed via nuclear fission of larger, unstable nuclei.

A complete list of each stable noble gas isotope as well as all major formation processes has been compiled for Table 1.1 using data from Ozima & Podosek and Porcelli *et al.* (Ozima & Podosek, 2002; Porcelli *et al.*, 2002).

Isotope	Primary terrestrial source	Parents	Half life
^{3}He	Nucleosynthesis, Radiogenic	^{3}H	12.26a
^{4}He	Radiogenic	^{232}Th, ^{235}U, ^{238}U	14.01Ga, 703.8Ma, 4.468Ga
^{20}Ne	Nucleosynthesis, Nucleogenic	^{17}O (α,n)	N/A
^{21}Ne	Nucleosynthesis, Nucleogenic	^{18}O (α,n), ^{24}Mg (n,α)	N/A
^{22}Ne	Nucleosynthesis, Nucleogenic	^{25}Mg (n,α)	N/A
^{36}Ar	Nucleosynthesis, Radiogenic	^{36}Cl	0.301Ga,
^{38}Ar	Nucleosynthesis		
^{40}Ar	Radiogenic	^{40}K	1.251Ga
^{78}Kr	Nucleosynthesis		
^{80}Kr	Nucleosynthesis		
^{82}Kr	Nucleosynthesis		
^{83}Kr	Nucleosynthesis	^{235}U ^{238}U	703.8Ga, 4.468Ga
^{84}Kr	Fissiogenic	^{235}U ^{238}U, ^{244}Pu	703.8Ga, 4.468Ga 80Ma
^{86}Kr	Fissiogenic	^{235}U ^{238}U, ^{244}Pu	703.8Ga, 4.468Ga 80Ma
^{124}Xe	Nucleosynthesis		
^{126}Xe	Nucleosynthesis		
^{128}Xe	Nucleosynthesis		
^{129}Xe	Radiogenic, Fissiogenic	^{129}I	15.7Ma
^{130}Xe	Nucleosynthesis		
^{131}Xe	Fissiogenic	^{235}U ^{238}U, ^{244}Pu	703.8Ga, 4.468Ga 80Ma
^{132}Xe	Fissiogenic	^{235}U ^{238}U, ^{244}Pu	703.8Ga, 4.468Ga 80Ma
^{134}Xe	Fissiogenic	^{235}U ^{238}U, ^{244}Pu	703.8Ga, 4.468Ga 80Ma
^{136}Xe	Fissiogenic	^{235}U ^{238}U, ^{244}Pu	703.8Ga, 4.468Ga 80Ma

Table 1.1. Terrestrial noble gas isotopes and their major sources. Secondary and minor sources have been omitted. Data from Ozima & Podosek and Porcelli *et al.* (Ozima & Podosek, 2002; Porcelli *et al.*, 2002).

As Table 1.1 indicates, the noble gases and their respective isotopes are derived from a wide range of processes. Many of these processes are ongoing and continue to add significantly to the terrestrial stockpile of noble gases e.g. ^{40}K → ^{40}Ar = 102.2 atoms/gram per year for average continental crust (Ballentine & Burnard, 2002). However other nucleosynthetic noble gases (e.g. ^{3}He or ^{129}Xe) are only produced by either relatively minor terrestrial processes (e.g. cosmogenic) or from the decay of unstable nuclei with rapid decay chains which are now exhausted. The terrestrial balance of these isotopes can therefore be considered constant in most scenarios with minor production factored in where required.

As both extinct and extant noble gas isotope sources exist for noble gas isotope production it can be logically assumed that noble gas isotopic ratios have not stayed constant since the formation of the Earth. For example, over the last 4.5 Ga the overall ratio of ^{21}Ne/^{20}Ne in the crust has slightly decreased by approximately 0.5% while the ^{22}Ne/^{20}Ne ratio has increased by around 0.7% (Leya & Wieler, 1999). Over the same time period the ^{3}He/^{4}He ratio (R_A) in the convecting mantle has evolved from 120 to ~8 R_A (Graham, 2002) Furthermore, as the distribution of parent materials are not homogenously distributed, the resultant production rates of noble gas isotopes in different reservoirs are also different, further distorting original isotopic values. For example, uranium and thorium decay, which are the primary sources of ^{4}He, are both more concentrated in the crust (250 ppm) (Vinogradov, 1988) than in the mantle (0.5 – 2.4 ppm) (Seitz & Hart, 1973); this has resulted in a greater rate of ^{4}He production per volume in the crust than in the mantle. ^{3}He, on the other hand is far more abundant in the mantle than in either the crust or the atmosphere (Lupton & Craig, 1975) due to it being captured primarily within the mantle during accretion (Tolstikhin, 1975). Other noble gases and their parent elements are similarly unequally distributed within different terrestrial components. Thus three discrete noble gas reservoirs have developed, each possessing a distinctly unique set of isotopic ratios and absolute concentrations. These ratios have evolved over time as certain noble gas isotopes are created and the reservoirs have interacted with one another (Porcelli & Ballentine, 2002).

Within the Earth we can consider three main distinct reservoirs; the atmosphere, the crust and the mantle. The core is currently not known to be a significant reservoir of noble gases, although this is still recognised to be a potential viable fourth reservoir (Porcelli & Halliday, 2001; Ballentine *et al.*, 2005). Due to the vast majority of geological systems of interest involving interactions with more than one such reservoir via processes such as groundwater flow or influxes from the mantle reservoir it is important each reservoir is fully documented to provide us with a means to quantify each reaction.

1.3.3 The atmospheric reservoir

Out of the three reservoirs this reservoir is the best constrained due to its easily accessible nature. The noble gases which exist in the atmospheric reservoir are listed in Table 1.2 alongside their relative abundances to a single isotope for each noble gas and the percent molar abundance.

Isotope	Relative Abundances	Percent Molar Abundance
^{3}He	(1.399 ± 0.013) x 10^{-6}	0.00014
^{4}He	≡ 1	100
^{20}Ne	9.80 ± 0.08	90.5
^{21}Ne	0.0290 ± 0.0003	0.268
^{22}Ne	≡ 1	9.23
^{36}Ar	≡ 1	0.3364
^{38}Ar	0.1880 ± 0.0004	0.0632
^{40}Ar	295.5 ± 0.5	99.6
^{78}Kr	0.6087 ± 0.002	0.3469
^{80}Kr	3.9599 ± 0.002	2.2571
^{82}Kr	20.217 ± 0.004	11.523
^{83}Kr	20.136 ± 0.021	11.477
^{84}Kr	≡ 100	57
^{86}Kr	30.524 ± 0.025	17.498
^{124}Xe	2.337 ± 0.008	0.0951
^{126}Xe	2.180 ± 0.011	0.0887
^{128}Xe	47.15 ± 0.07	1.919
^{129}Xe	649.6±0.9	26.44
^{130}Xe	≡ 100	4.07
^{131}Xe	521.3 ± 0.8	21.22
^{132}Xe	660.7 ± 0.5	26.89
^{134}Xe	256.3 ± 0.4	10.43
^{136}Xe	217.6 ± 0.3	8.857

Table 1.2. The noble gas isotopic ratios characterising a standard air sample. Data from Porcelli *et al*. 2002 (Porcelli *et al.*, 2002).

This reservoir was initially formed during early mantle degassing approximately 80 Ma after formation (Brown, 1952; Allegre *et al.*, 1987; Turner, 1989; Ozima & Podosek, 2002; Ballentine & Holland, 2008) and as such the noble gas isotopic signature initially mirrored the volatile composition captured during the Earth's accretionary period whist at the same time depleted the other reservoirs of this isotopic fingerprint (Pepin & Porcelli, 2002). Subsequent degassing from both the crust and the mantle containing a significant primordial and radiogenic noble gas content together with late input of further cometary (Holland *et al.*, 2009) or chondritic (Halliday, 2013) sources have resulted in this reservoir evolving and obtaining its current isotopic signature (Porcelli & Ballentine, 2002; Holland *et al.*, 2009; Marty, 2012; Halliday, 2013). Compositionally the dominant noble gas present in this reservoir is argon; this comprises 0.943% of the total atmosphere and therefore constitutes a major component; all other noble gases exist in significantly smaller trace amounts and as such are best represented as relative isotopic abundances (Table 1.2). Other key isotopes present in the atmospheric signature are ^{20}Ne, ^{22}Ne, ^{36}Ar, ^{38}Ar and ^{84}Kr, none of which are produced in any significant volumes in either the mantle or the crust (Ballentine & Burnard, 2002; Ballentine & Holland, 2008; Sherwood-Lollar & Ballentine, 2009) which render them suitable as quantifiable markers for the atmospheric reservoir when interacting with other reservoirs. Given the strong radiogenic presence in this phase (e.g. ^{40}Ar ^{129}Xe) resulting from outgassing, relative to nucleogenic-derived noble gases, a dearth of ^{4}He is noted. This is due to its short residence time (approximately 1 Ma) within this reservoir, before it is lost to space (Torgersen, 1989; Pepin & Porcelli, 2002). No other noble gases are known to leave the terrestrial system.

By constraining the unique isotopic ratios which are present within this reservoir it is possible to quantitatively indicate the contributions made by this reservoir to a geological system involving interactions with other reservoirs. Recently the atmospheric isotopic signature has been used to indicate that a significant amount of the heavy noble gases now in the mantle have been recycled (Ballentine *et al.*, 2007; Ballentine & Holland, 2008). It has also been used to assess the extent of atmospheric enrichment which has occurred in oil and gas reservoirs (Ballentine *et al.*, 1991; Ballentine *et al.*, 1996; Torgersen & Kennedy, 1999) and in dating the ages deep mine water in South Africa (Lippmann *et al.*, 2003).

A common way for an atmospheric component to enter a subsurface geological system is via groundwater flow. At the surface a small fraction of atmospheric noble gases partition into surface water. Over geological timescales this atmospheric equilibrated water migrates into crustal systems and where it interacts with other fluids such as oil, gas or carbon dioxide. During these interactions a fraction of the noble gases within the water enters the new phase. Therefore the atmospheric signal is transferred and preserved within geological systems. As all noble gas partitioning is considered temperature dependent (e.g. Crovetto *et al.*, 1982; Smith, 1985; Ballentine *et al.*, 2002) it is also possible to analyse the noble gas content of groundwater to derive palaeotemperatures of a region (Stute *et al.*, 1992) or determine groundwater flow rates within hydrothermal regions (Heilweil *et al.*, 2012). An in-depth evaluation of the factors affecting partitioning is discussed in sections 1.3.8 – 1.3.11 and in the summary at the end conclusion of this literature review.

Thus the unique isotopic noble gas signature of this reservoir can therefore be applied to better constrain complex geological systems. For example it has been used to resolve the crustal neon isotopic ratios (Kennedy *et al.*, 1990), and indicate noble gas isotopic differences within the subcontinental lithosphere (Dunai & Porcelli, 2002). Additionally where its unique isotopic signature is absent it can be used to discount geological processes which involve the atmospheric reservoir (e.g. Gilfillan *et al.*, 2008). Furthermore atmospheric noble gas ratios can also be used to indicate sample contamination issues. Geological samples which yield isotopic ratios close to that of the air standard suggest they may have become compromised and therefore are not suitable representatives of their original system. Where atmospheric contamination is only minor corrections can be applied to restore original values (e.g. Ballentine *et al.*, 2002; Sano *et al.*, 2012). Thus our understanding of the atmospheric signal can provide a method of preserving the integrity of a study (Dunai & Porcelli, 2002; Ballentine *et al.*, 2005).

1.3.4 Mantle

Compared to the atmospheric reservoir the isotopic signature of the mantle is poorly constrained. It is generally considered to be the main store of primordial noble gases which accumulated during the early accretionary period of the Earth (Lupton & Craig, 1975; Allegre *et al.*, 1987; Caffee *et al.*, 1999) coupled with those which are radiogenically derived (Ballentine & Holland, 2008). The primary source of data on the noble gas isotopic ratios has been derived from Mid Ocean Ridge Basalts (MORB) and Oceanic Island Basalts (OIB). OIBs are commonly thought to originate from mantle plumes thus providing samples from the lower, undegassed mantle uncontaminated by other noble gas sources. This is not necessarily the case for MORB. The key isotope which is used to indicate the presence of mantle noble gases within a geological system is ^{3}He, trapped during accretion (Tolstikhin, 1975) and depleted from both the crust and the atmosphere (Pepin & Porcelli, 2002). Also existing in relative abundance are primordial ^{20}Ne and ^{36}Ar which are also potential indicators of a mantle component. However these isotopes are prone to atmospheric contamination. Consequentially ^{3}He remains the noble gas isotope of choice for unequivocally determining mantle fluid contributions to a geological system (e.g. Tolstikhin, 1975; Allegre *et al.*, 1987; Pepin & Porcelli, 2002; Ballentine & Holland, 2008; Hu *et al.*, 2012; Pinti *et al.*, 2013).

A recent review of all available data on noble gas contents for both MORB and OIB samples indicates that a significantly higher average ^{3}He/^{4}He ratio (up to 40 R_A) exists in OIB samples and this varies considerably depending on the sample location. This variation is considerably greater than in MORB which has approximately a normal distribution function of values between 6.5 – 9.5 R_A (Graham, 2002). This primarily suggests the existence of compositionally distinct regions existing within the mantle which are the source for MORB and OIB respectively. This in turn suggests less depleted regions may exist within the mantle with compositions closer to that of Bulk Silicate Earth (BSE), the initial ratios when the Earth formed. This contrasts with the ^{20}Ne/^{22}Ne ratio which appears potentially uniform for both MORB and OIB (Graham, 2002; Moreira & Kurz, 2012). However this apparent ^{20}Ne/^{22}Ne homogeneity has recently been contested by reproducible studies which indicate a ^{20}Ne/^{22}Ne ratio within mantle plumes closer to solar values than ratios measured in the upper mantle (Caffee *et al.*, 1999; Yokochi & Marty, 2004). One proposed solution to account for the inferred existence of two isotopically distinct regions is that the Earth initially formed with the original solar isotopic ratios. The Earth then underwent extensive degassing although some deep mantle reservoirs retained their nucleogenic noble gas signature. Solar wind-derived noble gases then enriched the mantle and provided the majority of noble gas material thus becoming the dominant ratios, although the minor deep mantle reservoirs containing the original ratios now act as plume sources providing the isotopic discrepancy (Ballentine *et al.*, 2005).

Unfortunately our current understanding of upper-lower mantle interactions are poorly constrained and so the validity of this compared with any alternative hypotheses cannot be tested further until this flux is better understood. Furthermore, due to difficulties in obtaining unequivocally uncontaminated OIB and MORB samples definitive noble gas isotopic values for these mantle sources remain unconfirmed at this time (Pepin & Porcelli, 2002; Ballentine *et al.*, 2005). Despite these limitations, critically reviewing the evidence for any mantle heterogeneity and subsequently determining the origins, distribution and extent of mixing, remain a key focus for the mantle geochemistry community.

1.3.5 Crust

In addition to the mantle and the atmosphere, the Earth's crust also acts as both origin and reservoir of a significant proportion of terrestrial noble gas isotopes. Furthermore the crust is where the majority of economically important geological systems are found such as aquifers or those bearing oil. As such it is essential that the processes involving formation and interactions of noble gases within this system are constrained to the best of our abilities. The crustal region possesses a significant (~ 40%) amount of the Earth's radioactive material budget (Vinogradov, 1988; Rudnick & Fountain, 1995). Therefore the crust acts as a key source of many of the noble gases formed via radioactive decay within the Earth. The most important radiogenic isotopes produced in this reservoir are ^{4}He, ^{21}Ne and ^{40}Ar which are produced both directly and indirectly by the decay of ^{235,} ^{238}U, ^{232}Th and ^{40}K. Due to the concentrations of these parent isotopes within the crust, production rates by volume of these noble gas isotopes are far greater in this reservoir compared to the mantle or atmosphere. A detailed list of isotopic production is outlined in Table 1.3:

Isotope	Present day production (cm^3 STP/year)	Total produced in crust (cm^3 STP over 4.5 Ga)	Atmospheric reservoir % comparison
^{3}He	6.00×10^{4}	4.49×10^{14}	1549%
^{4}He	7.98×10^{12}	5.93×10^{22}	285484%
^{20}Ne	3.53×10^{4}	2.62×10^{14}	0.0004%
^{21}Ne	3.65×10^{5}	2.71×10^{15}	1.4051%
^{22}Ne	7.29×10^{5}	5.39×10^{15}	0.0810%
^{36}Ar	5.73×10^{4}	4.26×10^{14}	0.0003%
^{38}Ar	2.63×10^{4}	1.97×10^{14}	0.0008%
^{40}Ar	1.46×10^{12}	2.95×10^{22}	79.94%
^{83}Kr	1.41×10^{2}	9.25×10^{11}	0.0002%
^{84}Kr	5.11×10^{2}	3.35×10^{12}	0.0001%
^{86}Kr	3.36×10^{3}	2.20×10^{13}	0.0028%
^{131}Xe	1.90×10^{3}	1.25×10^{13}	0.0170%
^{132}Xe	1.26×10^{4}	8.27×10^{13}	0.0892%
^{134}Xe	1.81×10^{4}	1.18×10^{14}	0.3297%
^{136}Xe	2.18×10^{4}	1.43×10^{14}	0.4690%

Table 1.3. The current and total noble gas isotope production values within the crust. Total production is also compared to the current composition of atmospheric reservoir. Table modified from Ballentine & Burnard ,2002 (Ballentine & Burnard, 2002) with atmospheric reservoir percentages originally derived from Ozima & Podosek, 2002 (Ozima & Podosek, 2002).

From Table 1.3 it can clearly be observed that even assuming no significant loss of crustagenic noble gases the radiogenic and nucleogenic production of ^{4}He, ^{21}Ne and ^{40}Ar has occurred in sufficient quantities to alter the initial nucleosynthetic values. Although ^{3}He has also been produced via radioactive decay, the ^{4}He production rate is much higher (~1x 10^{8} greater) resulting in progressively much lower R_A numbers (average ~0.01 R_A) in the crust (Ballentine & Burnard, 2002) than in either the atmosphere ($R_A = 1$) or mantle ($R_A = 6.5 – 40$). These three isotopes, which are most measurably increased in crustal systems, can be combined with other noble gas isotopes to obtain isotopic ratios which characterise the crustal noble gas component. By defining this reservoir via isotopic ratios it is possible to distinguish crustal values from other inputs. For example, despite the atmosphere possessing a significant volume of ^{40}Ar, it also has significantly greater amounts of both ^{36}Ar and ^{38}Ar compared to the crust. Thus key isotopic ratios for each reservoir are unique. The unambiguous nature of such ratios allows for straightforward quantification and correction for any atmospheric contamination within samples (Ballentine *et al.*, 2002; Sano *et al.*, 2012). In addition to these primary isotopes production of other noble gases also deviate from atmospheric values. As a result specific noble gases such as ^{20}Ne, ^{84}Kr and ^{136}Xe can also be used in combination with other noble gases to give unique crustal ratios. These also provide means for quantitative determination of crustal inputs within complex systems (e.g. Kennedy *et al.*, 1990; Ballentine & Burnard, 2002; Zhou *et al.*, 2012).

As highlighted in Table 1.3 the production rates of each noble gas isotope are unique. Isotopic ratios are therefore expected to have evolved over time. Prime examples of this are the isotopic ratios of neon ^{20}Ne/^{22}Ne and ^{21}Ne/^{22}Ne (Kennedy *et al.*, 1990). By defining the rate of change it is possible to constrain the age of systems based on the subsequent accumulation (Kennedy *et al.*, 1990). The evolution of these ratios can also be plotted against one another to generate an isotopic gradient which is representative of the reservoir. Deviations from this gradient indicate a non-crustal component. Therefore these deviations can be used to quantitatively determine additional reservoir components within a crustal system (Kennedy *et al.*, 1990; Ballentine, 1997; Zhou *et al.*, 2012). This is displayed graphically in Figure 1.1.

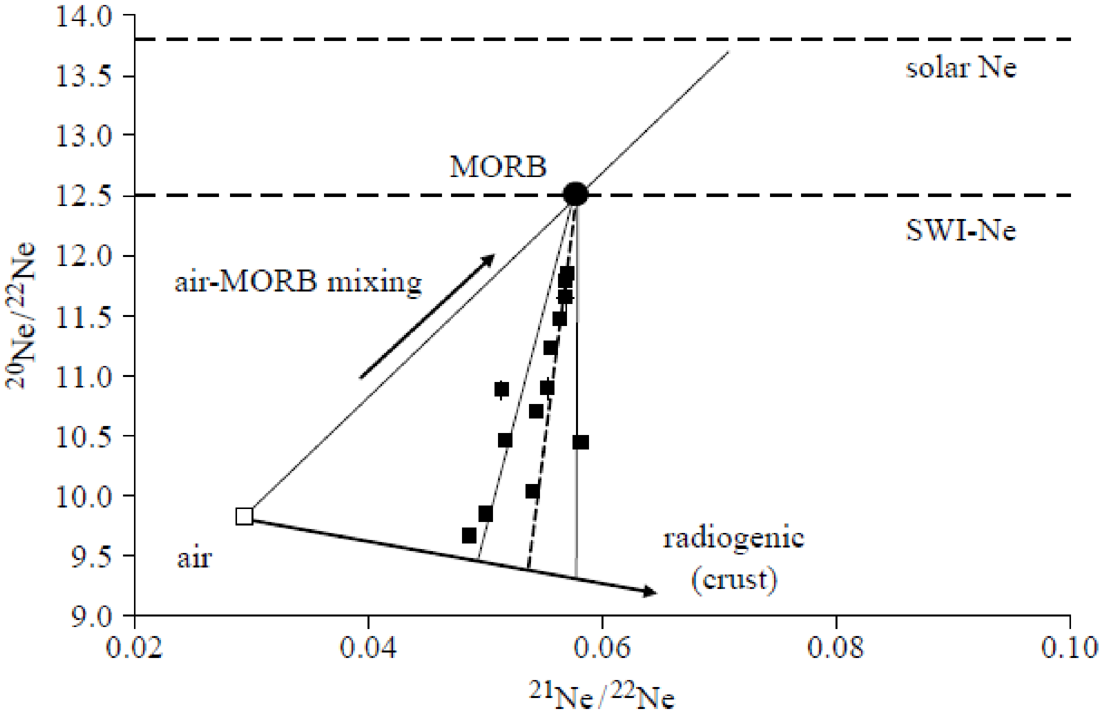

Fig. 1.1. The neon isotopic ratios in the atmosphere, the mantle (MORB) and in the crust (reproduced from Ballentine & Holland, 2008). The unique isotopic ratios allow quantification of all noble gas inputs from each reservoir. Plotted data from analysed CO_2 well gas samples (Ballentine *et al.*, 2005; Holland & Ballentine, 2006).

Cosmic ray interactions with the uppermost region of the crust can also generate noble gases, primarily ^{3}He and ^{21}Ne. However production is restricted to only the uppermost region (~3.5 m) of the crust with attenuation of cosmic rays resulting in an exponential decrease of production with depth (Niedermann, 2002). Absolute production rates are reproduced in Table 1.4.

Percentage	Crustal production (cm^{3} STP/year)	Cosmogenic production (cm^{3} STP/year)	Percentage (%)
^{3}He	6.00×10^{4}	1.29×10^{3}	2.15
^{4}He	7.98×10^{12}	1.29×10^{3}	1.62×10^{-8}
^{20}Ne	3.53×10^{4}	2.93×10^{-2}	8.30×10^{-5}
^{21}Ne	3.65×10^{5}	2.93×10^{-2}	8.03×10^{-6}
^{22}Ne	7.29×10^{5}	2.93×10^{2}	4.02×10^{-6}
^{36}Ar	5.73×10^{4}	7.31×10^{2}	1.28
^{38}Ar	2.63×10^{4}	7.31×10^{2}	2.78
^{40}Ar	1.46×10^{12}	7.31×10^{2}	5.01×10^{-8}

Table 1.4. The cosmogenic production of noble gases within the crust compared with total production rates. The cosmogenic production is additionally presented as a percentage of total production. Values from Ballentine & Burnard, 2002 (Ballentine & Burnard, 2002).

Comparing the values in Table 1.4, total crustal production indicates that cosmogenic noble gases can reasonably be considered negligible for most geological systems.

1.3.6 Noble gases as solute particles

The formation of many geological systems and their subsequent evolution frequently involves the interactions of at least two chemically distinct phases. These can be single events such as injection of magmatic CO_2 into an aquifer, continuous events such subsurface groundwater migration or combinations of the two. The extent to which we are able to identify and quantify these interactions underpins the limits of our understanding of such systems. Frequently it is impractical to accurately constrain system-specific qualities directly; in such cases proxies (e.g. tracers) must be relied upon to fill in the gaps. As previously discussed with key examples, the noble gases are such a group of conservative tracers which are currently employed in this fashion to document systems to a previously unknown degree of detail. It is their physical behaviour within these phases coupled with their reactions to changing conditions which are detected, measured and interpreted to allow construction of a well-constrained system model. However, it follows that for this modelling approach to be considered viable the noble gas interactions must be well constrained for expected conditions within the chosen system. What follows is an overview of our current level of understanding for the physical behaviour of noble gases within geological environments. Identified gaps and limitations to our understanding are indicated where applicable.

1.3.7 Rayleigh fractionation

Where a geological system is considered closed the noble gas isotopic ratios at any given time can be considered as a function of respective isotope production rates added to initial values. However, most commonly a system possesses a degree of openness whereby noble gas bearing fluids can both enter and leave the system, for example via groundwater flow or gaseous migration. As different noble gases possess different diffusion coefficients and solubilities (Jahne *et al.*, 1987; Krause & Benson, 1989; Bourg & Sposito, 2008) such migration in and out of the system can significantly alter noble gas isotopic ratios (Ballentine *et al.*, 2002). This process of isotopic fractionation can therefore result in systems being progressively enriched or depleted in particular noble gases relative to one another (Ballentine *et al.*, 1991). It is necessary therefore that this fractionation be taken into account. Where the movement of noble gases in, out or within a geological system is primarily due to diffusion processes the rate of diffusion is considered to be a function of the mass of the noble gas (Jahne *et al.*, 1987). In these instances individual isotopes of the same noble gas are expected to diffuse at different rates. Consequentially isotopic ratios for any given noble gas are liable to be affected over time. More commonly, however, isotopic fractionation between noble gas species is due to mass independent processes such as partitioning between two or more phases. In these scenarios all isotopes for a given noble gas are assumed to behave uniformly. Under these conditions noble gas behaviour can commonly be described using the Rayleigh fractionation law which has been normalised to argon values. For example, when considering the effect of gas bubbles within a previously equilibrated water phase the adjustment process is as follows:

$$([i]/[Ar])_{water} = ([i]/[Ar])_o F_{Ar}^{(\alpha-1)} \quad (1.1)$$

where $([i]/Ar)_{water}$ is the current isotopic ratio of noble gas i to argon in water, $([i]/Ar)_o$ is the original isotopic ratio, F_{Ar} is the remaining fraction of Ar in the water phase and α is the gas/liquid fractionation coefficient. This coefficient is derived from the Henry's constant for each noble gas at the system temperature and pressure:

$$\alpha = (K_i/K_{Ar}) \quad (1.2)$$

where K_i is the Henry's constant for the noble gas in question and is identical for all isotopes (Crovetto *et al.*, 1982; Smith, 1985).

1.3.8 Solubility and thermodynamics

Noble gases are present in most environments at trace levels. Whilst their highly volatile nature results in a strong affinity for the gaseous phase, in cases where a liquid phase is also present a fraction of the noble gas content will also enter this phase to maintain chemical equilibrium. The absolute amount of each noble gas entering the liquid phase depends on the respective volumes in contact with one another and is both temperature and pressure dependent. As the chemical potential of each noble gas is different it logically follows that their solubilities are also dissimilar. The relationship between noble gas solubility and pressure at a given temperature can be expressed using Henry's Law:

$$P_i = K_i x_i \quad (1.3)$$

where P_i is the pressure of the noble gas in the gaseous phase, K_i is Henry's constant for species i, empirically derived at a given temperature (T) and x_i is the molar fraction of the noble gas within the liquid phase. As stated in section 1.3.7, isotopic effects on solubility are assumed to be insignificant allowing for each noble gas to be considered as a single species. This equation allows for the relationship between noble gases in both phases to be thermodynamically quantified. It is this relationship which underpins the usefulness of noble gases as proxies for geological systems.

However Equation 1.3 is only valid in its current form when ideality is assumed in both phases. As ideality is not expected in the majority of geological systems deviations from ideality in both phases must be taken into account.

1.3.9 Non-ideality in the gaseous phase

In order to reconcile ideality with reality for the noble gases it is essential a modifier to the apparent pressure is included in order to yield an effective pressure which correlates to the true chemical potential of the gas. This modifier is known as the gas phase fugacity coefficient *Φ*:

$$\Phi_i P_i = K_i x_i \tag{1.4}$$

This modifying factor is dependent on temperature, pressure and gas composition. As noble gas partitioning is a result of chemical equilibrium between the noble gases in each phase it is essential that this coefficient is considered for each noble gas to facilitate accurate estimations of solubility within the water phase. To calculate a fugacity coefficient for a given gas the real molar volume of the gas (V_m) is required. This can be calculated by rearranging a virial equation of state consisting of empirically derived coefficients (Ballentine *et al.*, 2002; Dymond *et al.*, 2002):

$$PV_m / RT = 1 + B(T)/V_m + C(T)/V_m{}^2 \tag{1.5}$$

V_m can be determined to a high degree of accuracy from this via Newton's iterative method of approximation. The resulting value for the real molar value can then be used to calculate the fugacity constant at the given temperature and pressure:

$$\Phi(P.T) = \exp[\,B(T)/V_m + (C(T) + B(T)^2 / 2V_m{}^2)] \tag{1.6}$$

Coefficient values for *B* and *C* for pure noble gas phases at a range of temperatures are taken from the work of Dymond *et al.*, (Dymond *et al.*, 2002):

	Helium		Neon		Argon		Krypton		Xenon	
T (K)	*B(T)*	*C(T)*	*B(T)*	*C(T)*	*B(T)*	*C(T)*	*B(T)*	*C(T)*	*B(T)*	*C(T)*
273.15	12.63	111.50	10.70	305.40	-21.30	1280.00	-61.650	2596.50	-152.80	6510.00
298.15	11.70	102.25	11.40	227.00	-15.65	1206.67	-50.867	2214.00	-131.37	6093.00
323.15	11.58	102.50	12.00	212.67	-11.15	1120.00	-41.960	2239.00	-110.00	5195.33
348.15	11.36	96.67	12.20	230.00	-7.20	1046.67	-34.367	1888.67	-95.250	4591.67
373.15	11.42	101.20	12.43	298.00	-4.00	1031.67	-28.300	1935.50	-82.367	4058.75
398.15	11.20	93.33	12.85	211.00	-1.15	925.00	-22.600	1630.67	-70.600	3483.00

Table 1.5. Coefficient values for *B* and C for a range of temperatures. Values are averages from Dymond *et al.*, 2002 (Dymond *et al.*, 2002).

Using values from Table 1.5 the effect of fugacity on a pure noble gas phase at different temperatures and pressures can be considered:

	Helium		Neon		Argon		Krypton		Xenon	
T (K)	Φ_1	Φ_2	Φ_1	Φ_2	Φ_1	Φ_2	Φ_1	Φ_2	Φ_1	Φ_2
273.15	1.03	1.09	1.02	1.08	0.96	0.90	0.87	0.74	2.50	8.31
298.15	1.03	1.08	1.03	1.08	0.97	0.93	0.89	0.76	1.72	4.23
323.15	1.03	1.08	1.03	1.08	0.98	0.95	0.91	0.80	1.25	2.31
348.15	1.03	1.08	1.03	1.09	0.99	0.98	0.92	0.83	1.05	1.67
373.15	1.03	1.08	1.03	1.09	0.99	1.00	0.94	0.86	0.95	1.33
398.15	1.02	1.08	1.03	1.09	1.00	1.02	0.95	0.89	0.87	1.11

Table 1.6. Fugacity values for each noble gas at 50 (Φ_1) and 150 (Φ_2) bar pressure between 273.15 – 398.15 K. Maximum deviation from ideality occurs at low temperatures and high pressures. Values above 1 indicate a higher chemical potential in the gas phase than predicted under ideal conditions and so correspond with greater solubility within the water phase. All values are given to 2 decimal places.

As displayed in Table 1.6 fugacity can have a significant impact (≥ 5%) on partial pressures of noble gases and result in the effective pressure being considerably different from the ideal pressure. However it should be reiterated that this fugacity is only for pure noble gases phases; the effect a mixed gas phase comprised of other molecular types would have on the fugacity of a noble gas component has not yet been considered. For molecular species existing in high concentrations within this gas it is reasonable to assume that intermolecular interactions between unlike molecules would occur so infrequently so as to be considered insignificant. For such components the Lewis-Randall rule can be applied which assumes ideal mixing for real gases. In this environment the fugacity can be approximated using the following equation:

$$f_i = f_i^\theta (P, T) x_i \tag{1.7}$$

where f_i is the gas fugacity of i, f_i^θ is the fugacity of pure i at the selected pressure and temperature and x_i is the molar fraction of i in the gas. However this relies on the gas in question being the primary constituent of the gas phase; the same approximation cannot be made for minor components within the gas (i.e. noble gases) as the dominant interactions for these molecules will be between unlike molecules. However no such data on fugacity exists based on trace amounts of noble gases within a CO_2 phase and so fugacity correction values are assumed to be similar to the pure noble gas phase fugacity within the published literature. This is done to include a reasonable fugacity correction for an obviously non-ideal system. Considering that maximum deviation from ideality occurs at low temperatures and high pressures (Ballentine *et al.*, 2002) at low molar fractions which have not been investigated for noble gases, the legitimacy of this assumption is questionable for many geological systems. As such the use of these fugacity values with no supporting evidence has the potential to introduce an element of error into the expected partitioning values for all studies which have used this approach to resolving fugacity. In the absence of any empirical data the extent of the introduced error cannot be presently determined.

1.3.10 Non-ideality in the liquid phase

Similarly to the gaseous phase, deviations from ideal behaviour within the liquid phase must be taken into account. This is achieved by the inclusion of the liquid phase activity coefficient γ_i within Henry's law:

$$\Phi_i P_i = \gamma_i K_i x_i \tag{1.8}$$

Deviation from ideality (i.e. the activity coefficient) for the liquid phase is typically due to additional solute particles within the solvent. The effect electrolytes have on noble gas solubilities can be determined using the Setschenow equation:

$$\ln[S_i^o(T)/S_i(T)] = Ck_i(T) \tag{1.9}$$

where S_i^o is the non-electrolyte i solubility in pure water at a specified temperature (T), S_i (T) is the non-electrolyte i solubility in the salt solution at the same temperature, C is the molar concentration of the electrolyte and $k_i(T)$ is the empirically derived Setschenow coefficient at temperature (T). Since the only difference between S_i^o (T) and S_i (T) is the consideration of the liquid phase activity coefficient γ_i in the saline solution, this equation can be rewritten as:

$$\gamma_i = e^{(Ck_i(T))} \tag{1.10}$$

From Equations 1.9 & 1.10 it is apparent that for instances where k_i (T) is positive γ_i is greater than 1 and solubility is decreased. Where k_i (T) is negative corresponding solubilities are increased. Concentration acts as a multiplying factor on the effect of the electrolyte on solubility and as the concentration approaches 0, γ_i moves towards 1 (i.e. ideality in the water phase).

To generate a Setschenow coefficient for a chosen electrolyte, an experimental dataset is required which covers the desired temperature range. Such studies exist which record the effect sodium chloride has on noble gas solubility and ideality (Weiss, 1971; Smith & Kennedy, 1983). The most notable of these was the study by Smith & Kennedy which measured noble gas solubilities in brines from 0 – 5.2 molar sodium chloride solution between 273.15 – 338.15 K. This allowed the formation of an equation to calculate k_i at a given temperature for each noble gas:

$$k_i(T) = G_1 + G_2/(0.01T) + G_3\ln(0.01T) \tag{1.11}$$

where G_1, G_2 and G_3 are empirically derived constants:

Noble Gas	G_1	G_2	G_3
Helium	-10.0810	15.1068	4.8127
Neon	-11.9556	18.4062	5.5464
Argon	-10.6951	16.7513	4.9551
Krypton	-9.9787	15.7619	4.6181
Xenon	-14.5524	22.5255	6.7513

Table 1.7. Empirically derived Setschenow constants for each noble gas. These constants are valid from 0 – 5.2 molar NaCl solution and 273.15 – 338.15 K (Smith & Kennedy, 1983).

Using Table 1.7 the value of k_i can be plotted for each noble gas over temperature range at a fixed salinity to assess the relationship between temperature and noble gas solubility for sodium chloride solutions:

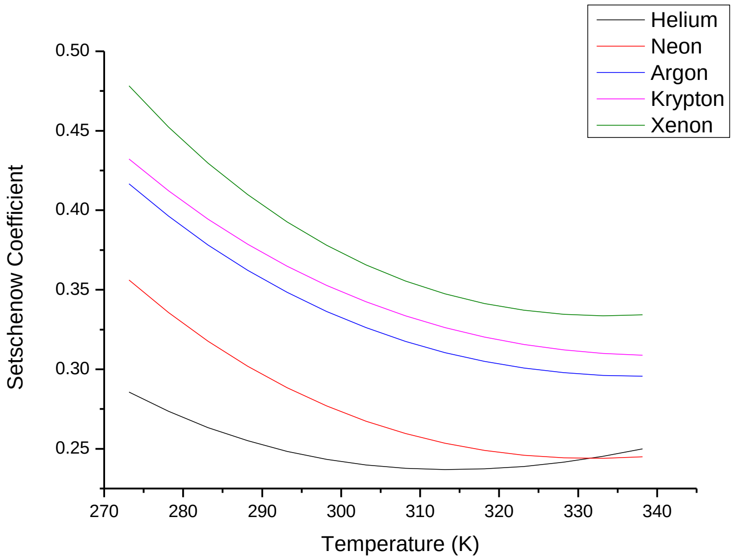

Fig. 1.2. The effect of temperature on the Setschenow activity coefficient for each noble gas at a fixed salinity (1 mol). Redrawn from Smith & Kennedy (Smith & Kennedy, 1983).

All noble gas Setschenow activity coefficients have a similar thermal trend; initial temperature increases result in reduced Setschenow activity coefficients (i.e. relative solubility increases). Progressively the gradient of this curve decreases indicating at the higher end of the experimental range temperature has less of an effect on lowering the activity coefficient. Helium alone reaches a minima value after which the activity coefficient increases once more resulting in lower solubilities. Given that helium alone reaches an observable lowest value and all noble gases are unique in their response to changing temperatures for this selected electrolyte it is not reasonable to extrapolate the activity coefficient beyond the experimental range for any noble gas. For most geological systems the application of the Smith & Kennedy dataset-derived activity coefficients (Smith & Kennedy, 1983) is considered sensible; applying values from a pure NaCl system to a multi-electrolyte system with an equivalent concentration provides a practical approach to calculating Setschenow coefficients (Weiss, 1971; Weiss & Price, 1989).

The effect non-electrolytes (e.g. gases) dissolved within the water phase have on noble gas partitioning are far harder to quantify. Typically non-electrolytes have low solubilities in the water phase and thus their effect can be ignored but under geological *P.T* conditions it is possible for the water to contain a significant dissolved gas component. This is currently still considered within the published literature to have no effect on noble gas partitioning although in the absence of supporting experimental evidence this is noted to be a potential shortcoming (Ballentine *et al.,* 2002). As it stands therefore no viable adjustment to expected partitioning values can be made for the presence of CO_2 within the liquid phase as its effect, if any, is not known. If it does have a bearing on noble gas solubility however this could potentially result in an observable departure from current expected values.

1.3.11 Poynting corrections for the liquid phase

Pressure acting on the liquid phase can also affect noble gas solubility at a given temperature. This will therefore modify the Henry's constant and must be corrected for using the Poynting correction. For this the chemical potential of species *i* in an ideal dilute solution (μ_i) is required. This is given by

$$\mu_i = \mu_i^0 + RT\ln x_i \tag{1.12}$$

where μ_i^0 is the excess chemical potential of *i* at infinite dilution. This excess chemical potential is pressure dependent. Up to this point however this effect has been neglected. If we include this pressure dependence via the Poynting correction, we obtain the expression

$$\Phi_i P_i = K_{i_i}^0 x_i e^{\left(\frac{\overline{V}_{mi}(P-P^0)}{RT}\right)} \tag{1.13}$$

where P is the pressure considered, P^0 is a reference pressure, $K_{i_i}^0$ is Henry's constant at the reference pressure and $\overline{V}_{mi}$ is the partial molar volume of i at infinite dilution, again at the reference pressure. To obtain this expression the assumption is made that this partial molar volume was pressure independent (Enns *et al.*, 1965; Gerth, 1983; Prini & Crovetto, 1989; Poling *et al.*, 2001). Any deviations from ideal-dilute behaviour are incorporated into the activity coefficient (1.3.10).

With regards to solubility in liquid water $\overline{V}_{mi}$ values are typically in the 10^{-5} m^3/mol region, R is 8.314 J/mol K and temperature (T) is usually >300 K. Using these figures significant pressure differentials are required (≥ 25 bar) to produce deviations outside of standard experimental uncertainty (± 5%). Therefore pressure is typically considered to only have a minor effect on noble gas partitioning and frequently is omitted from calculations (Ballentine *et al.*, 2002).

1.3.12 Noble gas solubility measurements

It is accepted therefore that non-ideality is distinctive for each phase under given thermodynamic conditions. This non-ideality is due to pressure, temperature and composition of each phase. Consequently noble gases within a given binary phase system will partition uniquely to maintain chemical equilibrium. Empirical measurements are therefore required to determine the ratio of partitioning (i.e. Henry's constants) of each noble gas between each phase. These Henry's coefficients can be used to derive equations which calculate partitioning within the empirical range. The most applicable example of this is the pivotal study by Crovetto *et al.* in 1982 which determined the noble gas solubility in water (except helium) using a pure noble gas-water system over a range of temperatures and pressures (Crovetto *et al.*, 1982). Values for helium were determined by Smith (Smith, 1985). These experimental studies resulted in an equation to predict the Henry's constant (K_i, GPa) at a given temperature (T, Kelvin):

$$\ln(K_i) = A_0 + A_1/(0.001T) + A_2/(0.001T)^2 + A_3/(0.001T)^3 \tag{1.14}$$

Coefficients for each noble gas are given in Table 1.8:

Species	A_0	A_1	A_2	A_3
Helium	-0.009528	0.107722	0.001969	-0.043825
Neon	-7.259	6.950	-1.3826	0.0538
Argon	-9.520	8.830	-1.8959	0.0698
Krypton	-6.292	5.612	-0.8881	-0.0458
Xenon	-3.902	2.439	0.3863	-0.2210

Table 1.8. Noble gas coefficients for calculating solubility in water. Taken from Ballentine *et al.*, 2002 (Ballentine *et al.*, 2002). Original sources: Crovetto *et al.*, and Smith (Crovetto *et al.*, 1982; Smith, 1985).

Using these values Henry's constants for each noble gas can be derived and the effect of temperature on solubility quantified:

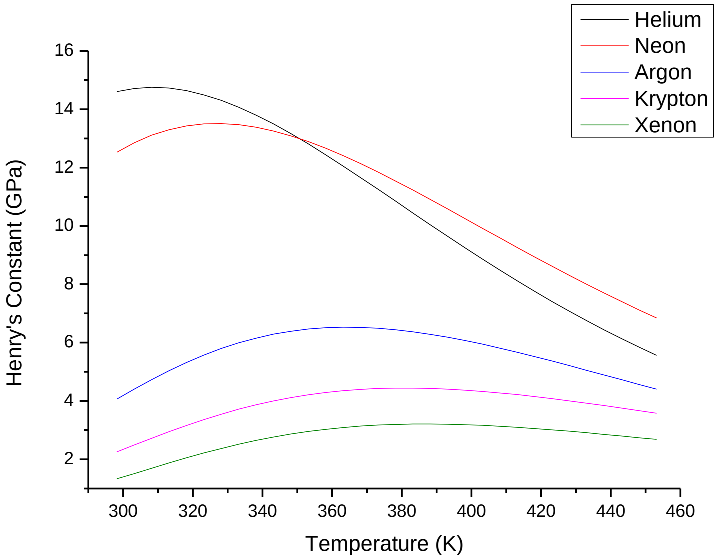

Fig. 1.3. The effect of temperature on Henry's constant for noble gas-water systems. At low temperatures an increase of temperature results in higher Henry's constants (i.e. lower solubilities) until a maxima is reached for each noble gas. After this point is reached Henry's constants decrease with increasing temperatures.

The effect of temperature is similar for all noble gases; initial decreases to solubility followed by progressive increases after a maxima is reached. However the absolute Henry's constants, the position of the maxima and the gradients of the curve are unique for each noble gas. Given that this partitioning and deviations thereof are a function of chemical potentials it is reasonable to assume that changing any *PVTX* properties of the system will affect the Henry's constant of each noble gas separately by an undefined degree. This further highlights the necessity for empirical assessment within any given binary phase system in order to generate reliable partition coefficients.

Despite this necessity no published study exists which documents noble gas partitioning between a CO_2 and water binary phase system. This deficiency requires addressing before the noble gases can be applied to CCS projects to act as legitimate proxies to quantify system processes.

Current modelling of natural analogues to CCS storage assumes the noble gas partitioning to be identical to this documented partitioning between a pure noble gas phase and water. However to date no corroborating experimental data exists which substantiates this assumption. This assumption, in the absence of supporting evidence, is even more fragile when it is considered that many of the geological CO_2 phases, assumed analogous to pure noble gas-water systems, exist close to or within the supercritical *P.T* regime for CO_2 (e.g. Ballentine, 1997; Gilfillan *et al.*, 2008; Zhou *et al.*, 2012). In such instances a further assumption is made; the behaviour of noble gases within high density gases and supercritical fluids is comparable to behaviour within their low density gaseous analogues. Essentially ideality is being assumed in strongly non-ideal circumstances with no evidence to support this. Although the behaviour of noble gas within supercritical water with regards to the structure of the water has been documented (Botti *et al.*, 2003), determining the effect a carrier solvent phase transition has on noble gas solubility has yet to be determined.

The tenuous assumptions currently made when applying pure noble gas-water Henry's constants to supercritical CO_2-water systems are not considered sufficiently reliable for legitimate application to CCS. Therefore this deficiency in our understanding of noble gas behaviour requires immediate attention. This is the primary aim of this research project.

1.3.13 Summary and justification for study

In the preceding sections the appliance of noble gas isotopes within multi-phase geological systems has been demonstrated as essential in defining system processes and properties which otherwise could not be directly quantified. The validity of their application is therefore intrinsically linked to our understanding and interpretation of their behaviour in such environments, especially those which are liable to promote non-ideality.

Partitioning of noble gases into a water phase has already been well-defined for a wide range of temperatures (Crovetto *et al.*, 1982; Smith, 1985) with deviations from ideality due to electrolytes on noble gas solubility similarly assessed (Smith & Kennedy, 1983). However the potential non-ideal effect of a significant CO_2 component is still poorly constrained. No published data exists which considers how noble gas behaviour and partitioning can be affected by a CO_2 solvent phase. Consequently neither supercriticality of this phase nor the dissolution of CO_2 within water are adequately understood. Presently these are all considered within the literature to have a negligible effect on water phase partitioning. Therefore the validity of this must be determined. If through careful experimentation and simulation these assumptions are considered legitimate it will provide greatly needed validation to all research dependent on these suppositions. If however these factors do have a discernible effect on noble gas behaviour then this empirical research and development of a robust model in this study will serve as a basis for reinterpretation of affected processes. It is this which forms the rationale for this work.

Chapter Two

Developing and commissioning of experimental system

2.1 Introduction

Due to the experimental nature of the project it was crucial that a robust Ultra High Vacuum (UHV) mass spectrometer system was developed. This system allowed for quantitative determination of the noble gas content of both a gaseous and liquid phase which in turn allowed partition coefficients to be generated under the experimental conditions. Additionally a suitable high-pressure system was developed in tandem with the ability to generate these noble gas-enriched water and CO_2 samples. This chapter provides a detailed overview of the equipment and techniques used for sample genesis and analysis to provide context for the experimentally defined partition coefficients. For reference a brief overview of the principles of mass spectrometry is also provided.

2.2 Principles of mass spectrometry

2.2.1 Theoretical basis of mass spectrometry

In order to quantify the amount of each noble gas isotope present within a sample it is necessary to isolate and measure each isotope separately. This is accomplished via mass spectrometry. This analytical technique ionises a minute quantity of the sample under UHV conditions which is then exposed to magnetic and/or electric fields. The responsiveness of ions to this field are mass dependent and so each mass can be isolated and measured. The relationship between mass and charge of each ion within a magnetic/electric field is:

$$E = eV = \frac{1}{2}mv^2 \tag{2.1}$$

where *E* is the kinetic energy of the ion, *eV* is the ionic charge, *m* is the mass and *v* is its velocity. Ions possessing the same charge (*eV*) will have the same kinetic energy (*E*) transferred after being exposed to the same magnetic/electric field. However as the kinetic energy is a function of both mass and velocity the corresponding change in velocity is unique for each mass. This distinctive relationship between the mass charge ratio (*m*/*z*) and velocity is taken advantage of by mass spectrometer systems carefully designed to ionise, isolate and measure each isotopic species. This procedure occurs respectively within three distinct sections of the mass spectrometer: the source, the analyser and the detector. The specific processes involved at each stage are dependent on which mass spectrometry approach is used. As this project utilises a quadrupole mass spectrometer for the experimental analysis, an overview of this method of mass spectrometry will now be outlined. For a fully expansive discussion of this and all other mass spectrometer approaches the published works of De Hoffman & Stroobant or Rouessac & Rouessac are recommended (De Hoffmann & Stroobant, 2007; Rouessac & Rouessac, 2007).

2.2.2 Quadrupole mass spectrometry

In order to render a sample responsive to a magnetic/electrical field it must first be ionised; this occurs within the source. For a quadrupole mass spectrometer this source is most commonly electron impact-based. A schematic of a standard electron ionisation source for a quadrupole is presented:

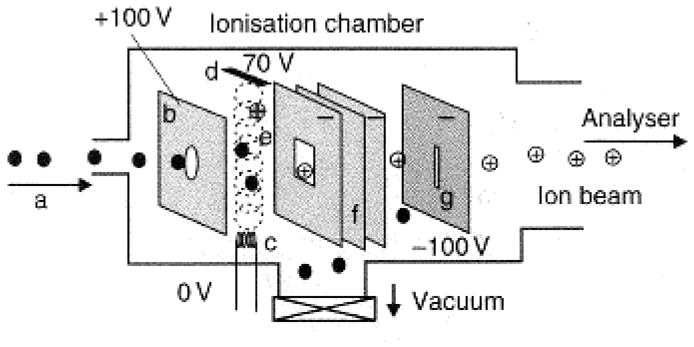

Fig. 2.1. Schematic of source used to ionise samples. (a) is the sample inlet, (b) is the positively charged ion selector, (c) is the filament used to generate electrons, (d) is the discharge anode, (e) is the electron beam (f) are the extraction plates and (g) is the exit slit which leads to the analyser. Used with permission from(Rouessac & Rouessac, 2007.)

A thermoionic process within the filament generates electrons (c). These produced electrons are subsequently attracted to a positively charged discharge anode (d) creating an electron beam (e). The standard energy of ionisation possessed by this beam can be determined from the potential difference between the source housing and the filament. The optimised value for this is 70 eV for noble gas analysers. Neutral particles entering the mass spectrometer (a) pass through an aperture within the positively charged ion selector and interact with this electron beam to produce positively charged ions. Through combined repulsion from the ion selector (b) and attraction towards the extraction plates (f) they are accelerated away from the source and leave via an exit slit (g) which filters out all ions except those travelling parallel to the analyser. This technique of ionisation, acceleration and ion filtration results in a focused ion beam which enters the analyser for mass separation.

The analyser section of a quadruple mass spectrometer consists of four perfectly parallel metallic rods, typically between 5 – 20 cm long. These four rods can be considered as two sets of rods at right angles to one another. By applying a positive and negative current to each pair respectively they act as two pairs of electrodes which create a hyperbolic cross section at 90° to the beam direction:

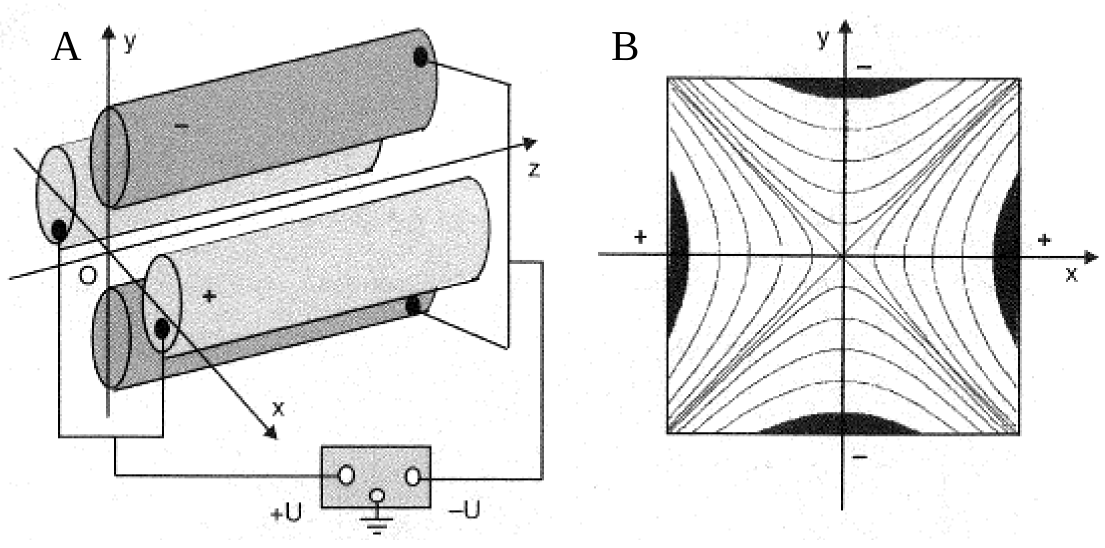

Fig. 2.2. The analyser of a typical quadrupole (A). The initial beam direction on entering the analyser is aligned to the z axis. Each set of opposing rods possess the same charge which alternates between positive and negative as a function of the applied DC and AC currents. A cross section through the analyser is given with the electrostatic force field equipotential hyperbolic lines drawn (B). Used with permission from(Rouessac & Rouessac, 2007.)

Each pair of rods possess an equal and opposite charge. Positive charges serve to repel the positive ions from the electrodes thereby focussing the beam whilst negative charges attract the positive ions to the electrodes thus defocusing the beam. Therefore at any given time the ion beam is being both focussed and defocused along the z axis in the x and y axes. The charge on each pair of rods is the net effect of superimposing an Alternating Current (AC) onto a baseline Direct Current (DC) potential (*U*). This combination of fixed and variable voltages generates an electrostatic potential field within the analyser which is in permanent flux. The rate of flux is dependent on the voltage of radiofrequency (RF). Consequentially ions entering the analyser are subjected to an electrostatic field which varies in both direction and intensity as a function of time (Figure 2.2B). Thus the velocity of each ion will be continually changing. This results in a complex mass-dependent corkscrew trajectory along the z-axis. For any given radiofrequency voltage only resonant ions possessing a specific mass to charge ratio will have a stable flight path along the z axis. These alone successfully reach the end of the analyser and enter the detector. The unstable flight path of all other ionic masses results in their premature discharge on one of the electrodes. Thus only ions possessing a particular mass charge ratio (m/z) for a given RF voltage successfully reach the detector. By progressively changing the RF voltage therefore it is possible to isolate and measure each desired isotopic mass in sequence. Typically quadrupoles are able to measure across the 1 – 200 AMU range which includes all stable noble gas isotopes.

Following the ionisation and isolation processes the absolute amount of each ion species present can be determined. This is typically achieved using a Faraday cup. Resonant ions which have successfully navigated the analyser collide with the surface of the Faraday cup. Connected to the Faraday cup is an amplifier with a 10^{11} Ω resistor which in turn is connected to a voltmeter. Each individual ionic collision with the cup neutralises the positive ion and in doing so generates a well-defined minute electrical current; this is called the elementary positive charge (*e*) which for a singly charged ion is 1.602×10^{-19} coulombs. This neutralisation of each positive ion corresponds to a voltage drop across the resistor. By measuring the change to voltage across the resistor for a specified RF voltage it is possible to back-calculate the current (*I*) generated from these ionic collisions over a set time period (*t*). From this the absolute quantity of a given ion (*N*) can be reasonably approximated:

$$N = {}^{It}\!/_{e} \qquad (2.2)$$

Uncertainties when calculating *N* are frequently due to doubly charged ions. As discussed the method for separating individual species relies on each possessing a unique mass/charge relationship. However, infrequently, ions are doubly charged at the source.

When this occurs the mass/charge relationship is almost identical to that for singly charged ions possessing half the mass:

$$\mathrm{m/2z} \approx 0.5\mathrm{m/z} \tag{2.3}$$

These species possess only subtly different m/z ratios. Therefore unless the mass spectrometer's ability to discern between mass units (resolving power) is sufficiently high the mass spectrometer cannot discern between these ions. Consequentially where the higher mass exists in high quantities doubly charged ions can significantly add to the ion count, resulting in artificially high measurements for these species. With respect to noble gas geochemistry this is a particular issue when measuring ^{20}Ne as doubly charged ^{40}Ar can result in an appreciable contribution. Similarly doubly charged CO_2 (mass 44) can interfere with ^{22}Ne measurements.

For instruments possessing a high sensitivity, secondary ions also have the potential to affect the measurement. Occasionally when the initial ion collides with the Faraday Cup an electron is ejected. If the angle of ejection is reasonably shallow then there is a high probability the electron will impact against the wall of the Faraday cup. This collision and subsequent discharge will lead to a negative elementary charge which will cancel out a positive ion collision and thus prevent it from being counted. To minimise this effect a repulsion plate is frequently installed at the end of the Faraday cup. This negatively charged plate is designed to deflect these electrons from the side of the cup and also prevent them from re-entering the Faraday cup and affecting the measurement. Whilst this prevents the majority of electrons from colliding with the Faraday cup those with shallow ejection angles are still likely to be included in the count and so their effect needs to be considered when calculating absolute isotopic values.

Further uncertainty in determining N arises when the lower limit of detection is approached (10^{-15} A on a Faraday cup). This is due to an enhanced uncertainty when measuring the voltage drop across the resistor against the background noise. Additionally when a particular species of ion exists in extremely low concentrations the rate of ionic discharge on the Faraday cup at any given time is less uniform. This can lead to observable variations in N over time, especially if the measurement time (t) is small. Where quantities are low therefore the signal requires amplification. Under these circumstances an electron multiplier is required to accurately determine low ionic concentrations from a sample.

2.2.3 Characteristics of experimental quadrupole

The quadrupole mass spectrometer used to generate partition coefficients for this project was a stainless steel Hiden Analytical (HAL) 200 quadrupole mass spectrometer, capable of measuring across the 1 – 200 AMU range at pressures between $1.33\text{x}10^{-13}$ – $1.33\text{x}10^{-9}$ bar. The ionising source was a tungsten filament and the standard energy of ionisation set to 70eV. RF voltages were used in the analyser to isolate each mass. All noble gas partial pressures were measured on a fixed Faraday cup. Due to the nature of a quadrupole the resolution of the mass spectrometer was defined as integer resolution i.e. only masses possessing 1 AMU or greater difference from each other were able to be detected. For the clean UHV system used for this project this only created an issue for neon due to doubly charged ^{40}Ar (19.981 AMU) and doubly charged CO_2 (22.005 AMU) interfering with ^{20}Ne (19.992 AMU) and ^{22}Ne (21.991 AMU) respectively. As a result it was considered impossible to quantitatively investigate these overlapping masses to any reasonable degree of confidence using the current analytical procedure. ^{21}Ne however was free from any known significant isotopic overlap of 1 AMU or smaller and so was used as the primary neon isotope to derive partition coefficients.

During sample analysis measured isotopic values for selected noble gas isotopes were recorded to a 3.5” floppy disc in the quadrupole controller unit. These were analysed on a PC using the methodology presented in 2.5.4. The selected noble gas isotopes are presented in Table 2.1.

Noble gas	Mass (AMU)
Helium	4
Neon	(20), 21, (22)
Argon	36, 40
Krypton	82, 84
Xenon	132, 136

Table 2.1. Noble gas isotopic masses measured during sample analysis. ^{20}Ne and ^{22}Ne were also measured but they could not be isolated from their interference ions.

These isotopic masses were selected as they include the most abundant isotopes for each noble gas. All three major isotopes of neon were measured but only ^{21}Ne was clear of interference peaks. A second isotope was also selected for each noble gas to confirm all partition coefficients generated from the more prevalent isotope. It was assumed therefore that no isotopic fractionation would occur. Only ^{4}He was measured as ^{3}He would not be observable above the baseline. In addition to the noble gases other masses were also measured. These included 1 (hydrogen), 18 (water), 28 (nitrogen/carbon monoxide) and 44 (CO_2). These were measured as routine to assess the cleanliness of the sample entering the quadrupole to ensure no issues had developed during the sample preparation stage.

2.2.4 Standards

Due to the highly sensitive nature of mass spectrometry a degree of variability is expected during measurement. Thus values from identical samples can vary significantly between instruments. Furthermore variability is liable to occur within a single instrument over time. Consequentially a method of cross-calibration is required to allow for an absolute determination of the noble gas content. For this standards are used. These standards are typically gases with a well-defined absolute noble gas composition such as air (or isotopically-spiked variants thereof). These can be used to define the present relationship between absolute quantities of noble gasses and the measured intensity on a mass spectrometer. Therefore they provide a means to correlate between measured and absolute values which can be subsequently applied to experimental data. Additionally standards are employed to assess the stability and reliability of an analytical technique. This is achieved by determining how reproducible an isotopic value is from an identical set of samples over a set time period. The use of standards within the context of this project is fully discussed in 2.3.2.

2.3 Characterising the noble gas extraction line

Due to the requirements of the project a robust mass spectrometer system was developed which accurately analysed the noble gas content of both gaseous and liquid samples. These were then used as the basis for calculating partition coefficients. Originally the system had been developed as a tritium sample preparation line for a static mass spectrometer. As a result the original system required adaptation to fulfil its new role. These extensive adaptations required the development of new protocols for sample analysis. The reconfigured line will now be discussed in greater detail.

2.3.1 Current analytical layout

A schematic of the analytical line is presented in Figure 2.3.

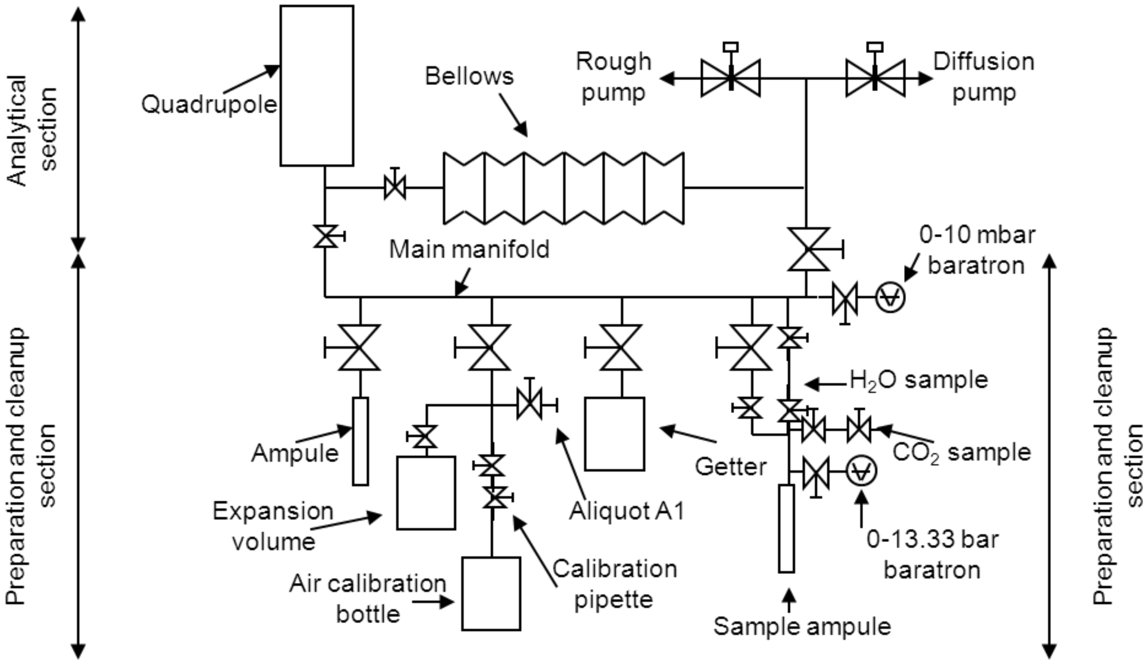

Fig. 2.3. A schematic of the analytical line in its current configuration. The line can be easily isolated into the analytical section and the preparation and clean-up section.

The system in its current configuration is displayed in Figure 2.3. Broadly speaking the entirely stainless steel vacuum system can be subdivided into two sections; a preparation section and an analytical section, with the main manifold acting as the central component for each. Depending on necessity the main manifold can be fully isolated from all preparation components or from the analytical section as required. It can also be isolated via a stainless steel valve from both pumps connected to the line. The two pumps used are a roughing pump and a HS2 diffusion pump which is backed up by another roughing pump. The roughing pump is capable of pumping the system from atmospheric pressure down to pressures of 1.33 x 10^{-6} bar. Once this pressure is reached the diffusion pump is used to reach stable vacuum pressures of 2.67 x 10^{-11} bar or better. Valves to both pumps are opened and closed by a manual switch controlling the flow of compressed air.

The preparation section consists of the sample mounting subsection, the SAES NP10 getter, the air calibration bottle and three known volumes for post-initial expansion sample storage. Each of these is connected to the main manifold by valves, allowing them to be isolated as required. Additionally on both the central manifold and the sample mounting section are MKS baratron capacitance manometers, capable of measuring 0 – 10 mbar and 0 – 13.33 bar respectively. The analytical section is primarily the Hiden Analytical HAL200 quadrupole mass spectrometer which is connected via a valve to the central manifold. Bellows also connect the mass spectrometer to the pumps directly allowing for low vacuum conditions to be maintained during sample preparation when the manifold is fully isolated from the quadrupole and the pumps.

2.3.2 Assessing the stability of the system

Before sample analysis could take place the stability and reproducibility of the quadrupole needed confirmation. This was accomplished via air standards. This provided a means to analyse multiple identical samples containing a known absolute noble gas content. An assessment of the correlation of each analysis with one another defined the reproducibility and stability of the mass spectrometer. Due to the relatively low sensitivity of the Hiden, ^{40}Ar was the only naturally occurring noble gas isotope present in sufficient quantities within a reasonably sized air shot which could be measured.

However, before standards could be run, an air standard bottle was required. Given its importance, this required careful preparation of the calibration bottle. Therefore a protocol was developed specifically for this project. Adhering to this protocol was essential in producing uniform standards which could be legitimately used.

To generate an air standard of sufficient quality the air calibration bottle was fully evacuated and pumped down to a good vacuum (below 1.33 x 10^{-6} bar). This ensured any existing gas content was removed. The bottle was then sealed under vacuum and transported to the top of the George Kenyon building, on the University of Manchester Campus. This is where the Whitworth Meteorological Observatory was located. The valves isolating the calibration bottle were then opened to air for six hundred seconds to allow thermal and barometric equilibration. After this time it was resealed and remounted onto the analytical line as depicted in Figure 2.3. Environmental conditions at the time of resealing are recorded from the Whitworth Meteorological Observatory live data feed to give temperature, pressure and humidity. These and the correction for altitude are then used to calculate the exact amount of ^{40}Ar being put into the system each time from the calibration pipette. Given that the calibration pipette volume is so small (0.2264 cm^3) compared to the calibration bottle volume (925 cm^3). it was determined that this process only needs to be repeated every one hundred standards, by which time the pressure of air standard would have been reduced by approximately 2.4%, assuming constant laboratory conditions.

With the addition of a reliable air standard to the analytical line a protocol was subsequently needed for the isolation and analysis of the ^{40}Ar content. The procedure developed to analyse air standards is now described.

The valve separating the calibration pipette and the calibration bottle was opened and left for thirty seconds, to allow the air standard to equilibrate. After this the valve was closed, isolating the standard once more. As the aliquot was several orders of magnitude too high for analysis it was necessary to dilute it by expanding into larger volumes then taking aliquots for analysis from this. At this stage the clean-up section of the line comprising of the main manifold was isolated from both the diffusion pump and the quadrupole. The NP10 getter was also isolated at this stage. The pipette volume was then expanded into the clean-up line and left for 120 seconds after which point the A1 aliquot was isolated from the rest of the line. This preserved a diluted aliquot of the original standard. The valves isolating the clean-up section were then reopened to the rest of the line and the whole system was then pumped down for at least an hour, until the pressure reached below 6.67×10^{-11} bar. At which point it was safely assumed any residual gases from the expanded sample had been removed from the system. Once this stage was reached the diluted A1 aliquot volume was analysed.

The clean-up section of the line was closed off once more from the rest of the system and the sample from the A1 aliquot section was re-expanded back into this section. By allowing the standard to interact with the getter at approximately 523 K all reactive gases were progressively removed over a six hundred second period. During this stage a baseline on the quadrupole was measured. After this the standard was introduced into to the quadrupole which had been isolated from the diffusion pump. Thus the sample was analysed. To ensure a good average value was reached the sample was analysed for six hundred seconds to provide approximately ten data points. After analysis was complete the whole section was vented for another six hundred seconds to ensure a good baseline was recorded.

Figure 2.4 is a graph displaying the results from a series of six air calibration analyses taken over a single day:

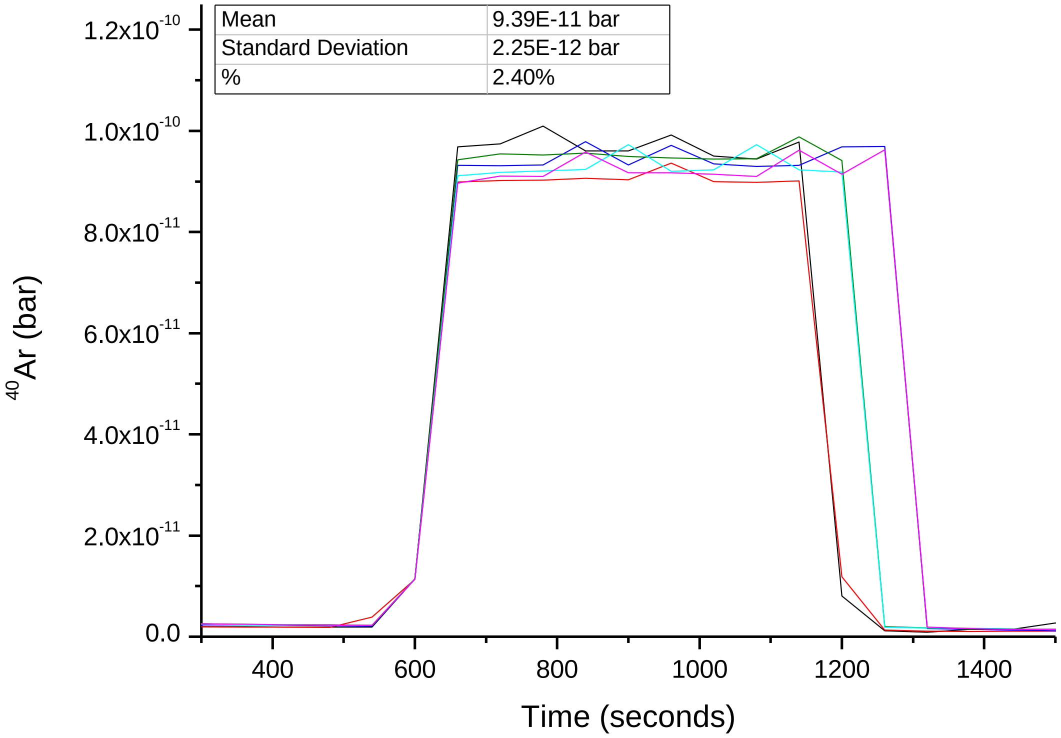

Fig. 2.4. The ^{40}Ar content of six single-shot air calibrations analysed over a single day. The mean ^{40}Ar measurement was derived for each peak as described in section 2.5.4. A mean value and the associated standard deviation were calculated from the six averages. This standard deviation is also given as a percentage of the mean value.

The high degree of accuracy achieved in reproducing the same signal from an identical volume of noble gas both proved the validity of the analytical technique and demonstrated the high reproducibility that can be obtained using this mass spectrometer system over the course of a single day. Additionally when these calibrations were compared to four previous calibrations, analysed on consecutive days six months earlier, again a high standard of reproducibility is observed. This is graphically displayed in Figure. 2.5.

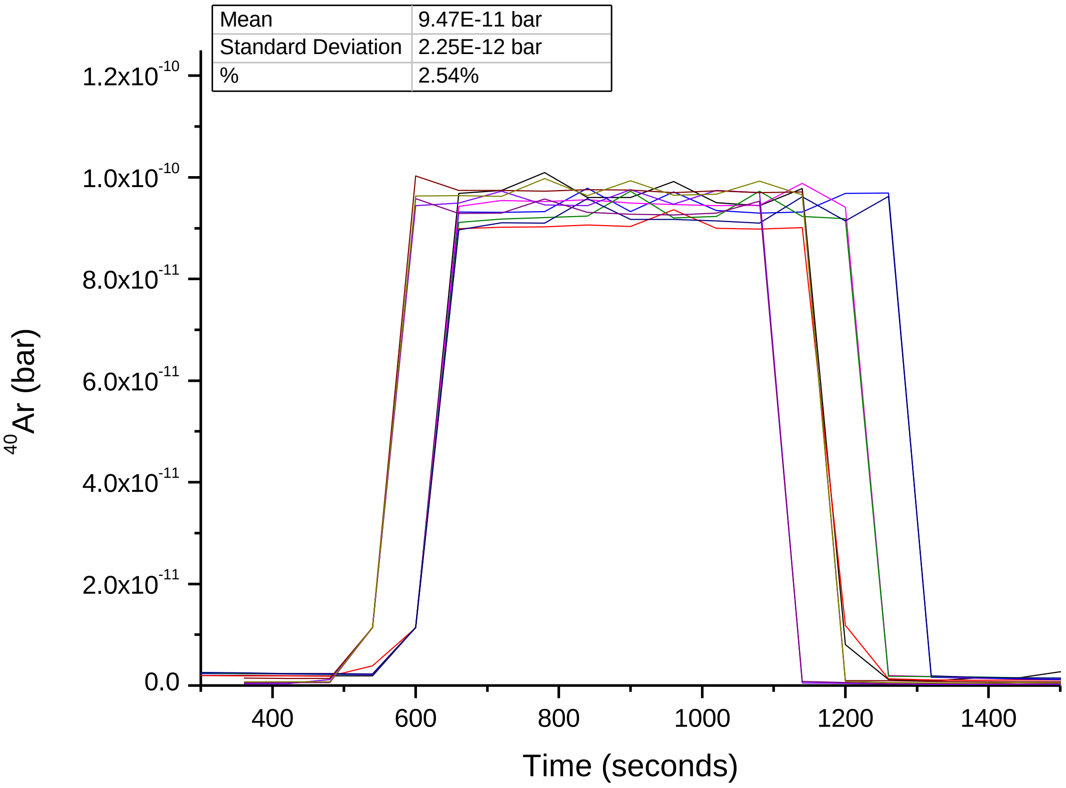

Fig. 2.5. The ^{40}Ar content of ten single-shot air calibrations analysed over a six month period. The mean ^{40}Ar measurement was derived for each peak as described in section 2.5.4. A mean value and the associated standard deviation were calculated from the ten averages. This standard deviation is also given as a percentage of the mean value.

Clearly the inclusion of four additional calibrations analysed six months previously does not significantly affect the measured values. Therefore even over long operating periods the relationship between quantity of noble gas and signal strength remains highly consistent. Thus confirmation of the stability and reproducibility of the system was attained. This proved the system was sufficiently reliable to allow quantitative measurement of samples unknown samples.

2.4 Developing the high pressure system

2.4.1 Sample generation

Samples were generated using the high pressure, high temperature gas laboratory at the British Geological Survey (BGS), based in Keyworth, UK. A specialised setup was required for generating research quality partitioning data as no suitable existing analogues were available. The required system needed to be able to contain a pressurised system at temperatures and pressures comparable to geological storage sites. Furthermore the materials used in construction needed to not react significantly with any of the fluids within the vessel. This was to both maintain system integrity and preserve the geochemistry of the experiment. The resulting high pressure experimental layout for sample generation constructed especially for this project is depicted in Figure 2.6.

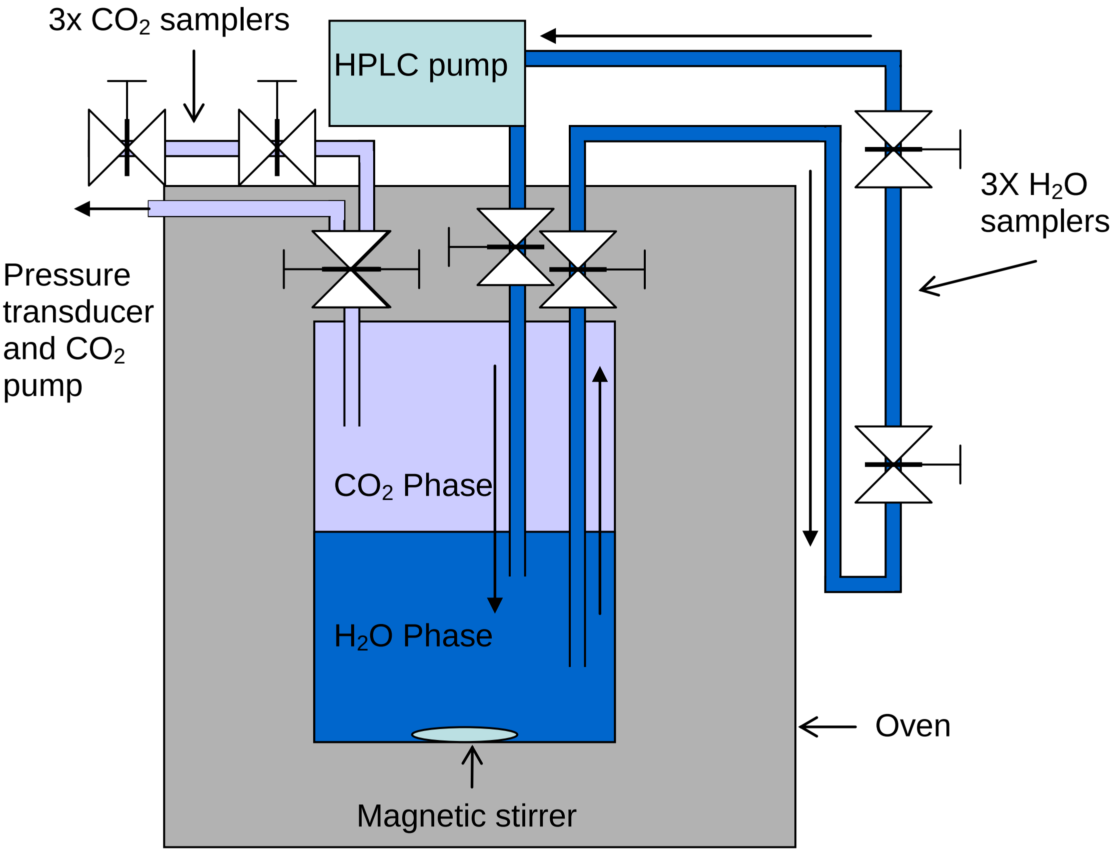

Fig. 2.6. A schematic diagram of the high pressure and high temperature experimental layout. The water phase was stirred within the reactor and circulated through the samplers via an HPLC pump. Samples of each phase were collected in triplicate and were connected in series. For simplicity only one sampler of each phase is shown.

To generate the experimental setup as depicted in Figure 2.6 a 200 cm^3 stainless steel batch reactor, pressure-rated to 550 bar, was used. This was filled with 100 cm^3 deionised water. Next the head of the reactor was welded on to ensure an adequate seal between body and head. This batch reactor head had three 0.2159 cm internal diameter (1/8”) Swagelok tube connections; one to allow CO_2 to be pumped in and subsequently for CO_2 phase sampling and the other two to allow for water to be cycled through the system for equilibration and for water phase sampling. All connections to the reactor were not tightened with the exception of the water intake connection. At this stage all water valves were closed and the water samplers were disconnected from the water intake connection valve. CO_2 was subsequently pumped into the system via the CO_2 inlet at a slow rate to displace any air from the system. After six hundred seconds the connections were tightened in order of proximity to the CO_2 inlet thus ensuring an air-free system. Once this was complete the system was pressurised to approximately 30 bar and the integrity of all connections tested using a detergent-based leak detector. Any leaks discovered at this higher pressure were fixed. Pressure was monitored and logged from this point via a transducer, capable of measuring to ± 1 bar.

At this stage the water connections needed to be similarly cleared of air and pressure tested. This was achieved by connecting the base of the water sampler to a water pump which slowly pumped water through the system to displace any air within the line. Each loose connection, once water began weeping through the 0.2159 cm internal diameter tube fitting, was tightened in sequence until all connections were leak-tight. The lowermost sample valve was then closed and removed from the water pump. This was then loosely connected to the closed water intake connection valve which was already attached to the pressurised reactor vessel. This valve was then opened a small amount to allow pressurised water from the reactor to pressurise the loose connection and displace any air. After a small amount of water had wept out (~1 cm^3) this connection was fully tightened. The sampler valves were then all fully opened to pressurise the water samplers and HPLC pump to reactor pressures. At this stage the Jasco HPLC pump was switched on and cycled water from the reactor through the samplers at a rate of 0.1 cm^3/min. The magnetic stirrers were also turned on at this point and set to a speed of 300 rpm to ensure equilibrium was maintained with the overlying CO_2 phase. The system was then pressurised up to approximately 40 bar and the oven set to the required temperature (± 0.5 K). Once at pressure the system was isolated from the CO_2 pump and left for a day to equilibrate thermally during which its stability was monitored and any small leaks identified and resolved. Once stability had been reached and the system had no discernible leaks it was ready for the spike to be injected.

A 1.5 cm^3 noble gas spike holder containing 31.96% helium 31.97% neon 17.02% argon 10.98% krypton and 8.07% xenon at 0.5 – 0.8 bar was connected to the CO_2 pump. This were flushed through with CO_2 creating a volume of noble gas-enriched CO_2 which was injected into the reactor. The system was then pressurised to 80 – 90% of the desired pressure and left to equilibrate with the system. During this equilibration process the total pressure fluctuated due to both thermal expansion and dissolution of CO_2 until equilibrium was reached. At this stage pressure remained constant. If the pressure was too low then further CO_2 was added if required while if it was too high excess CO_2 was removed via the pump. The system was then left isolated for at least seven days with the water phase being both stirred and circulated. After this period the system was considered to be fully at equilibrium and ready for sampling of each phase.

2.4.2 Samplers

Examples of samplers used to collect the samples are displayed in Figure 2.7.

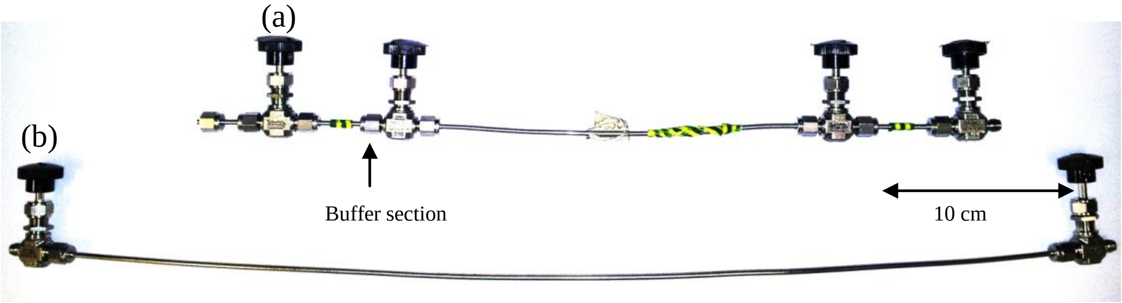

Fig. 2.7. Samplers used to collect samples from the CO_2 phase (a) and water phase (b). The CO_2 samplers included a buffer section to help preserve sample integrity. Sampler volumes were ~1 cm^3 and ~1.5 cm^3 respectively.

Both sample types were collected in 0.2159 cm internal diameter stainless steel tubes with Swagelok needle valves at each end able to maintain pressure to 230 bar. All connections used standard 0.2159 cm internal diameter (tube fittings. As an additional precaution the CO_2 samplers included a small buffer section at each end.

2.4.3 Sample collection

Samples of CO_2 and water for each data point were collected in triplicate. The methodology for sampling each phase was as follows.

At least thirty minutes prior to sampling the magnetic stirrer was turned off to avoid perturbations to the equilibration of the water phase. At the same time a high precision platinum temperature probe with an accuracy of ± 0.2 K was inserted into the oven and left to thermally equilibrate. Once the thirty minutes had elapsed the experimental pressure and temperature were recorded from the pressure transducer and temperature probe respectively. Now sampling was initiated, starting with the water phase. The HPLC pump was turned off and the valves to the water samplers were closed sequentially starting from the closest to the HPLC pump. Once all valves were closed (i.e. water samples have been collected) the water inlet and outlet valves were isolated from the system and the pressure transducer was also isolated. Next the CO_2 samplers were connected in series and attached to the batch reactor at the CO_2 inlet/outlet valve. At this stage all CO_2 sampler valves were closed. The valves were subsequently fully opened in order so as to allow CO_2 to pressurise up the samplers. This stage is depicted in Figure 2.8.

Fig. 2.8. Opening the sampler valves on samplers A1, A2 and A3 to sample the CO_2 phase.

When all samplers were fully pressurised the final valve was slightly opened to vent any air-contaminated CO_2. Once 120 – 130 cm^3 STP of CO_2 had been purged the samplers were considered to be adequately flushed and so all valves were closed and the samplers removed. The water samplers were also removed at this stage. All samplers were duly disconnected from each other and transported back to the analytical line in Manchester. Thus at the experimental pressure and temperature three CO_2 and three water samples had been collected and were ready for analysis.

2.4.4 Assessing the sampling procedure

It was imperative that this experimental procedure had a proven ability to generate viable partition coefficients. The simplest way to accomplish this was to replicate partitioning at low pressures where the partition coefficients of Crovetto et al. and Smith can legitimately be applied (Crovetto *et al.*, 1982; Smith, 1985). This was achieved by slightly modifying the experimental setup (Figure 2.6) to adapt it for low pressures.

Similarly to the water samplers the CO_2 samplers were attached at both ends to the reactor to produce a closed system. However no circulating pump was attached. A noble gas spike was also connected in series to the CO_2 samplers. After the system was pressure tested at 40 bar it was slowly vented through a 0.2159 cm internal diameter stainless steel pipe with the end immersed in water. This step prevented air from re-entering the system. After several days the system pressure had dropped sufficiently and was close to atmospheric. Within this low pressure CO_2 regime experimental partitioning should replicate published values. This venting valve was then closed, isolating the experimental system. All sampler valves were then opened, the pump was set running and the stirrer was turned on. The noble gas spike was then opened so the noble gases could equilibrate within the system. For simplicity the oven was not used therefore the experiment was left to equilibrate at the ambient laboratory temperature.

After allowing ten days for full equilibration the system was sampled. As with the high pressure samples the stirrer was turned off thirty minutes before sampling and the temperature was measured. Next the pump was turned off and all sampler valves were closed. With the CO_2 samplers being on a closed system the usual venting stage was omitted. All samplers were then detached from the experiment and transported to Manchester. Samples were analysed and partition coefficients and their respective uncertainties were derived in accordance with the protocols outlined in sections 2.5 and 2.6. Isotopic values were combined as for the experimental values as outlined in section 4.3 to produce a single partition coefficient for each noble gas. The results from this assessment of the experimental methodology are presented in Table 2.2.

Noble gas	Published partition coefficient	Experimental partition coefficient	Uncertainty (1 σ)
Helium	106.1	60.3	35.1
Argon	29.5	27.4	8.2
Krypton	16.4	15.5	4.3
Xenon	9.7	13.8	3.1

Table 2.2. Comparing experimental partition coefficients with their published counterparts. All partition coefficients are given as unitless ratios. Ratios were derived from ^{4}He, ^{40}Ar, ^{82}Kr, ^{84}Kr, ^{132}Xe & ^{136}Xe. Neon values were not discernible from background values and so low pressure partition coefficients could not be determined. Published partition values are taken from Crovetto *et al.*, and Smith (Crovetto *et al.*, 1982; Smith, 1985). Uncertainty for each value is given as 1 σ confidence.

For both argon and krypton the published values were experimentally reproduced within uncertainty. Although xenon partitioning was over-predicted the published values easily fit within 2 σ (95% confidence) of the experimental values. Consequentially for this project it was reasonable to assume xenon also acceptably reproduced published values. However the validity of this should be confirmed in future work. Experimental values of helium though did not indicate reasonable agreement with their published counterparts. During analysis it was noted that concentrations were extremely low, especially within the water phase. This low concentration resulted in the standard deviations as a percentage of the total concentrations being extremely high (25 – 34%) which produced the observed high degree of uncertainty for this noble gas. Consequentially they were not considered to be of sufficient standard to generate legitimate partition coefficients for this low pressure assessment. For the high pressure experiments spikes were injected more frequently into the system thus helium was present in greater abundance and the uncertainties were much lower. Therefore partition coefficients at high pressure for helium with acceptable 1 σ values (10% or less) were still obtained (Table 4.2).

From the three viable isotopes a good agreement with the expected published values was attained. This indicated that the experimental setup at the BGS could be used to generate legitimate partition coefficients. Additionally it served as further proof that the analytical protocols generated valid noble gas data from both the CO_2 and water phase. These protocols are now discussed.

2.5 Sample analysis

The samples generated at the BGS were analysed using the line depicted in Figure 2.3. A pair of CO_2 and water samples were prepared and then separately analysed for their noble gas content over the course of a day. This process of preparation and analysis is now explained.

2.5.1 Sample preparation

A CO_2 and a water sample were each selected and mounted to the analytical line. The line was then pumped down to a high vacuum using the rough and diffusion pumps. These sampler connections required testing to ensure system integrity before analysis could occur. This was accomplished by spraying laboratory-grade helium in short bursts at each connection whilst scanning for ^{4}He on the quadrupole mass spectrometer at the highest sensitivity (1.33×10^{-13} bar). Any external leaks resulted in a corresponding increase above background levels. This allowed identification of the location and magnitude of any leaks within the newly made connections. Any found leaks were resolved by tightening connections or replacing fittings. Once this process was complete, any leaks resolved and standard operating pressures were reached (i.e. below 6.67×10^{-11} bar) the system was ready for sample analysis. The CO_2 phase was analysed first.

2.5.2 CO_2 samples

As previously outlined a sample buffer was added to each end of the CO_2 samplers. This required removal before the sample could be analysed. This was accomplished by expanding the buffer into the system and pumping it away using the roughing pump. After approximately 120 seconds, when the pump reached 2.67×10^{-5} bar, the buffer valve was closed and the system was pumped down to reach operating pressures of 6.67×10^{-11} bar or lower. The pressure at isolation was approximately three orders of magnitude lower than when expanded and so represents ~0.1%. Therefore any remaining noble gases remaining within the buffer section at most contributed a similar addition to measured values within the sample. Thus any buffer-derived noble gases had a negligible effect on overall measured values.

Once operating pressures were reached the sample was expanded and subsequently analysed. For this all the clean-up section was isolated. The ampule and the A1 aliquot were left open. The sample was then allowed to expand into this clean-up section and was left to equilibrate for 120 seconds. After this time the A1 aliquot valve was closed to preserve a small aliquot of the CO_2 sample. The remaining sample was then pumped away using the rough pump then the diffusion pump until operating pressures were once again reached. The A1 aliquot could then be analysed.

For this the preparation and clean-up section of the line was isolated from the analytical section. Next the A1 aliquot was expanded into this clean-up section where the getter was opened to react out all active gases for six hundred seconds. After six hundred seconds the quadrupole was isolated from the diffusion pump and the sample, now stripped of all but the noble gases, was introduced to the quadrupole and analysed for a further six hundred seconds. Once this was complete the whole system was opened back up to the diffusion pump to vent the sample. After three hundred seconds of pumping a baseline noble gas reading for each noble gas was collected for a further three hundred seconds. After the baseline was collected the analysis was complete. The system was left until standard operating pressures were again reached at which point the water sample analysis could occur.

2.5.3 Water analysis

For the water sample analysis it was important to separate the noble gases completely from the water at the earliest stage. This was accomplished by a two tier approach; the light noble gases (helium and neon) were separated out from the water sample using liquid nitrogen while an acetone slush allowed the heavier noble gases to be isolated. First the light noble gases were removed and analysed.

The sample mounting section of the line was fully isolated from the rest of the system and the valve holding the water sample was opened, allowing the water sample to drop into the sample ampule below it. This sample ampule was subsequently immersed in an ultrasonic bath which was turned on for nine hundred seconds to fully degas the water. Liquid nitrogen was then used to cool the lower section (bottom 2 cm) of the sample ampule and freeze this degassed water. After 300 seconds a heat gun was used to heat up the sample tube to force any remaining water into the sample ampule where it then froze. After three hundred seconds this heating process was repeated twice more after which the level of the liquid nitrogen on the sample ampule was raised to the second mark (7 cm above sample ampule base). The heating cycle was repeated a further two times to ensure any remaining water vapour was frozen out. The liquid nitrogen was then raised to its final level (10 cm above sample ampule base) to ensure any trapped water at the second mark remained captured in the event of any fluctuations in the liquid nitrogen level.

As with the CO_2 sample, the water sample was now ready for expansion. Again the clean-up section was isolated from the analysis section. The aliquot ampule and the A1 aliquot were left open. The sample was then allowed to expand into this clean-up section and was left to equilibrate for 120 seconds. After this time the aliquot ampule valves were closed to preserve two small aliquots of the water sample and the sample mounting section was then resealed. The clean-up section was then opened to the diffusion pump and left to reach standard operating pressures which took approximately twenty minutes. At this point the aliquots could be analysed for their noble gas content. This analysis was identical to the CO_2 aliquot sample analysis.

After light noble gas analysis the heavy noble gases required similar separation from the frozen water sample. To accomplish this first the sample ampule was immersed in warm water to rapidly melt the frozen sample. After thirty minutes the sample was considered to be fully liquid once more and was once again placed in the ultrasonic bath for nine hundred seconds to fully degas argon, krypton and xenon from the sample water. Once degassing was complete the sample ampule was immersed in an acetone slush (178 K) which was cold enough to refreeze the water sample but warm enough to allow all noble gases would remain gaseous. As with the light noble gas water sample procedure the sample ampule was initially immersed at the lowest mark (2 cm from the bottom) and after nine hundred seconds the acetone level was raised up to the middle mark then after a further nine hundred seconds, raised to the top mark. This was done as before to ensure that an overwhelming majority of the water remained trapped as ice and would not be released if the acetone level fluctuates slightly. Due to the extremely flammable nature of the acetone the heat gun was not used during this process.

Once the acetone slush was at the highest mark on the sample ampule the sample gas was ready to be expanded and aliquots preserved, to subsequently be analysed for their noble gas content. The procedure for this was identical to the light noble gas water sample.

2.5.4 Data Reduction

Once a sample pair have been analysed for their noble gas content a data reduction stage is required to determine noble gas concentrations within each sample from the raw data. This process is described fully in this section.

Initially the noble gas peak is identified from the raw data. As concentration is measured as a function of time by the quadrupole this can be easily determined by observing the point at which a noble gas mass rises above the baseline.

Both the initial and final peak value are then trimmed from the dataset thus eliminating the possibility of erroneous data from unequilibrated measurements being included in the average. Next a baseline correction is required. For this a non-peak section of the scan for each mass is selected. Arithmetic means, standard deviations and standard errors are calculated for the peak and a mean value is calculated for the background. Standard deviation is taken as 1 σ uncertainty for the peak average.

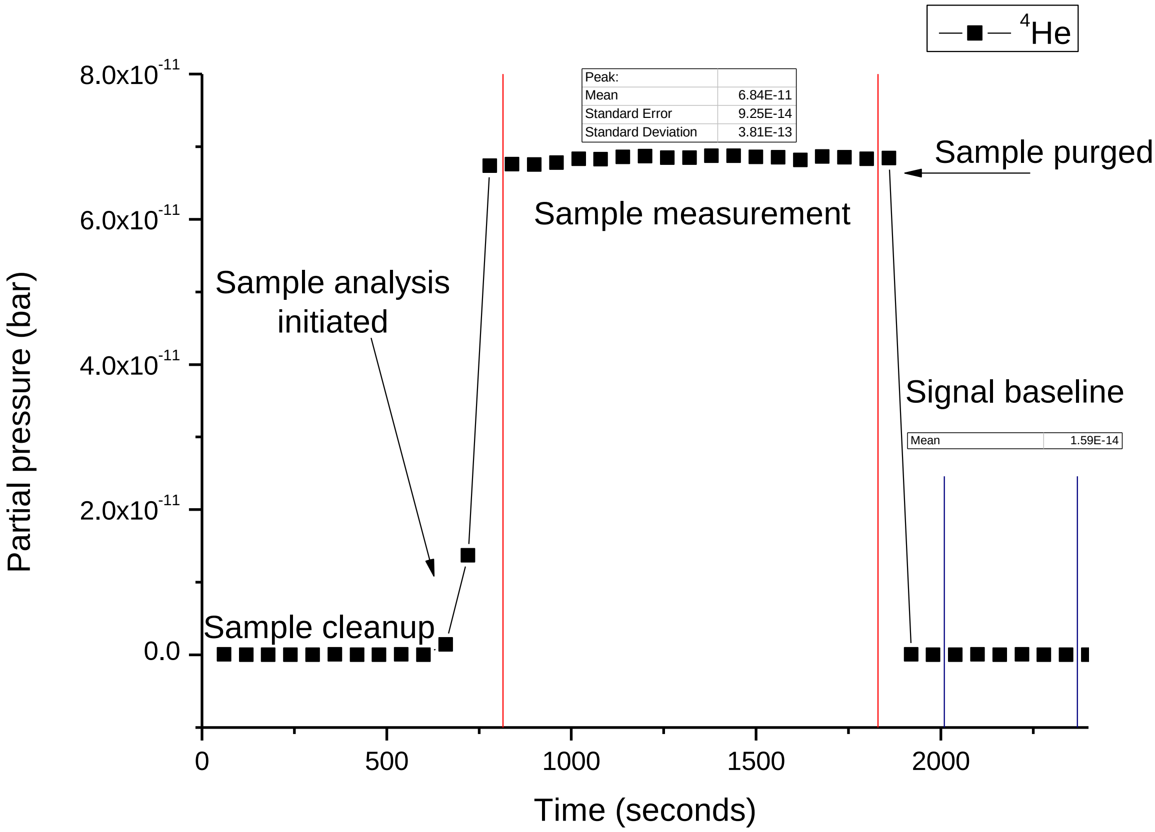

Fig. 2.9. Annotated example graph depicting peak analysis. Averages, standard deviation and standard error of both peak and background are indicated.

The average baseline value was then subtracted from the average peak value. The uncertainty in the measured baseline was considered negligible since even with the noble gases in the water phase possessing the lowest values, the baseline was one or more orders of magnitude lower than that. Due to the high system stability the associated uncertainty is estimated to represent <1-2% of the peak intensity. Full procedural blanks indicated that noble gas concentrations did not increase above the background values during the analytical timeframe. Therefore taking an adjacent baseline as representative of the baseline during analysis was justified.

Thus from the raw data the sample noble gas concentration was determined with a 1 σ uncertainty.

2.5.5 Sample rejection criteria

To ensure a robust dataset a rigorous procedure of acceptance/rejection was required. At this stage three duplicate paired samples from each given P,T experiment had been analysed for their noble gas content and corrections applied to the data (2.6). These were then used to derive partition coefficients for each noble gas. As expected, most duplicates yielded similar partition coefficients for the respective noble gases. However, occasionally when two partitioning values were reasonably concordant (± 20% of an average) the third significantly deviated from its two counterparts. In these cases noble gas values within both phases were compared to phase averages derived from their counterparts to check for consistency.

Often it was the case that while one of the suspect samples was reproducing values in line with expected values (± 20% of the phase average) its counterpart had consistently produced values significantly below this range for all noble gases. Sometimes this discrepancy was more than an order of magnitude and indicated sample leakage: these were considered compromised and so were omitted from the dataset. Similarly samples which contained much greater argon values (≥ +50% average) were considered compromised by an atmospheric component either during sampling, storage or analysis and so were also rejected. Details of these rejected samples are listed in Table 2.3:

Sampler	Experiment	Phase	Reason for rejection	Evidence
A1	322.85 K, 112.7 bar	CO_2	Internal leak	Noble gas sample values 30 – 40% below average
W5	322.85 K, 112.7 bar	Water (pair of above)	Air contamination	^{40}Ar values 6166% of average
A3	322.85 K, 134.12 bar	CO_2	Internal leak	Noble gas sample values 60 – 90% below average
A3	374.15 K, 92.64 bar	CO_2	Internal leak	Noble gas sample values 25 – 50% below average
W5	373.14 K, 134.26 bar	Water	Compromised during transportation	Water observed escaping at end of valve

Table 2.3. List of omitted samples with justification.

Where single partitioning values slightly deviated from the other two but no deviation trend due to leaks or contamination could be observed rejection could not be justified and those partition coefficients were retained. Similarly in instances where all partition coefficients displayed a degree of heterogeneity determining the validity of one point with respect to another was not possible. Under these circumstances all data was again included.

2.6 Corrections applied to data

The relationship describing the partitioning of noble gases in each phase can be expressed as:

$$D_{i(P,T)} = \frac{C_{i(P,T)}}{W_{i(P,T)}} \tag{2.4}$$

where $D_{i(P,T)}$ is the unitless partitioning ratio of noble gas i between each phase at a given pressure (P) and temperature (T), $C_{i(P,T)}$ is the partial pressure of noble gas i in the CO_2 phase and $W_{i(P,T)}$ is the partial pressure of noble gas i in the water phase.

Due to variations in both sampling and analysis of each phase, further corrections were required to calculate the partition coefficient as at this stage only the raw noble gas values for *i* in each phase were known. These are defined as $C_{Raw(\mathrm{P,T})}$ and $W_{Raw(\mathrm{P,T})}$ respectively. During sampling different-sized aliquots were taken for the CO_2 and water phases (2.4.2). Similarly during analysis different-sized aliquots were analysed for their noble gas content (A1 aliquot for CO_2, ampule for H_2O). These incorporated volumetric variations require elimination via corrections. Lastly, as sampling occurred at room temperature, a correction was required to incorporate the effects of thermal change on the samples.

The corrections need to be applied to give representative noble gas values in each phase where:

$$\mathrm{C}_{\mathrm{i(P,T)}} = \mathrm{C}_{\mathrm{raw(P,T)}} \times \mathrm{correction} \quad \mathrm{W}_{\mathrm{i(P,T)}} = \mathrm{W}_{\mathrm{raw(P,T)}} \times \mathrm{correction} \tag{2.5}$$

2.6.1 Sampling Volume Correction

As the samplers for the CO_2 and water phases were of significantly different volumes (~1 cm^3 and ~1.5 cm^3 respectively), a correction was needed to ensure that the analysed peaks were representative of identically-sized samples. Sampling of both phases occurred in triplicate for each partition coefficient. For each of the six unique aliquots normalisation was achieved by dividing each average peak value by the absolute volume of the associated sampler. An accurate calculation of the volume of each was obtained by weighing each sampler when empty ten times and repeating when filled with deionised water. By assuming the density of water at room temperature and pressure can be approximated to 1 g/cm^3 (0.998 g/cm3 at 292.39 K, 1 atmosphere. Source: NIST, 2013) the difference in weight was therefore equal to the volume of sampler. The sampler weights were as follows:

Sampler	Type	Volume (cm^3)	Uncertainty (S.E.)
A1	CO_2	0.973	0.412%
A2	CO_2	0.982	0.338%
A3	CO_2	0.996	0.395%
A_{1-3} Average	**CO_2**	**0.983**	**0.382%**
W1	Water	1.438	0.377%
W2	Water	1.442	0.249%
W3	Water	1.421	0.093%
W_{1-3} Average	**Water**	**1.449**	**0.239%**
W5	Water	1.570	0.331%
W6	Water	1.553	0.252%
W10	Water	1.657	0.285%
$W_{5,6,10}$ Average	**Water**	**1.593**	**0.289%**

Table 2.4. A list of all samplers used for data collection and their respective volumes and associated uncertainty. All samplers were weighed ten times when empty and ten times when filled on a set of scales, accurate to ± 0.005 g. Averages were made of each sampling set comprising three CO_2 and three H_2O samplers. Uncertainty was calculated as standard error of the ten measurements.

Using the values in Table 2.4 differences of noble gases concentrations due to variations in sample volumes were corrected where:

$$SVC = \frac{C_{Raw(P,T)}}{C_A} \Big/ \frac{W_{Raw(P,T)}}{W_A} = \frac{C_{Raw(P,T)} W_A}{W_{Raw(P,T)} C_A} \qquad (2.6)$$

SVC is Sample Volume Correction and C_A and W_A are the volumes of the CO_2 and water samplers and are measured in cm^3. By dividing $C_{i(P,T)}$ and $W_{i(P,T)}$ by the sampler volumes the effect of different sample sizes were removed.

2.6.2 Aliquot Correction Factor

Although both CO_2 and the water samples were initially expanded to the same volumes during the analytical process (discussed in detail in 2.5), different aliquots were subsequently preserved for each phase for noble gas analysis. Aliquot A1 was used for CO_2 (2.5.2) while the larger ampule was used for the water samples (2.5.3). A larger aliquot was used to generate a strong signal in the water phase which had lower noble gas concentrations relative to the CO_2 phase. Consequentially the analytical process amplified the noble gas signal derived from the water aliquots relative to the CO_2 aliquots necessitating a correction to account for the amplification. To determine the amplification factor the relative volumes of each aliquot were required.

This relative difference in volume was ascertained by expanding an air calibration shot from the pipette (0.2264 cm^3) into the line and subsequently isolating aliquot A1, the ampule and the pipette. Thus all three volumes were isolated at the same pressure. By measuring the pressure increase on the 0 – 10 mbar baratron for each aliquot the volumes relative to one another could be determined using Boyle's law. The increase in volume relative to the air calibration pipette provided absolute determinations of aliquot volumes. This process was repeated ten times in total over a series of days to generate robust averages. The resulting volumes are given in Table 2.5.

Aliquot	Analytical Role	Relative volume to pipette	Absolute volume (cm^3)	Uncertainty (S.E.)
Pipette	Air calibrations	1.00	0.2264	0.234 %
A1	CO_2 noble gas peaks	3.56	0.8068	0.625 %
Ampule	H_2O noble gas peaks	134.46	30.4425	0.509 %

Table 2.5. Relative and absolute volumes of each aliquot. Uncertainty was calculated as standard error of the ten repeat measurements.

From this it was possible to determine the volume of the larger aliquot (ampule) relative to the smaller (aliquot A1) to provide a correction factor for the CO_2 peaks:

Ratio	Correction factor	Uncertainty (S.E.)
Ampule:A1	37.73	0.338%

Table 2.6. Relative volumes of each aliquot. Uncertainty was calculated as standard error of the ten repeat measurements.

The ampule was thus determined to be larger than the A1 aliquot by a factor of 37.73. All CO_2 noble gas values were therefore increased by this factor to remove differences of noble gases concentrations due to variations in aliquot volumes:

$$\text{SVC \& AVC} = \frac{C_{\text{Raw}(P,T)} W_A F}{W_{\text{Raw}(P,T)} C_A} \tag{2.7}$$

where *AVC* is the Aliquot Volume Correction and *F* is the 37.73 correction factor applied to the CO_2 phase.

2.6.3 Density correction

During the sampling process (2.4.3) all samplers were at room temperature. However the phases being sampled were at elevated temperature within the oven (2.4.1). Samples taken from each phase would therefore progressively cool during sampling, leading to an increased sample density. This resulted in a greater absolute quantity of each phase being sampled; this being significantly greater for the more responsive CO_2 phase relative to the water phase. Therefore this required correction which was achieved by comparing experimental and sampling densities. By determining the factor increase in density during sampling for a given phase the total sample increase could be determined. The measured noble gas signals were then scaled down by this density factor to correct for the greater density within the samplers.

Accurate density values were therefore required for both CO_2 and water at sampling and experimental conditions. For experimental conditions where pressure and temperature were well defined density was calculated via the NIST website (NIST, 2013) using published equations of state for pure CO_2 and water (Span & Wagner, 1996; Wagner & Pruss, 2002). Densities of pure components were used given the extremely low mutual solubility in each phase (Spycher *et al.*, 2003). Thus densities of the samples under experimental conditions were calculated. Determining the exact pressure and temperature conditions during sampling however required a more rigorous approach.

For both the liquid water and the supercritical CO_2 samples rapid cooling was expected during sampling due to the small sample size. However neither the absolute rate nor the uniformity of sample cooling was known. It was expected that the samples would be at or close to laboratory temperatures (292.39 K) during sampling. At these temperatures supercritical CO_2 would have condensed into a liquid phase. Given the high incompressibility of liquids, the reduction of experimental pressures during the sampling process (approximately 5%) would not significantly affect density of either phase. Thus experimental pressures and laboratory conditions were reasonably assumed for the samples. The density correction applied to the data was therefore:

$$\text{SVC, AVC \& DCO} = \frac{C_{\text{Raw(P,T)}} W_A F}{\rho_C} \bigg/ \frac{W_{\text{Raw(P,T)}} C_A}{\rho_W} = \frac{C_{\text{Raw(P,T)}} W_A F \rho_W}{W_{\text{Raw(P,T)}} C_A \rho_C} \tag{2.8}$$

where DCO is Density Correction, ρ_c and ρ_w are the correction factors due to increased density when sampling the CO_2 and water phases respectively. These were calculated as:

$$\rho_C = \frac{\rho_{\text{sampling(C)}}}{\rho_{\text{experimental(C)}}}, \rho_W = \frac{\rho_{\text{sampling(W)}}}{\rho_{\text{experimental(W)}}} \tag{2.9}$$

where $\rho_{sampling(c)}$ and $\rho_{sampling(w)}$ are the densities when sampling the CO_2 and water phases respectively and $\rho_{experimental(c)}$ and $\rho_{experimental(w)}$ are experimental densities of the same phases. This correction provides a reasonable initial approach to removing the effect of sampling on each phase. However, due to uncertainty in accurately determining sampling conditions, this technique required validation.

2.6.4 Assessing the validity of the density correction

Initial estimates of sampling density assumed laboratory temperatures and experimental pressures. However empirical validation for these densities was required. This was investigated during the analysis of the CO_2 samples.

During analysis the entire CO_2 sample was expanded to the line which resulted in the liquid CO_2 sample becoming gaseous. This gas pressure was measured on the 0 – 13.33 bar baratron. However the phase change meant pressure could not be simply back-calculated using the gas laws to calculate density; a further stage was required. The same samplers at atmospheric pressure were connected and expanded to the line. Again the pressure was measured on the 0 – 13.33 bar baratron. This was repeated ten times. Using the ideal gas equation the total number of moles within the samplers at atmospheric pressure was determined:

$$n = \frac{PV}{RT} \tag{2.10}$$

where n is number of moles, P is pressure within the sampler in Pa, and V is sampler volume in m^3, R is the gas constant and T is temperature in Kelvin.

Property	Value	Units
P	101325	Pa
V	1.96E-06	m^3
R	8.3144621	$m^2\ kg\ s^{-2}\ K^{-1} mol^{-1}$
T	296.15	K
n	8.04901E-05	mol

Table 2.7. Values used for calculating the number of moles within the samplers. n was calculated using Equation 2.10.

Thus the relationship between number of moles and the pressure response was defined:

Number of moles	Pressure response (Pa)	Standard error
8.04901E-05	1947.84	0.215%
1	24.2×10^6	0.215%

Table 2.8. The relationship between number of moles and pressure. Values are scaled to show the pressure effect of one mole.

By applying this ratio to the CO_2 sample pressures the number of moles could be determined. By multiplying the number of moles by the molecular weight of CO_2 and dividing it by the sampler volume a density value was obtained. Examples of densities derived this way are presented in Table 2.9:

Experiment	Estimated density (kg/ m^3)	Sampler density (A3, A2 & A1) (kg/ m^3)	% difference
322.85 K, 112.7 bar	875.61	1033.26, 912.49, N/A	+18.0, +4.21, N/A
347.77 K, 113.46 bar	876.38	809.62, 845.62 & 851.8	-7.62, -3.51, -3.95
348.22 K, 129.3 bar	891.25	820.98, 857.74 & 883.98	-7.88, -3.64, -0.82
377.15 K, 112.84 bar	875.75	782.98, 820.08 & 802.47	-10.59, -6.36, -8.38

Table 2.9. Comparisons of calculated density with baratron-derived density. Calculated values assume experimental pressure and laboratory temperature. N/A indicates sample was considered invalid. Samples are listed in order of proximity to batch reactor.

Although baratron-derived and calculated densities conformed reasonably well, the former were generally lower. Neither the middle nor the furthermost sampler expressed any consistent density trend although the samplers closest to the experiment on average had the lowest densities. This may have been indicative of a minor thermal gradient which was supported by increases to the negative deviation at higher temperatures. This implied that CO_2 temperatures within the samplers were slightly above laboratory temperatures. However this assumed baratron-derived densities were valid, which therefore required assessment.

This was achieved by applying these alternative density corrections to the dataset and observing the effect on the partition coefficient standard deviation (Table 2.10):

Noble gas	Calculated density S.D.	Baratron density S.D.	Change
^{34}He	4.579	5.748	+25.529%
^{21}Ne	25.759	26.165	+1.579%
^{36}Ar	5.313	6.452	+21.432%
^{40}Ar	4.857	5.671	+16.751%
^{82}Kr	3.178	3.487	+9.723%
^{84}Kr	1.952	2.696	+38.097%
^{132}Xe	1.629	2.038	+25.059%
^{136}Xe	2.895	3.142	+8.555%

Table 2.10. Assessing the effect on partitioning of implementing the baratron-derived densities compared with the calculated values derived using laboratory temperature and experimental pressure. As partitioning is a ratio the standard deviations are unitless.

An absolute calculation of the CO_2 density for each sample should provide more accurate correction which, in turn, should reduce discrepancies within the data. However from Table 2.10 it is clear that baratron densities cause the data to become more dispersed for all noble gas isotopes. Additionally one baratron expansion (322.85 K, 112.7 bar) produced positive density deviations. This seemingly indicated pressures were above experimental and/or temperatures were below those in the laboratory neither of which are feasible.

Clearly issues of accuracy were present when the baratron technique was used to derive sample density. This was probably due to inaccuracies in defining the original moles/pressure relationship because of the uncertainty of each measurement. Additionally it is possible that other underlying issues were present for this method of density determination. Therefore until a greater accuracy is obtained with this technique it is considered too unreliable for absolute quantification of sample densities; however it can still be legitimately used as a qualitative aid to assess other techniques.

Overall the calculated and baratron-derived densities were acceptably similar. Therefore it was reasonable to continue assuming experimental pressures and laboratory temperatures when calculating sample density. It was recognised, though, that this was potentially an oversimplification which omitted any possible thermal gradients and therefore requires future investigation.

Although this simple assumption was liable to introduce a minor degree of uncertainty within the dataset all outstanding uncertainties were reasonably duly considered when calculating final experimental and procedural uncertainties (2.6.8).

2.6.5 Sensitivity

The sensitivity of a mass spectrometer is prone to vary slightly over time (2.3.2). As a result the measured partial pressure of a noble gas is liable to change, even if the absolute quantity remains constant. Traditionally air standards with a known noble gas quantity are analysed on each day a sample is run. These determine the relative shift in sensitivity and so allow for correction to calculate the absolute quantity of noble gas content within a sample:

$$P_{i(\mathrm{absolute})} = P_{i(\mathrm{measured})} \times \mathrm{Rs} \tag{2.11}$$

where $P_{i(absolute)}$ is the absolute partial pressure of noble gas i, $P_{i(measured\ )}$ is the measured partial pressure of noble gas i and Rs is the relative sensitivity of the mass spectrometer as determined by air calibration analysis. This can be applied to both phases of the partition coefficient:

$$\mathrm{SVC,\ AVC,\ DCO\ \&\ RSC} = \frac{C_{\mathrm{Raw(P,T)}} W_A F \rho_W \mathrm{Rs}_C}{W_{\mathrm{Raw(P,T)}} C_A \rho_C \mathrm{Rs}_W} \tag{2.12}$$

where RSC is the Relative Sensitivity Correction, Rs_C and Rs_w are the relative shifts to sensitivity for the CO_2 and water phase respectively. For deriving partition coefficients therefore it is the relative difference of sensitivity when measuring each phase which will affect partitioning. By analysing sample pairs within a single day it can be reasonably assumed that the relative sensitivity will remain plausibly constant for both phases (i.e. $Rs_C = Rs_w$). The demonstrated reproducibility of the air calibrations (2.3.2) prove the validity of this assumption. These terms cancel out, therefore, and Equation 2.8 is still valid; thus no corrections to the dataset to account for sensitivity were necessary.

By applying the sample volume correction, the aliquot volume correction and the density correction all heterogeneity due to the sampling and analytical process was removed. Thus it was possible to derive the final partial pressures of each noble gas in each phase:

$$C_{i(P,T)} = C_{Raw(P,T)} W_A F \rho_W \tag{2.13}$$

$$W_{i(P,T)} = W_{Raw(P,T)} C_A \rho_C \tag{2.14}$$

These could then be substituted into Equation 2.4 to determine Henry's constants for each paired sample from the raw data:

$$D_i = \frac{C_{Raw} W_A F \rho_W}{W_{Raw} C_A \rho_C} \tag{2.15}$$

2.6.6 Generating partition coefficients

The partition coefficient (D_i) is derived using the corrections described and the raw data:

$$D_{i(P,T)} = \frac{C_{i(P,T)} A}{W_{i(P,T)} B} \tag{2.16}$$

where A and B are the unique correction factors for a given pair analysis based on the volume of the samplers analysed and the density of each phase. The resultant partition coefficient was therefore a unitless ratio between each phase. An example of how this is calculated along with its associated uncertainty is shown in the appendix (AI.1).

Experimentally determined partition coefficients derived from the corrections outlined in this section were suitable for direct comparison to low pressure partitioning ratios derived from the Crovetto *et al.* and Smith datasets (Crovetto *et al.*, 1982; Smith, 1985) determined for the same experimental temperatures. This is the process by which partition coefficients were calculated for each paired sample.

2.6.7 Determination of uncertainty

As with any experimentally-derived values there is an inevitable associated degree of uncertainty. Uncertainty for each observational component must be propagated when deriving the final uncertainty for a partition coefficient. As density correction factors were calculated purely from differences in temperature at a constant pressure, uncertainty in temperature and pressure values were considered proxies for density. All uncertainties considered are shown in Table 2.11:

Uncertainty Factor	Symbol	Calculated Uncertainty	Units
Noble gas *i* in CO_2 phase	$\Delta C_{i(P,T)}$	1 σ of peak average	bar
Noble gas *i* in H_2O phase	$\Delta W_{i(P,T)}$	1 σ of peak average	bar
Volume of CO_2 sampler	ΔC_A	1 standard error of mean	cm^3
Volume of H_2O sampler	ΔW_A	1 standard error of mean	cm^3
Aliquot correction factor	ΔF	0.1275 (1 S.E. of mean)	N/A
Density correction for CO_2 phase	$\Delta \rho_C$	Measurement uncertainty in pressure and temperature	kg/m^3
Density correction for H_2O phase	$\Delta \rho_W$	Measurement uncertainty in pressure and temperature	kg/m^3
Uncertainty in pressure	ΔP	$\frac{1}{P_{\exp}}$	bar
Uncertainty in temperature	ΔT	$\frac{0.2}{T}$	°C

Table 2.11. Experimental uncertainty of each partition coefficient factor. For the uncertainty associated with each sampler the reader is directed to Table 2.4. For temperature and pressure the uncertainty was specified by the manufacturers of the thermocouple and transducer respectively and are given in original units.

In line with previous experimental studies of noble gases using quadrupoles e.g. (Podosek *et al.*, 1980; Shibata *et al.*, 1998; Kulongoski & Hilton, 2002; Sano & Takahata, 2005) a 1 σ uncertainty approach was applied to the peak values. It is noted that this 1 σ approach of calculating uncertainty allows reasonable consideration of signal intensity as a factor. Where a peak is clearly defined and easily measurable the reproducibility will be high and so $\Delta C_{i(P,T)}$ and $\Delta W_{i(P,T)}$ will be small, thus giving a small overall uncertainty.

However as the signal size gets smaller relative to the background the uncertainty in measuring values will result in increases to the value of 1 σ for both $\Delta C_{i(P,T)}$ and $\Delta W_{i(P,T)}$ resulting in a progressively larger associated uncertainty.

The overall density uncertainty is determined by the measurement uncertainty ($\Delta\rho_{Meas}$) and the uncertainty in the density correction, relative to each phase ($\Delta\rho_{Corr}$).

$$\frac{\Delta\rho}{\rho} = \sqrt{\left(\frac{\Delta\rho_{\mathrm{Meas}}}{\rho_{\mathrm{Meas}}}\right)^2 + \left(\frac{\Delta\rho_{\mathrm{Corr}}}{\rho_{\mathrm{Corr}}}\right)^2} \tag{2.17}$$

Density is derived through temperature and pressure (2.6.3); so, in order to generate the uncertainty for the density correction factor ($\Delta\rho$) for each phase the associated uncertainty of each variable (ΔT and ΔP) must be determined. As the same equipment was used for all pressure and temperature determinations $\Delta\rho_{Meas}$ was identical for both phases. However each sample would possess a unique $\Delta\rho_{Corr}$. CO_2 samples, which expressed the greatest density changes, would be strongly affected by any uncertainty when determining the density correction factor. This is in contrast to the water phase where any uncertainty in the extremely low (~1.01) correction factor would have a negligible effect.

However, $\Delta\rho_{Corr}$ was intrinsically linked to the validity of the calculated densities which for sampling are only simple estimates (2.6.4). Additionally no estimate of uncertainty is provided for the NIST calculations of CO_2 and water density which, although considered low, represent an unknown component required for calculating $\Delta\rho_{Corr}$. Therefore, given these ambiguities no viable way presently exists for reasonably calculating $\Delta\rho_{Corr}$. Future work is therefore required before this uncertainty can be numerically determined for individual experimental data points. Nevertheless, by calculating the uncertainty associated with procedural reproducibility (2.6.8) all sources of uncertainty, even those not directly quantifiable for individual analyses are suitably accounted for.

The relative density uncertainty for each phase is therefore simplified:

$$\frac{\Delta\rho}{\rho} \approx \sqrt{\left(\frac{\Delta\rho_{\mathrm{Meas}}}{\rho_{\mathrm{Meas}}}\right)^2} \tag{2.18}$$

This equation is valid for density calculations of both phases. This relative uncertainty in any density measurement is determined by relative uncertainty in temperature and pressure. As each factor is independent the relative uncertainties are squared, summed, then square-rooted (i.e. added in quadrature). Density correction is derived from both experimental (ρ_{Exp}) and sampling (ρ_{Samp}) densities. These relative uncertainties associated for each phase can be expressed as:

$$\frac{\Delta\rho_{\mathrm{Samp}}}{\rho_{\mathrm{Samp}}}=\sqrt{\left(\frac{\Delta \mathrm{T}}{\mathrm{T_{Samp}}}\right)^2+\left(\frac{\Delta \mathrm{P}}{\mathrm{P_{Samp}}}\right)^2},\ \frac{\Delta\rho_{\mathrm{Exp}}}{\rho_{\mathrm{Exp}}}=\sqrt{\left(\frac{\Delta \mathrm{T}}{\mathrm{T_{Exp}}}\right)^2+\left(\frac{\Delta \mathrm{P}}{\mathrm{P_{Exp}}}\right)^2} \tag{2.19}$$

These are added in quadrature to generate the uncertainty for each phase.

$$\frac{\Delta\rho_{\mathrm{Meas}}}{\rho_{\mathrm{Meas}}}=\sqrt{\left[\sqrt{\left(\frac{\Delta \mathrm{T}}{\mathrm{T_{Samp}}}\right)^2+\left(\frac{\Delta \mathrm{P}}{\mathrm{P_{Samp}}}\right)^2}\right]^2+\left[\sqrt{\left(\frac{\Delta \mathrm{T}}{\mathrm{T_{Exp}}}\right)^2+\left(\frac{\Delta \mathrm{P}}{\mathrm{P_{Exp}}}\right)^2}\right]^2} \tag{2.20}$$

Which reduces to:

$$\frac{\Delta\rho_{\mathrm{Meas}}}{\rho_{\mathrm{Meas}}}=\sqrt{\left(\frac{\Delta \mathrm{T}}{\mathrm{T_{Samp}}}\right)^2+\left(\frac{\Delta \mathrm{P}}{\mathrm{P_{Samp}}}\right)^2+\left(\frac{\Delta \mathrm{T}}{\mathrm{T_{Exp}}}\right)^2+\left(\frac{\Delta \mathrm{P}}{\mathrm{P_{Exp}}}\right)^2} \tag{2.21}$$

As exactly the same temperatures and pressures were used to generate density for both the CO_2 and water phases it follows that the value of $\frac{\Delta\rho_{Meas}}{\rho_{Meas}}$ is identical for both phases. Therefore the total density-derived uncertainty ($\Delta\rho_{Tot}$) applied to each partition coefficient can be expressed:

$$\frac{\Delta\rho_{\mathrm{Tot}}}{\rho_{\mathrm{Tot}}}=\frac{\Delta\rho_{\mathrm{Meas(C)}}}{\rho_{\mathrm{Meas(C)}}}+\frac{\Delta\rho_{\mathrm{Meas(W)}}}{\rho_{\mathrm{Meas(W)}}}=2\times\sqrt{\left[\left(\frac{\Delta \mathrm{T}}{\mathrm{T_{Samp}}}\right)^2+\left(\frac{\Delta \mathrm{P}}{\mathrm{P_{Samp}}}\right)^2+\left(\frac{\Delta \mathrm{T}}{\mathrm{T_{Exp}}}\right)^2+\left(\frac{\Delta \mathrm{P}}{\mathrm{P_{Exp}}}\right)^2\right]} \tag{2.22}$$

This density uncertainty, coupled with all other uncertainties (listed in Table 2.11), can be expressed as uncertainties relative to their measured values:

$$\frac{\Delta \mathrm{C_{i(P,T)}}}{\mathrm{C_{i(P,T)}}},\frac{\Delta \mathrm{W_{i(P,T)}}}{\mathrm{W_{i(P,T)}}},\frac{\Delta \mathrm{C_A}}{\mathrm{C_A}},\frac{\Delta \mathrm{W_A}}{\mathrm{W_A}},\frac{\Delta \mathrm{F}}{\mathrm{F}},\frac{\Delta\rho_{\mathrm{Tot}}}{\rho_{\mathrm{Tot}}} \tag{2.23}$$

This cancels out all unit terms. Now it is possible to combine all uncertainties to generate the uncertainty associated with the partition coefficient (ΔD_i) and was achieved by adding all relative uncertainties in quadrature. As before this involved the squaring and summation of all independent relative uncertainties. The sum total is then square-rooted to give the overall relative uncertainty ($\frac{\Delta D_{i(\mathrm{P,T})}}{D_{i(\mathrm{P,T})}}$) for a single partition coefficient:

$$\frac{\Delta D_{i(\mathrm{P,T})}}{D_{i(\mathrm{P,T})}}=\sqrt{\left(\frac{\Delta C_{i(\mathrm{P,T})}}{C_{i(\mathrm{P,T})}}\right)^2+\left(\frac{\Delta W_{i(\mathrm{P,T})}}{W_{i(\mathrm{P,T})}}\right)^2+\left(\frac{\Delta C_A}{C_A}\right)^2+\left(\frac{\Delta W_A}{W_A}\right)^2+\left(\frac{\Delta F_i}{F_i}\right)^2+\left(\frac{\Delta\rho_{tot}}{\rho_{tot}}\right)^2} \tag{2.24}$$

As an aid to the reader a worked example of uncertainty propagation for helium from a paired sample set is given in the appendix (AI.1).

2.6.8 Combining partition coefficients

Partition coefficients with associated uncertainty have been generated for each valid pair of CO_2-water samplers. The next stage therefore was to combine these individual data points to produce a single, representative partition coefficient with an uncertainty for each experiment.

As all partition coefficients were considered equally valid the representative partition coefficient was calculated as a simple arithmetic mean:

$$\overline{D}_{i(P,T)} = \frac{\left(\sum_{1}^{n} D_{i(P,T)}\right)}{n_{(P,T)}} \qquad (2.25)$$

where $\overline{D}_{i(P,T)}$ is the mean partition coefficient for noble gas i for a given pressure and temperature, $D_{i(P,T)}$ is each individual partition coefficient and $n_{(P,T)}$ is the number of samples.

The uncertainty for the mean partition coefficient $(\Delta\overline{D}_{i(P,T)})$ was the overall experimental uncertainty $(\Delta\overline{D}_{iExp(P,T)})$ for each experiment combined with an uncertainty relating to the procedural reproducibility of all data points for the isotope $(\Delta\overline{D}_{i\mathrm{Proc}})$.

$$\frac{\Delta\overline{D}_{i(P,T)}}{\overline{D}_{i(P,T)}} = \sqrt{\left(\frac{\Delta\overline{D}_{iExp(P,T)}}{\overline{D}_{iExp(P,T)}}\right)^2 + \left(\frac{\Delta\overline{D}_{iProc}}{\overline{D}_{iProc}}\right)^2} \qquad (2.26)$$

The overall experimental uncertainty was a combination of the uncertainties from each partition coefficient $(\Delta D_{i(P,T)})$ used to generate the mean partition coefficient value for each experiment. However, not all sources of uncertainty (e.g. density), could be easily factored in for each individual partition coefficient. The cumulative effect of these factors is an additional degree of uncertainty which could not be satisfactorily derived from any individual analysis. This additional uncertainty is termed the procedural reproducibility.

To calculate the overall experimental uncertainty for each experiment each individual experimental uncertainty was divided by its corresponding absolute value to give the relative uncertainty ($\frac{\Delta D_{i(P,T)}}{D_{i(P,T)}}$). These relative uncertainties for each individual data point are added in quadrature. They are then divided by the number of samples used for creating this average ($n_{(P,T)}$). Finally the output is square-rooted to give the average relative uncertainty derived from the experimental process for a given experiment:

$$\frac{\Delta\overline{D}_{\exp(P,T)}}{\overline{D}_{\exp(P,T)}} = \sqrt{\frac{\sum_{1}^{n}\left(\frac{\Delta D_{i(P,T)}}{D_{i(P,T)}}\right)^{2}}{(n_{(P,T)})}} \tag{2.27}$$

Thus as the number of samples for each experimental condition increases, assuming measurement uncertainty remains the same, the experimental uncertainty will decrease.

To ensure a representative procedural reproducibility-based uncertainty was applied to the data, the average deviation of partition coefficients from the mean values was used. The absolute deviation of each partition coefficient ($D_{i(P,T)}$) was calculated by subtracting it from the mean $(\overline{D}_{i(P,T)})$; to ensure this is positive the modulus of each deviation is used. Dividing each deviation by the calculated mean value therefore gives the relative deviation of each individual data point. These relative uncertainties for every partition coefficient are then all added in quadrature, then are divided by the total number of samples (n_{tot}). Finally this is square-rooted to generate the average relative uncertainty derived from the procedural reproducibility. This average relative uncertainty can be used as a reasonable estimate for the procedural reproducibility uncertainty for each experiment:

$$\frac{\Delta\overline{D}_{\mathrm{Proc}(P,T)}}{\overline{D}_{\mathrm{Proc}(P,T)}} = \sqrt{\frac{\sum_{1}^{n_{tot}}\left(\frac{(\left|\overline{D}_{i(P,T)} - D_{i(P,T)}\right|)}{\overline{D}_{i(P,T)}}\right)^{2}}{n_{tot}}} \tag{2.28}$$

As progressively more data points are added the true variability in precision for each isotope can be better estimated using this approach. Thus procedural reproducibility is reasonably taken into account when calculating average uncertainty values. This average uncertainty associated with procedural reproducibility for each isotope is stated in Table 2.12.

Isotope	Average Uncertainty (%)
^{4}He	7.897
^{21}Ne	24.535
^{36}Ar	12.288
^{40}Ar	12.175
^{82}Kr	8.724
^{84}Kr	6.803
^{132}Xe	6.117
^{136}Xe	6.941

Table 2.12. Average procedural reproducibility uncertainty for each isotope. Averages were collected from 23 discrete data points.

A worked example calculating the procedural reproducibility uncertainty for ^{4}He is given in the appendix (AI.2). This procedural reproducibility uncertainty could then be combined with the experimental uncertainties to give the overall uncertainty for each data point.

By substituting Equations 2.27 and 2.28 into Equation 2.26 a formula for calculating the overall uncertainty associated with each data point at a given pressure and temperature (*P*,*T*) can be derived:

$$\frac{\Delta\overline{D}_{i(P,T)}}{\overline{D}_{i(P,T)}} = \sqrt{\frac{\left[\sum_{1}^{n}\left(\frac{\Delta D_{i(P,T)}}{D_{i(P,T)}}\right)\right]^{2}}{n_{(P,T)}} + \frac{\left(\sum_{1}^{n_{tot}}\left|\frac{(\overline{D}_{i(P,T)} - D_{i(P,T)})}{\overline{D}_{i(P,T)}}\right|\right)^{2}}{n_{tot}}} \qquad (2.29)$$

Using this approach a representative data point and associated uncertainty was generated for every isotope at each pressure and temperature. These are presented in Chapter 4.

Chapter Three

Development of Modelling

3.1 Introduction

It has become possible in recent years to simulate complex multi-phase systems to a high degree of accuracy in order to investigate key system properties. This is due to the exponential increase in computing power of recent years coupled with a decrease in computational costs. Thus it was feasible to construct, in tandem with the experimental aspect of this project, a simulation to predict partitioning of noble gases at any pressure-temperature regime. The two modelling approaches which were considered most applicable were Molecular Dynamics (MD) and Monte Carlo (MC).

The first part of this chapter gives a concise overview of each of these modelling techniques. Supplementary information is provided in respective references and in the following publications; Allen & Tildesley and Frenkel & Smit (Allen & Tildesley, 1987; Frenkel & Smit, 2002). Techniques and molecular models identified as suitable during this review are then combined to construct a simulation capable of generating noble gas partition coefficients which can be compared to experimental values. This construction and verification process is fully documented at the end of this chapter.

3.2 Molecular Dynamics

Molecular dynamics simulations are a subset of models which most closely replicate molecular interactions at an atomistic scale. They simulate the interactions of molecules over time. Each molecule is comprised of atoms, all of which possess a mass, a charge (if applicable), a position in three dimensional space and an associated momentum. Each molecule also has a van der Waals interaction force with all other molecules.

When the simulation is initiated each molecule is assigned a velocity taken from a Maxwell-Boltzmann distribution. The initial force acting on each molecule is calculated from the positions of all the other molecules combined with a knowledge of the force laws. After a user-defined time step the new positions of each molecule are calculated. These are derived from their previous velocities and accelerations using the classical laws of motion. At their new position the effect of interatomic forces from nearby atoms must be factored into current velocities. Positions, velocities and accelerations can then be updated for each molecule using an algorithm. These updated values are used as the basis for the next time step. The most commonly used algorithm is the Verlet algorithm (Verlet, 1967) and subsequent modifications thereof (e.g. Omelyan *et al.*, 2002; Min, 2005; Wang *et al.*, 2013) due to the highly optimised nature and recognised accuracy of this algorithm in calculating molecular displacement as a function of time (Allen & Tildesley, 1987). The duration of each time step is user-defined but is usually in the 1 – 60 femtosecond range. Larger time steps result in a faster simulation; but increasing the interval between recalculating trajectories can also result in molecules not interacting appropriately with one another (Fincham, 1986).

From the initial starting positions the system therefore gradually evolves as molecules progressively interact with one another. After sufficient simulated time has passed the system reaches a steady state. At this point, although individual molecules are still in a state of flux, the system as a whole is at equilibrium internally and with its surroundings. As a result the bulk thermodynamic properties such as volume, density or total internal energy fluctuate around constant values. When this stage is reached the system is said to be in dynamic equilibrium and data on the thermodynamic properties of the system can be collected.

3.2.1 Calculating the forces

Given the nature of this simulation type the accuracy of the outcome is intrinsically linked to accurately calculating intermolecular forces for each step. For this modelling approach these forces are subdivided into non-polar and electrostatic forces. The non-polar forces exerted on atoms within a given molecule by neighbouring atoms are the sum total of the long range attractive forces combined with the short range repulsive forces. Where these atoms are sufficiently distal to one another the long range attractive forces are dominant; as this distance is reduced the short range repulsive forces become progressively stronger in comparison until they become the dominant force acting on the atomic pairs. These intermolecular forces are known as the van der Waals interaction.

These complex interactions are most commonly approximated using the Lennard-Jones 12 – 6 potential. This approximation describes the relationship between the attractive and repulsive interactions of each molecular pair and the resultant effect on the relative potential energy. This is illustrated in Figure 3.1.

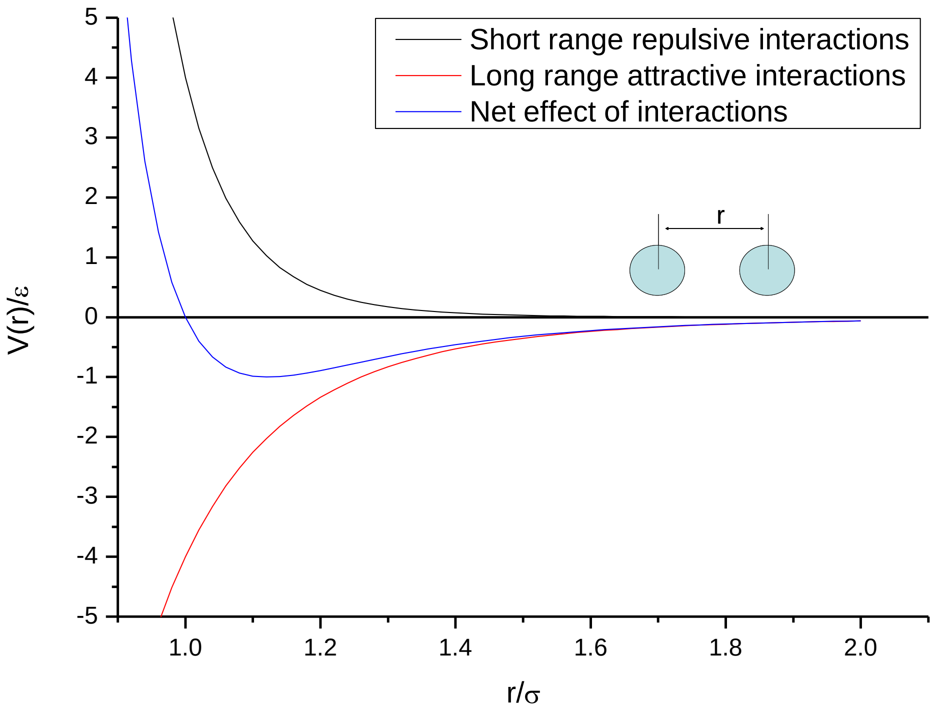

Fig. 3.1. The Lennard-Jones potential. The net effect of short range repulsive interactions and the long range attractive interactions on the potential energy ($V(r)/\varepsilon$) are calculated as a function of intermolecular distance (r).

In its standard form the Lennard-Jones 12 – 6 potential is written

$$V(r) = 4\varepsilon\left[\left(\frac{\sigma}{r}\right)^{12} - \left(\frac{\sigma}{r}\right)^{6}\right] \tag{3.1}$$

where $V(r)$ is the Lennard-Jones 12 – 6 potential, r is the intermolecular distance, ε is the depth of the potential well and σ is the distance at which the potential between the two atoms is zero. The point at which $V(r)$ reaches the minimum (r_m) is the equilibrium distance at which attractive and repulsive interactions are balanced and the potential energy is at its lowest, i.e. the atoms are occupying their most optimal positions relative to one another. Although this most favourable position is frequently reached between individual pairs of atoms, external interatomic forces on each atom from other proximal atoms result in sufficient energy to escape this localised energy minima. As a result the system remains dynamic, even when the equilibrium stage is reached. Values of ε and σ for each atom are defined within each molecular model and are fully discussed in 3.4.

For polar molecules charge is unevenly distributed over the molecule. This is modeled by assigning each atom a potential charge. These electrostatic forces must also be considered. The sum total of the electrostatic potentials of interaction operating within the system can be written as $\sum_{\alpha,\beta} \frac{q_\alpha q_\beta}{4\pi\varepsilon_0 r_{\alpha\beta}}$. Here q_α and q_β are the point charges on particles α and β respectively, ε_0 is the vacuum permittivity and $r_{\alpha\beta}$ is the distance between the two charges. Charges for each ionic particle are also defined within the molecular model. In order to treat this long range interaction accurately the Ewald summation technique is used. This divides the electrostatic potential into short- and long-ranged components. These are then calculated in both real space and Fourier space respectively. The key advantage of this approach is that Fourier space allows for a far faster evaluation of long range electrostatic charges when compared to calculating these charges in real space. Thus the overall electrostatic potential energy is obtained from charged atoms in the most efficient way.

3.2.2 Periodic Boundary Conditions

The majority of simulations focus on simulating the bulk properties of the system. However due to the finite nature of the simulation box a considerable proportion of the simulated molecules will be affected by their proximity to the box edge. This can potentially bias the results as the effect of surfaces on bulk properties for real systems is considered negligible. This issue is negated by invoking periodic boundary conditions whereby the box is surrounded with ghost images of itself (Figure 3.2).

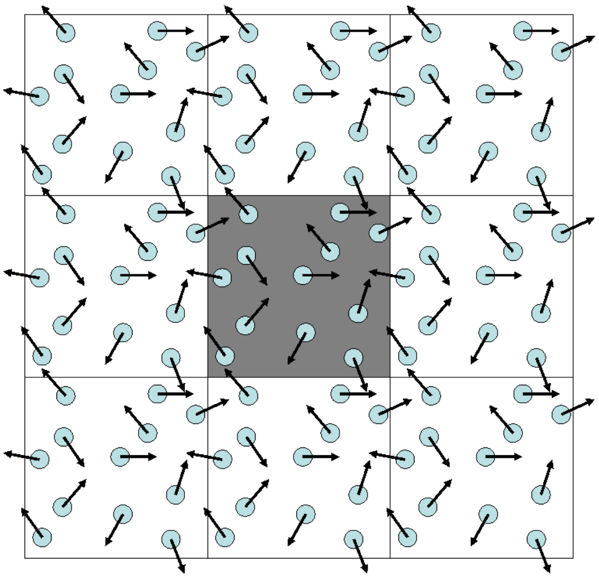

Fig. 3.2. A two-dimensional depiction of periodic boundary conditions. The simulated box (grey) is surrounded by ghost images of itself on all sides. As a molecule moves beyond the dimensions of the simulated box a ghost counterpart possessing the same velocity enters the box from the opposite face.

Replicating the original box in this way provides all molecules close to the edge of the box with an appropriate number of molecules to interact with beyond the absolute limit of the box. When one molecule leaves the simulation box its ghost particle possessing an identical vector enters from the opposing side. Thus each molecule is be simulated as if it were at infinite distance from any surface. This therefore provides a way of accurately determining bulk properties of the system. These 'ghost' images allow the Ewald summation to realistically simulate electrostatic potentials acting on each particle.

Whilst periodic boundary conditions are imposed, it is essential cut-off distances for all Lennard-Jones interactions are imposed. This is known as the nearest image convention and is required to prevent an atom from interacting with ghost images of itself or with multiple copies of another molecule. Such interactions would never occur within a real system. Intermolecular forces operating at lengths greater than the cut-off distance are assumed to be negligible. The usual cut-off distance is set at half the whole box length (Allen & Tildesley, 1987). Consequentially it is essential that the system size is sufficiently large for molecular interactions occurring beyond the cut-offs to have a negligible impact on molecules interacting with their neighbours. However the larger the system the higher the computational cost and the longer it takes to reach equilibrium. Therefore the system needs to be the smallest it can be without being affected by the cut-offs. This is a most commonly determined by progressively scaling a system size up and observing the results. Where the results become reproducible the system size is considered acceptable.

3.2.3 Maintaining system conditions

In any simulated molecular system there are always three fixed thermodynamic properties defined by the user: number of molecules (*N*), chemical potential (μ), temperature (*T*), pressure (*P*), volume (*V*) and entropy (*E*). These can be combined in the following simulation types: *NVE*, *NVT*, *NPT* and μVT. During these simulations all other thermodynamic properties are allowed to fluctuate. When equilibrium is reached, these properties may be calculated as averages over fluctuating instantaneous values. For this state to be achieved the three defined properties must be kept as constant as practically possible. This is achieved using an algorithm for each fixed thermodynamic parameter. This maintains the system property to within a defined tolerance thus preventing significant deviation from the specified values during the course of the simulation. Common algorithms include the Nosé-Hoover (Hoover, 1985) or Berendsen (Berendsen *et al.*, 1984) for temperature and Langevin (Quigley & Probert, 2004) or Nosé-Hoover (Melchionna *et al.*, 1993) for pressure.

3.2.4 Initial system configuration

When simulating systems via molecular dynamics the initial position and orientation of each molecule must be carefully considered. By ensuring an appropriate starting configuration is used the time spent in reaching a state of dynamic equilibration is minimised. To create the initial configuration, the system box is given an initial volume by the user which is then subdivided into a number of smaller boxes. A molecule (*n*) to be simulated is inserted into each box until all molecules have been inserted ($n = n_{total}$). This method of discrete insertion ensures no molecular overlaps exist in the starting configuration. Once this initial matrix is filled then all molecular positions and orientations must be constrained to acceptable values. This is achieved using another algorithm e.g. SHAKE (Ryckaert *et al.*, 1977) or RATTLE (Andersen, 1983) which iteratively adjust the orientations of each molecule until a reasonable configuration is reached, within a specified degree of tolerance. The molecules can then be assigned velocities taken from a Maxwell-Boltzmann distribution. The system is now ready for simulation.

3.2.5 Limitations of Molecular Dynamics

Provided that the system size is suitably large and all molecular interactions are accurately accounted for any molecular dynamics simulation has the potential to accurately model a system across a wide range of conditions. However, although algorithms and subroutines have been developed to minimise costs, this approach is computationally expensive, as after each time step all changes to the intermolecular forces acting on each molecule must be recalculated and all trajectories redetermined. This issue is exacerbated when large systems and/or smaller time steps are implemented.

The major disadvantage to molecular dynamics-based simulations however is the inability to easily simulate multiphase systems: to accomplish this a phase interface would be required through which molecules could physically migrate. Maintaining such an interface and preventing molecular interactions at the boundary from affecting the bulk properties of the two phases would present many complications. Instead, multiple-phase systems are typically simulated using Monte Carlo-based simulations.

The goal of the modelling aspect of this project was to replicate noble gas partitioning within the experimental binary phase system. Therefore it was considered that using a molecular dynamics simulation as a basis was not suitable. As Monte Carlo simulations have a proven ability to simulate multiphase systems a model based on this approach was the obvious choice. This simulation technique will now be discussed in more detail.

3.3 Gibbs Ensemble Monte Carlo

3.3.1 Overview of GEMC approach

An alternative classical simulation technique for investigating molecular systems is Monte Carlo-based modelling. This approach makes use of random numbers to generate an equilibrium distribution of states for the system of interest. Appropriate averages over these states yield key information about the thermodynamic properties of the system. Depending on the system of interest different Monte Carlo approaches can be used to investigate these properties. For simulating co-existing phases a highly suitable Monte Carlo approach is the Gibbs Ensemble Monte Carlo (GEMC) technique (Panagiotopoulos, 1987). This method uses two boxes to simulate a binary phase gas-liquid system. The box containing a high density of molecules is termed the liquid phase (*I*) while the box possessing the lower density is considered the vapour/gas phase (*II*). Initially, as with a Molecular Dynamics (MD) simulation, the volume of each box and the corresponding number of molecules within each box are defined by the user to create the initial molecular configuration of the system (3.2.4). Once this initial configuration has been created it is possible to calculate the total potential energy of the system (U_{tot}) from the sum of all molecular interactions within each phase $(\sum U_{(I)} + \sum U_{(II)})$.

$$U_{tot} = \sum U_{(I)} + \sum U_{(II)} \tag{3.2}$$

The key interactions which control the potential energy in each box are divided into two categories; intra-molecular forces and inter-molecular forces.

$$\sum U = \sum U_{Intra} + \sum U_{Inter} \tag{3.3}$$

The intra-molecular forces correspond to the variation of bond lengths, bond angles and dihedral angles while the inter-molecular forces are the net effect of the van der Waals interactions and the coulombic electrostatic forces. These are discussed further for each model in 3.4. For this project all molecular models used had no degree of flexibility in either bond angle or bond length. These rigid molecules therefore contributed no intramolecular potential energy. Therefore Equation 3.3 could be simplified:

$$\sum U = \sum U_{Inter} \tag{3.4}$$

The potential energy of interaction is calculated identically in both Monte Carlo and Molecular Dynamics approaches. For example the potential energies derived from the van der Waals forces are most commonly approximated using the Lennard-Jones 12 – 6 potential. However, alternatives such as the hard sphere potential, the London potential or the Exponential-6 potential are occasionally used (e.g. Attard, 1993; Galliero *et al.*, 2006). The coulombic interaction energy is most commonly calculated using the Ewald sum. The specifics involved in calculating both types of intermolecular interaction are identical for Gibbs Ensemble Monte Carlo and for molecular dynamics (3.2.1).

By considering each type of interaction it is possible to calculate the current potential energy of both the system and each box. To ensure the calculated potential energy is representative of the bulk liquid and gas phases periodic boundary conditions are invoked (3.2.2). Additionally as with Molecular Dynamics simulations all user-defined system properties (e.g. pressure or temperature) are maintained using algorithms (3.2.3)

3.3.2 Modelling a binary phase system

Once the initial configuration has been generated and the potential energy calculated the system may evolve in one of three ways:

- Varying box size (Figure 3.3b)
- Moving molecules within a box (Figure 3.3c)
- Moving molecules between boxes (Figure 3.3d)

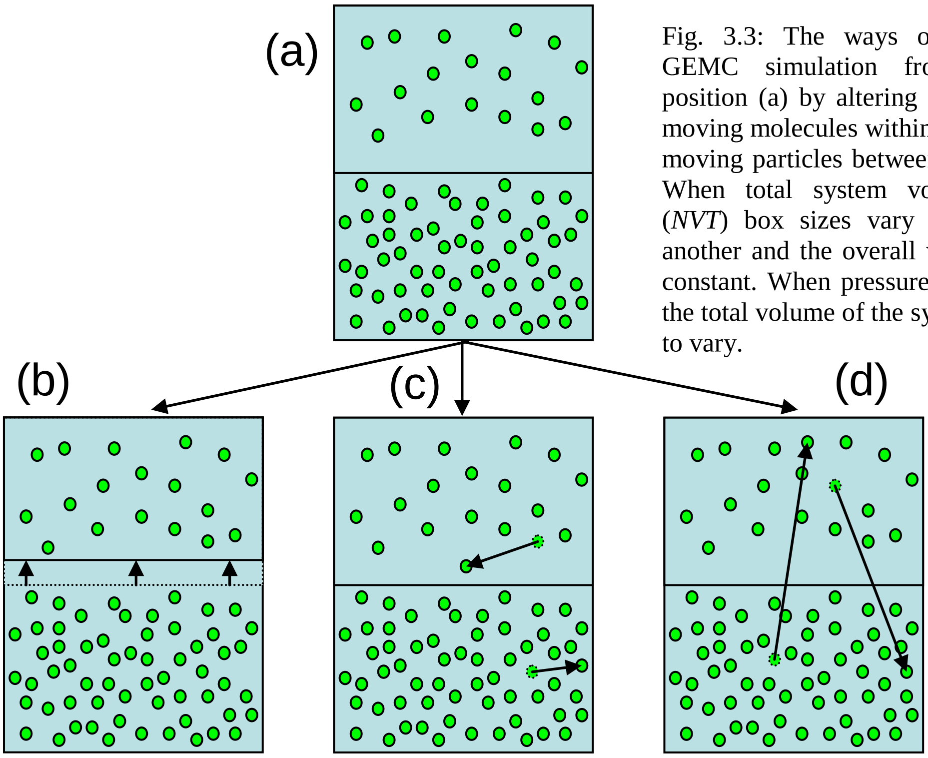

Fig. 3.3: The ways of perturbing a GEMC simulation from a starting position (a) by altering the volume (b), moving molecules within the box (c) and moving particles between the boxes (d). When total system volume is fixed (*NVT*) box sizes vary relative to one another and the overall volume remains constant. When pressure is fixed (NPT) the total volume of the system is allowed to vary.

To avoid bias the type of move and magnitude are randomly determined via a Markov chain random number generator. After the random move is applied to the system the overall change of potential energy is assessed. The new configuration is either accepted or rejected based on the Metropolis algorithm (Metropolis *et al.*, 1953). Moves resulting in a lower energy state are always accepted. Those resulting in higher energy states are either accepted or rejected based on a series of acceptance criteria.

For the volume move (Figure 3.3b) corresponding to a *NPT* system (i.e. no absolute volume limit) the change to the potential energy (ΔW) can be expressed:

$$\Delta W = \Delta U + P\Delta\Delta - nkT\ln\left(\frac{V+\Delta V}{V}\right) \tag{3.5}$$

where *P* is pressure, *V* is volume, *n* is the number of atoms in the box where the perturbation is occurring, *k* is the Boltzmann constant and *T* is the temperature. Δ denotes a change to a system property. Where the volume change corresponds to a relative change in volume but the overall system is at a constant volume (*NVT*) the overall change to the potential energy (ΔW) is the net potential energy change to both boxes. This can be expressed:

$$\Delta W = \Delta U_I + P\Delta\Delta_I + \Delta U_{II} + P\Delta\Delta_{II} - n_I kT\ln\left(\frac{V_I+\Delta V}{V_I}\right) - n_{II}kT\ln\left(\frac{V_{II}+\Delta V}{V_{II}}\right) \tag{3.6}$$

where *I* and *II* denote box one and two respectively. The proposed move is then accepted or rejected using the Metropolis algorithm. As previously outlined where the change is energetically favourable the move is accepted:

$$\Delta W \leq 0 = \text{Accept Move} \tag{3.7}$$

The acceptance criterion for energetically less favourable systems is defined:

$$P_{acc} \geq P_{rand} = \text{ Accept Move} \tag{3.8}$$

P_{acc} is the probability of accepting a less favourable new configuration and P_{rand} is a system-generated random number between 0 and 1. P_{acc} for each unfavourable move is calculated using Equation 3.9.

$$P_{acc} = e^{-\left(\frac{\Delta W}{KT}\right)} \tag{3.9}$$

For displacements both within an individual box (Figure 3.3c) and between two discrete boxes (Figure 3.3d) the change to the system energy (*ΔU*) is used. The Metropolis-derived acceptance/rejection of these types of move is similar to those for the volume change. For the displacement within a box the acceptance criteria are therefore:

$$\Delta U \leq 0 = \text{Accept Move} \tag{3.10}$$

$$P_{acc} \geq P_{rand} = \text{ Accept Move} \tag{3.11}$$

However, calculating P_{acc} varies. For a simple move within a box this is defined as:

$$P_{acc} = e^{-\left(\frac{\Delta U}{KT}\right)} \tag{3.12}$$

When moving a molecule from one box (I) to another box (II) proves unfavourable, the change in system energy in both boxes must be considered for accepting or rejecting the move. Therefore for this move type P_{acc} is defined by Equation 3.13.

$$P_{acc} = e^{-\left[\frac{\left(\Delta U_{(I)}+\Delta U_{(II)}+KT\ln\frac{V_{(II)}(n_{(I)}+1)}{V_{(I)}n_{(II)}}\right)}{KT}\right]} \tag{3.13}$$

By using the Metropolis algorithm acceptance/rejection criteria as outlined in Equations 3.5 – 3.13 the correct Boltzmann distribution for the system is ensured. As the proposed changes to the system becomes progressively less energetically favourable (ΔW or $\Delta U \rightarrow$ infinity), the probability of acceptance exponentially decreases ($P_{acc} \rightarrow 0$). Only slightly less favourable configurations are ever therefore accepted. Thus the probabilistic distribution of potential energy within a real system (Figure 3.4) is replicated.

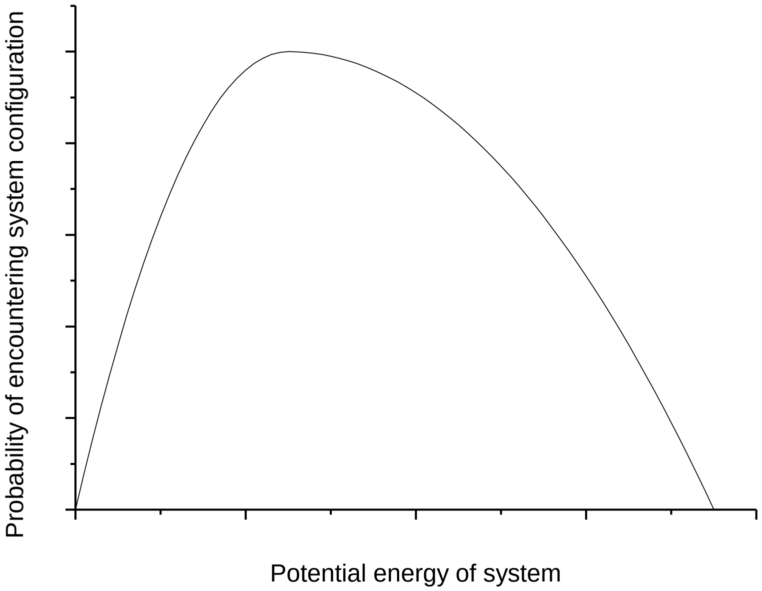

Fig. 3.4. The probabilistic distribution of potential energy within a real system.

Where the potential energy of the system is plotted on the x-axis and probability is plotted on the y-axis. At the graph origin the molecules within the system exists as a flawless crystalline structure while at the far right (at infinity) molecules may overlap completely. Obviously while both configurations are theoretically possible, in reality no system will ever approach either of these two extremes. In reality a system is in a state of perpetual flux around the most probable configuration. The role of the metropolis algorithm therefore is to replicate this within a simulation.

The use of the exponential term within the Metropolis algorithm to determine acceptance of a less favourable system perturbation ensures that the highly unfavourable system configurations which have a very low probability of occurring within a real system are seldom accepted. However those which only result in slightly unfavourable conditions may be accepted. When the system is close to the highest probability region these configurations are frequently encountered and therefore often accepted. By allowing slightly less favourable configurations to be accepted prevents the system from moving only in one direction, towards the pure crystalline state. Equally important it prevents the system from being potentially being ‘trapped’ within a local energy minima which would unfairly bias system averages. The Metropolis algorithm therefore allows the most probable system configurations to be selected with the highest frequencies. This ensures that the probabilistic distribution function for the potential energy of every possible permutation of the system is correctly adhered to. This results in the simulated system at equilibrium replicating configurations expected within its real counterpart.

3.3.3 Acceptance ratios

It follows that the probability of move being accepted is a function of the absolute magnitude of the perturbation being proposed. Moves with a larger displacement are more likely to result in unfavourable molecular configurations leading to the move being rejected. However, when these moves are accepted, a greater overall effect on the system is observed. Consequentially attempting these kinds of moves can allow the system to more rapidly explore phase space. An efficient GEMC simulation therefore attempts a reasonable amount of both large and small perturbations to maintain a dynamic system.

This is typically achieved using a feedback algorithm to obtain a target acceptance ratio, i.e. the desired percentage of moves which are accepted. This is usually set to 50% for all applicable move types. Initially maximum displacements for all applicable perturbations are defined. After a given number of perturbations the acceptance of each move type (P_{acc}) is calculated. Low acceptances ($P_{acc} < 50\%$) result in a decrease to the maximum displacement while high acceptances ($P_{acc} > 50\%$) result in increased maximum displacement. Thus a reasonably dynamic system is maintained which reaches dynamic equilibrium quickly. Interbox perturbations do not involve a magnitude and so a target acceptance ratio is not applicable.

3.3.4 Calculating system averages

Once the system reaches dynamic equilibration system properties calculated from each configuration can be sampled to generate system averages. Values for each thermodynamic property of interest are incorporated into a rolling average. After a sufficiently long sampling this average is representative of the system average at the specified conditions. Typically the number of moves required for adequate system averages lie within the region of 10^7 – 10^8 although this is strongly dependent on system variables such as system size or complexity, with more sensitive properties generally requiring averages from longer runs than less variable counterparts.

3.3.5 Limitations

Although the GEMC technique is widely recognised as a powerful analytical tool it is not without its challenges. For example difficulties have been identified concerning the insertion of molecules into a dense liquid phase. As insertions are more prone to rejection reaching true equilibrium between each phase for such system takes significantly longer and result in a greater statistical uncertainty (Lopes & Tildesley, 1997). For similar reason difficulties have also been noted when moving large molecules within a system (e.g. Frenkel & Smit, 2002; Chun, 2003; Rane *et al.*, 2013).

Despite these issues the use of GEMC simulation packages in investigating binary phase systems, especially those containing CO_2 and water phases is unparalleled e.g.(Harris & Yung, 1995; Vorholz *et al.*, 2000; Zhu *et al.*, 2009; Vlcek *et al.*, 2011). Given, therefore, the proven ability of Gibbs Ensemble Monte Carlo modelling at simulating the primary system of interest this modelling approach was chosen to replicate the experimental system.

3.4 Molecular models

3.4.1 Introduction

To construct a GEMC model containing CO_2, water and noble gases interacting with one another it follows that suitable molecular models for CO_2, water and noble gases were identified from the literature. A critical analysis of key models for each now follows.

3.4.2 Carbon Dioxide

The most prevalent atomistic models for CO_2 are the MSM (Murthy *et al.*, 1981), EPM2 (Harris & Yung, 1995), TraPPE (Potoff & Siepmann, 2001) and the Errington model (Errington & Panagiotopoulos, 1998). Key properties of each model is presented in Table 3.1.

Model name	$(\varepsilon_{C\text{-}C}/k_B)$ (K)	$\sigma_{\text{C-C}}$ (Å)	$(\varepsilon_{O\text{-}O}/k_B)$ (K)	$\sigma_{C\text{-}C}$ (Å)	α	q_C	q_O	$l_{C\text{-}O}$ (Å)
MSM	29.000	2.785	83.100	3.014	-	+0.596	-0.298	1.160
EPM2	28.129	2.757	80.507	3.033	-	+0.651	-0.326	1.149
TraPPE	27.000	2.800	79.000	3.050	-	+0.700	-0.350	1.160
Errington	29.070	2.753	83.200	3.029	14	+0.647	-0.323	1.143

Table 3.1. The parameters of each CO_2 molecular model. ε and σ refer to the Lennard-Jones potential values for like particles, α is Buckingham potential used in the Errington model, q_C and q_O are the charges on the carbon and oxygen atoms respectively and $l_{C\text{-}O}$ is the bond length between these atoms. Modified from Zhang and Duan (Zhang & Duan, 2005a). All values given to 3 decimal places.

All four selected CO_2 models had fixed length bonds between the oxygen and carbon atoms and the angle between these bonds was fixed at 180°. All are therefore simulated as rigid molecules. Although the original EPM2 model contained a term for the bond angle to be flexible, the energy required to deviate from 180° was extremely high

(1236 kJ/mol/rad^2). Thus this flexible term is usually omitted and the model is also typically treated as rigid.

In order to ascertain which of these models were most accurate, published studies compared the thermodynamic data from each of these models with experimental data (e.g. Vorholz *et al.*, 2000; Zhang & Duan, 2005a; Mognetti *et al.*, 2008; Zhu *et al.*, 2009; Nielsen *et al.*, 2012). From these studies notable issues were raised regarding the accuracy of both the Errington and the TraPPE models, especially when the critical point of CO_2 is approached. Furthermore the Errington model interactions used the Buckingham potential (i.e. they were not approximated using the Lennard-Jones approach) which rendered this model unsuitable for incorporation into Lennard-Jones-based simulations. The MSM model, from which the EPM2 model is based, has been noted as inferior to its successor in most thermodynamic predictions (Harris & Yung, 1995; Chatzis & Samios, 2003). These three models therefore were not considered further.

The EPM2 model in comparison has been repeatedly considered the most suitable model for CO_2 and as such is frequently encountered in molecular simulations e.g. (Vorholz *et al.*, 2000; Lisal *et al.*, 2001; Cichowski *et al.*, 2005; Li & Maroncelli, 2006). Crucially this model has been proven to accurately predict thermodynamic properties of supercritical CO_2 (Saharay & Balasubramanian, 2004; Higashi & Tamura, 2010; Vlcek *et al.*, 2011) which was a fundamental requirement for this research project. Furthermore this model has been used to predict the critical point to within the experimental error bars (Harris & Yung, 1995; Vorholz *et al.*, 2000) indicating that the model can perform to a high standard even when phase boundaries are approached. These key advantages possessed by the EPM2 model resulted in it being considered most suitable for use within this project.

3.4.3 Water

Water is one of the hardest substances to accurately model. The difficulty arises as a result of the specific hydrogen bonding interactions between water molecules which produces a particularly strong electrostatic interaction between the hydrogen and oxygen atoms. This interaction has a strong bearing on both the overall thermodynamic behaviour and on the atomic structure and coordination (Poole *et al.*, 1994). The magnitude of this bond is known to vary significantly with temperature (Rapaport, 1983). Hydrogen bonding therefore not only has a strong bearing on its ability to act as a solvent but also significantly affects its thermodynamic properties (Kalinichev, 2001). The primary difficulty faced when modelling water therefore is synthesising this molecular potential accurately at different temperatures. To this end over 40 molecular potentials have been proposed, developed for different desired thermodynamic properties (e.g. Jorgensen, 1981; Berendsen *et al.*, 1987; Lobaugh & Voth, 1997; Paricaud *et al.*, 2005). However no single model can be considered perfect for all applications (Vorholz *et al.*, 2000; Zhang & Duan, 2005b).

As the majority of these published models are minor iterations of several well-established models, optimised for specific systems, the focus of this project will be on these ‘original’ molecules. They have been selected based on their highly cited nature and proven published record for a wide range of applications. These models which are frequently used to model liquid water at elevated temperatures and pressures are the SPC/E, TIP4P, TIP5P and EP. Details of each are listed in Table 3.2.

Model Name	($\varepsilon_{O\text{-}O}$) (K)	$\sigma_{O\text{-}O}$ (Å)	α	q_O	q_M	q_H	$l_{O\text{-}H}$ (Å)	$l_{O\text{-}M}$ (Å)	$r_{H\text{-}O\text{-}H}$ (°)
SPC/E	78.197	3.166	-	-0.847	-	+0.424	1.000	-	109.47
TIP4P	78.020	3.154	-	-	-1.040	+0.520	0.957	0.150	104.52
TIP5P	80.516	3.120	-	-	-0.241 (x2)	+0.241	0.957	0.700 (x2)	104.52
EP	159.78	3.195	12	-0.737	-	+0.369	1.067	-	109.50

Table 3.2. A table containing the parameters of each molecular model for water. For all proposed models of water the Lennard-Jones potentials of hydrogen are considered negligible and thus set as zero. ε and σ refer to the Lennard-Jones potential values for the oxygen atom, α is Buckingham potential used in the Errington model, q_O or q_M and q_H are the electrostatic charges on each atom and $l_{O\text{-}H}$ and $l_{O\text{-}M}$ are the bond length between these atoms. Where the negative charge is displaced from the oxygen atom to point ‘*m*’ q_M and $l_{O\text{-}M}$ are given. All relevant values given to 3 decimal place.

In all models both bond lengths and angles are fixed and thus are considered rigid molecules. The charges on these models are equally fixed and therefore no polarisable potential is considered. While some models do exist which explore the possibility of flexible models (e.g. Lobaugh & Voth, 1997; Wu *et al.*, 2006) or polarisable models (e.g. Bernardo *et al.*, 1994; Smith & Dang, 1994) the added degree of freedom serves to increase processing demands and simulation time. No significant overall improvement to simulated thermodynamic properties has been definitively observed for these models (Wallqvist & Teleman, 1991; Mountain, 1995; Guillot & Guissani, 2001; Sala *et al.*, 2010; Sirk *et al.*, 2013). Consequently, due to their proven ability to replicate experimental data, coupled with a relatively low computational cost, only rigid water molecules were considered for this project.

The first model in Table 3.2, SPC/E, has a positive polar charge (*q*) on both the hydrogen atoms and a negative charge on the oxygen. Only the oxygen however has a Lennard-Jones potential. Hydrogen van der Waals forces for water molecules are commonly considered negligible. This model has been extensively applied to a wide range of studies since its inception e.g. (Goldman *et al.*, 1994; Vorholz *et al.*, 2000; Jungwirth & Tobias, 2002; Zhang *et al.*, 2003; Birkett & Do, 2007; Lopez-Rendon & Alejandre, 2008) with simulated results close to experimental values. It was created by significantly modifying a previous model (Berendsen *et al.*, 1981) and was optimised using high-quality experimental data to predict most thermodynamic properties to within experimental uncertainty (Berendsen *et al.*, 1987). It is noted however that while it is highly proficient for simulating water in the liquid phase, when simulating gaseous water the SPC/E model significantly underestimates the density (Vorholz *et al.*, 2000).

The TIP4P model was created in a similar way to the SPC/E model: iteration-based optimisation of a previous model (Jorgensen, 1981). This model uses four sites for interaction, instead of the standard three. Instead of all forces acting from each molecule the negative charge was removed from the oxygen atom and placed nearer the hydrogen atoms at point *M*. The addition of an extra charge however has not lead to a significant improvement in modelling water when compared to the SPC/E which still remains the better overall model for water (Zhang & Duan, 2005b).

TIP5P, the third model in Table 3.2 is a further alteration to the TIP4P model and adds yet another interaction site (M_1 and M_2) which allows half the negative charge on each (Mahoney & Jorgensen, 2000). Although this extra site results in a greater processing demand and longer simulation times there is no noticeable improvement on other, simpler models (Zhang & Duan, 2005b).

The final model is the EP which was formed primarily to reproduce vapour-liquid phase equilibrium (Errington & Panagiotopoulos, 1998). It utilises the three point charge system like the SPC/E model. The key difference between the two is that, as with their proposed CO_2 model, it uses the Buckingham exponential-6 potential, not the Lennard-Jones potential for calculating non-polar molecular interactions. As noted for CO_2 this creates a significant issue when modelling interactions with Lennard-Jones-based models which severely limits its application.

Due to the proven success of the SPC/E model at predicting thermodynamic properties with minimal deviation from experimental values and the well-documented shortcomings of other models, this water model is considered the most suitable from the selection available for modelling geological systems. Thus it was the preferred choice for this project.

3.4.4 Noble gases

Noble gases are modelled as single atoms with no associated electrostatic charges. Thus all intermolecular interactions within a simulation are purely the result of the Lennard-Jones forces. Several examples of modelling noble gases already exist in the literature (Swope & Andersen, 1984; Carlton, 1985; Even *et al.*, 2005; Bourg & Sposito, 2008) although appreciably fewer published studies exist compared with those on water or CO_2 models. Consequently the noble gas models which do exist have not been extensively tested and optimised to the same extent. This has resulted in a greater variance in the proposed Lennard-Jones potentials (Swope & Andersen, 1984; Carlton, 1985; Even *et al.*, 2005).

However, one extensive study (Klein *et al.*, 1984) has been published which compiled all existing noble gas models and assessed their ability to predict experimentally defined values. From these experimental comparisons the optimum Lennard-Jones potentials were determined. These are reproduced in Table 3.3.

Noble gas	ε (°K)	σ (Å)
He	10.80	2.967
Ne	42.25	3.087
Ar	143.20	3.759
Kr	199.90	4.012
Xe	282.35	4.363

Table 3.3. The Lennard-Jones potentials for the noble gases. Table redrawn from Tang & Toennies (Tang & Toennies, 1986) using values originally from Klein *et al*. (Klein *et al.*, 1984)

These models have been used since in noble gas based studies e.g. (Tang & Toennies, 1986; Bourg & Sposito, 2008). While other noble gas models, proposed since the review was published (e.g. Carlton, 1985; Du *et al.*, 2008), have not been as extensively compared to experimental values. Therefore, given the Lennard-Jones potentials in Table 3.3 have the most robust experimental justification these were selected for this project.

3.4.5 Constraining unlike interactions

In the preceding sections the most appropriate atomistic models for CO_2, water and each noble gas were identified. For each model all applicable attractive and dispersive atomic interactions for both like and unlike atoms have been defined using the Lennard-Jones potential. All electrostatic charges on each atom were also indicated where applicable. Thus each model was able to replicate a pure phase to a high degree of accuracy. However, for the simulation to be viable it was equally important that each model interacts accurately with one another. Therefore a suitable approach to determine all expected molecular and electrostatic interactions was required.

For electrostatic considerations this was not an issue as each electrostatic force is modelled as a single point charge of a defined magnitude; this is independent of atomic species and so could be resolved using the Ewald sum (3.2.1).

For the attractive and dispersive van der Waals forces, though, generating unlike pair potentials between models can frequently prove problematic. This is because such models have seldom been developed specifically to interact with one another.

Consequentially a mixing rule is applied to generate approximate unlike pair potentials ($_{ij}$) from the two existing like-like potentials ($_{ii}$ and $_{jj}$) on each model.

These unlike pair potentials are most commonly calculated using the Lorentz-Berthelot mixing rules. This method calculates the arithmetic mean of the potential well positions (σ) for each molecules and the geometric mean of the two well depths (ε) as indicated:

$$\sigma_{ij} = \frac{(\sigma_{ii} + \sigma_{jj})}{2} \tag{3.14}$$

$$\varepsilon_{ij} = \sqrt{(\varepsilon_{ii}\varepsilon_{jj})} \tag{3.15}$$

where $_{ii}$ indicates two particles of type i, $_{jj}$ indicates two particles of type j and $_{ij}$ is the resultant Lennard-Jones potential values for the two unlike particles (Allen and Tildesley, 1987). There is a reasonable justification for using the arithmetic mean of σ for unlike pairs as it averages the distance at which the repulsive forces become dominant between both molecules. However the argument for using the geometric mean of ε is harder to defend as it makes several gross assumptions about the short range repulsive forces which may not necessarily be valid (Smith, 1972). Indeed several documented studies highlight cases where using this simplistic mixing rule introduces significant error into a simulation (e.g. Delhommelle & Millie, 2001; Song *et al.*, 2003; Boda & Henderson, 2008; Forsman & Woodward, 2010). Given these issues alternative combining rules with a higher associated complexity have been proposed in the literature e.g. Hudson & McCoubrey (Hudson & McCoubrey, 1960) or Kong (Kong, 1973). However despite the development of these alternative models the Lorentz-Berthelot mixing rules are still commonly applied to derive unlike pair potentials.

Frequently the issue of inaccuracies in unlike pair potentials is resolved by iterative optimisation. Using this approach a mixing rule is used to generate a first order approximation for the σ_{ij} and ε_{ij} terms which are then optimised to reconcile the simulation with published experimental results. This provides a method for generating potentials for unlike atoms which allow a modelled system to closely replicate empirical data (e.g. Fotouh & Shukla, 1997; Huang *et al.*, 2009). However cross-terms developed using this approach can only be considered valid for the specified models.

For this research project, unlike Lennard-Jones potentials terms were therefore required for the water model (SPC/E), the CO_2 model (EPM2) and the noble gas models

(Klein *et al.*, 1984). With no Lennard-Jones potentials being applied to the hydrogen in SPC/E water only the interactions between oxygen and unlike atoms required defining.

For the terms describing pair interactions between the SPC/E and EPM2 models values were taken from a published study. This study optimised the unlike potentials for these two models to create a thermodynamically accurate supercritical CO_2-water GEMC binary phase system (Vlcek *et al.*, 2011). This study therefore provided a means to accurately describe supercritical CO_2-water interactions with no adjustment required. Details of these unlike interactions are included in Table 3.4.

Unlike interaction	ε (K)	σ (Å)
$C_{(CO2)}$-$O_{(H2O)}$	66.283	2.841
$O_{(CO2)}$-$O_{(H2O)}$	90.061	3.152

Table 3.4. Unlike pair potentials between each EPM2 atom ($C_{(CO2)}$ & $O_{(CO2)}$) and the oxygen on the water ($O_{(H2O)}$). Values taken from Vlcek *et al.* (Vlcek *et al.*, 2011). All values given to 3 decimal places.

For the noble gas-water and noble gas-CO_2 potentials, however, no suitable pair potentials were available from the literature. Consequently it was decided to use the Lorentz-Berthelot mixing rules to create initial values for these Lennard-Jones potentials. However during the project it was determined that the noble gas-water interactions required an optimisation process. This is discussed further in 3.4.6. Time constraints did not permit a study of the optimisation between CO_2 and noble gases.

The initial Lennard-Jones pair potentials for all noble gas-water and noble gas-CO_2 are given in Table 3.5.

Noble Gas	ε (K)	σ (Å)
He-$O_{(H2O)}$	29.061	3.067
He-$C_{(CO2)}$	17.430	2.862
He-$O_{(CO2)}$	29.487	3.000
Ne-$O_{(H2O)}$	57.479	3.127
Ne-$C_{(CO2)}$	34.474	2.922
Ne-$O_{(CO2)}$	58.322	3.060
Ar-$O_{(H2O)}$	105.820	3.463
Ar-$C_{(CO2)}$	63.467	3.258
Ar-$O_{(CO2)}$	107.371	3.396
Kr-$O_{(H2O)}$	125.026	3.589
Kr-$C_{(CO2)}$	74.987	3.385
Kr-$O_{(CO2)}$	126.860	3.523
Xe-$O_{(H2O)}$	148.590	3.765
Xe-$C_{(CO2)}$	89.119	3.560
Xe-$O_{(CO2)}$	150.769	3.698

Table 3.5. All initial unlike pair potentials for each noble gas. Values were derived using the Lorentz-Berthelot mixing rules. Values given to 3 decimal places.

3.4.6 Optimising unlike noble gas potentials

During this project it was determined that the unlike pair potentials between each noble gas and water (3.4.5) required further attention. Initial noble gas solubilities were being reasonably predicted using the Lorentz-Berthelot mixing rules. These results are presented in 5.2. However in the case of helium and neon, solubilities in the water phase were being consistently over-predicted. Argon and krypton solubilities on the other hand were always lower than expected. Therefore a method of optimisation was required to reconcile experimental and simulated values. It had already been noted that the ε potential between each noble gas and water was the most contentious (3.4.5). Therefore this value was changed whilst σ remained constant and the effect on solubility was assessed. For the noble gases expressing excessive solubility this ε value was scaled down to lower the strength of interaction between the noble gas and water molecules. For noble gases producing lower than expected solubilities this value was increased. Table 3.6 highlights the ε scaling factors applied to each noble gas.

Noble gas	Initial interaction (ε_{ij})	Changed values (scaled ε_{ij})
Helium	1	0.5, 0.85, 0.91, 0.95, 2
Neon	1	0.75, 0.80, 0.85, 0.91, 0.95
Argon	1	1.05, 1.1, 1.15,
Krypton	1	1.05, 1.10
Xenon	1	0.5, 1.02, 1.05, 1.10, 2

Table 3.6. A list of scaled $\varepsilon_{noble\ gas\text{-}water}$ potentials. All scaling is relative to initial ε_{ij} values generated by the Lorentz-Berthelot mixing rules (Table 3.5).

The process of running each simulation and generating resultant partition coefficients were derived as for the initial ε values. This process is fully documented in 3.6.2 and 3.7. The results of both optimised and unoptimised values are presented in 5.2. The pair potentials which best replicated the experimental solubilities between noble gas and water are presented in Table 5.6.

As discussed in 3.4.5 due to time constraints no optimisation process between the noble gases and CO_2 was implemented and so unmodified Lorentz-Berthelot mixing rules were applied. It was acknowledged that a future optimisation step could be required between these unlike molecules at higher pressures. However noble gas partitioning within CO_2-water systems at low pressure did not vary significantly from expected values (5.3). Therefore the Lorentz-Berthelot derived values for these unlike potentials were considered reasonable for use within the project.

3.5 Constructing the simulation

3.5.1 Introduction

At this stage a viable technique for simulating a binary phase had been identified (GEMC). Similarly accurate molecular models and suitable potentials had been determined for each component. It was therefore possible to begin the process of combining these in order to assemble the required model. The purpose of this section is to document the initial construction and testing of the model.

3.5.2 Towhee

The GEMC simulation package adapted for use with this research project is an open-source molecular code called Towhee (Martin, 2013). In its current iteration this program has a proven ability to produce simulation data of a publishable quality e.g. (Martin & Thompson, 2004; Lithoxoos *et al.*, 2010; Vlcek *et al.*, 2011).

Each Towhee simulation consists of two distinct file types: input files and output files. The input files specify the details of the simulation and are read by the Towhee executable file which runs the GEMC simulation. The results of the simulation are presented in the output files. The files involved in this process are displayed in a flow diagram in Figure 3.5.

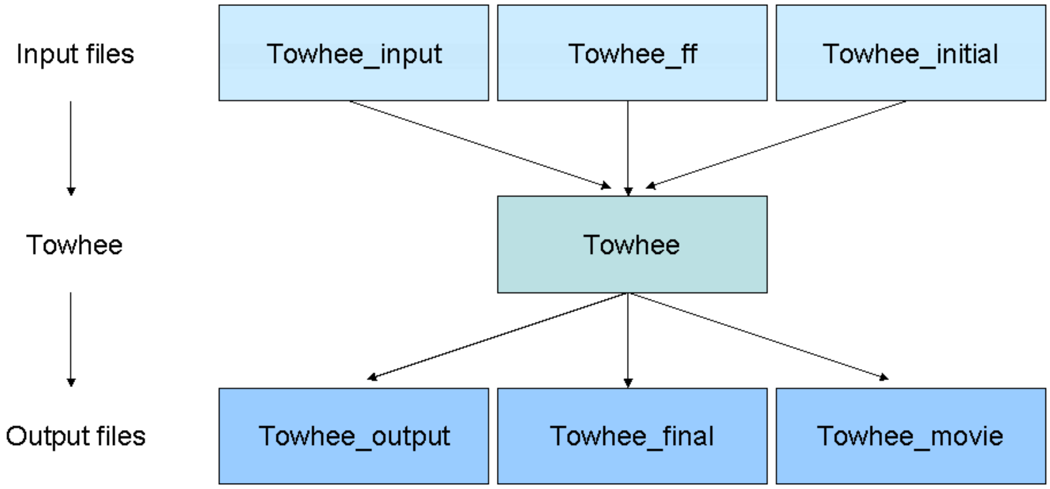

Fig. 3.5. A flow diagram displaying the primary input and output files for a standard Towhee simulation.

Towhee_input contains the run-specific information. It lists the thermodynamic conditions for the running of the simulation, the molecular types to be simulated and the weighting of each particular Monte Carlo perturbation move to be performed. It also lists the total number of moves to be attempted and the number of discrete blocks needed to generate average system properties. The *Towhee_ff* files are the force field parameters for each molecule. Each ff file defines atomic composition, bond lengths, bond angles and intermolecular interactions from a single molecular model. Lastly, when a simulation is initiated using a previous configuration as a starting point, *Towhee_inital* is used. This file defines the box size of each phase and lists the coordinates of each atom within that box. These files therefore provide all required information to initialise the simulation.

Towhee_output is the primary output file. As the simulation progresses an updated list of each move type attempted and the amount accepted is periodically outputted to this file. Once each simulation block is complete the thermodynamic averages are calculated and then recorded. When the simulation is complete the block averages and the overall average for the entire run are recorded at the end of this file. *Towhee_final* contains the final box sizes and atomic coordinates. Its format is identical to that of *Towhee_initial* and if required can be renamed and used as the starting configuration for a successive run. Lastly, *Towhee_movie* is an optional output file which periodically records all atomic positions within the boxes. The interval period of this is defined within the Towhee_input file. This file can be used to construct a visual depiction of the system and can be used to provide visual confirmation that no obvious artefacts exist within the system. Additionally this file can be analysed to determine average distribution functions if required. However given the sizes that this file can reach (>1 GB) it was not generated as standard practice for these simulations. This was a preventative measure to limit the storage space required for each run.

Each simulation was run from individual folders containing the listed input files at the required thermodynamic conditions. All output files were written to the same folder as the input files for a given run. Details of all simulation types run as part of the model development are listed in 3.5.3.

3.5.3 Simulation techniques

To run multiple simulations of Towhee simultaneously for different conditions for extended periods of time it was essential to use a computer cluster based at the University of Manchester. The Computational Shared Facility (CSF) cluster possessed a total of 3824 cores (1680 Intel 2144 AMD) subdivided into 178 nodes with between 2 – 8 GB of memory per core. The majority of the Intel cores were linked together via Gigabit Ethernet while all AMD and the remaining Intel cores are networked using Infiniband. The operating system on the cluster was Scientific Linux 6.2.

User access to the cluster is obtained through a Secure Shell (SSH) client to log in to the head node. From here it is possible to navigate to the unique folders containing all necessary Towhee input files (3.5.2) from where each separate simulation is submitted. Each Towhee job is submitted using a Sun Grid Engine (SGE) script which specifies the details of the run and location of the folder to ensure the job is processed correctly. Once submitted each job is added to a queue from which jobs are progressively run as cores become available. All jobs are allowed to run for a maximum of 7 days before they are automatically terminated.

Due to the relative simplicity of each Towhee simulation, all jobs were configured to run as single processor jobs. The total runtime of each simulation was dependent on total number of moves, types of moves implemented, system size and molecular types. This runtime was optimised for each run by altering the total number of moves so each simulation completed within 7 days. This allowed for the greatest amount of statistical sampling to occur in each simulation whilst maintaining its integrity by allowing it to terminate successfully.

3.5.4 Calibration simulations

As with the experimental system, it was a requirement that the simulation was able to reproduce existing data for the chosen molecular models. By achieving this it would confirm that the use of both Towhee and the selected models were valid for this project. Considering that the project required a successful simulation of a binary phase system the logical test was to partially replicate Vapour-Liquid Equilibrium (VLE) curves for pure CO_2 (Harris & Yung, 1995) and pure water (Vorholz *et al.*, 2000). These would allow an assessment of Towhee's capabilities for simulating a multiphase system whilst determining the ability of each model to exist in more than one phase. Due to the high associated complexity with modelling near the critical point only lower temperatures were reproduced. For the noble gases however, given their extremely highly volatile nature and low boiling points, simulating accurate VLE curves for the lighter noble gases was considered highly problematic. Instead they were modelled as pure gaseous phases at 1.01325, 2.0265 and 10.1325 bar between 293.15 – 333.15 K. The densities from these simulations were then compared to published experimental values derived from the NIST website (NIST, 2013). Details of the VLE simulations are specified in Table 3.7 and details of the noble gas simulations are specified in Table 3.8.

System property	Value
Simulation type	NVT (Constant volume and temperature)
Number of molecules	333
Equilibration run length	27 million moves
Sampling run length	27 million moves
Total sampling block averages	10
Temperature range	220 – 290 K (CO_2) 350 – 600 K (H_2O)
Initial dimensions of each box	24^3 Å (liquid) 55^3 Å (vapour)
Initial molecular distribution of Box 1	200
Initial molecular distribution of Box 2	133
Volumetric Move Probability	2% (target acceptance 50%)
Interbox Move Probability	93% (target acceptance N/A)
Intrabox Move Probability	5% (target acceptance 50%)

Table 3.7. Details of Vapour-Liquid Equilibrium sampling runs for both EPM2 CO_2 and SPC/E water. Block averages indicate the total number of discrete averages taken during sampling. Target acceptance in terms of perturbation refers to the ideal percentage of attempted moves which are accepted. This is not applicable to interbox moves.

System property	Value
Simulation type	NPT (Constant pressure and temperature)
Number of molecules	512
Equilibration run length	70 million moves
Sampling run length	70 million moves
Total number of block averages	10
Temperature range	293.15 – 333.15 K
Pressure range	1.01325, 2.0265 & 10.1325 bar
Initial box dimensions	35^3 Å
Volumetric Move Probability	2% (target acceptance 50%)
Intrabox Moves Probability	98% (target acceptance 50%)

Table 3.8. Details of single phase runs for all noble gas models. Block averages indicate the total number of discrete averages taken during sampling. Target acceptance in terms of moves refers to the ideal percentage of attempted moves which are accepted.

The partial VLE curves for both CO_2 and water are presented in Figure 3.6 and Figure 3.7 respectively. Absolute values are presented in Table 3.9 and Table 3.10. Reference values are included for comparison for each VLE curve.

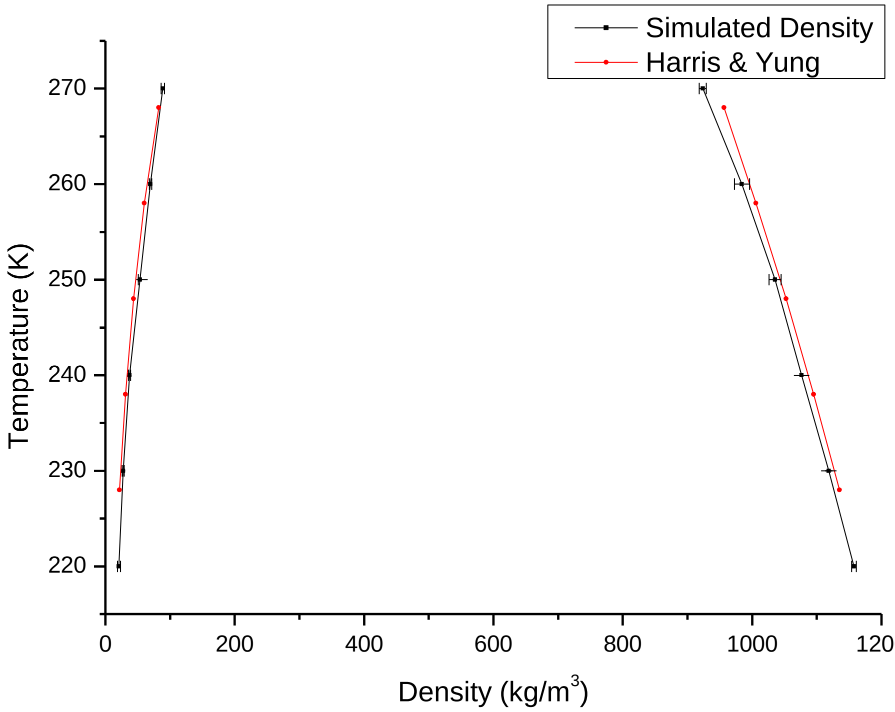

Fig. 3.6. Vapour-Liquid Equilibrium curve for EPM2 CO_2. Simulated values from this work (black) are compared with experimental values (red) taken from Harris & Yung (Harris & Yung, 1995).

Temperature (K)	Ref. Vapour Density (kg/m^3)	Sim. Vapour Density (kg/m^3)	Std. Err (%)	Ref. Liquid Density (kg/m^3)	Sim. Liquid Density (kg/m^3)	Std. Err (%)
220		21.0	10.9		1157.5	0.3
228	21.8			1134.9		
230		27.5	5.5		1118.6	0.3
238	31.2			1094.9		
240		37.3	4.3		1076.5	0.3
248	43.7			1052.6		
250		53.7	5.6		1035.5	0.9
258	60.2			1006.1		
260		69.8	2.5		984.3	1.2
268	82.4			956.6		
270		88.9	2.8		923.7	0.6

Table 3.9. Data for EPM2 CO_2 Vapour-Liquid Equilibrium graph. Reference values were taken from Harris & Yung (Harris & Yung, 1995). All values given to 1 decimal place.

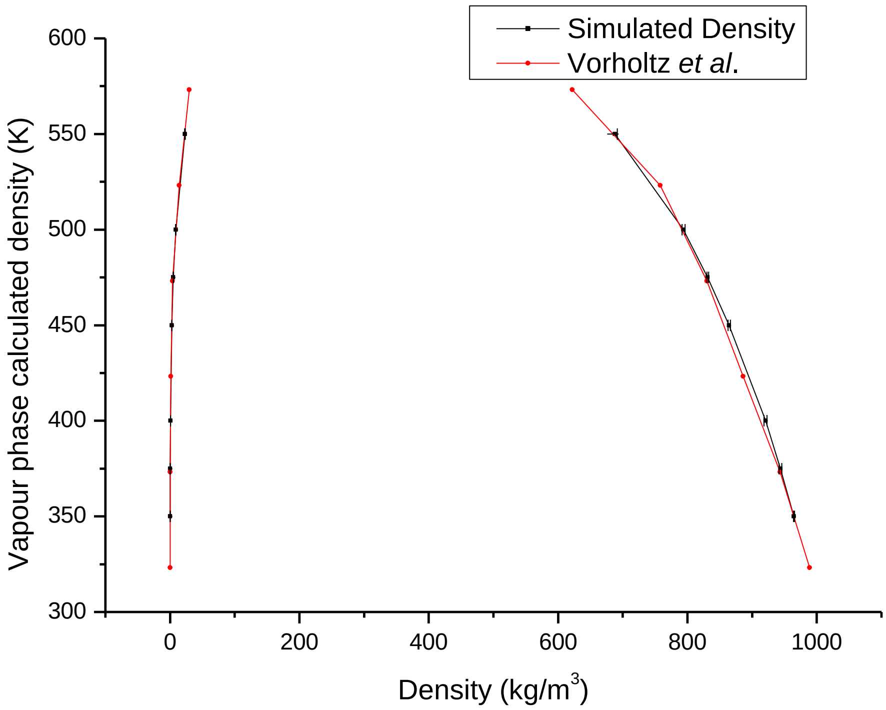

Fig. 3.7. Vapour-Liquid Equilibrium curve for SPC/E water. Simulated values from this work (black) are compared with simulated values (red) taken from Vorholz *et al.* (Vorholz *et al.*, 2000).

Temperature (K)	Ref. Vapour Density (kg/m^3)	Sim. Vapour Density (kg/m^3)	Std. Err (%)	Ref. Liquid Density (kg/m^3)	Sim. Liquid Density (kg/m^3)	Std. Err (%)
323.15	0.04			989.0		
350		0.1	3.4		964.8	0.1
373.15	0.2			943.0		
375		0.3	4.8		943.7	0.2
400		0.6	2.4		920.8	0.2
423.15	1.2			886.0		
450		2.6	3.5		864.5	0.2
473.15	4.0			830.0		
475		5.1	2.4		831.4	0.2
500		8.8	2.9		794.0	0.3
523.15	14.1			758.0		
550		23.0	1.8		688.1	0.5
573.15	29.7			622.0		

Table 3.10. Data for SPC/E water Vapour-Liquid Equilibrium graph. Reference values were taken from Vorholtz *et al*. (Vorholz *et al.*, 2000). All values given to 1 decimal place.

As indicated by Figures 3.6 and 3.7 the simulation-defined VLE curves for CO_2 and water accurately reproduce both the expected liquid and gas phase density for the range investigated. A slight deviation was observed at the highest temperature for CO_2 (290 K). However this discrepancy was less than 4% of experimental values and given the reasonable proximity to the critical temperature (304.19 K) this minor deviation was not considered a significant issue. The ability to reasonably reproduce these VLE graphs confirmed the suitability of using these models and Towhee for simulating the binary phase system. CO_2 was not tested in the supercritical phase here. However the ability of using Towhee to simulate the EPM2 model correctly was proven. Additionally the EPM2 has an established capability for accurately simulating supercritical CO_2 (e.g. Vorholz *et al.*, 2000; Chatzis & Samios, 2003; Vlcek *et al.*, 2011). Therefore it was considered reasonable to assume supercritical CO_2 would be accurately simulated for this research project.

For the pure noble gas phase simulations (Table 3.8) a density was generated at each pressure and temperature. This was compared to the density from the experimental dataset (NIST, 2013) to generate a percentage deviation. For each pressure an average density deviation was calculated from each individual temperature alongside a standard error to assess the uncertainty for the average value. The results are presented in Table 3.11.

Noble Gas	1 atm	Std. Error	2 atm	Std. Error	10 atm	Std. Error
Helium	10.3 %	3.9	5.5 %	2.2	0.8 %	0.4
Neon	-1.2 %	0.1	-1.7 %	0.6	-1.0 %	0.01
Argon	-1.6 %	0.7	-0.6 %	0.3	0.7 %	0.1
Krypton	-2.0 %	0.9	0.9 %	1.5	1.8 %	0.2
Xenon	-1.8 %	1.0	0.03 %	0.5	5.5 %	0.5

Table 3.11. An assessment of the accuracy of simulated noble gas densities (Klein *et al.*, 1984) compared to experimental data (NIST, 2013). Values are given to 1 decimal place unless this would give a zero value where instead the first significant figure is shown.

From Table 3.11 it is clear that, with the exception of helium, all noble gases simulations produced a comparable density to the experimental dataset. Although helium was noted to have higher densities than expected, especially at low pressure, it still replicated experimental densities reasonably well (± 15%). This discrepancy was considered to be due to difficulties in simulating a small molecule with very low inter-molecular interactions using a classical approach. Despite this issue all noble gases replicated experimental densities to a sufficiently standard for the project.

3.6 Replicating real systems

3.6.1 Introduction

Thus all suitable molecular models had been determined (3.4), all pair potentials defined (3.4.5 & 3.4.6) and a program for simulating the binary phase identified (3.5.2). All individual components were assessed and proven to be simulated correctly (3.5.4). Previous studies (Vorholz *et al.*, 2000; Vlcek *et al.*, 2011) have proven the ability of these models to accurately simulate CO_2-water systems at elevated pressures and temperatures. The next requirement therefore was to simulate realistic systems and generate partition coefficients for noble gases. Initially the experimental technique of Crovetto *et al.* and Smith was replicated (Crovetto *et al.*, 1982; Smith, 1985).

3.6.2 Noble gas-water binary phase partitioning

A pre-requisite for creating the final model was that it must have a proven ability to replicate results from previous experimental studies. Therefore the benchmark experimental studies of Crovetto *et al.* and Smith (Crovetto *et al.*, 1982; Smith, 1985) were selected for comparison. In this study experimental partition coefficients were derived by simulating a pure noble gas phase interacting with a pure water phase at different temperatures and pressures. This binary phase system was replicated using Towhee. Using the molar fraction of a given noble gas (i) within the water phase (x_i) it was possible to derive a Henry's coefficient (K_i) for the thermodynamic conditions using Equation 1.3 (3.7.1). Individual simulations were run for each noble gas at 1.01325 and 10.1325 bar between 293.15 – 353.15 K. After an initial equilibration period the simulations were run three times during which the partition coefficients were calculated. Details of these simulations are outlined in Table 3.12.

System property	Value
Type of simulation	NPT (Constant pressure and temperature)
Number of molecules	1024 (512 H_2O, 512 noble gas)
Equilibration run length	70 million moves
Sampling run length	105 million moves
Total number of block averages	10
Temperature range	293.15 – 353.15 K
Pressure range	1.01325 & 10.1325 bar
Initial dimensions of each box	35^3 Å (H_2O) 35^3 Å (noble gas)
Initial molecular distribution of Box 1	512 (510 H_2O, 2 noble gas)
Initial molecular distribution of Box 2	512 (510 noble gas, 2 H_2O)
Volumetric Perturbation Probability	1% (target acceptance 50%)
Interbox Perturbation Probability	49% (target acceptance N/A)
Intrabox Perturbation Probability	50% (target acceptance 50%)

Table 3.12. Simulation details for noble gas-water binary phase system. Block averages indicate the total number of discrete averages taken during sampling. Target acceptance in terms of moves refers to the ideal percentage of attempted moves which are accepted. This is not applicable to interbox moves.

At the conclusion of the final sampling run the output file was analysed and interpreted using the methods outlined in Chapter 3.7. The results of these partition coefficients are presented in Chapter 5.2.

It was at this stage where the optimisation process for noble gas-water was implemented. This is fully discussed in section 3.4.6. For this process the original values of ε_{ij} for noble gas-O$_{(water)}$ (Table 3.5) were scaled by the values in Table 3.6. These scaled values were also simulated using the conditions specified in Table 3.12. The values which best replicated the Crovetto *et al*. and Smith dataset (Crovetto *et al.*, 1982; Smith, 1985) were identified then used for the remainder of the project (5.2). These optimised values are presented in Table 5.6.

3.6.3 Partitioning within CO_2-water systems

To incorporate a CO_2 phase the optimised binary phase system of Vlcek *et al.* (Vlcek *et al.*, 2011) was replicated. Details of all optimised pair potentials for EPM2-SPC/E interactions are given in Table 3.4. However this system needed adaptation in order to include a method for determining noble gas partitioning. Simply including a noble gas component within the CO_2 phase to determine noble gas solubilities was not considered viable though. Given the low solubility of noble gases within water, in order to to generate statistically significant partition coefficients a similar number of noble gas molecules as before (i.e. 512) would be required. However, within CO_2-water binary phase systems, noble gas-noble gas interactions in both phases are considered negligible. Therefore noble gas-noble gas interactions when simulating such systems also had to be negligible. To attain this with 512 noble gas molecules present the overall system would have required scaling up by several orders of magnitude. The resulting system would far larger than could be reasonably simulated. Consequently an alternative approach based on chemical potentials was used.

This process involved simulating a pure CO_2-water binary phase system in accordance with a standard GEMC simulation. Perturbations to the system therefore only affected CO_2 and water molecules. However after every perturbation a single noble gas molecule was inserted and removed a specified number of times into each phase. During the insertion the chemical potential of the noble gas in each phase was calculated. For each insertion the molecule was also inserted into a large, empty box with no cut-offs to calculate the chemical potential in isolation. The average of this was subtracted from the average chemical potential from insertion to give the average excess chemical potential from a single configuration. By repeating the process over many steps an overall value for the excess chemical potential in each phase could be calculated; this could then be used to generate a partition coefficient. This process is covered in detail in 3.7.2. Thus partition coefficients at infinite dilution within CO_2-water systems were obtained.

Typically partition coefficients are derived in terms of total chemical potential. However this calculation process relies on an $N+1$ term where N is the number of molecules within the simulation. When N is very low (i.e. at infinite dilution) significant systematic errors are encountered when calculating partition coefficients (Martin &

Siepmann, 1998). Therefore Towhee instead uses the excess chemical potential as a basis for deriving the partition coefficients when N<<1.

This chemical potential approach was initially applied to low pressure experiments and compared to the existing dataset to ascertain the validity of this experimental technique. Additionally simulating under these conditions provided a way of assessing the suitability of using the Lorentz-Berthelot mixing rules for noble-gas-CO_2 interactions. The results of both assessments are presented in 5.3. This method was then used to simulate partitioning of noble gases in line with the experimental aspect of this project. The agreement between experiment and simulation could then be assessed. Results and model evaluation are presented in 5.4. Details of all chemical potential simulations are listed in Table 3.13.

System property	Value
Type of simulation	NPT
Number of molecules	1000 (500 H_2O, 500 CO_2)
Equilibration run length	90 million perturbations
Sampling run length	135 million perturbations
Total number of block averages (1)	2
Total number of block averages (2)	9
Temperature range 1	293.15 – 353.15 K
Temperature range 2	322.85 – 377.15 K
Pressure range 1	1.01325 & 10.1325 bar
Pressure range 2	89.4 – 134.26 bar
Initial dimensions of each box	35^3 Å (H_2O) 35^3 Å (CO_2)
Number of chemical potential insertions per step	500 (100 for each noble gas)
Initial dimensions of each box	35^3 Å (H_2O) 35^3 Å (CO_2)
Initial molecular distribution of Box 1	500 (490 H_2O, 10 CO_2)
Initial molecular distribution of Box 2	500 (10 H_2O, 490 CO_2)
Volumetric Perturbation Probability	1% (target acceptance 50%)
Interbox Perturbation Probability	39% (target acceptance N/A)
Intrabox Perturbation Probability	60% (target acceptance 50%)

Table 3.13. Simulation details for CO_2-water binary phase system. Range 1 refers to low pressure simulations. Range 2 values are simulations compared experimental values derived from the experimental aspect of this project. Block averages indicate the total number of discrete averages taken during sampling for low pressure (1) and experimental comparisons (2). Target acceptance refers to the ideal percentage of attempted moves which are accepted. A full list of experimental conditions is given in Table 4.1.

This chemical potential based approach therefore provided a means to generate partition coefficients for each noble gas within a CO_2-water binary phase system. Most importantly as only one noble gas molecule was inserted at any given time, the resultant partition coefficients were calculated on the basis that noble gases were at infinite dilution within each phase. Therefore the chemical potential approach created a method of modelling which was able to replicate all key aspects of the experimental system.

3.7 Generating partition coefficients

Two different approaches had been used to determine noble gas partitioning for different systems: noble gas phases interacting with a water phase had been simulated (3.6.2), and a chemical potential approach was applied to a simulated CO_2-water phase system (3.6.3). From both of these approaches a method of calculating the partition coefficients was required. These could then be compared to their experimental counterparts for evaluation. The procedure of generating partition coefficients for each simulation type is now discussed.

3.7.1 Solubility partition coefficients

The overall production run was subdivided by Towhee into discrete blocks over which system averages were generated (Table 3.12). In each block the average thermodynamic properties of the system were recorded. This included the molar fraction of noble gas within the water phase. These averages could be combined for each block in each run to generate an average molar fraction of the noble gas within the water phase $(\bar{x}_i)$. As the pressure of the system was already known it was possible to use the average molar fraction to derive a Henry's coefficient by rearranging Equation 1.3.

$$K_i = \frac{P_i}{\bar{x}_i} \tag{3.16}$$

Thus the Henry's coefficient was derived. At low pressures the Henry's constants are experimentally well-defined (1.3.11). Therefore a direct comparison between the simulation-derived and experimentally determined Henry's coefficient could be easily achieved to assess noble gas-water partitioning (3.6.2). The results for these simulations are presented in 5.2.

3.7.2 Chemical potential partition coefficients

Using the chemical potential approach (3.6.3) it was possible to determine partition coefficients for each noble gas using excess chemical potentials calculated for each phase:

$$K_i = \exp\left[-\frac{1}{kT} (\mu_i{}^{E}{}_{H_2O} - \mu_i{}^{E}{}_{CO_2}) \right] \tag{3.17}$$

where K_i is Henry's constant for noble gas i, T is the temperature of the simulation, k is the Boltzmann constant $\mu_i{}^{E}{}_{H_2O}$ is the excess chemical potential of i in the water phase and $\mu_i{}^{E}{}_{CO_2}$ is excess chemical potential of i in the CO_2 phase.

This excess chemical potential is calculated for each phase by subtracting the chemical potential of i in isolation ($\mu^{I}{}_{i}$) from the chemical potential of i resulting from a full insertion into the specified phase ($\mu^{FI}{}_{i}$).

$$\mu_i{}^{E} = \mu^{FI}{}_{i} - \mu^{I}{}_{i} \tag{3.18}$$

Representative values for these are derived from system averages calculated during a simulation at constant pressure.

$$\mu^{FI}{}_{i} = -kT\ln(< VW > / < V >) \tag{3.19}$$

$$\mu^{I}{}_{i} = -kT\ln(< W^{I} >) \tag{3.20}$$

where V is volume, W is the Rosenbluth weighting and W^I is the full Rosenbluth weight calculated for inserting the selected molecule within an extremely large empty simulation box without the inclusion of any cut-offs. $<X>$ denotes the ensemble average for system property X. The ensemble average of the Rosenbluth weighting is directly linked to the excess chemical potential of a molecule within a fluid phase (Frenkel & Smit, 2002). This is calculated for each phase by Towhee as it temporarily inserts the molecule in question into each box. After insertion the molecule is removed again. The calculated Rosenbluth weighting value is then multiplied by the system volume to give *VW*. This step is repeated a designated number of times after each attempted perturbation. *VW* values for the entire simulation are averaged to give <*VW*>. For each insertion the same molecule is also inserted into a large empty simulation box with no cut-offs applied. This allows a value of W^I to be calculated for each *VW* value. This is also averaged out over the simulation run to generate $<W^I>$. Using these values the chemical potential of *i* in isolation (μ^I_i) and the chemical potential of *i* resulting from a full insertion (μ^{FI}_i) are calculated for both phases. These values can then be substituted into Equations 3.17 – 3.20 to derive a partition coefficient of *i* within the binary phase system.

As the chemical potentials were averaged out during the entire simulation a single partition coefficient for each noble gas was generated per run. Therefore each simulation was repeated twice for each low pressure run and nine times for the experimental runs. An arithmetic mean was used to define the Henry's coefficient value for each specified pressure and temperature. All simulated results are presented in 5.3 and 5.4.

3.8 Uncertainty in simulation

As with the experimental values it is important that the uncertainty with simulated partition coefficients be reasonably accommodated. However, unlike experimental approaches, uncertainty derived when quantifying any individual component is much lower. The precision of measurement is many orders of magnitude greater than experimental values due to all values within a simulation being numerically derived as opposed to empirically observed. Given modern day processing power any uncertainty in rounding can be considered to have a negligible effect so it is reasoned all outlined parameters within the simulation have no relative uncertainties with them. Therefore the sole source of variation within the data set is considered to be due to collecting data over a finite time period from probabilistic simulations.

As the simulations are all GEMC-based they are probabilistic in nature. As a result no two simulations, even run under identical conditions, will follow the same evolution over time. Consequentially when equilibrated they all will oscillate around the most probable system configurations; averages generated from each simulated system will all yield slightly different values. Therefore there an inherent uncertainty exists for all system properties determined by this approach.

A method was therefore required to calculate the relative uncertainty associated the average partition coefficient for both simulation approaches. The partition coefficients for all simulated values (3.7) were derived from the arithmetic average of independent measurements of an identical system. Therefore, although two different simulation approaches were applied to generate partition coefficients, the method of determining uncertainty was identical.

The logical approach to calculating the uncertainty derived from variation within the dataset was to simply use the standard error. This is reasonable as the confidence given to the calculated mean value should increase as more system configurations are added. The inferred assumptions made by using the standard error therefore are that the system is in a state of equilibrium when sampling occurs and that sampling takes place over a statistically significant number of moves. The former was verified by observing other system properties (e.g. phase density) to ensure reasonable values were being generated with no significant fluctuations ($\sigma \geq 5\%$ of mean). Given the number of moves within the sampling period were equal or greater than the values used in other similar published GEMC studies (e.g. Vorholz *et al.*, 2000; Lisal *et al.*, 2001; Zhu *et al.*, 2009), the simulation lengths were considered appropriate. Therefore this approach to determining uncertainty was considered acceptable. All stated uncertainty values for simulated noble gas partitioning therefore were the standard errors calculated from the simulation-derived partition coefficients.

Chapter Four

Measured partition coefficients

4.1 Introduction

Currently the only noble gas partition coefficients applied to high pressure CO_2-water geological systems are those presented by Crovetto *et al*. and Smith (Crovetto *et al.*, 1982; Smith, 1985). The effects of sodium chloride are incorporated as experimentally derived coefficients affecting the water phase (Smith & Kennedy, 1983). These partition coefficients are used to quantify fundamental system properties which are applied to both natural and man-made CCS storage sites. All coefficients were derived using pure noble gas phases interacting with a water phase under conditions where ideality within the gas phase can be assumed. This is due to the pure noble gas phases possessing a low corresponding density rendering intermolecular interactions low enough to be reasonably ignored. Similarly low densities are encountered when noble gases exist as tracers within other gas phases at relatively low pressures. Again molecular interactions are relatively infrequent due to the low densities and do not have a significant bearing on the gas behaviour. By employing a small fugacity coefficient therefore any minor molecular interactions can be incorporated into otherwise ideal behaviour.

Difficulties however are anticipated when assumptions of ideality are made at much higher densities. Under such conditions the absolute amount of molecules within a given volume is much higher. As a consequence the extent and magnitude of intermolecular interactions will be much greater than at low densities. These enhanced intermolecular interactions will affect the overall thermodynamic properties and behaviour of the phase. This directly poses a serious challenge to any assumption of ideality within high density fluids. It is an inescapable fact therefore that by applying these published partition coefficients to highly dense CO_2 systems ideality is being expected within non-ideal environments. No published study to date has assessed the legitimacy of this assumption.

4.2 Experimental design

The primary focus of this project was to evaluate the physical and chemical response of noble gases under CCS conditions. Although P,T conditions which promote the highest densities of supercritical CO_2 are the most favourable (IPCC, 2005) it is expected that the storage sites will exist within a wide variety of geothermal and hydrostatic pressure regimes (Bachu, 2003; Bachu *et al.*, 2007; Friedmann, 2007) which will result in variable densities of supercritical CO_2. Under most geological settings the maximum density of the stored CO_2 will be in the range of 600 – 800 kg/m^3 (Bachu, 2003; IPCC, 2005; Friedmann, 2007). Consequently thermodynamic conditions in this work were selected which extended midway into this range. The experiments were organised in a 3×3 grid within pressure-temperature space. This allowed an assessment of partition coefficients at three fixed pressures varied as a function of temperature and vice versa. These are presented graphically in Figure 4.1 and numerically in Table 4.1.

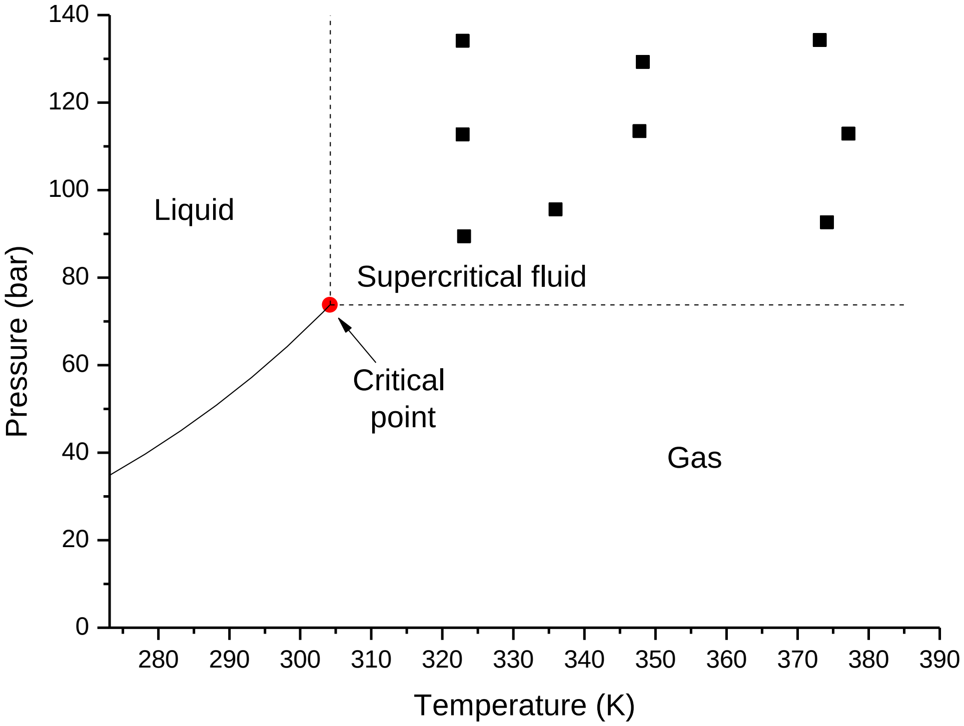

Fig. 4.1. The locations of experiments in a 3 x 3 grid within P,T space. Three pressure and temperature regimes can be isolated horizontally and vertically respectively to assess the effect each have on partition coefficients.

Experiment	Viable samples	Temperature (K)	Pressure (bar)	CO_2 Density (kg/m^3)
1	3	323.07	89.40	280.83
2	2	322.85	112.70	534.80
3	2	322.85	134.12	655.70
4	3	335.96	95.55	252.41
5	3	347.77	113.46	290.00
6	3	348.22	129.30	362.73
7	2	374.15	92.64	169.39
8	3	377.15	112.84	215.69
9	2	373.14	134.26	283.84

Table 4.1. A list of all pressure and temperature conditions for all experiments displayed graphically in Figure 4.1. Viable samples are those which passed the rejection criteria (2.5.5). Density of the CO_2 phase was calculated using the NIST website (NIST, 2013).

4.2.1 Heterogeneity within the experimental grid

All appropriate steps were taken to ensure the 3×3 experimental grid was comprised of three identical pressures over three identical temperatures. However it was inevitable that minor pressure and temperature variations coupled with the measurement uncertainty resulted in slightly heterogeneous P,T conditions.

The experimental grid was divided up into three regimes of pressure: low (89.4 – 95.55 bar) middle (112.7 – 113.46 bar) and high (129.3 – 134.26 bar). At most, including uncertainty (± 1 bar), the pressure variance within each group represented 8 bar. Over a full range of about 45 bar this was considered low enough to not affect any overall observed trends within generated partition coefficient.

As with pressure, the experimental grid was divided up into three regimes of temperature: low (322.85 – 323.07 K) middle (335.96 – 348.22 K) and high (373.14 – 377.15 K). Overall, variations within temperature sets including uncertainty (± 0.2 K) were considered small and so would not affect any thermal partitioning trends. However

Experiment 4 was at a lower temperature (335.96 K) than its higher pressure analogues (347.77 K & 348.22 K). As such the partition coefficient for this experiment may express partition coefficient characteristics with more traits of the lower temperature analogue (Experiment 1). However as this experiment was still approximately 13 K warmer than Experiment 1 any significant thermal trend should still be easily discernible. Thus for all intents and purposes any heterogeneity within the experimental grid can be considered negligible.

4.2.2. Assessing internal consistency

Occasionally individual data points appear higher or lower than would fit the overall described trends. In other studies with well-defined trends this would provide a valid basis to omit these suspect values from the dataset. However no pre-existing trends have been documented for the system being investigated here. Therefore assessing individual points in terms of internal consistency where trends are not fully defined is not appropriate. Consequently all data which passed the sample acceptance criteria were included. Where internal discrepancies are observed for each noble gas they are highlighted and discussed.

4.3 Results

In total 9 unique partition coefficients were generated for each noble gas isotope, each with an associated uncertainty. For simplicity these are given as unitless coefficients describing the relative concentration per unit volume of noble gases in each phase (2.6.6). Higher values correspond to a greater amount of noble gases within the CO_2 phase relative to the water phase, while lower values indicate a greater degree of solubility within the water phase.

Absolute partition coefficient values for each experiment for all noble gases are presented in Table 4.2. Following this a brief assessment is made of the presented data.

Experiment	^{4}He	±1σ	^{21}Ne	±1σ	^{36}Ar	±1σ	^{40}Ar	±1σ	^{82}Kr	±1σ	^{84}Kr	±1σ	^{132}Xe	±1σ	^{136}Xe	±1σ
1	88.5	7.8	126.2	45.8	29.6	4.1	40.4	5.1	27.5	2.5	28.4	2.1	24.8	1.7	24.7	1.9
2	76.4	6.4	157.6	191.0	49.9	7.2	54.1	6.9	47.6	4.9	49.5	3.7	56.4	4.6	56.9	6.2
3	45.1	3.8	110.2	140.6	62.4	9.1	65.8	8.4	47.2	4.8	45.8	3.6	56.6	4.2	59.4	7.4
4	88.7	7.7	146.8	51.8	36.7	5.7	54.6	7.1	32.9	3.1	33.8	2.5	26.1	1.8	27.9	2.2
5	63.5	5.5	121.3	141.2	24.5	3.8	40.3	5.3	27.1	3.0	35.3	2.8	33.7	2.8	33.8	3.5
6	81.2	6.7	137.3	63.3	25.1	4.1	43.2	6.0	35.5	3.5	37.5	2.7	42.2	2.9	41.9	3.5
7	55.8	4.8	47.9	32.8	27.7	4.3	46.1	6.6	27.1	3.0	33.9	2.6	28.0	2.3	29.0	2.8
8	69.4	5.8	126.5	97.8	22.6	3.7	31.6	4.2	29.1	3.0	31.4	2.3	28.5	2.0	27.9	2.4
9	73.8	6.2	131.3	80.2	22.5	3.7	34.7	4.8	30.9	3.3	32.6	2.5	33.7	2.5	33.1	2.8

Table 4.2. The partition coefficients for all measured noble gas isotopes for each corresponding experiment. Uncertainty for each value is given as 1 σ confidence to the corresponding partition coefficient. Partition coefficients presented here are given as unitless ratios between each phase (2.6.6) and are quoted to 1 decimal place.

4.3.1 Discussion of raw data

The raw data are now discussed briefly to identify any trends within the data set which are not easily resolved within the published data set. Additionally the quality of the data are discussed.

4.3.2 Helium

From the raw results it was clear that there is considerable variation within the derived partition coefficients for ^{4}He. The partition coefficients ranged from 45.1 to 88.7 indicating solubility within the water phase was varying by a factor of two within the experimental range. This variation was appreciably greater than predicted by the published values (Crovetto *et al.*, 1982; Smith, 1985).

Additionally this range was observed within a single thermal regime with partition coefficients decreasing as a function of pressure. Therefore heterogeneous partition coefficients were present where all partition values should be identical. It was clear that definite trends existed within the experimental data which were not present in the published studies. Further assessment and quantification of these trends were thus warranted. It was anticipated that the associated uncertainties for this noble gas are sufficiently low to allow a reasonable quantification of these trends.

4.3.3 Neon

Alongside ^{21}Ne, both ^{20}Ne and ^{22}Ne were additionally measured in both phases. However the quadrupole mass spectrometer lacked sufficient resolution to discern between ions of these species and doubly charged interference ions ($^{20}Ne^{+}$ & $^{40}Ar^{++}$, $^{22}Ne^{+}$ & CO_2^{++}). As no way existed to quantitatively remove either interference no legitimate partition coefficients could be generated for either of these isotopes and so they are not discussed further.

Therefore, only ^{21}Ne measurements were available for generating unambiguous neon partition coefficients. Given its relatively low abundance within the noble gas spike this resulted in a much higher associated uncertainty when measuring concentrations. This was especially true for the water phase where noble gases are much less prevalent. The resultant uncertainty represented a large fraction of the coefficient which at times exceeded the value it represented. Given this high associated uncertainty it was determined that a realistic quantitative assessment of the physical behaviour of neon was not possible. Additionally no trends could be categorically observed within the data which lay convincingly outside of this uncertainty. Unfortunately therefore it was recognised that for this project no firm conclusions for the behaviour of neon within supercritical CO_2-water systems were possible. Thus, although neon graphs are presented for completeness (4.5), no interpretations are made. Methods to resolve this issue for future studies are presented in Chapter 6.

4.3.4 Argon

To investigate partition coefficients two isotopes of this noble gas were employed: ^{36}Ar and ^{40}Ar. It was expected that partition coefficient values for both isotopes would be identical. However the raw results indicated this is not the case. All ^{36}Ar partition coefficients were considerably lower than their ^{40}Ar counterparts to the extent where even by applying maximum uncertainty to the values only 2 of the 9 data points could be reconciled. The source of this poor isotopic correlation required investigation.

Likely causes of this included either air contamination or variations of relative sensitivity of the quadrupole during sample analysis. However all samples contaminated by a major atmospheric component had been rejected and the average offset between the two isotopes was calculated as being 12.2 with a standard error of 1.9. This relatively stable offset precludes the likelihood of minor air contamination as this would involve all samples being affected similarly.

This isotopic offset was therefore determined to be due to variations in the relative sensitivity of the quadrupole when measuring isotopes at different concentrations. Given that the concentration of ^{40}Ar in the samples was an order of magnitude more abundant than ^{36}Ar and possessed a lower relative uncertainty this isotope was considered more reliable out of the two. Additionally this isotope was known to be able to replicate previous experimental data (2.4.4). Thus observations of major trends were therefore based on this isotope. ^{36}Ar partitioning values are not considered further in this work.

From ^{40}Ar the range of partition coefficients (31.6 – 65.8) indicated solubility in the water phase was varying by a factor of two over the thermodynamic range. Again this change in solubility is far in excess when compared to published values. Furthermore the partition coefficients were highest at the highest pressures and lowest temperatures. This indicated a pressure response not factored in by current predictions of partition coefficients. Clearly therefore additional factors were affecting the physical chemistry of argon in this system which were beyond the remit of the published low pressure data sets. Hence these factors required additional investigation.

4.3.5 Krypton

Two isotopes of krypton were investigated; ^{82}Kr and ^{84}Kr. A good agreement between these was observed when uncertainty was considered. Such conformity of the two isotopes was in line with expected behaviour. Additionally the uncertainty associated with each experiment appeared similar for both isotopes, although slightly higher for ^{82}Kr values. Given this good level of agreement of each isotope the process of amalgamating them into a single partition coefficient for this noble gas was straightforward. A simple arithmetic mean of both partition coefficient values for each isotope for each experiment provided the average partition coefficient. For calculating uncertainty, as the uncertainties were similar, an equal weighting was assumed so an arithmetic mean was also taken. However this value was also divided by $\sqrt{2}$. Thus a reduction in uncertainty by increasing total number of measurements was taken into account.

Even before combining these two isotopes it is clear a great variability in partition coefficients existed across the thermodynamic range (27.1 – 47.6 and 28.4 – 49.5 for ^{82}Kr and ^{84}Kr respectively). This represented a large variation of krypton solubility in the water phase. Additionally pressure had an effect; at low temperatures partition coefficients increased as a function of pressure. This was not reflected in the published datasets. These trends are discussed later (4.7).

4.3.6 Xenon

Experimental partition coefficients were generated for ^{132}Xe and ^{136}Xe. As with the two krypton isotopes these isotopes generated partition coefficients which fell within uncertainty of one another. The uncertainties represented approximately 5 – 10% of their respective values and were acceptable for observing trends within the data. Due to this good level of isotopic conformity and similar uncertainty the process of synthesising a single partition coefficient for krypton can be also legitimately applied here to generate a single partition coefficient for xenon. Even without this amalgamation strong trends were discernible for the Henry's coefficients. The coefficients varied from 24.8 and 24.7 to 56.6 and 59.4 for ^{132}Xe and ^{136}Xe respectively. Thus experimental solubility varied by more than a factor of 2 over the thermodynamic range which is a much greater variability than in previous published studies. As with the other noble gases these maximum values were recorded at the highest pressures and lowest temperatures while the minimum values were observed at the opposite thermodynamic ranges.

4.3.7 Overview of raw results

For all noble gases except helium the highest partition coefficients were generally observed at the highest pressures and lowest temperatures and lowest values at low pressures and high temperatures. For helium though high pressure, low temperature conditions produced the lowest partition coefficients. Additionally individual thermal ranges for all noble gases expressed a range of partition coefficients at different pressures. This was not compatible with current predictions of noble gas behaviour in these environments. These predictions assume partition coefficients progressively increase as a function of temperature over the experimental range (with the exception of helium) while remaining independent of pressure (Crovetto *et al.*, 1982; Smith, 1985; Ballentine *et al.*, 2002).

Evidently the physical and chemical behaviour of noble gases within supercritical CO_2-water environments was not adequately predicted by simply assuming low pressure pure phases were analogous. Therefore all trends for each noble gas required full documentation.

4.3.8 Data processing

From the raw results methods were identified to combine different isotopes to produce representative partition coefficients for each noble gas. These rationalised partition coefficients are presented in Table 4.3. Reference values for noble gas partitioning from the published dataset are given in Table 4.4.

Experiment	Helium	± 1σ	Argon	± 1σ	Krypton	± 1σ	Xenon	± 1σ
1	88.5	7.8	40.4	5.1	27.9	1.6	24.8	1.3
2	76.4	6.4	54.1	6.9	48.5	3.0	56.6	3.8
3	45.1	3.8	65.8	8.4	46.5	2.9	58.0	4.1
4	88.7	7.7	54.6	7.1	33.4	2.0	27.0	1.4
5	63.5	5.5	40.3	5.3	31.2	2.1	33.8	2.2
6	81.2	6.7	43.2	6.0	36.5	2.2	42.1	2.3
7	55.8	4.8	46.1	6.6	30.5	2.0	28.5	1.8
8	69.4	5.8	31.6	4.2	30.3	1.9	28.2	1.6
9	73.8	6.2	34.7	4.8	31.8	2.1	33.4	1.9

Table 4.3. The rationalised partition coefficients for each noble gas for each corresponding experiment. Neon values are omitted. Uncertainty is quoted at 1 σ of the corresponding partition coefficients. Partition coefficients presented here are given as unitless ratios between each phase and are quoted to 1 decimal place.

Experiment	Helium	Argon	Krypton	Xenon
1	97.2	37.4	22.5	14.9
2	97.2	37.4	22.5	14.9
3	97.2	37.4	22.5	14.9
4	89.8	39.3	24.5	16.7
5	82.2	39.8	25.6	17.8
6	81.9	39.8	25.6	17.8
7	65.4	37.7	25.7	18.4
8	62.2	36.9	25.5	18.3
9	65.4	37.7	25.7	18.4

Table 4.4. Reference partition coefficients for helium, argon, krypton and xenon. Helium values were taken from Smith (Smith, 1985) and argon, krypton and xenon values were taken from Crovetto *et al.* (Crovetto *et al.*, 1982). These are the partition coefficient values which would currently be applied under identical conditions and be assumed accurate. Partition coefficients presented here are given as unitless ratios between each phase and are quoted to 1 decimal place. Neon values are omitted.

Experiment	Helium (%)	± 1σ (%)	Argon (%)	± 1σ (%)	Krypton (%)	± 1σ (%)	Xenon (%)	± 1σ (%)
1	-8.9	8.8	8.1	12.7	23.9	5.9	66.7	5.2
2	-21.4	8.4	44.9	12.8	115.3	6.3	281.0	6.7
3	-53.6	8.5	76.2	12.8	106.3	6.3	290.3	7.1
4	-1.2	8.7	39.0	13.1	36.0	6.0	61.6	5.3
5	-22.8	8.7	1.2	13.1	21.9	6.6	89.4	6.6
6	-0.9	8.3	8.5	14.0	42.4	6.1	135.6	5.4
7	-14.6	8.6	22.3	14.3	18.6	6.5	54.6	6.3
8	11.6	8.4	-14.5	13.4	19.0	6.3	54.1	5.5
9	13.0	8.4	-7.9	13.9	23.5	6.5	81.4	5.6

Table 4.5. Experimental partition coefficients displayed as percentage deviations from published values (Table 4.4). Neon values are omitted. Negative values indicate lower partition coefficients than expected which therefore indicate a greater solubility within the water phase than predicted. Uncertainty is quoted at 1 σ of the corresponding partition coefficients. All values are quoted to 1 decimal place.

These deviations in Table 4.5 are now displayed graphically as a function of pressure, temperature and CO_2 density for each noble gas. For density a second-order polynomial fit line and corresponding R^2 value is included to allow for relationship between density and deviation to be quantified for the assessed experimental range.

Thus the fit line is in the form of

$$y = ax^2 + bx + c \tag{4.1}$$

where *x* is the density, *a* and *b* are coefficients and *c* is the y-axis (% deviation) intercept. At low pressures a full reconciliation is expected with published values (1.3.11 & 2.4.4) i.e. as *x* tends to 0 so too will *y*. Therefore *c* is fixed at 0 and Equation 4.1 simplifies to:

$$y = ax^2 + bx \tag{4.2}$$

This assumes no additional effects are encountered when moving between subcritical and supercritical conditions. The legitimacy of this assumption is fully explored in 4.10.4. Coefficients and R^2 values are presented on each graph and summarised in Table 4.6.

4.4 Helium

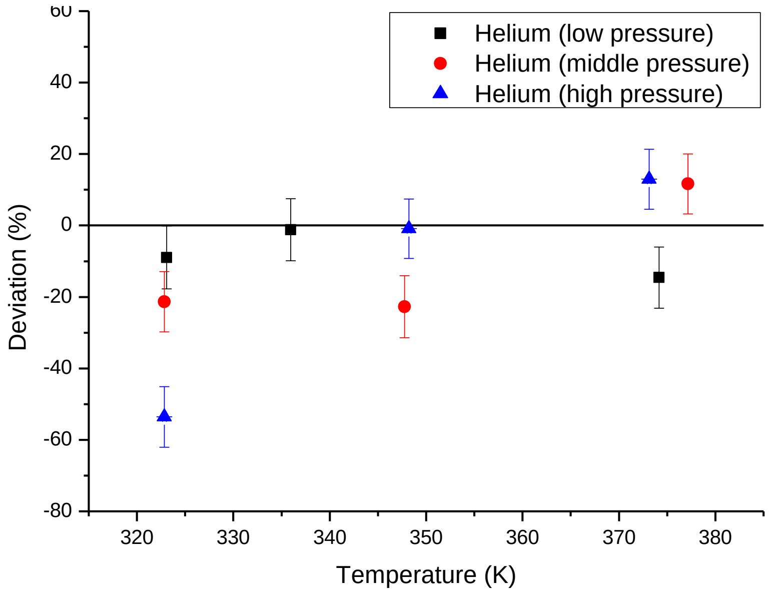

Fig. 4.2. Deviations from ideal helium partitioning as a function of temperature for three pressure regimes.

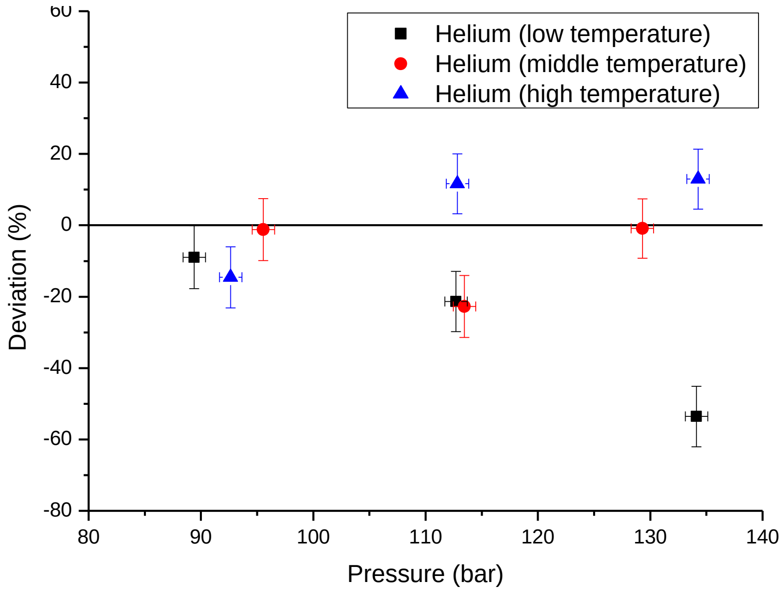

Fig. 4.3. Deviations from ideal helium partitioning as a function of pressure for three temperature regimes.

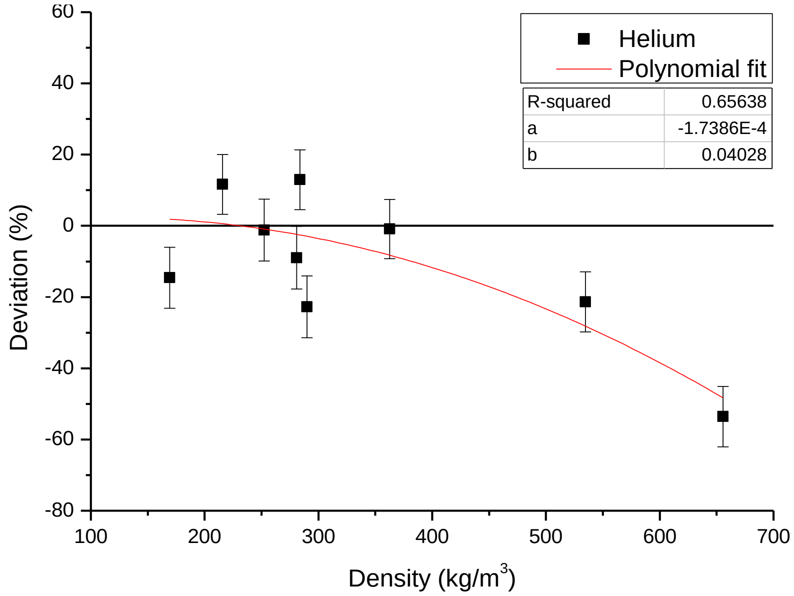

Fig. 4.4. Deviations of helium partition coefficients from ideal behaviour as a function of density.

4.4.1 The effect of temperature on pressure regimes

At the lowest temperature, deviation from predicted partition coefficients increased as a function of increasing pressure. At the lowest pressure deviations were negligible but reached -53.6% at the highest pressure. This was the highest deviation observed within this dataset.

The effect of increasing temperature on the lowest pressure had no discernible effect on deviation. However thermal trends were observed for both the middle and high pressure regimes. For both of these the effect of increasing temperature led to a transgression from negative deviations at low temperatures to similar slight positive deviations at the highest temperatures (-21.4% → 11.6% & -53.6% → 13.0%). Relative solubility within the water phase for both these pressure regimes therefore was lessened at these pressures by increasing temperature. This effect was most pronounced for the highest pressure regime.

4.4.2 The effect of pressure on temperature regimes

At the lowest pressures all three thermal regimes were reasonably concordant with published partition coefficients. The effect of increasing pressure on the lowest temperature range increasing corresponded to a significant negative deviation. At the highest pressure this deviation reached -53.6%, indicating a much greater relative increase in solubility in the water phase than predicted by the existing dataset. However at high temperatures a minor positive deviation from expected values was observed when pressure was increased although this remained fairly close to expected values (13.0% ± 8.4%).

No significant deviation from expected values was observed for the middle temperature at both the lowest and the highest pressures. At the middle pressure (Experiment 5) however the deviation was negative (-22.8%) and was comparable to its low temperature counterpart. This did not correlate with the low or high pressures which both replicated predicted coefficients. Therefore this was potentially an erroneous value. However this was not excluded as per the consistency discussion (4.2.2). Regardless it is reasonable to currently assume that overall, the middle temperature regime expressed no major deviation trends as a function of pressure.

4.4.3 The effect of density

A fair degree of variability was observed within the data at low densities (between -22.8% and 13.0%) and no overall deviation trend from the published partition coefficients was observed up to 363 kg/m^3. Again it was noticed that the partition coefficient for Experiment 5 (290 kg/m^3) was low (-22.8%) compared to other values within this range which fluctuated between -14.6% and 13%. This also supported the argument that this was potentially not a valid partition coefficient data point for helium (4.4.2). Above 363 kg/m^3 a progressive negative deviation was observed as a function of increasing density. Thus at sufficiently high densities Henry's coefficients progressively decreased (i.e. water solubility increased) relative to published values. At the highest density (656 kg/m^3) the greatest deviation (-53.6%) from published values was observed. At this density helium solubility in the water phase was a factor of 1.5 greater than expected.

When the second order polynomial fit was applied to the entire set a fair agreement ($R^2 = 0.66$) with the data set was reached, despite the variability within the data set. This fit adequately reproduced the negative deviation as a function of density trend. Therefore a relationship between density and deviation was reasonably established for the experimental range. When this polynomial is applied to lower densities an agreement within 5% of the published values (i.e. within experimental uncertainty) was reached at 322 kg/m^3. At densities below this point values predicted by the polynomial are comparable to published values. Therefore this equation is believed to provide acceptable predictions of deviation as a function of density from low densities (~0 kg/m^3) up to the highest experimental density (656 kg/m^3). The assumption is made that no additional effect occurs when crossing the subcritical-supercritical "boundary" (4.10.4).

4.5 Neon

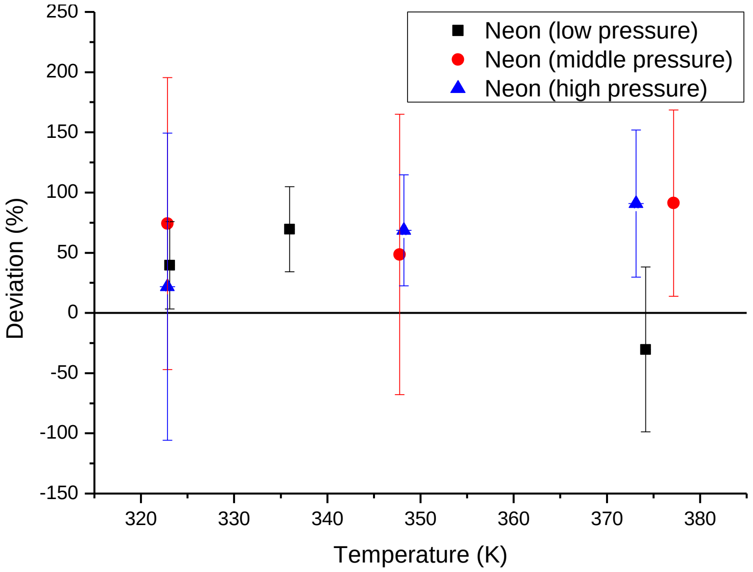

Fig. 4.5. Deviations from ideal neon partitioning as a function of temperature for three pressure regimes.

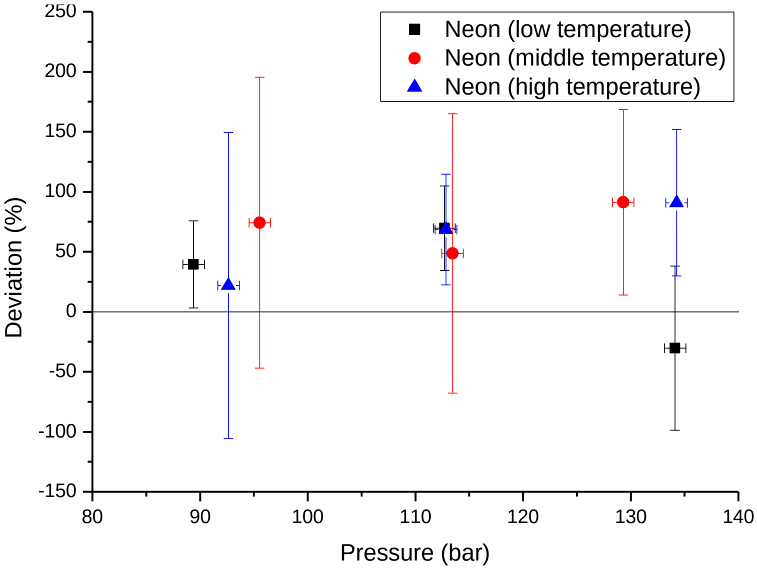

Fig. 4.6. Deviations from ideal neon partitioning as a function of pressure for three temperature regimes.

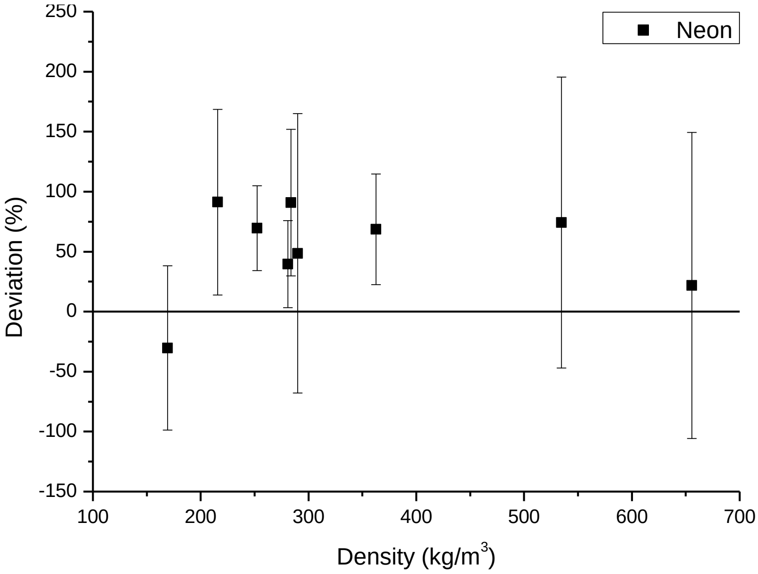

Fig. 4.7. Deviations of neon partition coefficients from ideal behaviour as a function of density. Due to the high uncertainty (4.4.2) no fit is given. Thus no legitimate neon trends were available for interpretation.

4.5.1 Neon trends

As previously discussed (4.3.3) given the high uncertainty for all data points a quantitative analysis for neon is not possible. Therefore no trends or observations can be legitimately made from the data. Consequentially no further discussion of neon is made in this chapter. Thus neon remains an issue to be resolved in future work (6.2).

4.6 Argon

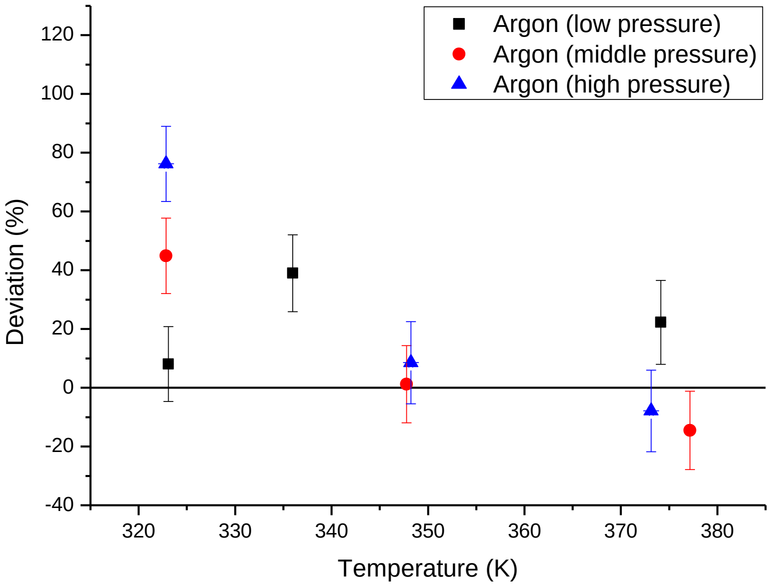

Fig. 4.8. Deviations from ideal argon partitioning as a function of temperature for three pressure regimes.

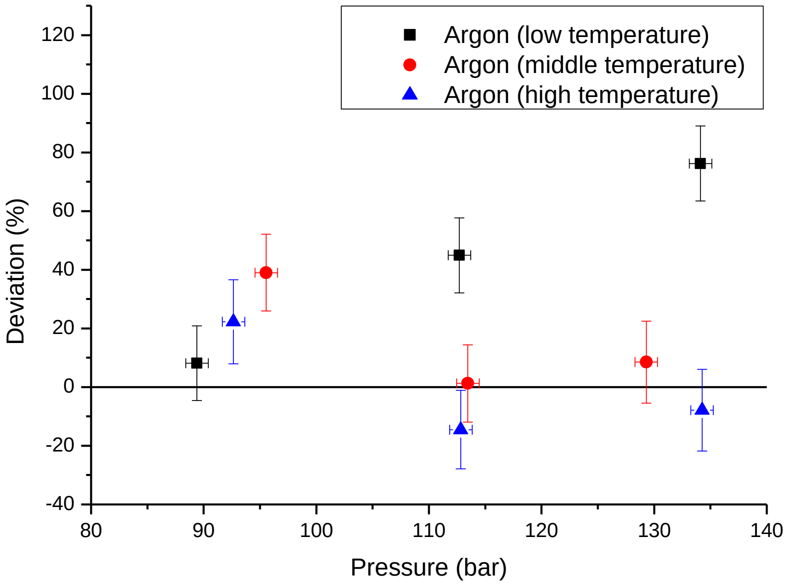

Fig. 4.9. Deviations from ideal argon partitioning as a function of pressure for three temperature regimes.

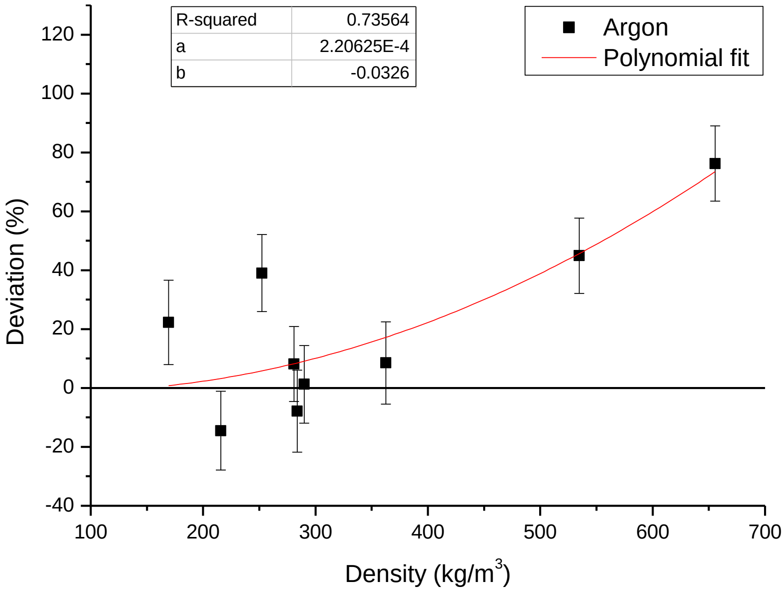

Fig. 4.10. Deviations of argon partition coefficients from ideal behaviour as a function of density.

4.6.1 The effect of temperature on pressure regimes

For the lowest pressure regime all values expressed a slight positive deviation and the effect of temperature proved negligible. At both middle and high pressures though high positive deviations were observed at the lowest temperature. Deviation at high pressure (76.2%) was greater than at middle pressure (44.9%). These represented the greatest observed deviations within the data. As temperature increased both these positive excursions progressively decreased until they were comparable with published values. Thus relative solubility within the water phase was most affected at the highest pressures and lowest temperatures and represented a factor decrease of 1.76, relative to published values. The effect of reducing pressure and/or increasing temperature progressively reduced this disparity between published values and experimental observation.

4.6.2 The effect of pressure on temperature regimes

At the lowest pressure no discernible deviation was noted for the lowest temperature set. However increasing pressure for this low temperature regime resulted in positive deviations from expected values which reached 76.2% at the highest pressure. This was the greatest deviation recorded. For the middle and high temperature regimes the effect of increasing pressure produced a minor negative trend from their initial, slightly positive, values. This fully reconciled both with published coefficient values.

Overall therefore only the lowest temperature regime was significantly affected by increasing pressure which resulted in positive deviations from published values. Corresponding solubilties in water were therefore relatively reduced under these conditions.

4.6.3 The effect of density

As with helium no overall deviation trend from the published partition coefficients was observed up to 363 kg/m^3. Again some variability was observed within the lower density range (-14.5% – 39.0%); however the majority of data points conformed to published values. At densities beyond this point progressive positive deviations were observed, i.e. at high densities experimental Henry's coefficients progressively increased relative to published values. This therefore corresponded to a relative decrease in argon solubility within water. The greatest deviation (76.2%) was observed at the highest density (656 kg/m^3) at which point the solubility was decreased by a factor of 1.76.

Again the applied polynomial reached a fair agreement (R^2 = 0.74) with the data. Additionally the overall deviation trend at high densities was reproduced well. Therefore this fit satisfactorily predicted the experimental results and allowed the density-deviation relationship to be numerically quantified. When applied to lower densities the polynomial reaches agreement within 5% of published values at 242 kg/m^3. Below this density calculated values are comparable to published values within expected experimental uncertainty. Thus this polynomial can reasonably determine deviation as a function of density for argon for the 0 – 656 kg/m^3 range assuming no subcritical-supercritical "boundary" effect (4.10.4).

4.7 Krypton

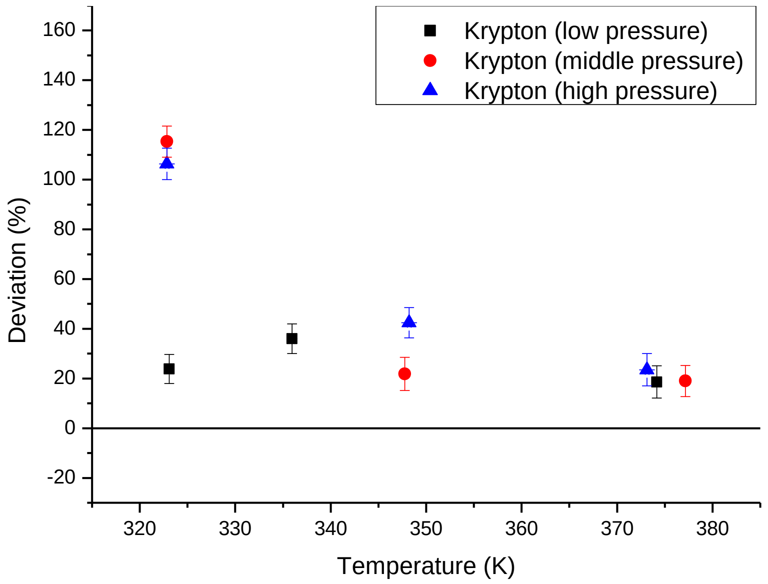

Fig. 4.11. Deviations from ideal krypton partitioning as a function of temperature for three pressure regimes.

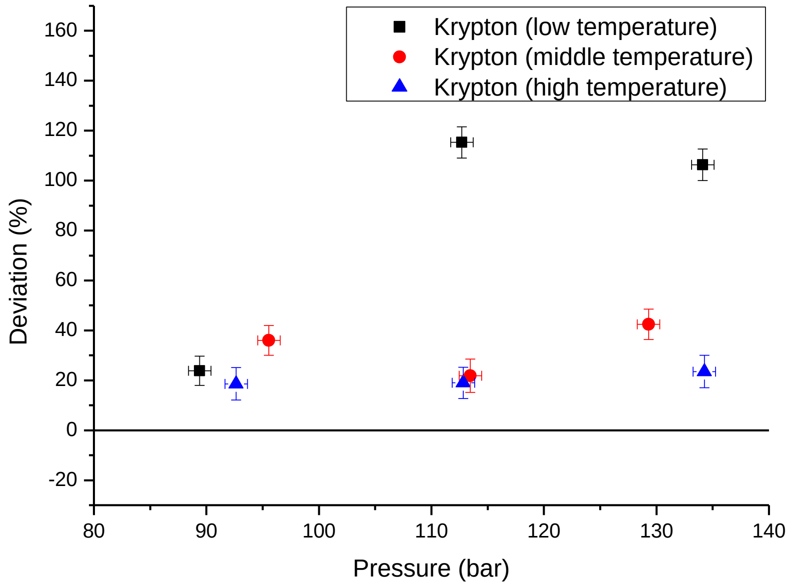

Fig. 4.12. Deviations from ideal krypton partitioning as a function of pressure for three temperature regimes.

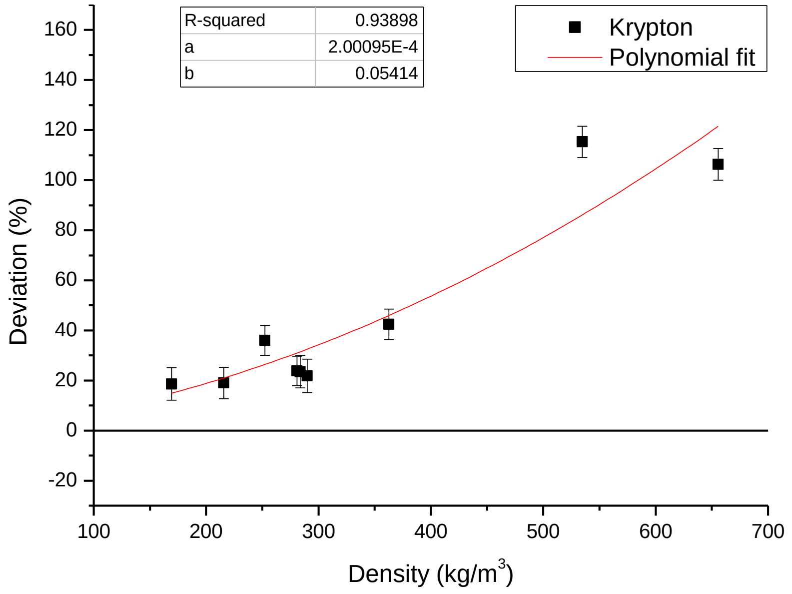

Fig. 4.13. Deviations of krypton partition coefficients from ideal behaviour as a function of density.

4.7.1 The effect of temperature on pressure regimes

At the lowest temperature all pressure regimes displayed a positive deviation from published values. These deviations were low at the lowest pressure (23.9%) and comparably high for middle and low pressures (115.3% & 106.3% respectively). These represented the greatest deviations from partition coefficients and were approximately double the published values. Under these conditions the corresponding solubility within the water phase was reduced by a factor of ~2 – 2.2, compared with published values.

For the low pressure regime deviations appeared independent of temperature. However for the higher pressure groups increasing temperature reduced the observed disparity. At the highest temperatures all three pressure regimes possessed similar slight positive deviations (18.6%, 19.0% & 23.5%).

When considered in terms of water solubility, at low temperatures increasing pressure decreased krypton solubility in water. However this effect is reduced as temperature increases. At the highest temperature, regardless of pressure, all solubilities were similarly reduced by a factor of ~1.2.

4.7.2 The effect of pressure on temperature regimes

At the lowest pressure all three thermal regimes were reasonably similar and possessed a slightly positive deviation. For the middle and high temperature regimes the effect of changing pressure resulted in no overall change to deviation. For the low temperature regime though increasing pressure from 89.4 to 112.7 bar resulted in deviations increasing from 23.9% to 115.3%. After this point the effect of increasing pressure for the lowest temperature had no discernible effect; at the highest pressure deviations were the same within uncertainty. These conditions resulted in the greatest deviation from published values. Under these conditions solubilities within the water phase were reduced by a factor of ~2 – 2.2.

4.7.3 The effect of density

The general density trend observed for krypton was similar to that present for argon i.e. as density increases so too does the relative increase in positive deviation. However unlike argon no agreement with published values is observed, even at low densities. When the polynomial trend line is applied to the data a good fit is achieved ($R^2 = 0.94$). Therefore a relationship between these two variables is established which can be legitimately predicted for the experimental data set using this fit. It was noted though that the two highest density deviations were extremely similar; this may be indicative of a maximum deviation. Given the paucity of data though this cannot be confirmed or denied at this stage. This does however raise valid concerns about extrapolating to higher densities than have been empirically investigated.

When applied to lower densities the polynomial does not reach full agreement with published values until density is 0 kg/m^3. However deviations are less than 5% at densities below 73 kg/m^3. At this point the discrepancy is within expected experimental uncertainty. Therefore at low densities an acceptable fit to expected values is reached. However further experimental work is advised in this lower density range to determine the absolute point at which deviations are observed as a function of density. This may result in slight adjustment to the a and b coefficients. However given the good fit to the experimental data, and the fair prediction at low densities it is concluded that this polynomial currently provides a valid method of defining deviation as a function of density for the 0 – 656 kg/m^3 range. As before no subcritical-supercritical “boundary” effect is assumed (4.10.4).

4.8 Xenon

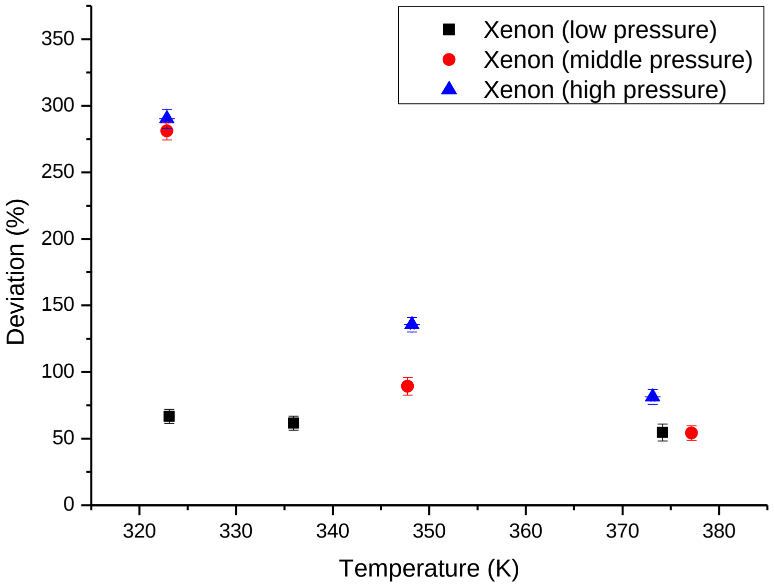

Fig. 4.14. Deviations from ideal xenon partitioning as a function of temperature for three pressure regimes.

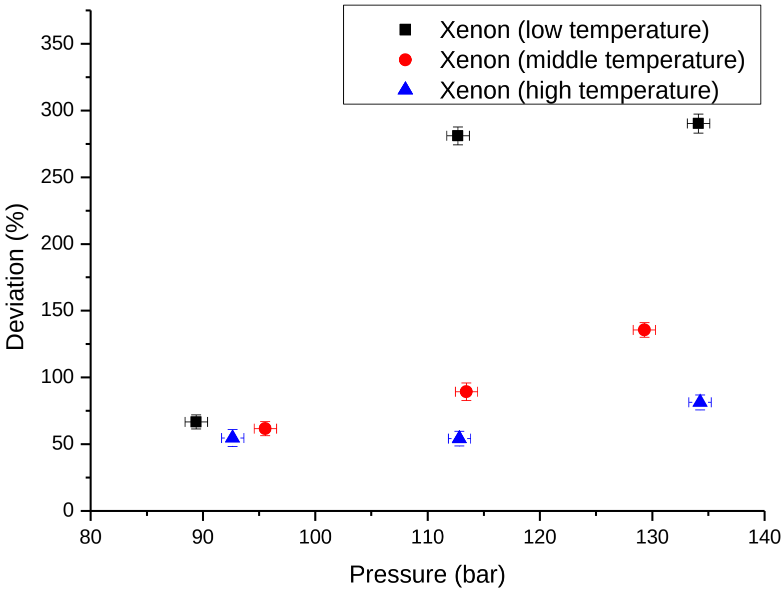

Fig. 4.15. Deviations from ideal xenon partitioning as a function of pressure for three temperature regimes.

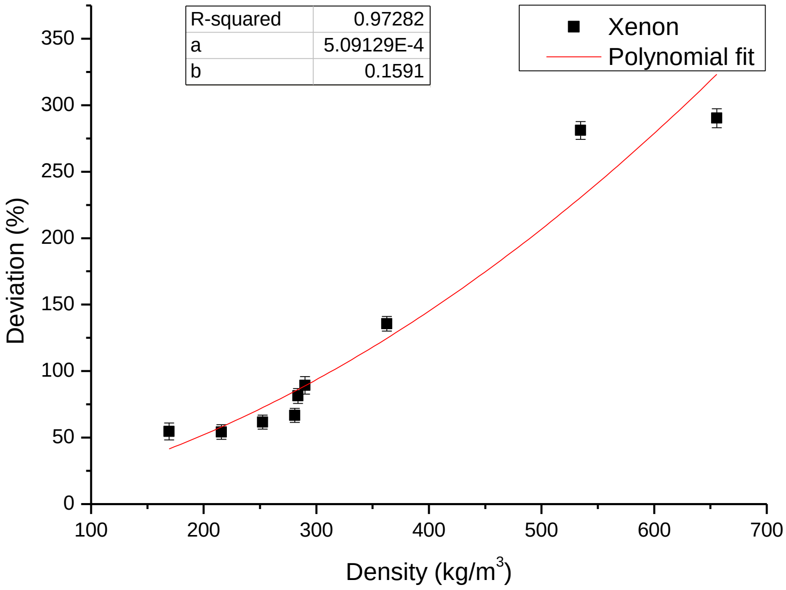

Fig. 4.16. Deviations of xenon partition coefficients from ideal behaviour as a function of density.

4.8.1 The effect of temperature on pressure regimes

All pressures consistently exhibited a positive deviation from published values across the thermal range (Figure 4.14). At the lowest temperature these deviations were lowest at the low pressure (66.7%) and similarly high for middle and low pressures (281% and 290.3% respectively). These high pressure low temperature deviations represented the greatest departure from published partition coefficients and were roughly four times the published values. Under these conditions the corresponding solubility within the water phase was reduced by a factor of ~3.8 – 3.9, compared with published values.

The effect of increasing temperature had no discernible effect on the lowest pressure. For the two higher pressure regimes an initial increase in temperature corresponded with a decrease in the magnitude of the positive deviation. This decrease was greater in the middle pressure regime than in the higher pressure regime (281% → 89.4% compared with 290.3% → 135.6%). As with the other noble gases at the highest temperatures all pressure sets had their lowest deviations from the published values. Middle pressure deviations (54.1%) reconciled with their low pressure counterparts (54.6%) while high pressure values were still slightly higher (81.4%).

When these trends are considered in terms of water solubility at low temperatures increasing pressure resulted in a relative decrease in xenon solubility. However this effect is reduced as temperature increases. At the highest temperature, pressure only has a minor effect on solubility.

4.8.2 The effect of pressure on temperature regimes

At the lowest pressure all temperature regimes exhibited similar positive deviations within uncertainty from expected partition coefficients. By increasing pressure all thermal regimes appeared to increase the positive deviation from published values. The lowest temperature range was most affected with xenon values increasing from 66.7% to 290.3%. For the middle temperature deviations varied less and increased from 61.6% to 135.6%.

Least affected were high temperature values which only increased from 54.6% to 81.4%.

Both middle and high temperatures displayed near linear increases of deviation as a function of pressure. This was not observed for the lowest temperature though. An initial increase of pressure from 89.4 to 112.7 bar resulted in the positive deviations increasing from 66.7% to 281.0%. However further increases in pressure produced no further discernible deviation from published values outside of experimental uncertainty. This trend was similarly observed for krypton values.

In terms of water solubility at low pressures all solubilities were similarly reduced by a factor of ~1.6 – 1.7. Increasing pressure resulted in further decreases in xenon solubility for all thermal regimes with the lowest temperature regime being most affected. Maximum decreases to relative solubility were observed here and represented a factor decrease of ~3.9 compared with expected values.

4.8.3 The effect of density

A clear relationship between increasing density and increasingly positive deviations was observed for xenon. Similarly to krypton no agreement is reached with published values even at the lowest experimental densities. When a polynomial fit was applied a very good correlation was obtained ($R^2 = 0.97$). Therefore this relationship between density and deviation is well defined for the experimental data set. Again, as with krypton, it was noted that the two highest density deviations were within uncertainty of one another and so could possibly infer a maximum deviation from experimental values is being approached. However further data is required to assess this.

When the polynomial is applied to lower densities total reconciliation with published only occurs when density is 0 kg/m^3. Predictions of deviations are less than 5% (i.e. within standard experimental uncertainty) at densities below 29 kg/m^3. Therefore at low densities an acceptable fit to expected values is reached. However given the total lack of experimental partition coefficients within this CO_2 density range further experimental work is advised to confirm these trends. Based on the current information though this polynomial both gives a good fit to the experimental data and acceptably reconciles with published values at low densities. Therefore this polynomial currently provides a viable way to derive deviation as a function of density for the ~0 – 656 kg/m^3 range. As for all other noble gases there is an assumption of no subcritical-supercritical “boundary” effects (4.10.4).

4.9 Overall trends within the data

4.9.1 Pressure and temperature trends

For all noble gases the greatest deviations occurred at the highest CO_2 pressures and lowest temperatures. These maximum deviations were positive for argon, krypton and xenon but were negative for helium. For those expressing a positive deviation the greatest magnitude was observed for xenon followed by krypton and least affected was argon. Overall the absolute magnitude of noble gas deviations decreased as temperature increased. For helium at the highest temperatures this deviation transgressed the 0% deviation line to become slightly positive. For argon increasing temperature reduced all observed deviations until a reasonable agreement was reached with published values. For krypton and xenon maximum deviations also decreased towards reasonable agreement with their low pressure counterparts. Therefore it was concluded that the effect of increasing temperature promoted progressive agreement with published values. At lower pressure regimes for all noble gases zero deviation was approached faster as a function of temperature than for their high pressure counterparts.

The greatest deviations occurred at the lowest temperature regimes for all noble gases. Initially average deviations for all three temperature regimes were in reasonable agreement with one another at low pressures. However the effect of increasing pressure on the lowest temperature group promoted significant deviations between the published and the experimental values. For the middle and high temperature ranges the effect of pressure on deviation was appreciably lower. For these regimes increasing pressure appeared to have a slight effect on reducing deviation for helium and argon but typically the degree of change was not much above the associated uncertainty for each of the data points and so was not considered indicative of any major theme. Middle and high temperature krypton values were similarly unaffected. The effect of increasing pressure on xenon though still corresponded to increased deviation for both these thermal regimes although this effect was considerably lower for the higher temperature regimes.

In summary at the lowest temperatures the greatest disparity with the published partition coefficient values were noted. This disparity increased as pressure increased. The middle and high temperatures only displayed a limited response to changes in pressure. Therefore in line with the pressure observations the maximum deviations occurred at the lowest temperatures and highest pressures.

It is useful to consider these deviations in terms of solubilities. At the greatest deviation, where pressures are highest and temperatures lowest, helium was considerably more soluble in water than predicted. All other noble gases though were significantly less soluble than expected. Increasing temperature served to reduce the discrepancy between experimental and published values for all noble gases i.e. enhance solubility for argon, krypton and xenon while reducing helium solubility.

4.9.2 Density trends

By observing the effect of CO_2 phase density on the experimental partition coefficients a method of reasonably combining the effects of pressure and temperature was achieved. Although individual trends and absolute magnitudes were unique for each noble gas one consistent theme was present; deviations increased as a function of density. All noble gases at high densities expressed a significant departure from published values. For helium increasing the density resulted in an increasingly negative deviation from existing partition coefficient (i.e. enhanced solubility in water). For all other noble gases higher densities corresponded with higher positive deviations (i.e. lower solubility in water). The maximum deviation was greatest for xenon, followed by krypton, argon and least for helium (290.3%, 115.3%, 76.2% & -53.6% respectively). Additionally, based on the polynomial fits, initial significant deviations (>5%) from published values are observed at the lowest density for xenon (29 kg/m^3) followed by krypton (73 kg/m^3), argon (242 kg/m^3) and lastly helium (322 kg/m^3). Consequently the trend lines for each noble gas predict xenon as most sensitive to density as a driving force for deviation and helium the least sensitive. This inferred a relationship existed between molecular size/weight and the effect of CO_2 density on partition coefficients.

Lastly it was noticed that the deviation of krypton and xenon did not increase significantly for the last two values. It was possible that this was simply due to natural variation within the dataset. However it is also recognised that it could represent a change to the relationship between density and deviation gradient at high densities. Such a change is expected and is discussed in 4.10.5 and 4.10.6. Given this uncertainty accurate predictions of behaviour at higher densities can only be made when further data is made available.

In summation all noble gases express significant deviation from published values as a function of density. These trends have been documented and acceptably quantified using a second order polynomial and so provide a means of calculating deviation as a function of CO_2 density between ~0 – 656 kg/m^3. Thus these deviations can be used to modify existing Henry's coefficients.

4.9.3 Reconciling published and experimental values

It has been proven that all noble gases can express significant deviations from published partition coefficients within supercritical CO_2 systems. These deviations are a function of CO_2 density with the greatest deviations occurring at the highest densities. The effect of this deviation can be quantified for each noble gas (i) using a deviation coefficient κ_i. As this coefficient represents the relationship between experimentally defined partition coefficients ($D_{i(exp)}$) and published partition coefficients under near ideal conditions ($D_{i(pub)}$) derived from Crovetto *et al.* and Smith (Crovetto *et al.*, 1982; Smith, 1985) it can be defined as:

$$\kappa_i = \frac{D_{i(exp)}}{D_{i(pub)}} \qquad (4.3)$$

When κ_i is greater than 1 the experimental partition coefficient is greater than the published value and the solubility in the water phase is lower than predicted. In instances where κ_i is less than 1 therefore solubility is enhanced.

Equation 4.3 can be rearranged to give experimental partition coefficients as a function of published values:

$$D_{i(exp)} = \kappa_i D_{i(pub)} \qquad (4.4)$$

Using the polynomial trend lines for each noble gas κ_i can be calculated as

$$\kappa_i = \frac{(ax_{(i)}^2 + bx_{(i)})}{100} + 1 \tag{4.5}$$

where a and b are fitted coefficients, $x_{(i)}$ is the density in kg/m^3 and $ax_{(i)}^2 + bx_{(i)}$ gives the percentage deviation from published values. When a positive deviation is observed κ_i is greater than 1. Negative deviations result in κ_i values less than 1 and when deviations are negligible $\kappa_i \approx 1$. Values of a and b for each noble gas are given in Table 4.6 alongside the R^2 confidence.

Noble gas	Coefficient a	Coefficient b	R^2 confidence
Helium	-1.74E-04	0.040	0.66
Argon	2.21E-04	-0.033	0.74
Krypton	2.00E-04	0.054	0.94
Xenon	5.09E-04	0.159	0.97

Table 4.6. Coefficients to fit Equation 4.5 to calculate deviation coefficient as a function of density between 0 – 656 kg/m^3. R^2 values are given to indicate confidence of polynomial fit to experimental values. All values here are given to three significant figures.

It is accepted that the coefficient values presented in Table 4.6 are liable to future minor adjustment as further experimental data becomes available which will allow fine-tuning to these trend lines. Additionally, although these second order polynomials provide a method of deriving partition coefficients between 0 – 656 kg/m^3, applying this correction to higher densities is not considered valid due to a poor understanding of noble gas behaviour at even higher densities. Despite this, possible extrapolation scenarios are presented in 4.10.5 and 4.10.6. These extrapolations are based on the discussion of the causal mechanisms (4.10).

With these caveats in place a legitimate method of adjusting published partition coefficients for application to dense CO$_2$ environments is presented. Thus an accurate determination of partition coefficients can now be achieved at densities expected within the majority of CCS environments.

4.10 Synthesis

In order to derive the most significant understanding from this study it is imperative that the underlying causal mechanism(s) for the deviations be determined. Once this is ascertained then the findings can be meaningfully applied to both existing and future datasets. Thus an accurate account of noble gas behaviour under similar conditions can be provided.

At the most basic level the change in observed partitioning must result from the change of one or more conditions from the original Crovetto *et al*. and Smith dataset (Crovetto *et al.*, 1982; Smith, 1985). From 4.9.3 a deviation coefficient κ_i was used as modify published partition values to incorporate the effect of a highly dense CO_2 phase. This coefficient is the cumulative effect of all factors which affect partitioning. Therefore to understand the underlying forces driving the observed deviations all changes must be identified and then assessed. Broadly speaking these changes can be considered in terms of the CO_2 phase (Φ_i) and the water phase (γ_i). What follows therefore is this process of determining all factors which may play a role in affecting solubility for each phase.

4.10.1 Water phase factors

It is expected that the effect of changing temperature on the water phase will not have contributed to any deviations from published noble gas partition coefficients. This is because the temperature range here was within the original range from which the published values were derived (Crovetto *et al.*, 1982; Smith, 1985). Consequentially any effect of changing temperature on activity coefficient of the water phase has already been incorporated within the original published dataset.

Typically any pressure effects on the water phase are considered negligible (Ballentine *et al.*, 2002). This is due to the highly incompressible nature of water. However, given the high experimental pressures within this study, such an assumption cannot be made. The magnitude of this effect can be estimated using the Poynting correction (1.3.11). To do this, partial molar volumes, $\overline{V}_{mi}$, for each noble gas at infinite dilution are taken from the literature. These are presented in Table 4.7:

Noble gas	Partial molar volume (cm^3/mol)
Helium	29.7
Argon	32.2
Krypton	32.8
Xenon	42.7

Table 4.7. Partial molar volumes of each noble gas at infinite dilution. Helium and argon values taken from Enns *et al.*, 1965 (Enns *et al.*, 1965), krypton value taken from Moore *et al.*, 1982 (Moore *et al.*, 1982) and xenon value taken from Biggerstaff & Wood, 1988 (Biggerstaff & Wood, 1988).

By combining the values in Table 4.7 with the Poynting correction (Equation 1.13) the effect of pressure on the liquid phase for the partitioning for each noble gas can be reasonably determined. These have been calculated for the highest experimental density where observed deviations were the greatest. Using this approach the extent to which this maximum deviation is derived from pressure alone can be assessed. These values are presented in Table 4.8.

Noble gas	Change to partitioning due to pressure (%)	Experimental deviation (%)	Outstanding deviation (%)
Helium	16.0	-53.6	-69.6
Argon	17.5	76.2	58.7
Krypton	17.8	106.3	88.5
Xenon	23.8	290.3	266.5

Table 4.8. Assessing the effects of the Poynting correction (Equation 1.13) on partition coefficients at the maximum deviation (322.85 K & 134.12 bar). Partial molar volumes for each noble gas are taken from Table 4.7. The outstanding deviation is the observed experimental deviation minus that which can be attributed to Poynting effects.

From Table 4.8 a reduced solubility within the water phase occurs for all noble gases at higher pressures when the Poynting correction is applied to low pressure partitioning. The heaviest noble gases are most affected with deviations ranging from 16.0% to 23.8% for helium and xenon respectively. However, this is a relatively small proportion of the experimentally determined deviation trends; with the exception of helium, at elevated densities significant positive deviations were observed. Therefore the observed deviations are only slightly reconciled with published values for argon, krypton and xenon by incorporating the effect of pressure within the water phase. Additionally, the Poynting correction indicates a lower helium solubility as a function of increasing pressure. However this was in contrast to the experimentally observed trend. The resultant deviation for helium was enhanced therefore by incorporating the effect of pressure on the water phase.

Although it is expected that pressure acting on the water phase has had some effect on partition coefficients this cannot satisfactorily explain the significant experimental deviations observed here. Consequentially the assessed effect of pressure acting on the water phase is relatively minor and therefore can be discounted as the driving force for these observed deviation trends.

In summary, as with the reference dataset, the effect of pressure on the water phase can still reasonably be considered minor (Ballentine *et al.*, 2002). This assumption may require revisiting in the future though for higher pressure systems. Thus with regards to the water phase the effect of temperature is already accommodated and pressure effects are marginal when considering factors within the water phase affecting noble gas partitioning. Therefore neither are expected to induce the experimentally observed deviations from published partition coefficients.

The only remaining water phase factor which could cause discrepancy with the published studies is compositional. In 1.3.10 the effect of modifying noble gas solubilities by adding an electrolyte (sodium chloride) to the water phase was discussed. A noticeable change in the partition coefficient of all noble gases was observed when an electrolyte component was present. Given this precedent it is feasible therefore that altering the composition of the water phase is a viable means of causing deviations to partition coefficients at a given pressure and temperature.

Initially the composition of the water phase was identical to that used for the original dataset. Both sets of experiments used deionised water for the water phase. However the effect of allowing equilibration with a high pressure gas phases results in the water phase containing a small dissolved gaseous component. In the original experiments using pure noble gas phases it was this which allowed the partition coefficients to be derived. For the experiments presented here however in the water phase an additional dissolved CO_2 component was present. The first stage in quantifying the effect this may have on noble gas partitioning is to determine the absolute amount of CO_2 entering the water phase. For this the compiled data table from Spycher *et al*. (and references therein) is used (Spycher *et al.*, 2003). Within the experimental thermodynamic conditions used for this project the maximum and minimum solubility of CO_2 could be derived from this data table. Maximum CO_2 solubility occurred at high pressures and low temperatures while minimum solubilities were found under the opposite thermodynamic conditions. Within the scope of this project this gives a maximum molar fraction range of 0.014 – 0.021 CO_2 within the water phase. By combining the density of water at with the respective molar fraction a concentration range of 0.73 – 1.13 mol/l CO_2 is calculated at the lowest and highest solubilities. As stated in section 1.3.10 the effect of this dissolved CO_2 on noble gas partition coefficients has not yet been absolutely defined (Ballentine *et al.*, 2002). However it is possible to use the findings of related studies to speculate on the effect that this aqueous CO_2 component may have on noble gas solubilities. What follows therefore is an attempt to constrain the effect this CO_2 may have on partition coefficients. It is however recognised that many of the assumptions made during this process are tentative. The validity of which will require revisiting at a later date.

Presently only one known study has investigated the effect of CO_2 on the solubility of a non-polar molecule. This study, by Price *et al*. investigated the effect of changing the CO_2 content of a CO_2-methane mixture on solubility of methane within brines (Price *et al.*, 1981). The results of this study concluded that as the molar fraction of CO_2 relative to methane was increased a greater amount of CO_2 phase dissolved within a brine. This led to a significant reduction in methane solubility relative to the molar fraction it represented. This was interpreted by the authors as a ‘salting out’ mechanism (i.e. an increase to the liquid phase activity coefficient). If this is applied to the data presented here then the inclusion of a CO_2 component within the liquid phase is liable to decrease solubility of the noble gases. However caution must be advised as one key issue was not considered by the original authors: how compositional changes affected thermodynamic properties in the CO_2-CH_4 phase. Without this consideration it is implied that the thermodynamic properties of this phase remain constant. This assumption is fairly reasonable where the CO_2/methane mixture exists as a gaseous phase approximating ideality. However the experiments were conducted between 345 – 1550 bar at 422 K. Under these conditions both CO_2 and methane are dense supercritical fluids with strongly non-ideal behaviour. As it stands therefore it is a strong possibility that this apparent salting out effect could be due to a different process altogether. The reduction in methane solubility with increasing CO_2 could instead be part or even entirely driven by a change to the fugacity (Φ) of the supercritical phase. A low fugacity of methane due to increasing CO_2 could result in lower concentrations of methane within the water phase. Thus the effect of CO_2 dissolved in the water may in reality produce a lessened or even negligible effect on methane solubility. This viable alternative interpretation was overlooked by the original authors.

Additionally it was also noted that CO_2 solubility was higher for this published study than in the experimental results presented here. As such any effect of aqueous CO_2 on noble gas solubility is likely to be appreciably lessened for the studied experimental range. Lastly, unlike methane, the non-polar solute molecules of interest in this study are in much lower abundance in both phases and so are not expected to have any significant self-interactions in either phase. Given the molar fractions and the densities investigated this was not the case in the Price *et al*. study (Price *et al.*, 1981). Thus this study cannot provide any useful insight into how aqueous CO_2 may affect noble gas solubilties.

Another approach to investigate the effect of aqueous CO_2 on partition coefficients is to compare it to aqueous sodium chloride. Obviously strong differences exist between each solute. While sodium chloride is an ionic compound made up of Na^+ and Cl^- ions, aqueous CO_2 will predominantly exist as a non-ionic solute. It is possible that due to minor amounts of speciation there will be a minor ionic effect from the solvated CO_2. However this effect is expected to be minor and so for the sake of simplicity can be reasonably ignored at this stage. The presence of both are expected to result in a lower noble gas solubility within the water phase. For sodium chloride this is based on empirical evidence (Smith & Kennedy, 1983). In the case of CO_2 though, in lieu of experimental data, a degree of inference is required to reach the same conclusion. It can be reasonably argued that at any given temperature and pressure there is a finite capacity for non-polar solute particles within the water phase. Consequentially when CO_2 is present within this phase in significant quantities less noble gas molecules are expected to be accommodated. Thus the solubility of noble gases will be lessened. As the CO_2 molecule is reasonably large, it is more likely to be accommodated where the larger noble gases would otherwise fit. Places where the smaller noble gases would fit are less likely to be affected. Similarly smaller particles may also fit into spaces formed around the solvated CO_2 molecule. The presence of CO_2 within the water phase therefore is expected to result in lower solubility for all noble gases. The heaviest noble gases are liable to be affected to a much greater extent than their lighter counterparts. The addition of aqueous CO_2 therefore is liable to result in the same trends as observed when sodium chloride is added.

In contrast with sodium chloride, the inclusion of CO_2 is not anticipated to have a major bearing on the overall behaviour or structure of this water phase. This is supported by experimental evidence indicating that the activity coefficient of aqueous CO_2 is equal to unity for the concentrations presented here (Diamond & Akinfiev, 2003). When the same molar concentration is applied to a sodium chloride solution at similar temperatures however significant deviations from unity of the activity coefficient are observed (Liu & Lindsay, 1972). Consequentially it is believed that the 'salting out' effect of sodium chloride should be greater than the effect of CO_2. This is a logical assumption to make as the water phase consisting of polar molecules should be more disrupted by the presence of an ionic solute compared with a non-ionic equivalent. Using this argument a comparable amount of sodium chloride should therefore result in a more significant change to the availability of spaces which solute noble gases can occupy. Thus it can be tentatively proposed that the effect of CO_2 on reducing noble gas solubility will most likely be lower than sodium chloride, on a mole for mole basis. With this expectation in place, it is possible to use the effect of sodium chloride to infer a maximum change to noble gas solubilities. By assuming the effect of the CO_2 molarity in the water is comparable to sodium chloride, the Setschenow coefficient can be used to calculate the reduction of noble gas solubility. As sodium chloride should reduce solubility more than CO_2 this calculated value can be used to indicate the maximum reduction to solubility. As discussed in 1.3.10 it is not reasonable to extrapolate beyond the experimental range for calculating the effect of salinity (273.15 – 338.15 K). Fortunately the thermodynamic region where CO_2 solubility is at a maximum for the experimental dataset lies within this experimental range. Furthermore this point is where the most experimental deviation of partition coefficients is observed. Therefore the extent to which this maximum deviation is derived from aqueous CO_2 can be assessed. This is presented in Table 4.9.

Noble gas	Experimental deviation from partition coefficients (%)	Max deviation attributed to CO_2 (%)	Outstanding deviation (%)
Helium	-53.6	+31.0	-84.6
Argon	76.2	+40.5	35.7
Krypton	106.3	+42.9	63.4
Xenon	290.3	+46.4	243.9

Table 4.9. The maximum deviation of each noble gas at 322.85 K & 134.12 bar. Maximum deviations attributed to CO_2 are calculated using constants from Smith & Kennedy based on a 'salinity' of 1.13 mol/l (Smith & Kennedy, 1983). The outstanding deviation is the observed experimental deviation minus that which can be attributed to CO_2.

From Table 4.9 it is apparent that the maximum effect of aqueous CO_2 can theoretically represent a significant fraction of deviations from published partitioning values. However, even if the assumption is made that the maximum deviation is the true effect of aqueous CO_2, a large, unresolved deviation from published values remains. For xenon the CO_2 component can only account for 16.0% of the total deviation. This fraction increases for krypton and argon (40.4% & 53.1% respectively) although again a large deviation still remains unaccounted for. In the instance of helium, for the conditions investigated, experimental partition coefficients were actually lower than expected from the published dataset. However, using sodium chloride as a proxy, aqueous CO_2 is expected to result in partition coefficients greater than the published values. This could be indicative of an inherent flaw in approximating CO_2 as sodium chloride. Alternatively it could be indicative of a much more dominant process affecting solubility which masks any aqueous CO_2 effect on helium solubility. At this stage it is impossible to determine the veracity of either hypothesis and so this remains an issue to be addressed by further work.

Presently no alternative method for constraining the effect of CO_2 in water currently exists. For this investigation sodium chloride is therefore considered an acceptable proxy for tentatively defining a maximum upper limit of aqueous CO_2-derived deviation. Based on the current evidence it is concluded that the CO_2 within the water phase is expected to result in deviations from predicted partitioning. However the effect is considered to be much less than that of sodium chloride which serves to represent a maximum possible deviation. Additionally the outstanding disparity to the helium partition coefficient solubilities is increased when the effect of aqueous CO_2 is taken into account. Given that even the maximum possible deviation predictions cannot account for a large proportion of the deviation encountered it is reasoned that a much more dominant process is responsible for the observed trends. As such it is concluded that the effect of aqueous CO_2 plays only a small role, if any, in affecting the partition coefficient for the noble gases for the experimental range. However, this assumption will inevitably require future verification.

With all identified potential sources of this discrepancy discussed for the water phase it therefore is concluded that the dominant process is a function of the CO_2 phase. I.e. κ_i is predominantly a function of Φ_i with γ_i only having a minor effect.

4.10.2 CO_2 phase factors

Having assessed the water phase for possible causes of the deviations the next logical step is to apply the same process to the CO_2 phase. The water phase was determined as only having a minimal bearing on deviations. Therefore it was concluded that non-ideality in the CO_2 was the driving force for deviation (i.e. $\Phi_i >> \gamma_i$). Therefore a relationship between fugacity (Φ_i) and the deviation coefficient (κ_i) must be established. From Equation 4.3 κ_i was defined. Under both ideal (Equation 1.3) and non-ideal (Equation 1.4) conditions partition coefficients (K_i) can be derived for noble gas *i*. Therefore these can be combined to give κ_i as a function of Φ_i.

$$\kappa_i = \frac{D_{i(exp)}}{D_{i(pub)}} = \frac{K_{i(exp)}/\Phi_i}{K_{i(pub)}} = \frac{1}{\Phi_i} \qquad (4.6)$$

Thus fugacity is inversely proportional to the deviation coefficient. Therefore for positive deviations to partition coefficients fugacity will be lower than unity. This indicates a greater preference to remain in the CO_2 phase. Consequentially the deviation coefficient will be greater than unity. Where negative deviations are encountered the opposite is true. Where ideality can be reasonably invoked both κ_i and Φ_i will represent unity.

It is recognised that fugacity is the net effect of all factors promoting non-ideality. Therefore each process requires independent assessment of the contribution towards fugacity. The Crovetto *et al.* and Smith studies determined noble gas solubilities using a pure noble gas phase interacting with a water phase (Crovetto *et al.*, 1982; Smith, 1985). Therefore the replacement of a pure noble gas phase with a CO_2 bearing trace noble gases presents a significant departure from the original experimental conditions. Considering that this the primary change to experimental conditions it follows therefore that it is this is the probable source of any of the observed deviations for this phase. However to cite this compositional change alone as the explanation cannot satisfactorily account for all observed deviations. Indeed in other systems where noble gases are similarly only present as tracers (e.g. the atmospheric reservoir) their partitioning remains in line with the published values (e.g. Kipfer *et al.*, 2002; Brennwald *et al.*, 2012). Therefore, although this change of environmental conditions must be the source of the discrepancy, it cannot be invoked alone as an all-encompassing explanation of observed deviations.

Within this experimental study noble gas partitioning is not uniformly affected by this change of environment. This is supported by the observed deviations not remaining constant for all experimental conditions. This is indicative of one or more underlying processes at work within this CO_2 phase which are actually responsible for the observed trends. The key properties and interactions within this phase under the investigated conditions must therefore be investigated to assess how and why these deviations occur. The two identified factors liable to affect fugacity are the composition and density of the CO_2 phase. These are now assessed.

Although the composition of the CO_2 phase is overwhelmingly CO_2 ($\geq$99%) this phase also possesses a minor water component. Theoretically this could play a role in affecting the behaviour of noble gas within this phase. Although this water component increases progressively as a function of temperature the absolute amount of water in the CO_2 phase remains very small. Estimates of water at the highest experimental temperatures within the CO_2 phase indicate a molar fraction of approximately 0.018 (Spycher *et al.*, 2003). This is on the same order of magnitude as the CO_2 in the water phase which was considered to only have a minor effect on solubility. Additionally it is noted that the greatest fraction of water exists in the CO_2 phase at high temperatures and low pressures. Under these conditions deviations of partition coefficients are at their lowest. Therefore the assumption is made here that water within the CO_2 phase has no effect on fugacity and so does not contribute towards the observed noble gas partitioning deviations.

The main difference between this system and both the reference system and other systems where noble gases are present as tracers is the density of the main carrier phase. Ideality can be reasonably assumed where density is low because intermolecular interactions are infrequent and have a small effect on the overall behaviour. However as density increases so too does the degree of molecular interaction. As this characterises non-ideality it follows that increasing density will increase deviation from the partition coefficients generated under near-ideal conditions. This is supported by trends observed for every isotope: increasing density led to the progressive deviations from expected values. Therefore a causal link between density and deviation can be assumed. However deviation is only observed when sufficiently non-ideal conditions are reached. Using the polynomial values fitted to the data and assuming deviations greater than 5% of low pressure values indicate the onset of significant deviation, this point is reached first for xenon (29 kg/m^3) followed by krypton (73 kg/m^3), argon (242 kg/m^3) and lastly helium (322 kg/m^3). Similarly, based on the maximum observed deviations, the change of deviation as a function of density was greatest for xenon followed by krypton, argon and lastly helium. Both of these identified trends indicated that the heaviest noble gases were most responsive to non-ideality.

Thus deviations can satisfactorily be explained by density-driven non-ideality within the CO_2 phase. At low pressures and temperatures fugacity will be negligible (i.e. $\Phi_i = 1$) and noble gas partitioning will replicate published values ($\kappa_i = 1$). However as density increases by changing temperature and/or pressure, the non-ideality in the CO_2 will also increase (i.e. $\Phi_i \neq 1$). Eventually, when deviations from ideality are significant, the effect would become present on noble gas partition coefficient values. Where the partition coefficient is greater than predicted (i.e. argon, krypton and xenon) Φ_i will be lower than 1 indicating a greater preference for remaining in the CO_2 phase. Where the partition coefficient is less than expected (i.e. helium) Φ_i will be greater than 1 and a lower affinity for the CO_2 phase will be expressed. κ_i values remain inversely proportional to Φ_i as outlined in Equation 4.6. The effect of this non-ideality affects the heaviest noble gases more than their lighter counterparts. This results in deviation occurring at lower densities and possessing a steeper gradient. This theory is in agreement with the experimental data presented in this study.

4.10.3 Explaining the relationship between density and deviation

A density-derived non-ideality mechanism has been presented to explain the dominant force affecting experimentally defined partition coefficients. Of equal importance are the underlying principles which drive this mechanism. By defining and understanding these as much as possible it is possible to create a logical basis for considering trends beyond the experimental limits.

It is clear that when sufficient density is reached noble gas partition coefficients are altered from predicted values at comparable temperatures. It is similarly recognised that as density of CO_2 increases so too does the expressed non-ideality. This is due to an enhanced degree of molecular interaction. Therefore it follows that it is this non-ideality within the CO_2 phase which results in altered partition coefficients. Xenon, the heaviest noble gas, is most affected while helium is least affected. For argon, krypton and xenon this deviation is expressed as a greater than expected affinity for the CO_2 phase ($\Phi_i < 1$). For helium though the opposite is true ($\Phi_i > 1$). The question which now needs to be addressed is how does non-ideality in CO_2 result in these observed deviations?

For the noble gases expressing a fugacity coefficient lower than unity a fairly straightforward explanation can be applied. It is widely accepted that dense CO_2 acts as a fluid solvent (e.g. Kamihira *et al.*, 1987; Black, 1996; Morgenstern *et al.*, 1996). Indeed it is this property which allows it to be implemented in a multitude of industrial applications. For example it can be used in the process of decaffeination (e.g. Mohamed *et al.*, 2002; Kim *et al.*, 2008) Enhanced Oil Recovery (EOR) (e.g. Blunt *et al.*, 1993; Ravagnani *et al.*, 2009) or in a multitude of pharmaceutical applications (e.g. Ferrieri, 2003; Reverchon *et al.*, 2009). Previous studies have indicated that the solvation power of a fluid is known to increase as a function of density (Giddings *et al.*, 1968; Yonker *et al.*, 1986). Therefore, as density is considered here to be an assessment of non-ideality in the CO_2 phase, it is logical to expect a direct link between non-ideality and solvation power (Muller, 1994; Baiker, 1999). An increase in solvation power should result in a noble gas molecule being more easily accommodated within the CO_2 phase. The overall effect will be a lower fugacity of a solute noble gas within this phase. Based on the experimental evidence xenon appears to be the easiest to solvate followed by krypton and then argon. Published studies have indicated that highly dense CO_2 phases possess polar properties (e.g. Reynolds *et al.*, 1996; Kauffman, 2001; Raveendran *et al.*, 2005). Therefore this pattern of solubility within the CO_2 phase is likely due to an induced polarisation effect on the noble gases, related to their respective polarisability. Xenon atoms possess the highest polarisability followed by krypton, argon and lastly helium which has the lowest polarisability (Kipfer *et al.*, 2002). Consequentially an increased solvation power of the CO_2 phase results in much greater enhanced solubility of xenon. Krypton and argon solubilities are enhanced accordingly. Similar solubility trends are due to induced polarisation occurring within the water phase

(Ballentine *et al.*, 2002; Kipfer *et al.*, 2002). While this explanation provides reasonable explanations for the behaviours of argon, krypton and xenon there is still the issue of helium. At higher densities non-ideality of CO_2 appears to reduce the affinity helium possesses for this phase. As a result negative deviations from the partition coefficient are recorded at the highest densities. This does not conform to the pattern observed for the other noble gases. Presently no definitive reason is known why this may be the case. However, if solubility within the dense CO_2 phase is associated with an increased polar function then, due to the low polarisability of helium, the resultant repulsive forces acting on this particular noble gas within this polar solvent could outweigh the enhanced attractive forces. Thus as the solvation power increases (i.e. ability to induce polarisation) as a function of density, solubility of helium within the CO_2 phase is likely to decrease. Helium behaviour can therefore also be tentatively explained by this physical process.

In summary, at elevated densities, CO_2 acts as a polar solvent which possesses an increased solvation power as density increases. Solvation of the noble gases within this phase occurs by inducing polarisation according to their respective polarisabilities. Therefore as xenon followed by krypton and argon in descending order are more easily polarised they become significantly more soluble within this phase as a function of density. Helium, with the lowest polarisability, becomes less soluble in a progressively dense CO_2 phase. This is thought to be due to the repulsive forces acting on helium outweighing attractive forces within this polar solvent.

4.10.4 The subcritical-supercritical “boundary”

In the preceding section effect of deviation as a function of density has been assessed. However under all experimental conditions CO_2 existed as a supercritical fluid. The subcritical-supercritical “boundary” therefore denotes a potential lower limit of applicability of the correction trends which must be assessed.

Traditionally when a thermodynamic boundary is passed for a single component material (e.g. solid → liquid or liquid → gas) there is a phase transition. Thermodynamic properties of the substance are intrinsically different either side of this boundary. This results in inherent differences between the two states. For example at 1.01325 bar, at the boiling point of water, the density of water decreases from 958 to 0.6 kg/m^3 (NIST, 2013).

When systems properties change to such an extent it follows that their ability to interact with tracers within the phase (e.g. noble gases) are also affected. For the subcritical-supercritical “boundary” to be considered a lower limit to the observed trends a similar sudden change in system properties such as density would be expected. However this is not generally considered to be a typical phase boundary. It is noted that when a change from gaseous or liquid to supercritical CO_2 is induced by increasing pressure at a fixed temperature or vice versa there is no sudden change to any thermodynamic properties (Span & Wagner, 1996; NIST, 2013). Properties such as density, enthalpy and viscosity do not deviate from their current trends when pressure or temperature changes induce supercriticality. Consequentially, the effect of crossing the subcritical-supercritical “boundary” is expected to have no effect on noble gas partitioning. Therefore it is legitimate to assume the second order polynomial fits, applied to accommodate deviation as a function of density, can be extrapolated to $y = 0$, even at subcritical conditions.

4.10.5 Upper limits to deviation?

Although maximum deviations were expressed at the two highest densities for all noble gases the relationship between these two points were not identical. For helium and argon a continued increase in deviation was observed for both noble gases. However for krypton and xenon the deviations associated with the two highest densities appeared to be of approximately the same magnitude. At present it is not known if this is due to variation within the dataset or whether this is indicative of a change in noble gas behaviour. From the available data it is impossible to ascertain which is true. However this uncertainty highlights the issue with attempting to extrapolate a density-based deviation trend beyond the current experimental range.

Regardless of this ambiguity it is not reasonable to expect deviation as a function of density to increase *ad infinitum*. This is especially true for the noble gases indicating a greater CO_2 affinity. For these noble gases, solubility within the CO_2 phase presently increases in line with density. The trends presented here based on the second order polynomial predict this relationship to continue indefinitely. This is not a legitimate assumption. A point will be reached whereby this phase becomes so dense that more noble gases cannot easily be accommodated. At this point the maximum deviation will be reached. After this point the effect of further increasing density will almost certainly serve to reduce the noble gas content of this phase, thereby reducing any positive deviation. Such a trend will be expected to continue with further increases in density. As a result a maximum should be reached for argon, krypton and xenon. As this point is approached the existing trend lines will no longer be valid. The density at which this occurs is likely to be unique for each noble gas and can only be defined empirically. Similarly no sensible prediction can be reasonably made for the behaviour of helium at much higher densities. Given this strong uncertainty it is not reasonable to extrapolate the empirically defined relationships beyond the range presented here without supporting experimental evidence.

4.10.6 Applying trends to the entire CO_2-water system

At this stage all key trends within the data have been quantified. Potential causal mechanisms for these trends have also been investigated. Present deviation trends as a function of density for the existing data set are well described by a second order polynomial fit. However the experimental range defined here is only representative of a small region of the entire system which spans from low densities to extremely high densities. Ultimately an equation will be required to describe deviation of noble gases for this entire system. Although at this stage a discussion of such an equation is purely academic it is expected that with the addition of further data this section will provide a basis for defining future numerical adaptations. Presently density derived deviations are described by a second order polynomial fit which can be reasonably applied from low densities up to the highest experimental density (656 kg/m^3). However this fit cannot be extrapolated beyond the experimental densities. At unspecified higher densities positive deviations are expected to reach an unknown maximum deviation for each noble gas followed by a reduction (4.10.5). Negative densities are expected to continue to decrease indefinitely, however, this rate of decreasing deviation cannot currently be predicted. Thus the expected trend for argon, krypton and xenon is graphically displayed in Figure 4.17.

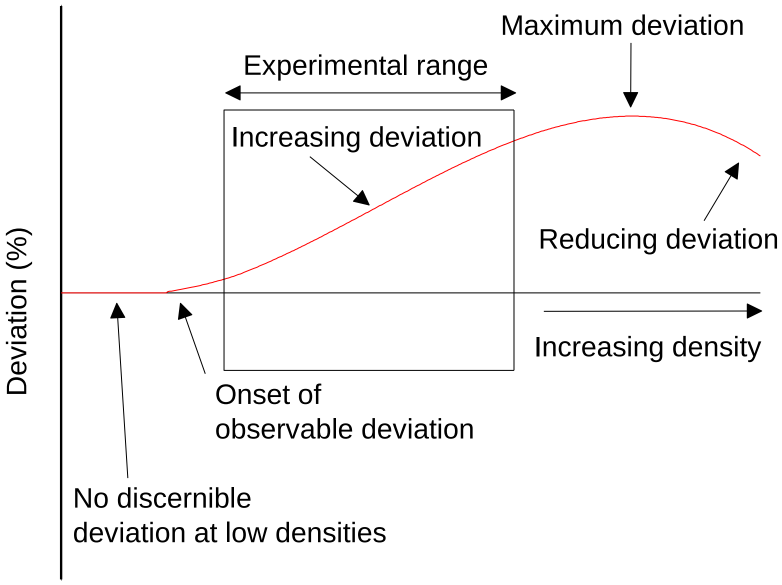

Fig. 4.17. Predicted deviations to partition coefficients as a function of density. This behaviour is applicable to argon, krypton and xenon for the expanded CO_2-water system. Absolute values of initial deviation, rate of deviation and maximum deviation are unique for each noble gas. Maximum deviation and rate of reducing deviations are not known. Approximate experimental range is indicated based on empirical observations of noble gas trends, although the point of initial deviation is observed for argon. Present second order polynomial fits have been applied for the experimental density range 0 – 656 kg/m^3 (4.3.8 & 4.9.3).

For helium no initial positive deviation is observed. However it has also been observed that as the noble gases become lighter so too do the gradients of deviation as a function of density. Therefore it is not unreasonable to postulate that any positive gradient of helium was so slight the uncertainty prevented it from being discernible from published values. Thus for helium the initial point of deviation is possibly the expected negative deviation, predicted after the maxima is reached. Therefore the overall characteristics of Figure 4.17 are tentatively applicable to all noble gases.

Using this as a template it is expected therefore that two points of inflection will occur within the data. The first is where the initial deviation as a function of density is observed and the second is where the maximum density deviation is reached. This trend is best described using a third order polynomial which would be written in the form of

$$y = a(\rho_{CO_2})^3 + b(\rho_{CO_2})^2 + c(\rho_{CO_2}) + d \qquad (4.7)$$

where ρ_{CO_2} is the density of CO_2, *a*, *b*, *c* and *d* are empirically defined coefficients and *y* is the resultant deviation for the specified density. Again at low density a full reconciliation is expected with published values (1.3.11 & 2.4.4) i.e. as ρ_{CO_2} tends to 0 so too will deviation (*y*). Therefore *d* is fixed at 0 and Equation 4.7 simplifies to:

$$y = a(\rho_{CO_2})^3 + b(\rho_{CO_2})^2 + c(\rho_{CO_2}) \tag{4.8}$$

Thus for the expanded range the density deviation coefficient κ_i is written:

$$\kappa_i = \left(\frac{a(\rho_{CO_2})^3 + b(\rho_{CO_2})^2 + c(\rho_{CO_2})}{100} \right) + 1 \tag{4.9}$$

which will allow corrections to be applied to low pressure partition coefficients for the expanded experimental range.

In conclusion it is expected that, although a second order polynomial fits the current experimental range, this third order polynomial will best describe the wider density range. However it is accepted that a lot of conjecture has been made based on only a small proportion of the total data required. Therefore further iterations to this process might be required in light of additional information. Additionally the assumption is maintained that the effects of changing water density, aqueous CO_2 and water within the CO_2 phase remain negligible. Such assumptions may prove untenable for extreme conditions and so additional terms incorporating these may be required to accurately predict noble gas partitioning for the expanded range.

4.10.7 The effect of salts on partitioning

Deviations to partition coefficients of all noble gases are primarily density driven. It is expected therefore that the addition of salts within the water phase should produce the same effect as observed at low pressures. i.e. a reduction of solubilities for all noble gases in line with the Setschenow coefficients (Smith & Kennedy, 1983). However the combined effect of salt and CO_2 on noble gas partitioning at high densities remains uncertain. This therefore will require addressing in future work.

4.10.8 Impacts of study on geological processes

Noble gas partition coefficients for dense CO_2 phases are clearly distinct from their low density counterparts. The next step therefore is to discuss the absolute effects on identified affected systems. As only the Henry's coefficients for the noble gases are considered to deviate from the assumed values there is absolutely no reason to believe any overall observed chemical or physical process occurring within any system component will be rendered void. For example groundwater will still flow within a system and interact with surrounding media and magma will still undergo degassing. However what is considered affected are both the rates and/or the magnitudes that these processes operate on. This study has observed that as density increases so to does the affinity of the heavy noble gases for this phase. As a consequence processes which contribute these noble gases to a dense CO_2 phase e.g. magma degassing will require scaling down to generate the same absolute concentrations. Processes which remove noble gases such as redissolution into a water phase however will require scaling up to maintain currently observed heavy noble gas concentrations. For helium where solubility in water is enhanced at higher densities the opposite adjustments will be required.

Additionally, as each noble gas is affected uniquely as a function of density noble gas ratios will also be affected. For example at higher densities solubilities of the heavier noble gases in water are reduced by a much greater degree than their lighter counterparts. Therefore ratios such as $^{84}Kr/^{36}Ar$, $^{130}Xe/^{36}Ar$ and $^{4}He/^{40}Ar$ will be either elevated or reduced depending on which phase is investigated. Where such ratios are invoked to quantify geological processes the respective changes to solubility will require consideration. Additionally, models involving open Rayleigh degassing will require recalculation. This is due to a change in the relative loss of one isotope relative to another within either a CO_2 or water phase.

It is concluded that overall observations of noble gas behaviour will remain valid. All input and output mechanisms will remain isotopically unique and thus quantifiable. However the change to partition coefficients means existing studies will require subtle recalculations of input and output mechanisms to maintain noble gas mass balance.

Specifically in terms of CCS projects previously assumed partition coefficients can now be adjusted for direct application to CCS environments. This therefore provides a way of generating accurate predictions of expected partition coefficients under storage conditions. This tighter constraint on expected partitioning values will allow for deviations due to subsurface interactions to be identified and quantified with a much higher degree of accuracy.

4.10.9 Impacts on published studies

From the findings of this study it is abundantly clear that under many geological conditions significant differences exist between the assumed partition coefficients and their actual values. An assessment must be made on how these observed deviations are liable to affect existing and any future studies. To accomplish this all affected systems require identification. This experimental dataset observed the effect of supercritical CO_2 on partitioning into a water phase. Therefore all noble gas publications involving systems of this nature will require some minor form of redress (e.g. Ballentine & Holland, 2008; Gilfillan *et al.*, 2008; Sherwood-Lollar & Ballentine, 2009; Klusman, 2011; Zhou *et al.*, 2012).

For example in the Gilfillan *et al.* study, noble gases in several systems were observed to exsolve from, then redissolve into groundwater due to the migration of a CO_2 rich phase (Gilfillan *et al.*, 2008). The densities of CO_2 within these systems ranged between 142 – 720 kg/m^3. After redissolution was complete ^{84}Kr/^{36}Ar and ^{130}Xe/^{36}Ar ratios in the gas phase were significantly greater samples from the higher density systems than expected from a simple gas/water equilibrium. These could not be resolved by the proposed model. However the expected ratios were derived from the Crovetto *et al.*, and Smith studies with the Smith & Kennedy data set adjusting for salinity (Crovetto *et al.*, 1982; Smith & Kennedy, 1983; Smith, 1985). These are now known to provide inaccurate estimations for partitioning under these conditions. From the findings presented here krypton and xenon possess a greater affinity for the CO_2 phase over argon than previously predicted. Therefore during the exsolution stage more krypton and xenon will exsolve relative to argon. Similarly less will subsequently redissolve. The highest density systems will be most affected and the lowest densities least affected. In this study the lowest density system (St John's Dome, 142 kg/m^3) closely replicated predicted ^{84}Kr/^{36}Ar values. The highest density system (McElmo Dome, 720 kg/m^3) however possessed a wide range of ^{84}Kr/^{36}Ar values which were poorly explained by ratios expected if they had been derived from Air Saturated Water (ASW). Additionally this high pressure system had much lower ^{20}Ne/^{36}Ar compared to ASW values. Although no neon data is currently available for high density CO_2 systems, it is legitimate to assume neon has a lower affinity for the CO_2 phase than argon. Therefore this observed isotopic fractionation may be due wholly or in part to non-ideality in the CO_2 phase. As such a revaluation the model to incorporate the findings of this study are required. Additionally, when neon data becomes available the absolute volumes of water required for stripping and redissolving a noble gas component will require minor recalculation.

From this example it is clear that the impacts of this study on previous studies can be readily identified. All prior conclusions based on identified system processes are expected to remain valid. However the quantification of these processes will require re-evaluation. This will be achieved by applying more accurate set of partition coefficients derived from this and future studies.

In addition to the discussed high density CO_2-water systems the implications of this study are considered to affect other systems. As it is the density of the CO_2 phase driving deviation, similar non-ideal behaviour should be expected in all systems with a dense CO_2 phase. One such system of considerable interest to the geoscience community is the CO_2-magma system. The role of noble gases within the magmatic system is discussed in 1.3.3. During the ascent of magma within the crust the effect of depressurisation results in the formation of separate phases (i.e. vesicles) within the melt. These separate phases consist of almost pure CO_2 (Carroll & Draper, 1994). At the temperatures and pressures in which they form the CO_2 will exist as a supercritical phase (Sparks, 1978). Given the highly volatile nature of the noble gases these too will preferentially enter this separate phase, although a fraction will remain within the liquid phase. This partitioning is used in determining rates of degassing, magmatic origins and other related magmatic processes. However estimations of partitioning assume only compositional variations within the magma phase affect noble gas partitioning. (Jambon *et al.*, 1986; Carroll & Draper, 1994; Hilton & Porcelli, 2003). Non-ideality in the CO_2 phase is ignored. Solubility therefore is considered to be a simple Henry's coefficient relationship, independent of pressure. Similarly to this project, this assumption is a result of applying low pressure partitioning experiments (Jambon *et al.*, 1986) to much higher pressures. Indeed recent simulation-based studies in this field have indicated that this is not a reasonable assumption to make when CO_2 is at much higher densities (Sarda & Guillot, 2005; Guillot & Sarda, 2006; Aubry *et al.*, 2013). The experimental values generated here for a related system adds credence to this. At the same time these studies provide further support to the argument presented here that the density of the supercritical phase results in deviations from Henry's constants at lower pressures and temperatures. It is recognised that the temperatures and pressures for these systems are far in excess of those investigated here. Therefore it is not reasonable to extrapolate any observations to attempt to quantify the effect on magmatic system-based partition coefficients. However the deviations to published partition coefficients presented here categorically highlight the shortcomings of assuming the applicability of low density partitioning analogues to dense CO_2 phases.

This magmatic example is the closest well-studied analogue which has had similar assumptions made on noble gas partitioning behaviour. However other, less studied, systems and processes exist involving a noble gas component which will similarly be affected by CO_2 non-ideality. These potentially include CO_2-hydrocarbon interactions, CO_2-mantle systems and CO_2-hydrothermal fluid interactions. However this list is by no means exhaustive. Essentially the behaviour of noble gases within all systems containing a dense CO_2 phase should be considered suspect. Consequentially is advised that wherever a dense CO_2 phase is in contact with other phases, the noble gas partitioning between each phase should not be expected to be comparable to low pressure analogues.

4.11 Summary

Noble gas partitioning within supercritical CO_2 phases does not replicate partitioning under ideal conditions. This is due to density-based non-ideality within the CO_2 phase. As density increases so too do deviations from predicted partition coefficients for all noble gases. These deviations are positive for argon, krypton and xenon and are expected to progressively increase as a function of density until a maximum deviation is reached after which solubility should decrease. Helium possesses a negative deviation as a function of density and is predicted to decrease as a function of density indefinitely. Xenon exhibits the greatest deviation at a given densities and is the first to deviate from published values as a function of density. Helium on the other hand is least affected and is the last to deviate. Deviations are due to the increase in the solvation power of CO_2 which increase as a function of density. This high density results in CO_2 acting as a polar solvent. This induces polarisation in line with their respective polarisabilities. The polarisability increases with the atomic mass and so xenon possesses the greatest affinity for the dense CO_2 phase followed by krypton and then argon. This results in positive deviations to the published partition coefficient. Helium being far less polarisable has a reduced solubility compared with when it was in a near-ideal gas. Therefore helium expresses negative deviations from predicted partition coefficients. Within the experimental range all of these relationships are reasonably described by a second order polynomial fit to the experimental results. This fit therefore provides a means to correct the existing published partition coefficients for use within high density CO_2 systems (4.9.3). Thus noble gases can now be used to interpret most CCS environments with confidence.

Chapter Five

Simulated Henry's constants

5.1 Introduction

A concurrent aim of this project was to create a robust way of modelling partitioning under experimental conditions. Currently partition coefficients for noble gases are derived from solubility curves defined from the experimental data. These provide a highly accurate means of determining partitioning under given conditions. However their applicability is limited to the experimental conditions in which they were generated. Consequently applying them to temperature-pressure-composition regimes outside the experimental limits cannot be justified. The goal of the simulation aspect of this project therefore was to construct a molecular based GEMC modelling approach capable of predicting noble gas partitioning at the elevated pressure temperature regime. Such a model would not be constrained by experimental boundaries and could be further adapted for related systems. The development of this model to its current iteration is documented in this chapter and the current progress summarised at the end.

No previous study has used a GEMC approach to simulate noble gas partitioning involving a water phase. Therefore no existing model was readily available for adaptation to the specific requirements of this project. As a result the model was constructed from scratch and verified at each stage of development.

Before it could legitimately be applied to high pressure CO_2-water systems the model had to fulfil two criteria. The model needed to have a proven ability for generating accurate partition coefficients for a pure noble gas-water binary phase system at low pressure which correlated with the published values of Crovetto *et al*. and Smith (Crovetto *et al.*, 1982; Smith, 1985). The model also needed to predict the same values to an acceptable degree of accuracy when a CO_2 phase at low pressure was introduced. Only when both of these criteria were attained could the model be legitimately applied to high pressure systems. Thus fulfilling these requirements served as the basis for the formation and justification of the final model. However they also represent significant achievements in applying a GEMC approach to investigating partitioning. As such they are considered results in their own right and hence their inclusion in this chapter. Details of each simulation are fully specified in 3.6.

As with the experimental data, all values are presented as deviations from published partition coefficients. At low pressure deviations should be negligible while at high pressure deviations should replicate experimental trends.

5.2 Optimising noble gas-water interactions

The ability of Towhee to predict partition coefficients at low pressure between a pure noble gas phase and a pure water phase required assessment. Therefore systems were simulated containing each noble gas as a pure phase interacting with a water phase (3.6.2). Each system was run at 1.01325 and 10.1325 bar between 293.15 – 353.15 K. The results from these simulations were used to determine noble gas partition coefficients (3.7.1). Partition coefficients were derived from linking pressure (P_i) and noble gas solubility within the water phase (x_i) in accordance with Equation 1.3. These could then be compared to their published experimental counterparts (Crovetto *et al.*, 1982; Smith, 1985) to assess the validity of this approach. Given that the simulations fall within the experimental range, simulated values should be indistinguishable from published values.

Additionally the ε Lennard-Jones potential parameter between each noble gas and the oxygen on the water molecule (ε_{ij}) required optimisation (3.4.6). For the initial simulations, ε_{ij} values were derived using the Lorentz-Berthelot mixing rules (3.4.5). Where the resultant partition coefficients were greater than published values, solubility within the water phase was lower than expected. Under these circumstances values of ε_{ij} were scaled-up to increase noble gas-water interactions and enhance solubility. Where partition coefficients were lower than published values, ε_{ij} values were scaled-down to reduce solubility. Thus a method was provided to optimise ε_{ij} to reconcile simulation results with experimental partition coefficients. These results are presented in terms of deviation from published coefficients. From these deviations simple arithmetic average values were generated to allow assessment of simulated values in terms of their experimental counterparts. Individual values at each temperature for all scaled ε_{ij} values for each noble gas are provided in Appendix II.

5.2.1 Helium

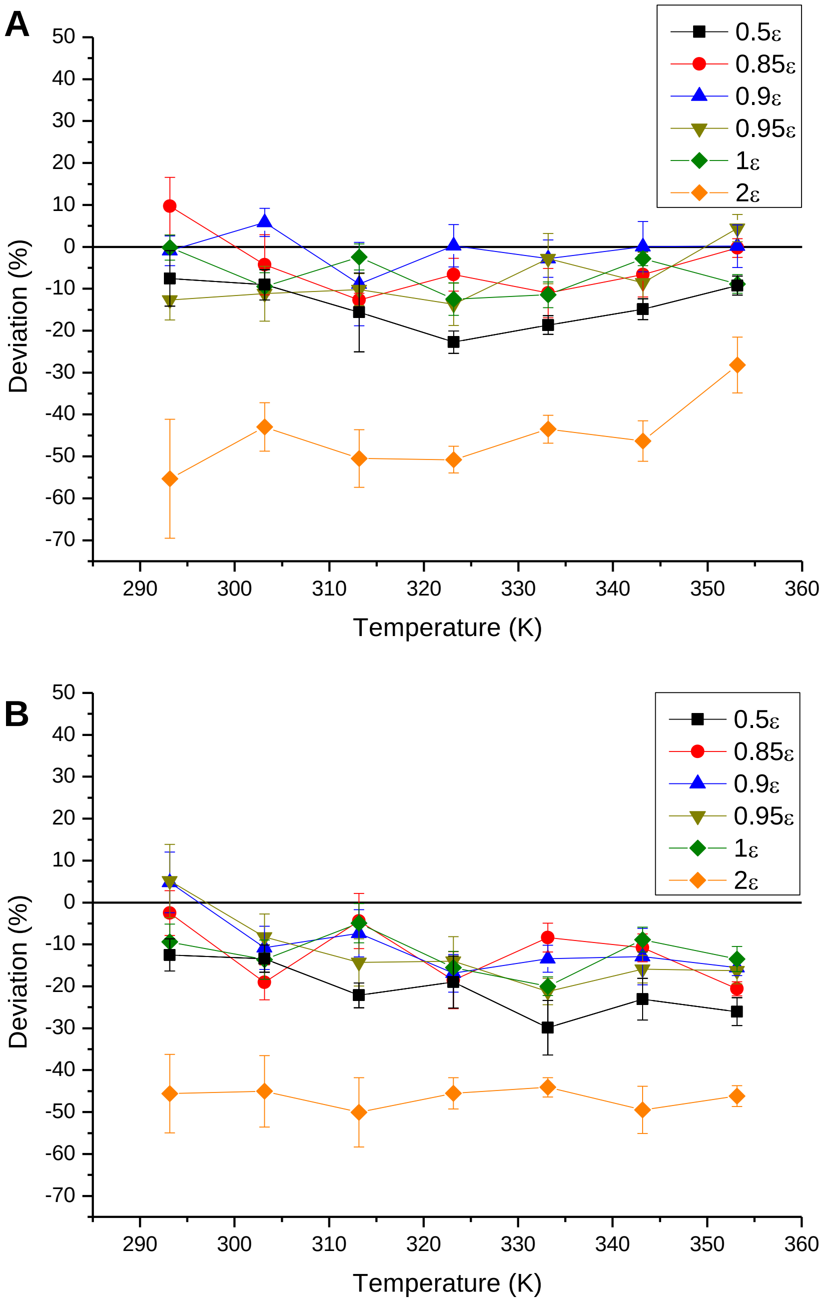

Fig. 5.1. Pure helium-water simulations for different values of ε_{ij}. Results have been presented as deviations from published partitioning coefficients between 293.15 – 353.15 K at (A) 1.01325 bar and (B) 10.1325 bar.

Epsilon scale factor	Average % deviation (1 atm)	Uncertainty (S.E)	Average % deviation (10 atm)	Uncertainty (S.E)
0.50	-14.0	4.2	-20.9	4.4
0.85	-4.5	4.7	.12.0	4.5
0.91	-0.9	5.4	-10.3	4.9
0.95	-7.8	5.2	-12.1	5.0
1.00	-6.8	2.9	-12.3	3.7
2.00	-45.4	6.4	-46.6	5.8

Table 5.1. Average deviations from published partition coefficients at 1.01325 & 10.1325 bar for different values of ε_{ij}. Uncertainty is quoted as standard error. All values are given to 1 decimal place.

As shown in Figure 5.1 for the original value of ε_{ij} there is a fair correlation between the simulated and published results for the partition coefficients of helium in water at both 1.01325 and 10.1325 bar. Average partition coefficients were consistently slightly under-predicted though at both pressures (-6.8% and -12.3%).

The overall effect of progressively decreasing the ε_{ij} term only had a marginal effect on the partition coefficients. Significant increases and decreases to ε_{ij} however both resulted in an observed decrease to partition coefficients when compared to the published values. This suggests that, contrary to what was expected, both increasing and decreasing the original ε_{ij} term enhances the simulated solubility of helium in water. However due to the marginal effect changing ε_{ij} has on helium solubility this effect is only observable when the deviation is significant enough. A possible minor thermal gradient was present at 10.1325 bar; the effect of increasing temperature here resulted in slightly reducing the simulated partition coefficient. This trend though was within uncertainty and so could not be stated with confidence. However a similar trend was much more noticeable in neon at the same pressure.

It is also noted from Figure 5.1, that the observed discrepancy between simulation and experimental results becomes further enhanced when the simulation is run at 10.1325 bar. All deviations are lowered by 5 – 10% for all values of ε_{ij}, indicating that increasing pressure may result in enhanced water solubilities in the model beyond that predicted by Henry’s law. This is considered further in 5.2.6. Overall the modified ε_{ij} value which best replicated the published partition coefficients was 0.91 ε_{ij}. This was because the reduced helium-water parameter replicated average partition coefficients within uncertainty at 1.01325 bar and has the lowest deviation from published values at 10.1325 bar. It was accepted that this scaling down did not fully rectify the issue as at the higher pressure an observed disparity was still present. Additionally this value was within the uncertainty for the original ε_{ij} value. Therefore it must be acknowledged that this optimised value may not truly be representative of an overall improvement to this potential. However this reduced value resulted in better overall predictions of solubility and at this stage it was considered indicative of a better pair potential than the original value.

5.2.2 Neon

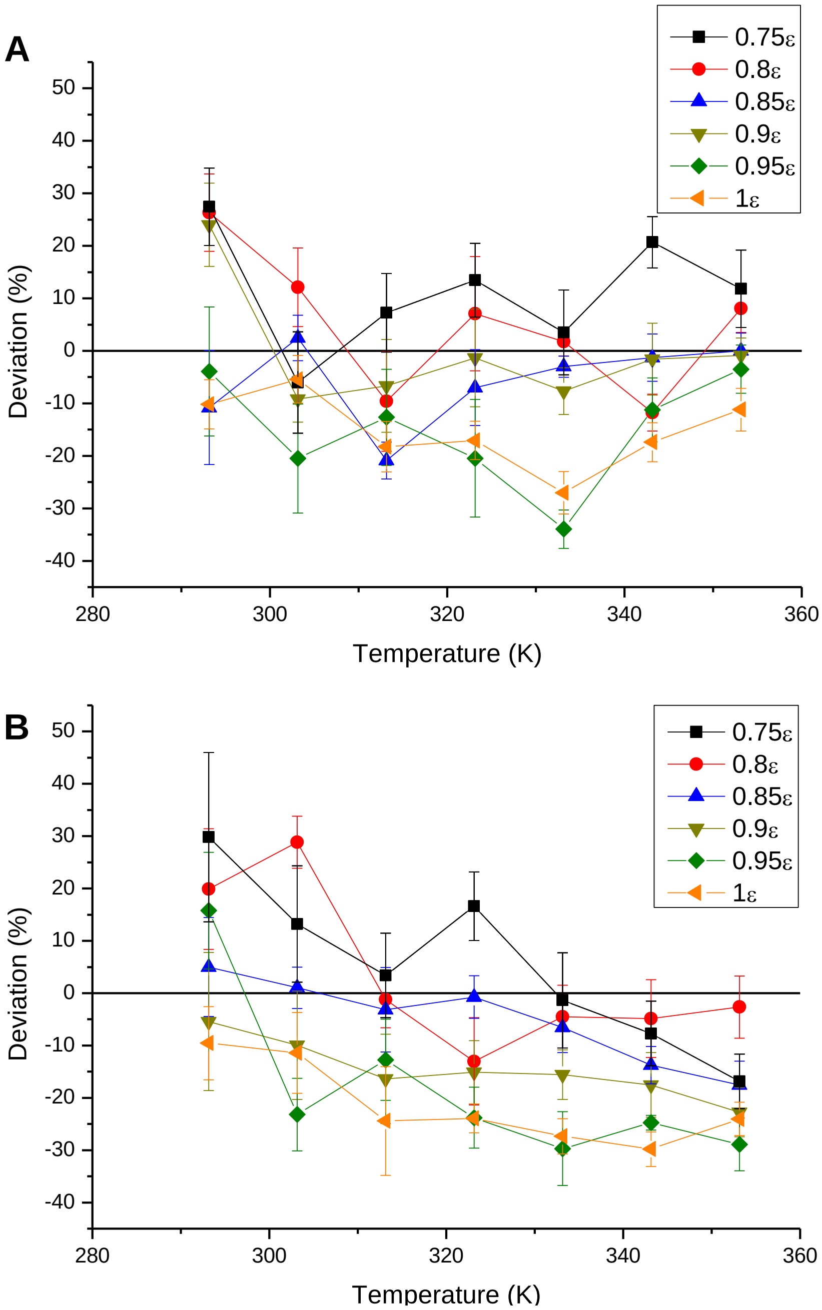

Fig. 5.2. Pure neon-water simulations for different values of ε_{ij}. Results have been presented as deviations from published partitioning coefficients between 293.15 – 353.15 K at (A) 1.01325 bar and (B) 10.1325 bar.

Epsilon scale factor	Average % deviation (1 atm)	Uncertainty (S.E)	Average % deviation (10 atm)	Uncertainty (S.E)
0.75	11.2	7.4	5.3	8.9
0.80	4.8	6.6	3.2	7.1
0.85	-5.8	5.1	-5.1	5.5
0.90	-0.5	6.4	-14.7	7.7
0.95	-15.2	8.2	-18.2	6.4
1.00	-15.2	4.2	-21.5	5.4

Table 5.2. Average deviations from published partition coefficients at 1.01325 & 10.1325 bar for different values of ε_{ij}. Uncertainty is quoted as standard error. All values are given to 1 decimal place.

From Figure 5.2 the average simulated partition coefficients of neon using the initial value of ε_{ij} was consistently slightly under-predicted at both pressures. This represented over solubility within the water phase when compared to the published dataset. The discrepancy between the experimental and simulation at 1.01325 bar was an average of -15.2%. When the pressure was increased to 10.1325 bar this deviation increased to -21.5%. However, in contrast to helium, the effect of reducing the ε_{ij} value resulted in a clear reduction in average water solubility at both pressures. When ε_{ij} is scaled down by a factor of 20% or more average partitioning coefficients transgress to positive deviations. At this point solubility within the water phase is lower than determined by the experimental dataset.

As with the helium model, the effect of increasing the pressure to 10.1325 bar resulted in decreases to the partition coefficients. This was observed for all values of ε_{ij}. The implication of this therefore is that the effect of increasing pressure increased solubility in the water phase to a greater extent than expected when Henry's law is assumed. An additional trend observed at this elevated pressure was that the effect of increasing temperature resulted in progressively lower partition coefficients for all values of ε_{ij}. This indicated that relative solubility was potentially related to temperature at higher pressures. However no legitimate reason for this was known.

Overall the ε_{ij} value which best corresponded to published values was determined to be 0.8 ε_{ij}. This was because at both pressures average deviations were negligible (within uncertainty) from published values. However it was accepted that given the thermal gradient at 10.1325 bar the highest and lowest temperatures were liable to express slight deviations from published values. Despite this the reduced ε_{ij} value provides a much improved correlation with the experimental data.

5.2.3 Argon

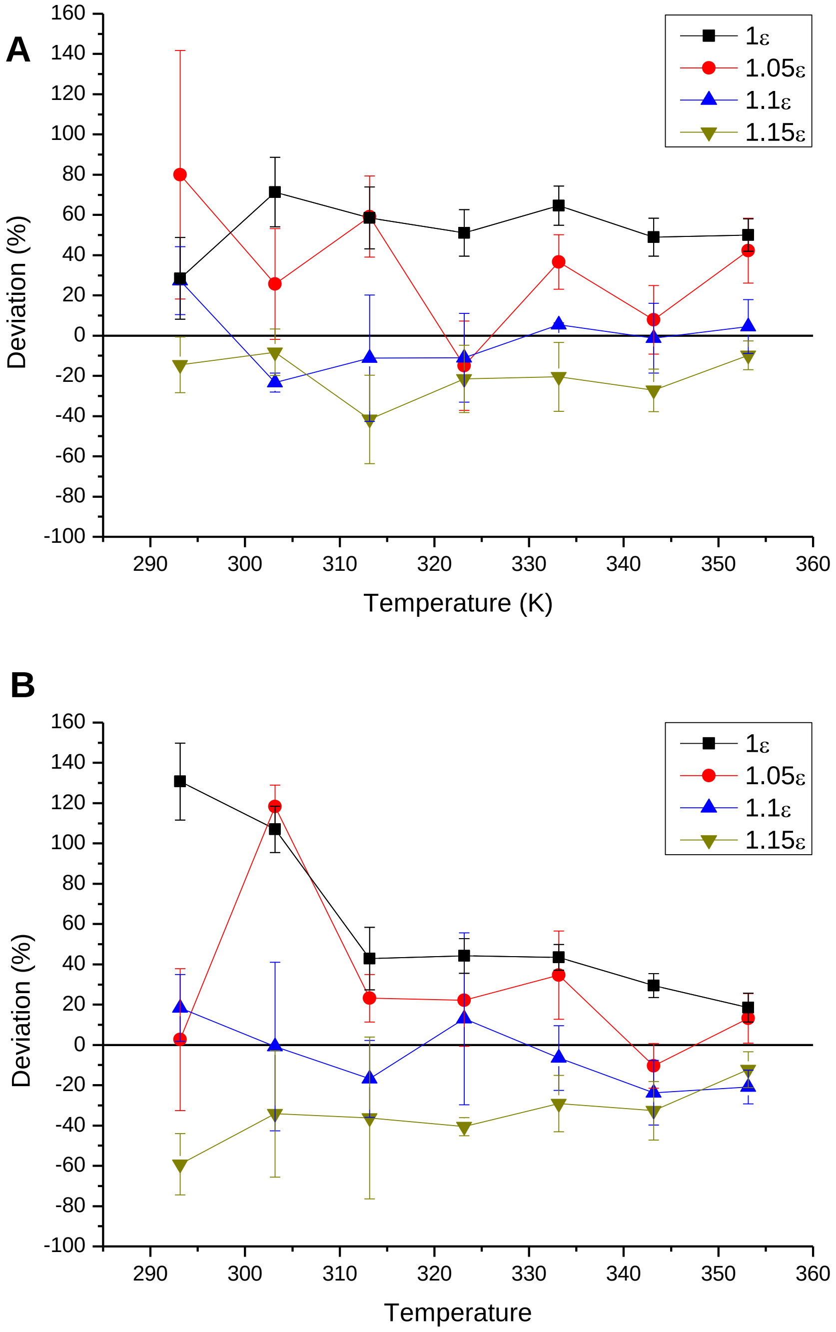

Fig. 5.3. Pure argon-water simulations for different values of ε_{ij}. Results have been presented as deviations from published partitioning coefficients between 293.15 – 353.15 K at (A) 1.01325 bar and (B) 10.1325 bar.

Epsilon scale factor	Average % deviation (1 atm)	Uncertainty (S.E)	Average % deviation (10 atm)	Uncertainty (S.E)
1.00	53.3	13.1	59.5	10.6
1.05	33.8	25.5	29.1	18.0
1.10	-1.4	15.3	-5.3	23.0
1.15	-20.5	14.2	-34.9	18.4

Table 5.3. Average deviations from published partition coefficients at 1.01325 & 10.1325 bar for different values of ε_{ij}. Uncertainty is quoted as standard error. All values are given to 1 decimal place.

In contrast to the lighter noble gases, initial ε_{ij} values produce partition coefficients for argon which are greater than the experimentally determined values. This indicates a lower solubility in the water phase than would be expected. At 1.01325 bar partition coefficients are over-predicted by 53.3% which increases to 59.5% at 10.1325 bar. As expected, the effect of increasing ε_{ij} correlates with an increased affinity between water and argon and so promotes enhanced simulated solubility. This relationship is significantly more sensitive for argon-water when compared to helium or neon. Increasing ε_{ij} by 15% resulted in partition coefficients decreasing by 73.8% and 94.4% at 1.01325 & 10.1325 bar to give negative deviations of -20.5% and -34.9%. As with helium and neon the effect of increasing the system pressure enhanced average solubility of argon. For this noble gas the enhanced pressure-derived solubility effect is predominantly observed for values of ε_{ij} which initially significantly over predict solubility at 1.01325 bar. It is noted though that water phase solubility for the original ε_{ij} value actually decreases slightly. However this change is only minor and within uncertainty of both data points so cannot be considered significant. Unlike neon, the effect of increasing temperature for the higher pressure regime results in no overall discernible change to the partition coefficients. So no thermal trend was observed, even at the higher pressure.

Overall it is clearly demonstrated that by increasing ε_{ij} by a factor of 1.1, average simulated partitioning values predict published partition coefficients within uncertainty. This is thus a significant improvement on initial values. However it is additionally noted that the relative uncertainty is fairly high at both pressures (± 15.3% and ± 23.0% respectively). Reducing this uncertainty therefore may allow for further optimisation in future studies; but at this stage 1.1 ε_{ij} produced reasonable coefficients which replicated published values. This optimisation was demonstrably better than initial values. Therefore this adjusted factor was used for all successive argon-water interactions.

5.2.4 Krypton

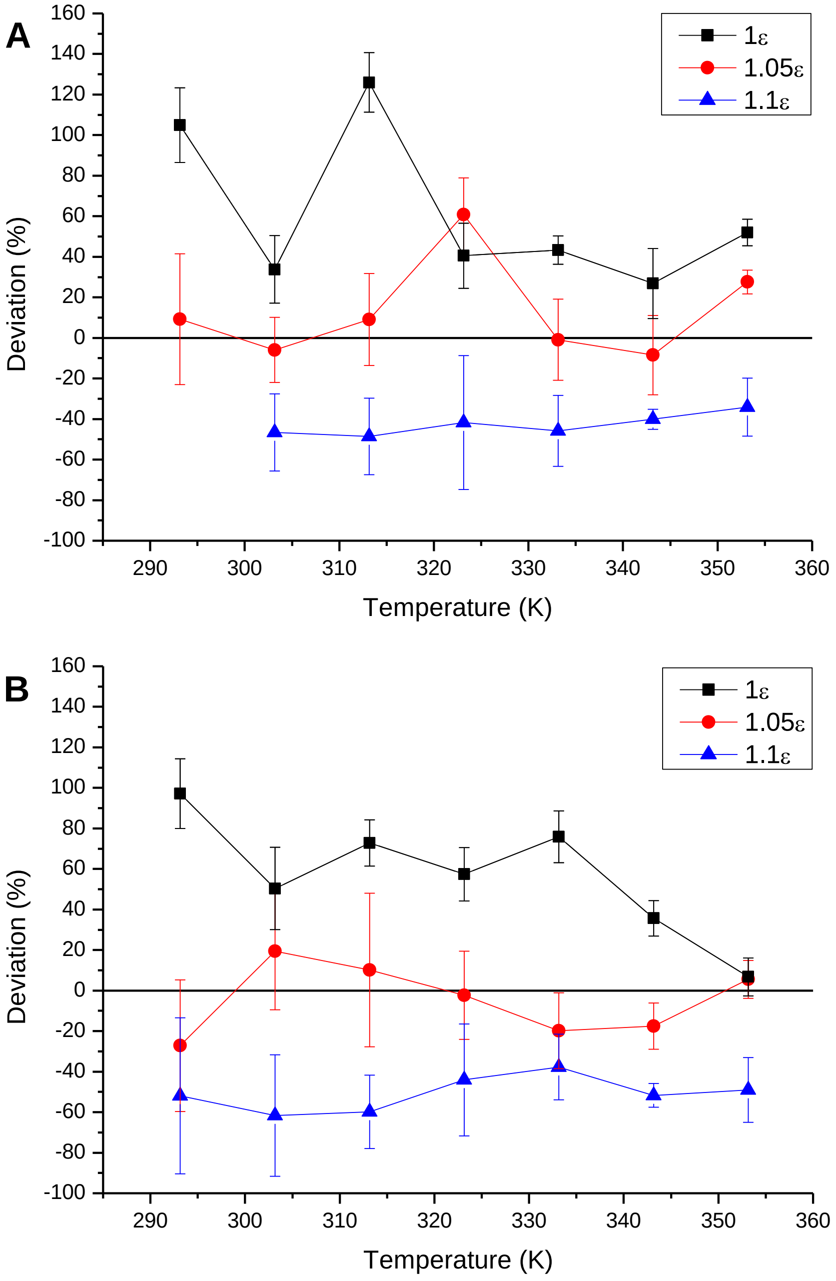

Fig. 5.4. Pure krypton-water simulations for different values of ε_{ij}. Results have been presented as deviations from published partitioning coefficients between 293.15 – 353.15 K at (A) 1.01325 bar and (B) 10.1325 bar.

Epsilon scale factor	Average % deviation (1 atm)	Uncertainty (S.E)	Average % deviation (10 atm)	Uncertainty (S.E)
1.00	61.0	13.8	56.6	13.3
1.05	13.1	19.2	-4.5	22.9
1.10	-36.7	15.4	-50.9	21.8

Table 5.4. Average deviations from published partition coefficients at 1.01325 & 10.1325 bar for different values of ε_{ij}. Uncertainty is quoted as standard error. All values are given to 1 decimal place.

Simulated krypton partition coefficients for the initial value of ε_{ij} were over-predicted by the same order of magnitude as for argon (61.0% at 1.01325 bar and 56.6% at 10.1325 bar). This indicated simulated solubility within the water phase was much lower than had been experimentally determined when this interaction was derived via the Lorentz-Berthelot mixing rules. Although fewer variants of ε_{ij} were simulated the effect of modifying ε_{ij} was still reasonably assessed. The main observation was that changing ε_{ij} affected the partition coefficients to a much greater extent than observed for the lighter noble gases. For example an increase of 10% from the initial ε_{ij} value results in the average partition coefficient deviation changing from 61% and 56.6% to -36.7% and -50.9% at 1.01325 & 10.1325 bar respectively. This resulted in a transgression from an average positive to a negative deviation which indicated solubilities progress from being under-predicted to over-predicted as ε_{ij} is increased. This fits with the expected trends.

For lighter noble gases an increase in pressure has corresponded to an observed enhanced overall solubility. This effect is also observed in krypton. The effect of increasing pressure to 10.1325 bar results in all partition coefficient deviations becoming more negative. This is indicative of an enhanced solubility relative to published values when the pressure is increased. However, due to each data point possessing a significant uncertainty coupled with only 3 variations of ε_{ij}, any trend associated with increasing pressure cannot be absolutely quantified for krypton at this stage. Similarly although the effect of temperature does not visibly affect simulated solubility values compared to experimental values at either 1 or 10.1325 bar this cannot conclusively be stated without further data. The associated uncertainty for krypton is on the same order of magnitude as argon. This similarly introduces a greater ambiguity in the absolute values than for both helium and neon. However due to the lack of any significant overlap in uncertainty for different ε_{ij} values trends can still be discerned. By increasing the ε_{ij} value by 5% the average deviation at both 1.01325 & 10.1325 bar is reconciled within uncertainty to the published values. Thus this modified value of ε_{ij} was applied to all krypton-water interactions. It is recognised though that only three values of ε_{ij} were investigated, all of which possessed a considerable degree of uncertainty. Therefore further refinement of this value remains a future possibility if uncertainties can be sufficiently reduced (6.3).

5.2.5 Xenon

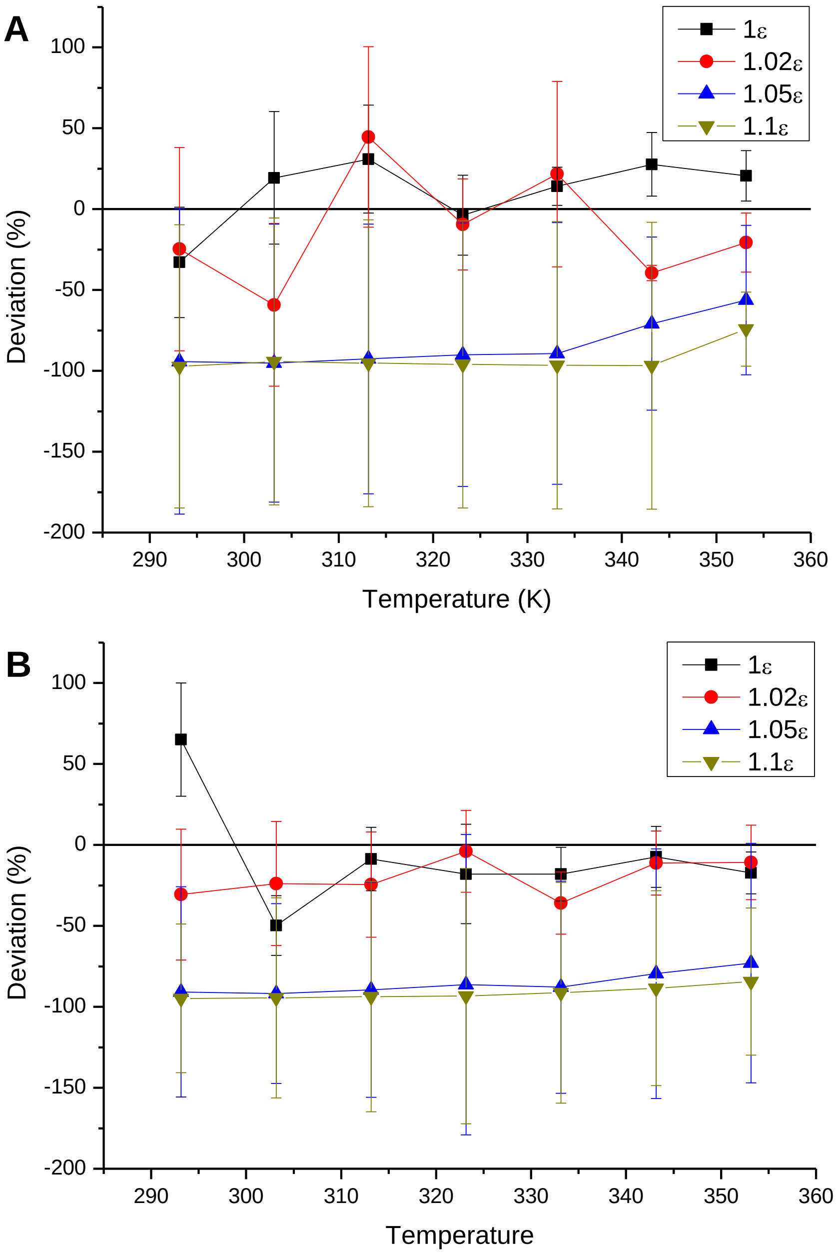

Fig. 5.5. Pure xenon-water simulations for different values of ε_{ij}. Results have been presented as deviations from published partitioning coefficients between 293.15 – 353.15 K at (A) 1.01325 bar and (B) 10.1325 bar. Given the strong deviations of 0.5ε and 2ε at both pressures (Table 5.5) both have been omitted.

Epsilon scale factor	Average % deviation (1 atm)	Uncertainty (S.E)	Average % deviation (10 atm)	Uncertainty (S.E)
0.5	8809.2	24.4	16011.9	25.8
1	10.9	25.8	-7.7	21.7
1.02	-12.5	39.6	-20.1	28.4
1.05	-84.0	75.1	-85.5	70.9
1.1	-92.9	79.2	-91.5	61.6
2	-99.9	4.1	-99.3	3.8

Table 5.5. Average deviations from published partition coefficients at 1.01325 & 10.1325 bar for different values of ε_{ij}. Uncertainty is quoted as standard error. All values are given to 1 decimal place.

The results for the xenon simulations compared to the previous noble gases have a considerable degree of associated ambiguity with them as highlighted by their large uncertainties. This is most likely due to the known difficulties of inserting large molecules into dense phases such as water within GEMC simulations. Despite this elevated level of uncertainty it is still possible to make several key qualitative interpretations from the simulation results. However it is considerably more difficult to fully quantify any such observations. As a consequence reservations should be made on all following absolute values.

Using the initial values of ε_{ij}, average simulated partition coefficients for xenon were higher than their experimental counterparts (10.9% at 1.01325 bar). However the effect of increasing the pressure to 10.1325 bar resulted in lower than expected partition coefficients (-7.7%); but, due to the relatively large uncertainty, both of these values were in agreement with the published values. For other values of ε_{ij} the overall trend of increasing pressure corresponds to a negligible change to relative partitioning values within the uncertainty. It is recognised that this large uncertainty obscures all but the greatest changes to solubilities. One such observation is the high sensitivity to ε_{ij} changes. Compared to the other noble gases xenon can be considered to be highly sensitive to modifications to the ε_{ij} value. Even a slight increase to this value corresponds to dramatic changes to the partition coefficient. For example a 5% increase leads to partition coefficient deviations of -84% and -85.5% for 1.01325 & 10.1325 bar respectively. When this ε_{ij} value is doubled or halved the respective change to partition coefficients is sufficiently large (-99.9% and 8809.2% for 2 ε_{ij} & 0.5 ε_{ij} respectively) that they cannot reasonably be incorporated into Figure 5.5. Given this extreme sensitivity to ε_{ij} changes coupled with the fair initial prediction of partition coefficients it was reasoned that no adjustments to the original ε_{ij} value should be applied at this time. This was in part related to the large underlying uncertainty associated with xenon data points. As obviously only small perturbations of ε_{ij} would be required to reconcile simulation and experiment any such reconciliation in all likelihood would be masked by the uncertainty. Therefore it was concluded further optimisation would only be possible when the uncertainty was significantly reduced. Thus the original values derived from the Lorentz-Berthelot mixing rule were used for the duration of this project.

5.2.6 Overall pressure trends

Although the initial ε_{ij} values generate passable partition coefficients there is a marked discrepancy between the experimental and simulated datasets for all noble gases except xenon. The partition coefficients of the two lightest noble gases (i.e. helium and neon) are consistently under-predicted over the temperature-pressure regime. Neon values were most affected (-15.2% & -21.5% compared to -6.8% & -12.3% for helium at 1.01325 & 10.1325 bar). The partition coefficients of argon and krypton on the other hand were consistently over-predicted when compared to their experimental counterparts. Both of these heavier noble gases possess similar positive deviations at both pressures (53.3% & 59.5% for argon and 61.0% & 56.6% for krypton at 1.01325 & 10.1325 bar). Average partition coefficients for xenon were slightly over-predicted at 1.01325 bar but slightly under-predicted at 10.1325 bar. However, given the magnitude of the uncertainty associated with xenon (averages: ± 25.8 & ± 21.7) coupled with the relatively small average deviations from expected values (10.9% & -7.7%), it is presently impossible to definitively state whether solubility is over or under-predicted at either pressure.

For helium, neon, argon and krypton the effect of increasing the pressure from 1.01325 bar to 10.1325 bar led to an apparent decrease of average partition coefficients. For most values of ε_{ij} this produced an increase in noble gas solubility within the water phase which was greater than predicted assuming Henry's law. Therefore a potential enhanced solubility effect as a function of pressure was observed. This change however is small enough to fall within the average uncertainty for most cases. Thus this change cannot be conclusively attributed solely to the increase in pressure. Instead it could simply be due to the distribution of average points within the data. However it is also noted that this observation is valid for 17 out of the 19 values of ε_{ij} for these four noble gases; so it is likely that there is at least some pressure related enhanced solubility, even if it is relatively small and mostly within uncertainty. To fully quantify this though further work would be required.

No specific cause of any pressure-derived enhanced solubility effect can be explicitly determined at this time. The most probable explanation for this is related to imperfect noble gas-water parameters. Where these interactions are poorly constrained elevating the pressure is likely to exacerbate the difference between simulation and experimental. Additionally unexpected thermal trends are likely to be present under these circumstances. This further reinforces the need for better unlike pair potentials for these simulations.

5.2.7 Thermal trends

For the majority of the noble gas simulations no observable thermal trends exist within the dataset. This indicates deviations from partitioning are largely independent of temperature. A possible slight thermal gradient though was noted for neon, and to a lesser extent helium, at 10.1325 bar. This indicated a decrease in simulated partition coefficients greater than expected from published data. However all gradients under these conditions lay within uncertainty so could not be conclusively determined. Although a minor thermal effect may be present for these lighter noble gases at elevated pressures, the magnitude of this is low and so was considered for all intents and purposes, negligible.

It is recognised though that when simulating at higher pressures it is possible that a thermal gradient within the deviations may be more pronounced. This is indicated by neon at 10.1325 bar. This may either be a legitimate trend which occurs at higher pressures or simply be due to the interactions being poorly constrained. However as this trend is not convincingly observed for any other optimised noble gas-water ε_{ij} value it is presently considered to be due to a poor noble gas-water interaction. Consequentially any thermal trends within the simulations are determined to be symptomatic of poorly constrained interactions becoming apparent at high pressure.

5.2.8 Responsivity to scaling potentials

Changing ε_{ij} clearly affected the simulated partition coefficients. In all cases except helium increasing ε_{ij} resulted in reduced partition coefficients while reducing them led to higher partition coefficients. However the responsivity of each noble gas was unique. When the original ε_{ij} value was changed proportionally, the effect on simulated partition coefficients became greater as the noble gas became heavier. For example the effect of increasing the original ε_{ij} value by 5% resulted in deviations changing for 1.01325 &

10.1325 bar by 19.5% and 30.4% for argon. 48.0% and 68.1% for krypton and 94.9% and 77.9% for xenon. However the initial ε_{ij} values were also greatest for xenon and least for argon. Therefore the increase in absolute terms to this potential was greatest for xenon. So this seemingly higher response to ε_{ij} changes could simply be due to an increased total change in the potential. When the changes are written as absolute values in the example given, the 5% increase in ε_{ij} for argon is 5.3 °K, 6.3 °K for krypton and 7.4 °K for xenon. When the respective changes in deviation are divided by these absolute values the responsivity as a function of absolute change to ε_{ij} is derived. At 1.01325 & 10.1325 bar these are 3.7%/°K and 5.7%/°K for argon, 7.7%/°K and 9.8%/°K for krypton and 12.8%/°K and 10.8%/°K for xenon. Similar absolute trends are noted for all other changes to ε_{ij} values. Therefore it is concluded that the heavier the noble gas the more responsive to both relative and absolute changes to the ε_{ij} value.

5.2.9 Optimisation summary

Due to the initial over-prediction of solubilities of both helium and neon compared to published values these were chosen for ε_{ij} reduction. With neon, successive reductions in ε_{ij} resulted in expected progressive reductions in solubilities at both pressures. This therefore increasingly reconciled the partition coefficients with their experimental counterparts. The scaled down value at which simulated solubility correlated best with experimental values was at 0.80 ε_{ij}. At this point the average deviations were 4.8% ± 6.6 at 1.01325 bar and 3.2% ± 7.1 at 10.1325 bar.

The same change in partition coefficients was not observed for helium when reducing ε_{ij}. Instead it was observed that initial reductions (0.95 ε_{ij}) resulted in a negligible change in helium solubility. Although further decreases (0.91 ε_{ij}) did result in a minor decrease in solubilities this was still within uncertainty of the initial solubility. After this point a further decrease to ε_{ij} resulted in lower partition coefficients and greater solubilities. This trend was the opposite of what was expected. To ensure these trends were real and not apparent, simulations were run at both 0.5 ε_{ij} and 2 ε_{ij}. The results of both produced solubilities greater than were generated for 1 ε_{ij}. This was more pronounced in the case of 2 ε_{ij} where average deviations of partition coefficients were -45.4% and -46.6% for 1.01325 & 10.1325 bar respectively. The deviations for 0.5 ε_{ij} although not as large were still significant (-14% & -20.9%).

Presently it is not fully understood why helium alone did not follow the expected pattern for changes to ε_{ij}. It is suspected that the initial values of ε_{ij} were already so low (i.e. the noble gas-water interactions are weak) that any decreases to this did not have any major effect on reducing solubility. However due to the nature of the Lennard-Jones 12 – 6 parameter (3.2.1) reducing the ε_{ij} value will decrease the potential energy of the cumulative Lennard-Jones forces as a function of r (Equation 3.1). The overall effect of this would lower the energy required for positioning helium atoms closer to the water molecules. This in turn would promote helium solubility within the water phase, despite the existence of a lower potential. This could explain the observed increase in solubility when ε_{ij} was reduced by 50%. However this causal mechanism is highly speculative and will require future investigation. Given that in the case of helium, 0.91 ε_{ij} provided the best agreement with the published values at both pressures this was selected as the optimal value out of those investigated. Nevertheless it was accepted that this good agreement was within uncertainty of 1 ε_{ij} and so may not represent a significant improvement over the initial value.

Due to the lower than expected solubilities of argon and krypton these values were progressively increased to enhance solubility within the water phase. As expected an increase in ε_{ij} corresponded with an increased solubility with predictions exceeding experimental values between increases of 5% and 10% ε_{ij} for both argon and krypton. The most suitable value of ε_{ij} from the simulations was at 1.1 ε_{ij} for argon and 1.05 ε_{ij} for krypton. These values produced the lowest deviations from published partition coefficients. These deviations at 1.01325 & 10.1325 bar were -1.4% and -5.3% for argon and 13.1% and -4.5% for krypton. Given the increased average uncertainty compared to helium or neon it was accepted that the effect of small changes to the ε_{ij} value would be hard to discern. Therefore until a feasible method to reduce the uncertainty was presented it was determined that no further iterative improvement to either ε_{ij} value was possible. The reason for this high uncertainty was related to the issue of inserting larger molecules into a dense phase (3.3.5). No universally accepted method of resolving this currently exists.

Due to the issues with xenon and the large associated uncertainty it was difficult to discern what, if any, alteration to ε_{ij} was needed. However as its closest two analogues, argon and krypton, required an increase of ε_{ij} based on their under-solubility at 1.01325 bar it was decided to predominantly focus on increasing ε_{ij} to assess the affect this had on average solubility. As before, increasing ε_{ij} led to an increase in solubility; the magnitude of the change, however, was significantly greater. An increase of 5% resulted in the partition coefficient deviations changing from 10.9% to -84% at 1.01325 bar and further increases resulted in extremely enhanced solubilities. Even a slight increase of 2% led to much lower than published partition coefficients. As expected a reduction of the ε_{ij} value corresponded to a strong decrease in solubility when compared to experimental values. However given the strong effect changing ε_{ij} has on solubility coupled with the reasonable initial prediction of solubility within the large uncertainty it was determined that the initial xenon-water interaction was most suitable for use under these circumstances. Optimising this interaction therefore will require addressing in the future (6.3).

Table 5.6 summarises the optimal noble gas-water ε_{ij} values as defined from this optimisation process.

Noble gas	Scaling ε_{ij} factor	Optimised ε_{ij} (°K)	σ (Å)
Helium	0.91	26.419	3.067
Neon	0.80	45.983	3.127
Argon	1.10	116.402	3.463
Krypton	1.05	131.278	3.589
Xenon	1.00	148.590	3.765

Table 5.6. Optimised value for ε between noble gas and oxygen atom on water molecule (O_w). Scaled ε_{ij} refers to the factor change from the initial unlike potential calculated via the Lorentz-Berthelot mixing rules. Values are given to three decimal places.

5.2.10 Comments on the optimising process

From both previous studies (e.g. Delhommelle & Millie, 2001; Song *et al.*, 2003; Boda & Henderson, 2008; Forsman & Woodward, 2010) and the GEMC simulation solubility data in this study it has been proven that the Lorentz-Berthelot combining rules are frequently inadequate for generating unlike Lennard-Jones 6 – 12 potentials between unlike atoms. As a result an iterative method of adjusting the initial Lorentz-Berthelot derived ε_{ij} values for noble gas-water interactions was applied to reconcile simulation results with the experimental dataset. By increasing ε_{ij} solubility was enhanced while a decrease in ε_{ij} corresponded to lower solubilities. Thus the ε_{ij} for each noble gas were progressively adjusted to increase or decrease solubilities accordingly. This approach created new noble gas-water Lennard-Jones pair potentials which significantly improved simulated solubilities of all noble gases except xenon for which the original values were kept.

Given the range of potential application of the noble gases it is likely that simulations including them as a key component will occur more frequently in the foreseeable future. The creation of these improved potentials will lead to an increase in the accuracy for all simulated noble gas-water interactions within such systems. As a consequence a greater degree of confidence can be assumed when simulating conditions beyond experimentally determined pressure and temperature regimes. Although further iteration would result in even better agreement between simulated and experimental the current limitation is the degree of uncertainty associated with the heavier noble gas molecules. It is this which first requires attention before the new noble gas-water pair potentials proposed here can be further iteratively improved. Possible ways of achieving this involve running the simulation for longer to reduce the statistical uncertainty, increasing the probability of insertion or reducing the total system size.

Despite this recognised limitation this optimisation process provided much better unlike parameters between water and noble gas molecules which could then be used for the next stage of model development (6.3).

5.3 Noble gas partitioning within gaseous CO_2-water systems

From the optimisation process noble gas-water Lennard-Jones ε_{ij} values were identified which allowed published partitioning to be suitably reproduced by Towhee. These were derived via pure noble gas phases interacting with a water phase. However such an approach could not be used to derive partition coefficients from a simulated binary phase CO_2-water system. Instead partition coefficients were generated by calculating the chemical potential of noble gases in each phase (3.6.3). It was imperative therefore that this approach was proven to accurately generate partition coefficients. Therefore a binary CO_2-water system was simulated at 1.01325 & 10.1325 bar between 293.15 – 353.15 K. Partitioning of each noble gas within these systems was determined via this chemical potential method (3.7.2). The optimised ε_{ij} values (Table 5.6) were used for noble-gas water interactions.

Under these simulated conditions noble gas partitioning is expected to remain accurately defined by the existing published data set (Crovetto *et al.*, 1982; Smith, 1985). Thus an assessment could be made on the application of the chemical potential approach in deriving partition coefficients.

Additionally unoptimised ε_{ij} values were simulated using the above method. This served as a means to assess whether optimised values remained superior at predicting partitioning within this new environment. These are presented graphically and averages for each run are tabulated and follow each respective graph. Also included are the optimised ε_{ij} values from the pure phase simulations (5.2) to assess the effect, if any changing the methodology and binary phase composition has on partition coefficients. As with pure phase interactions all results are presented in terms of deviation from the published dataset. Average deviations for each simulation type were calculated over the thermal range to allow simple assessment of simulated values in terms of their experimental counterparts. Individual deviation values are provided in Appendix III.

5.3.1 Helium

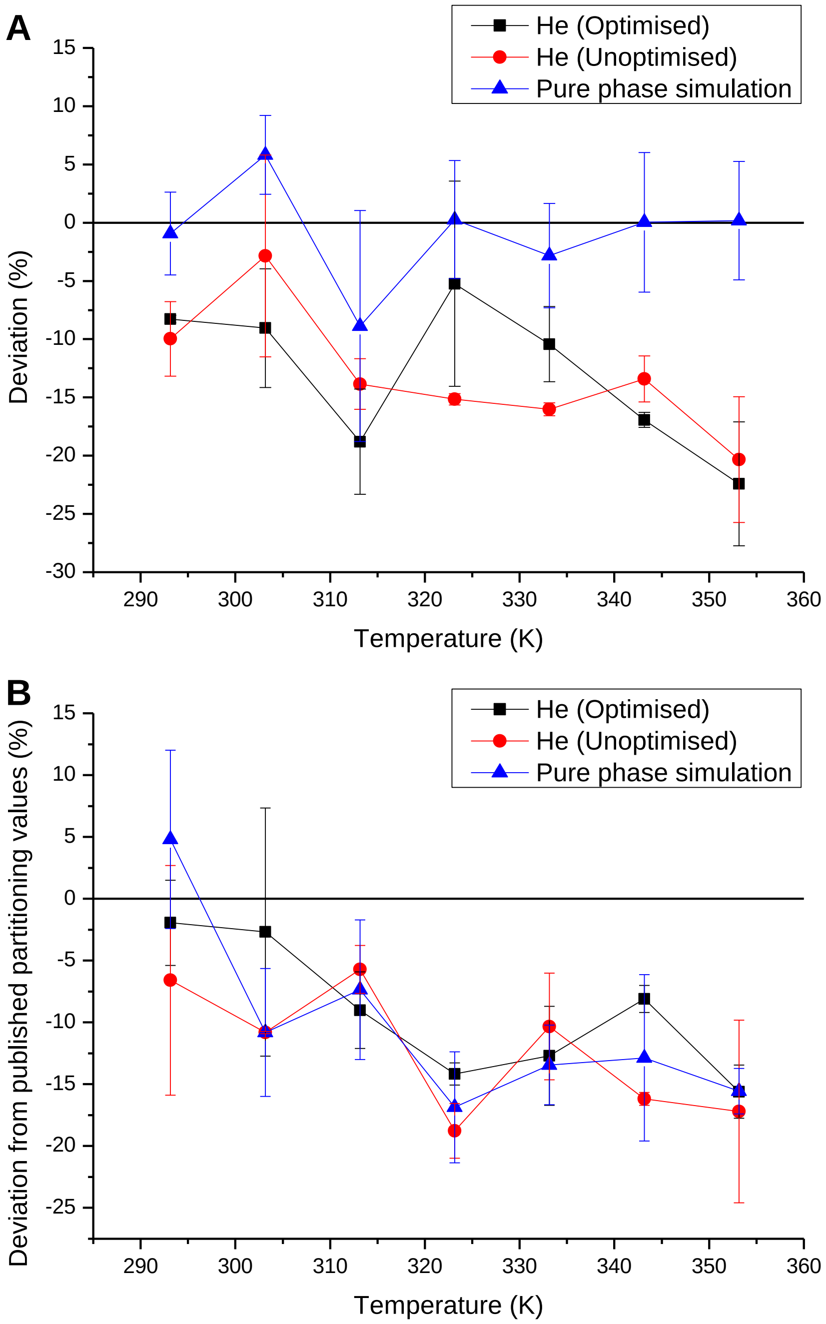

Fig. 5.6. Comparison of optimised and unoptimised values of ε_{ij} for helium partition coefficients generated within CO_2-water system. Results have been presented as deviations from published partitioning coefficients between 293.15 – 353.15 K at (A) 1.01325 bar and (B) 10.1325 bar. Optimised values from pure helium-water simulations are also plotted for comparison.

Epsilon scale factor	Average % deviation (1 atm)	Uncertainty (S.E)	Average % deviation (10 atm)	Uncertainty (S.E)
Optimised (0.91 ε)	-13.0	4.0	-9.2	3.5
Unoptimised (1 ε)	-13.1	3.2	-12.2	3.7
He-water (0.91 ε)	-0.9	5.4	-10.3	4.9

Table 5.7. Average deviations from published helium partition coefficients for optimised and unoptimised values of ε_{ij}. Partition coefficients were generated within a CO_2-water system between 293.15 – 353.15 K at 1.01325 & 10.1325 bar via the chemical potential approach. Optimised pure helium-water values are reproduced. Uncertainty is quoted as standard error. All values are given to 1 decimal place.

At 1.01325 bar, when compared to the pure phase results, the partition coefficient of the optimised value (-13.0%) was both lower than expected and indistinguishable from unoptimised values (-13.1%). This lack of significant improvement of the optimised value over the unoptimised value had already been observed during the previous optimisation process (5.2.1). These average values within the CO_2-water were lower than had been observed when simulating the pure phase system using the same pair potentials. Therefore the effect of the CO_2 phase and/or using the chemical potential approach resulted in greater overall solubilities in water when compared to the pure noble gas-water simulations. The effect of simulating at higher pressure corresponded to no change in either optimised or unoptimised average values within the CO_2-water system which remained lower than expected. However this reconciled the values with the pure helium-water system as partition coefficients were reduced under these conditions. Therefore at the higher pressures all helium simulations over-predicted solubility of helium within the water phase to a similar degree.

Overall, compared to the pure phase simulations, average partition coefficients for the optimised values were slightly less concordant with the published values. However this was only expressed at 1.01325 bar; at 10.1325 bar both indicated a similar degree of lower than expected partition coefficients. Additionally the optimised values did not result in significantly different deviations from their unoptimised counterparts. Due to the low change in solubility as a function of changing ε_{ij} this was expected. It was therefore determined that for helium, the optimised ε_{ij} values reasonably replicated expected partition coefficients. However it is acknowledged that given the inability to fully reconcile simulated and experimental partitioning a minor discrepancy is being incorporated into the model. Thus an alternative optimisation approach may be required in the future; but this discrepancy is relatively low and should not significantly interfere with observed experimental trends. Therefore despite this issue helium was considered suitable for application to the experimental pressures and temperatures investigated in this project.

5.3.2 Neon

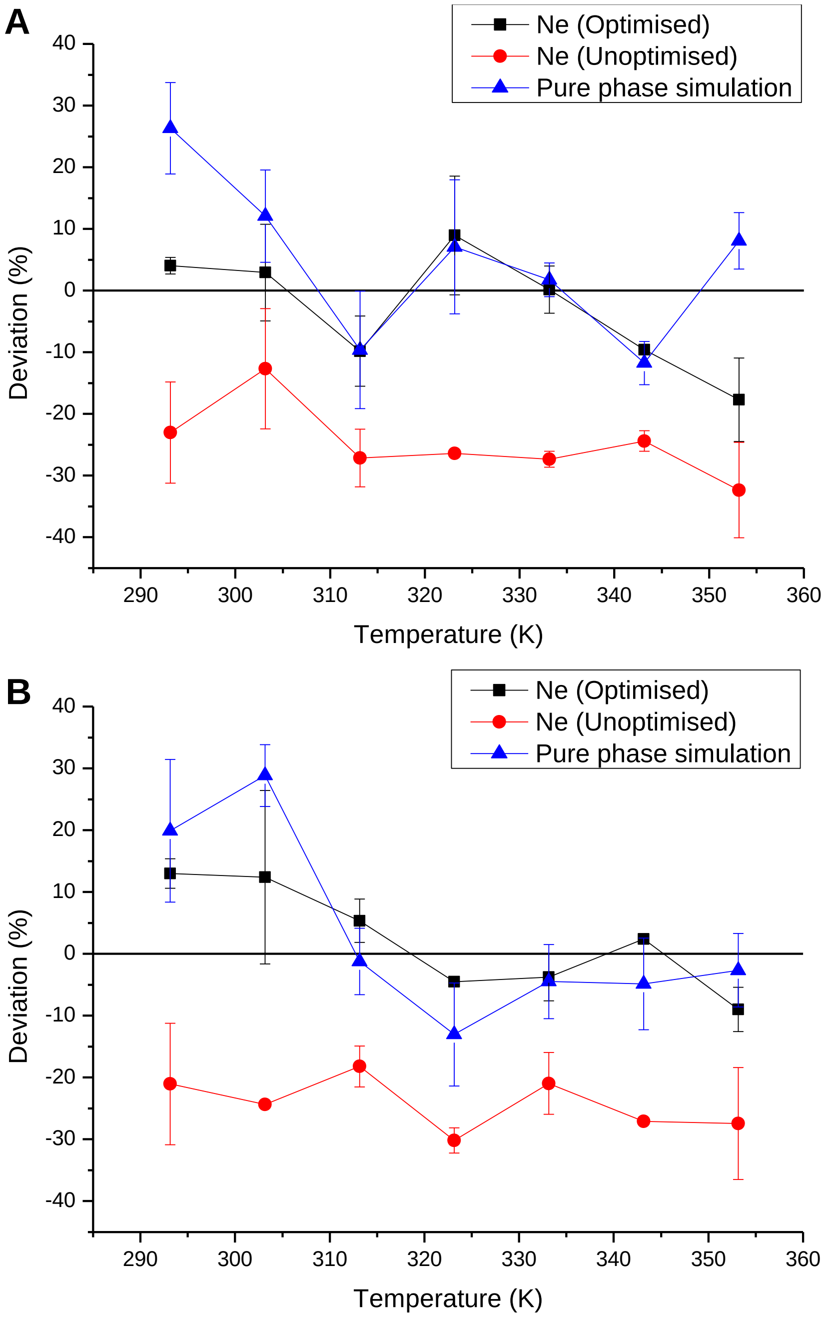

Fig. 5.7. Comparison of optimised and unoptimised values of ε_{ij} for neon partition coefficients generated within CO_2-water system. Results have been presented as deviations from published partitioning coefficients between 293.15 – 353.15 K at (A) 1.01325 bar and (B) 10.1325 bar. Optimised values from pure neon-water simulations are also plotted for comparison.

Epsilon scale factor	Average % deviation (1 atm)	Uncertainty (S.E)	Average % deviation (10 atm)	Uncertainty (S.E)
Optimised (0.8 ε)	-3.0	5.1	2.3	4.0
Unoptimised (1 ε)	-24.8	4.8	-24.2	4.3
Ne-water (0.8 ε)	4.9	6.6	3.2	7.1

Table 5.8. Average deviations from published neon partition coefficients for optimised and unoptimised values of ε_{ij}. Partition coefficients were generated within a CO_2-water system between 293.15 – 353.15 K at 1.01325 & 10.1325 bar via the chemical potential approach. Optimised pure neon-water values are reproduced. Uncertainty is quoted as standard error. All values are given to 1 decimal place.

In the case of neon it is clear that the same degree of accuracy is attained by the chemical potential approach. Average deviations produced from pure phase partition coefficients at both pressures (4.9% and 3.2%) were reproduced within uncertainty using this alternative method of generating partition coefficients (-3.0% and 2.3%). Additionally these values remained in good agreement with published values. Thus these optimised potentials also maintained a good overall fit to experimental values within uncertainty. When compared to the unoptimised potentials, also simulated for comparison, average neon solubilities from the optimised potentials were again far improved for all temperatures at both pressures.

In conclusion neon solubilities derived using the chemical potential approach still closely replicated simulated solubility within the pure phase systems and therefore still accurately replicated published values. This indicated that valid partition coefficients were being generated by using the optimised unlike potentials in conjunction with the chemical potential approach. As a consequence this method was considered suitable for simulating the experimental high pressure systems.

5.3.3 Argon

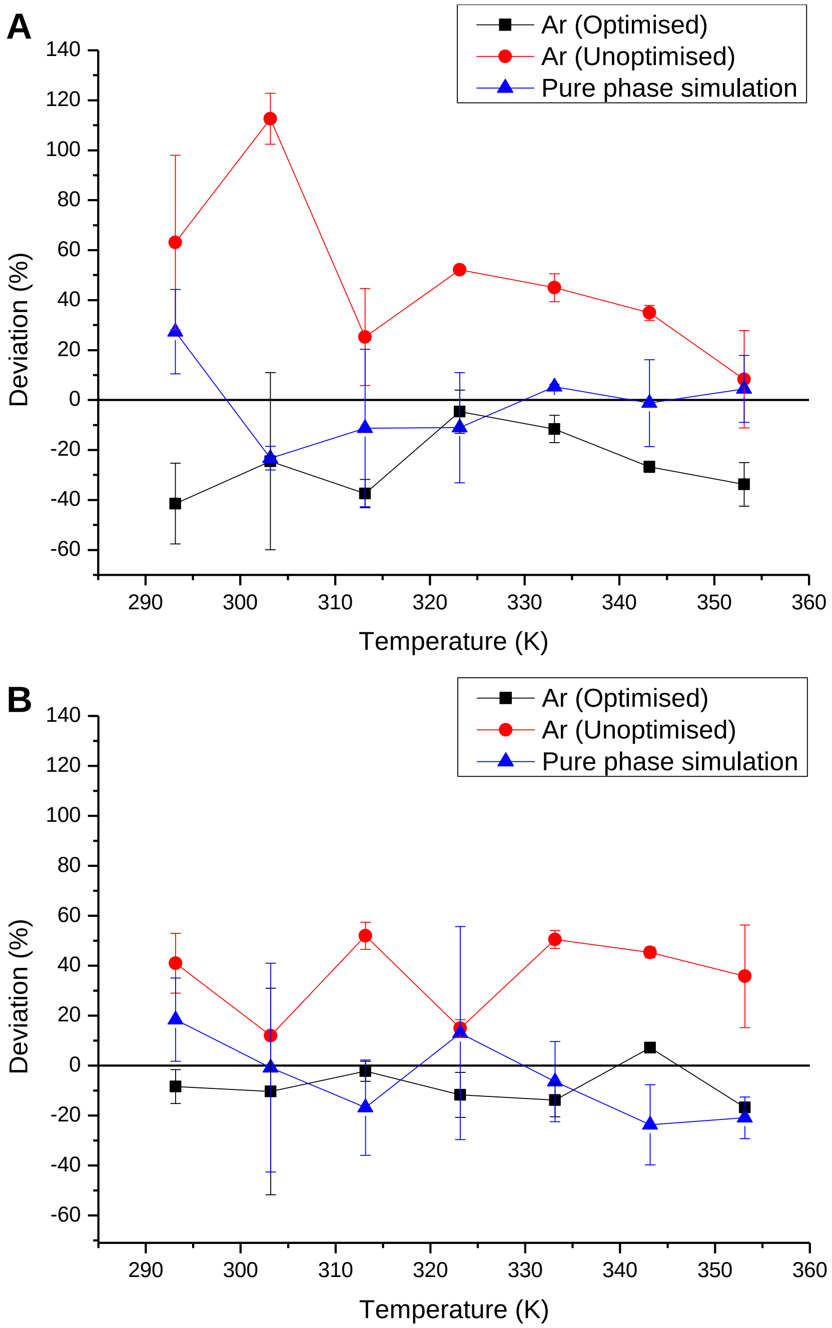

Fig. 5.8. Comparison of optimised and unoptimised values of ε_{ij} for argon partition coefficients generated within CO_2-water system. Results have been presented as deviations from published partitioning coefficients between 293.15 – 353.15 K at (A) 1.01325 bar and (B) 10.1325 bar. Optimised values from pure argon-water simulations are also plotted for comparison.

Epsilon scale factor	Average % deviation (1 atm)	Uncertainty (S.E)	Average % deviation (10 atm)	Uncertainty (S.E)
Optimised (1.1 ε)	-25.7	11.7	-8.0	9.8
Unoptimised (1 ε)	48.8	13.3	35.9	6.8
Ar-water (1.1 ε)	-1.4	15.3	-5.3	23.0

Table 5.9. Average deviations from published argon partition coefficients for optimised and unoptimised values of ε_{ij}. Partition coefficients were generated within a CO_2-water system between 293.15 – 353.15 K at 1.01325 & 10.1325 bar via the chemical potential approach. Optimised pure argon-water values are reproduced. Uncertainty is quoted as standard error. All values are given to 1 decimal place.

For argon the improved potentials were predicting partitioning coefficients to a greater degree of accuracy within a CO_2-water system when compared with their unoptimised counterparts. The unoptimised values consistently over-predicted partition coefficients at both pressures, relative to published values (48.8% and 35.9%). At 10.1325 bar a reasonable agreement was reached between pure phase and chemical potential simulations. However at 1.01325 bar the optimised values under-predicted the partition coefficients by -25.7% which was not observed for the pure phase counterpart. This was a possible indication that the chemical potential approach resulted in a slightly lower accuracy at low pressures. However, even with this taken into account the magnitude of average deviation is still considerably lower than the unoptimised values, especially at the higher pressure regime. This strongly indicates that they remain better potentials. Therefore, although it was recognised that future iterative refinement would improve these potentials further, at this stage of model development (6.3) they were acceptable for application to high-pressure CO_2-water systems.

5.3.4 Krypton

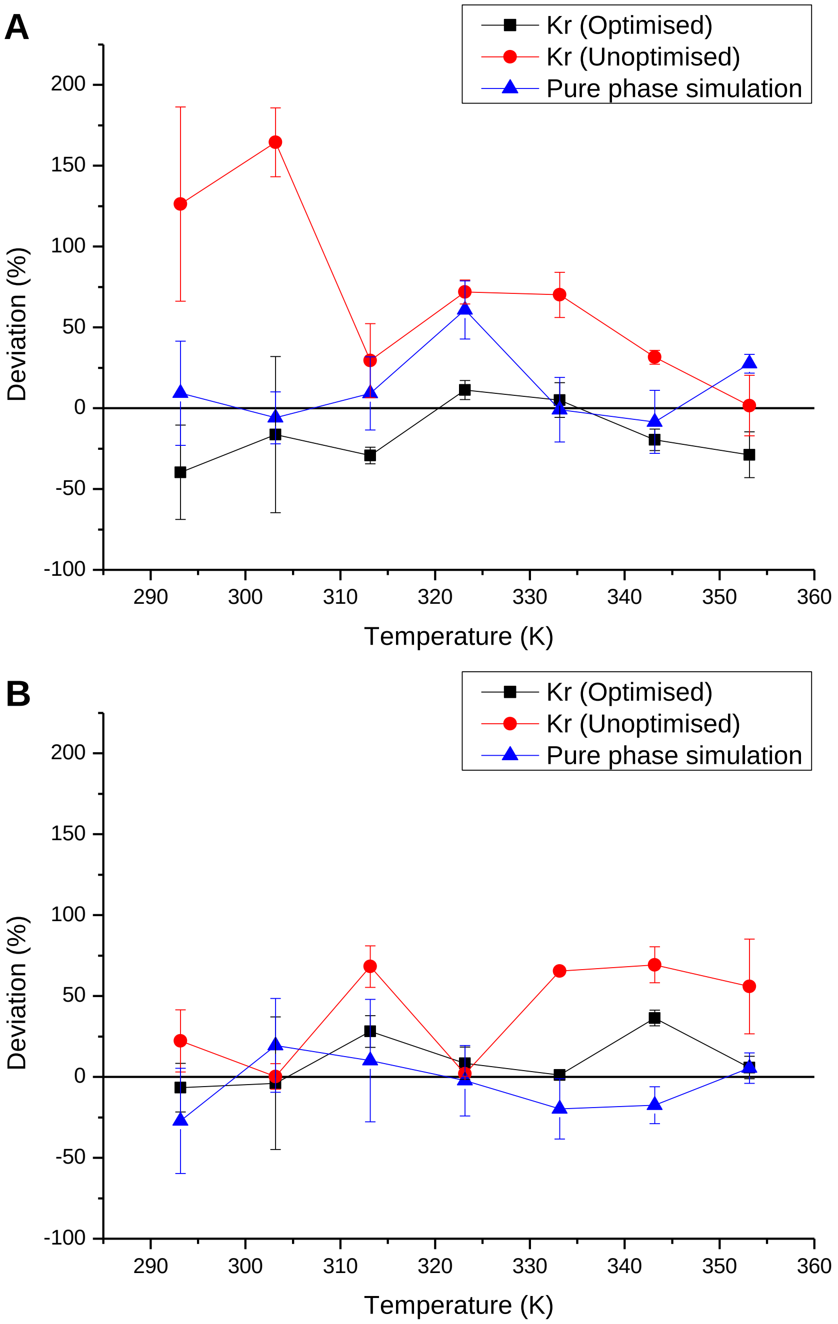

Fig. 5.9. Comparison of optimised and unoptimised values of ε_{ij} for krypton partition coefficients generated within CO_2-water system. Results have been presented as deviations from published partitioning coefficients between 293.15 – 353.15 K at (A) 1.01325 bar and (B) 10.1325 bar. Optimised values from pure krypton-water simulations are also plotted for comparison.

Epsilon scale factor	Average % deviation (1 atm)	Uncertainty (S.E)	Average % deviation (10 atm)	Uncertainty (S.E)
Optimised (1.05 ε)	-16.8	17.2	9.9	12.7
Unoptimised (1 ε)	70.8	21.2	40.5	11.8
Kr-water (1.05 ε)	13.1	19.2	-4.5	22.9

Table 5.10. Average deviations from published krypton partition coefficients for optimised and unoptimised values of ε_{ij}. Partition coefficients were generated within a CO_2-water system between 293.15 – 353.15 K at 1.01325 & 10.1325 bar via the chemical potential approach. Optimised pure krypton-water values are reproduced. Uncertainty is quoted as standard error. All values are given to 1 decimal place.

The simulation of krypton within a CO_2-water binary phase system also generated reasonable partition coefficients. The average optimised values at both 1.01325 & 10.1325 bar replicated pure phase optimised values predicted published coefficients within uncertainty.

In contrast the unoptimised values poorly predicted partitioning; average deviations of 70.8% and 40.5% were observed at 1.01325 & 10.1325 bar. Therefore, as with neon and argon, the optimised values clearly produce better partition coefficients within a CO_2-water system which agree well with experimental values. It is accepted that this agreement could in part be due to the level of uncertainty associated with the data. Therefore further optimisation may be possible by reducing this uncertainty for a better assessment of how well published values are being replicated. However given that such a process would require significant computational time this current optimised value was considered reasonable for application to high pressure systems. This possible additional optimisation therefore is indicated as future work (6.3).

5.3.5 Xenon

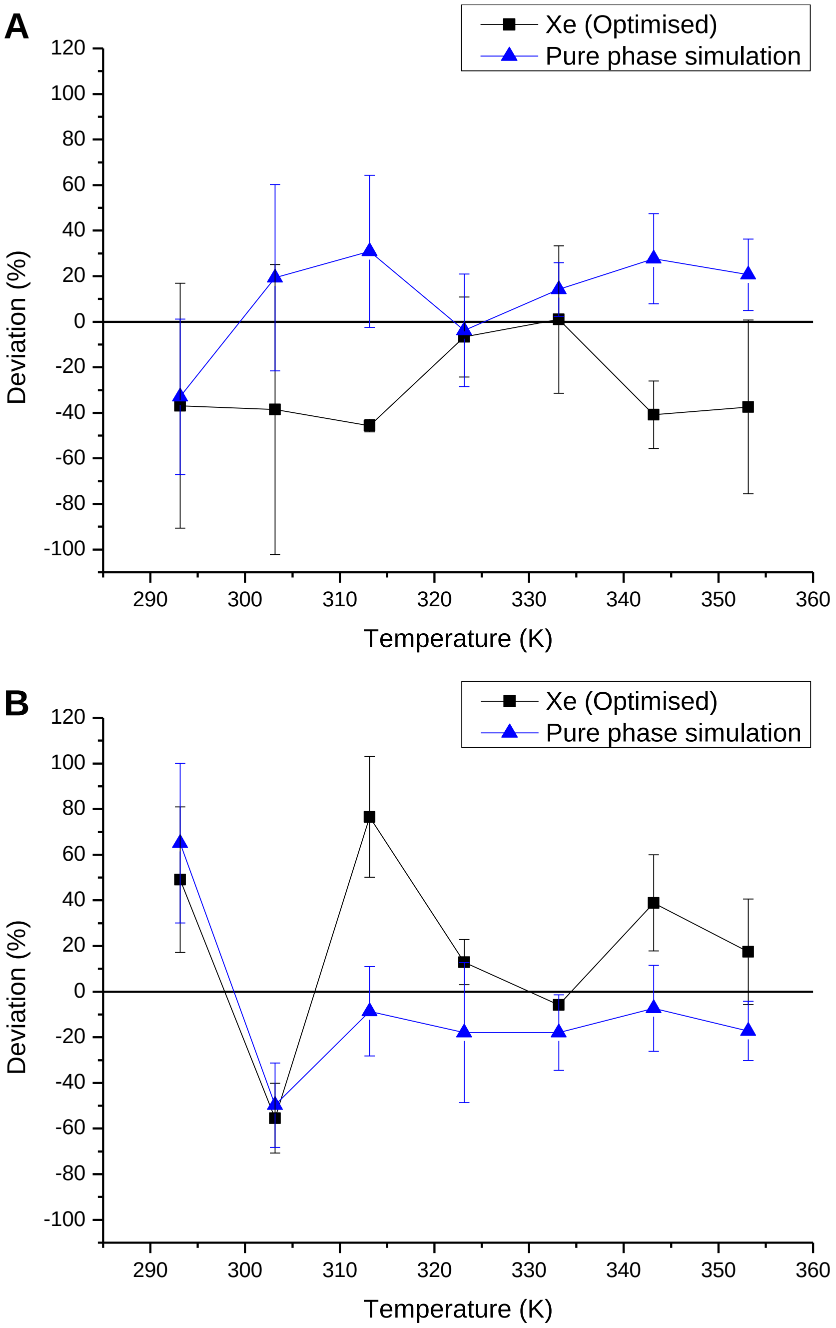

Fig. 5.10. Comparison of xenon partition coefficients generated within CO_2-water system with partition coefficients generated from optimised pure xenon-water simulations. Results have been presented as deviations from published partitioning coefficients between 293.15 – 353.15 K at (A) 1.01325 bar and (B) 10.1325 bar.

Epsilon scale factor	Average % deviation (1 atm)	Uncertainty (S.E)	Average % deviation (10 atm)	Uncertainty (S.E)
Unoptimised (1 ε)	-29.3	31.9	19.1	18.4
Xe-water (1 ε)	10.9	25.8	-7.7	21.7

Table 5.11. Average deviations from published partition coefficients for xenon. Partition coefficients were generated within a CO_2-water system between 293.15 – 353.15 K at 1.01325 & 10.1325 bar via the chemical potential approach. Pure xenon-water values are also reproduced. Uncertainty is quoted as standard error. All values are given to 1 decimal place.

In contrast to the other noble gases the xenon-water potential was not changed from its Lorentz-Berthelot value. This was due to the large degree of uncertainty associated with xenon coupled with an extreme sensitivity. Consequentially only 1 ε_{ij} was simulated and compared to the pure phase results. From the chemical potential results a high variability and uncertainty was expressed within the data set. The deviations ranged between -45.6% and 1.0% at 1.01325 bar and -55.5% and 76.6% at 10.1325 bar and the greatest uncertainties observed at 1.01325 and 10.1325 bar were ± 63.6% and ± 31.9% respectively. Additionally it was observed that at 1.01325 bar partition coefficients were generally under-predicted (average -29.3%), while at 10.1325 bar partition coefficients were over-predicted (average 19.1%). However when the associated uncertainty is considered (± 31.9 and ± 18.4) a good agreement is reached with published values. This agreement however is likely in part to be due to this large uncertainty. As with krypton therefore the possibility for future improvement of this potential exists if methods to reduce the uncertainty are implemented (6.3). Although the variation and the uncertainty were significantly large for this noble gas it was still considered useful to apply these values to the high pressure samples. This is because even with this large margin of variability, given the magnitude of the observed trends for xenon (Chapter 4), the experimental trends should still be evident within their simulation counterparts.

5.3.6 Summary of the chemical potential approach

Although slight discrepancies were observed when changing from pure noble gas systems to chemical potential insertion a good agreement was observed between the optimised values and the published values. Thus the validity of this technique was confirmed. Additionally for neon, argon and krypton the optimised values produced partition coefficients which remained in agreement with the published values, in contrast to their unoptimised counterparts. This overall good agreement served as additional confirmation of the overall superiority the optimised values possess in determining partition coefficients. For helium no significant improvement was observed although the accuracy was still comparable to the pure helium-water simulations. Xenon similarly reasonably predicted partitioning although this is likely to in part be a function of the high uncertainty which remains an outstanding issue at this time.

In summary this testing stage confirmed that accurate partitioning within a CO_2-water binary phase system was possible for each noble gas using the optimised values in conjunction with the chemical potential approach. It was therefore considered viable to simulate the experimental aspect of this project to attempt to replicate the density-derived deviation from published values. This therefore would allow an assessment of the accuracy of the model for predicting partition coefficients under conditions expected within CCS storage sites.

5.4 Testing model under experimental conditions

The previous sections documented the process of developing a modelling technique which had a proven ability to predict partition coefficients for each noble gas within a CO_2-water system. Thus a model was available which could be used to predict noble gas partitioning within supercritical CO_2-water systems. The optimised noble gas-water pair potentials and the chemical potential approach provided a means of generating reasonable partition coefficients for low pressure CO_2 systems. The next stage of model testing therefore was to replicate the experimental conditions investigated in this project and assess how close to agreement the different methods for generating partition coefficients were. These results are presented alongside their experimental counterparts for comparison of deviation as a function of density. Absolute values alongside CO_2-water mutual phase solubility data are provided in Tables AIV.1 and AIV.2 in Appendix IV.

5.4.1 Helium

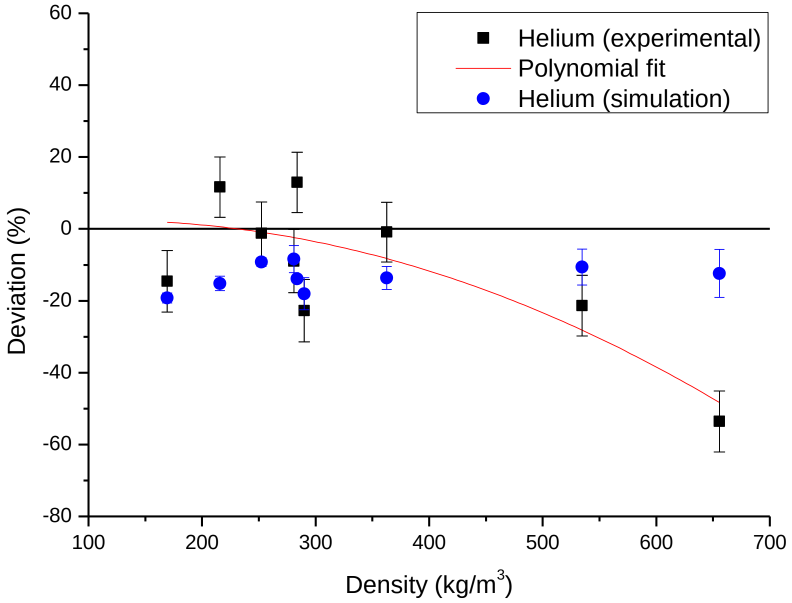

Fig. 5.11. Comparing the simulated partition coefficients (blue) with the experimental (black) dataset for helium. Published values occur where deviation is at 0%. Trend line included to aid assessment.

CO_2 Density (kg/m^3)	Experimental Deviation (%)	Uncertainty (S.E)	Simulated Deviation (%)	Uncertainty (S.E)
169.39	-14.6	8.6	-19.2	1.4
215.69	11.6	8.4	-15.2	2.0
252.41	-1.2	8.7	-9.2	1.2
280.83	-8.9	8.8	-8.4	3.8
283.84	13.0	8.4	-13.9	0.7
290.00	-22.8	8.7	-18.0	4.5
362.73	-0.9	8.3	-13.6	3.2
534.80	-21.4	8.4	-10.6	5.0
655.70	-53.6	8.5	-12.4	6.6

Table 5.12. Comparison of experimental and simulated helium partition coefficients in terms of deviation from published values. Uncertainty is quoted as standard error. All values are given to 1 decimal place.

On average there was a poor fit between the experimental and the simulated values for helium. While the experimental data displayed a negative deviation trend as a function of density no such trend was present within the simulations. Instead it was noticed that the simulated partition coefficients were consistently slightly under-predicted by -8.4% to -19.2% relative to published partition coefficients. This under-prediction did not vary significantly as a function of increasing density. Therefore an average was generated of -13.4% ± 3.2 across the whole density range. As this consistent slight under prediction was observed across the density range the indication was that the effect of increasing densities had no effect on simulated partition coefficients. This was in agreement with the predictions made from the low pressure data sets. Therefore this was in contrast to the trend observed in the experimental data where the highest densities expressed the greatest deviation from published partition coefficients. The inference therefore is that the simulation in its current iteration is not satisfactorily replicating the experimental trends observed at high density.

5.4.2 Neon

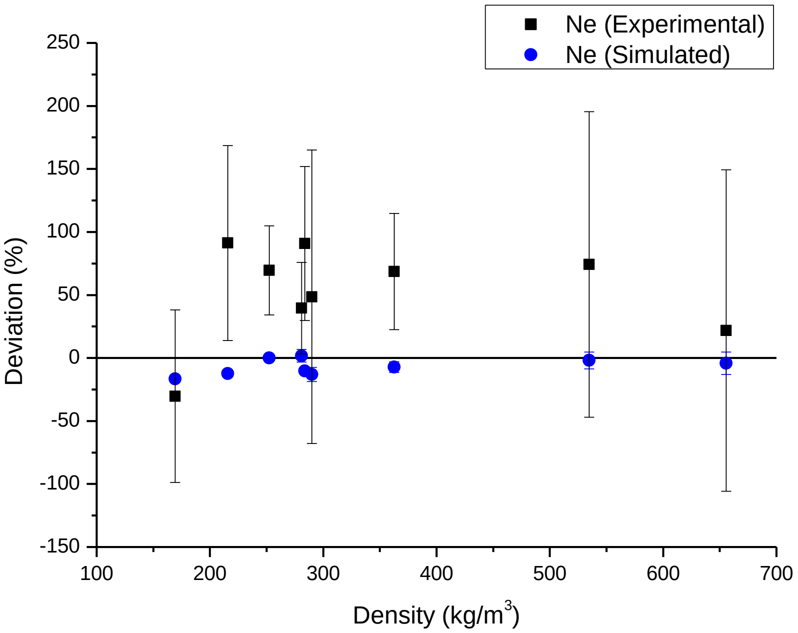

Fig. 5.12. Comparing the simulated partition coefficients (blue) with the experimental (black) dataset for neon. Published values occur where deviation is at 0%. No trend line was generated for this noble gas.

CO_2 Density (kg/m³)	Experimental Deviation (%)	Uncertainty (S.E)	Simulated Deviation (%)	Uncertainty (S.E)
169.39	-30.3	68.5	-16.6	1.8
215.69	91.3	77.3	-12.3	1.8
252.41	69.6	35.3	-0.1	1.6
280.83	39.5	36.3	1.8	5.0
283.84	90.9	61.0	-10.3	0.9
290.00	48.6	116.4	-13.0	5.6
362.73	68.5	46.1	-7.2	4.2
534.80	74.2	121.2	-1.9	6.6
655.70	21.8	127.6	-4.1	8.9

Table 5.13. Comparison of experimental and simulated neon partition coefficients in terms of deviation from published values for neon. Uncertainty is quoted as standard error. All values are given to 1 decimal place.

Although the experimental data was of insufficient quality for quantification (4.3.3 & 4.5) it was presented here as a visual aid in assessing the modelled partition coefficients. All values produced by the simulation were in reasonable agreement with the published values although values were occasionally slightly under-predicted. An average deviation of -7.1% ± 4.1 was calculated from deviations ranging between -16.6% – 1.8%. As with helium no deviation as a function of density was observed, even at the highest densities. Although no deviation trend could be observed experimentally for this noble gas, given the trends observed for all other noble gases a degree of deviation as a function of density would be expected. Therefore it is believed that the experimental neon behaviour at high densities was poorly replicated by the current model.

5.4.3 Argon

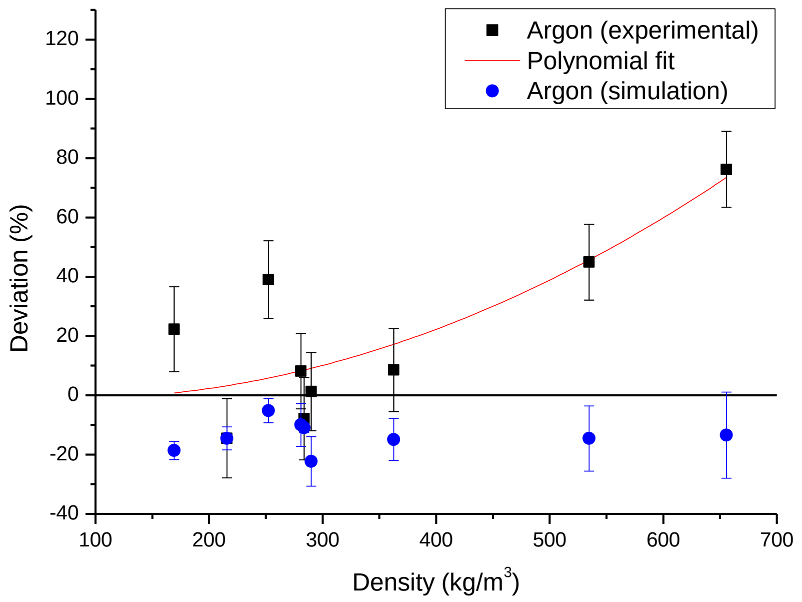

Fig. 5.13. Comparing the simulated partition coefficients (blue) with the experimental (black) dataset for argon. Published values occur where deviation is at 0%. Trend line included to aid assessment.

CO_2 Density (kg/m^3)	Experimental Deviation (%)	Uncertainty (S.E)	Simulated Deviation (%)	Uncertainty (S.E)
169.39	22.3	14.3	-18.6	3.1
215.69	-14.5	13.4	-14.5	3.9
252.41	39.0	13.1	-5.2	4.1
280.83	8.1	12.7	-10.0	7.2
283.84	-7.9	13.9	-10.9	1.6
290.00	1.2	13.1	-22.3	8.4
362.73	8.5	14.0	-14.9	7.1
534.80	44.9	12.8	-14.6	11.0
655.70	76.2	12.8	-13.5	14.5

Table 5.14. Comparison of experimental and simulated argon partition coefficients in terms of deviation from published values. Uncertainty is quoted as standard error. All values are given to 1 decimal place.

As for the lighter noble gases the average deviation of argon was similarly slightly under-predicted (-13.8% ± 6.8) and only expressed a low variability across the whole density profile (-22.3% – -5.2%). Similar trends had already been documented at low pressures. No discernible density-based trends were observed. This lack of responsivity to density changes therefore went against the experimentally observed trends which, for argon, indicated that at high density a high positive deviation was observed. Only at the lowest density were simulated and experimental partition coefficients in rough agreement with one another. This coincided with the density regime where argon partition values were not believed to deviate significantly from published values.

Overall it was determined that the effect of increasing density did not promote deviation to the simulated values. This was in agreement with the published partition coefficients and therefore in disagreement with experimentally defined trends. Thus the partitioning of argon between highly dense CO_2-water systems was not accurately simulated by the model in its present iteration.

5.4.4 Krypton

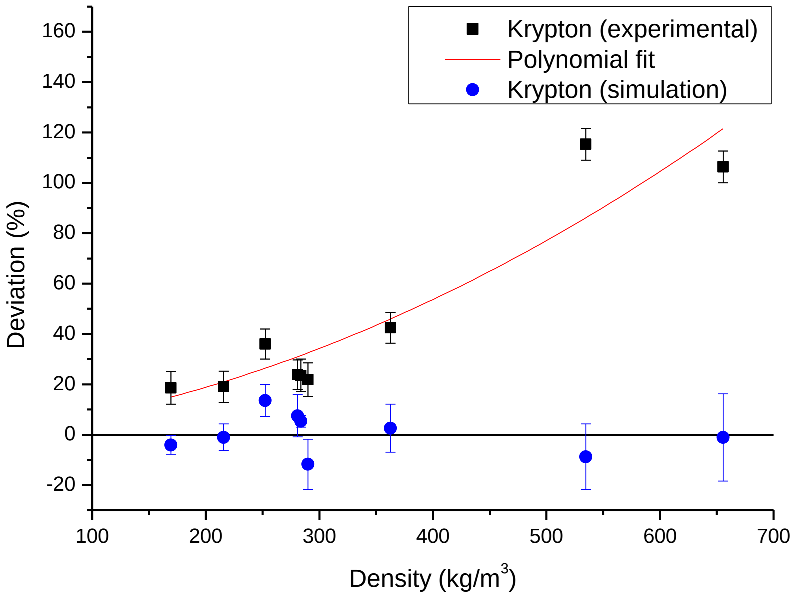

Fig. 5.14. Comparing the simulated partition coefficients (blue) with the experimental (black) dataset for krypton. Published values occur where deviation is at 0%. Trend line included to aid assessment.

CO_2 Density (kg/m^3)	Experimental Deviation (%)	Uncertainty (S.E)	Simulated Deviation (%)	Uncertainty (S.E)
169.39	18.6	6.5	-4.1	3.7
215.69	19.0	6.3	-1.1	5.3
252.41	36.0	6.0	13.5	6.3
280.83	23.9	5.9	7.5	8.4
283.84	23.5	6.5	5.3	2.3
290.00	21.9	6.6	-11.7	10.0
362.73	42.4	6.1	2.6	9.5
534.80	115.3	6.3	-8.8	13.1
655.70	106.3	6.3	-1.1	17.3

Table 5.15. Comparison of experimental and simulated krypton partition coefficients in terms of deviation from published values. Uncertainty is quoted as standard error. All values are given to 1 decimal place.

The trends observed in all lighter noble gas simulations were also present for krypton. From a low range (-11.7% – 13.5%) an average value with no significant deviation was observed (0.2% ± 8.4). This low range resulted in all simulation values closely replicating published values for all densities. This good agreement with published values therefore resulted in a poor agreement with experimental values which expressed significant positive deviation as a function of density. This inability of the model to replicate the experimental trends associated with high density therefore was indicative that further work was required to reconcile the simulation with the experimental data sets.

5.4.5 Xenon

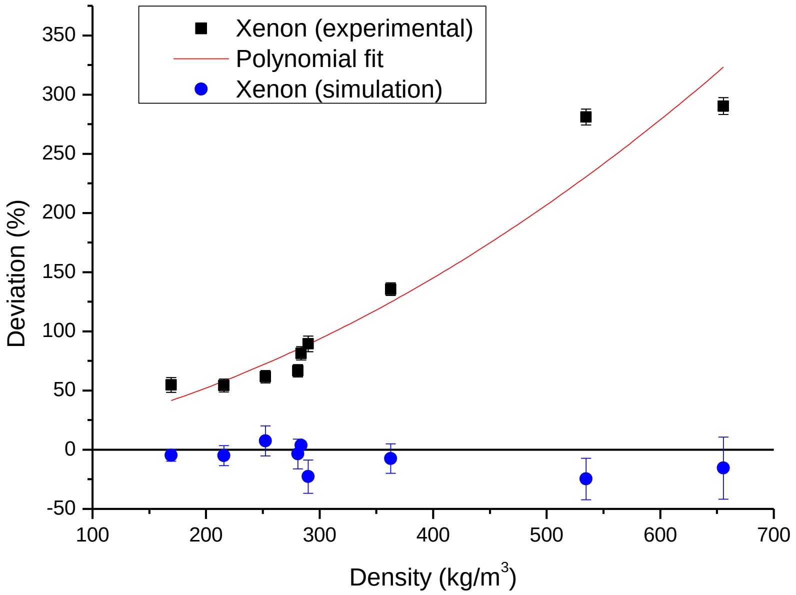

Fig. 5.15. Comparing the simulated partition coefficients (blue) with the experimental (black) dataset for xenon. Published values occur where deviation is at 0%. Trend line included to aid assessment.

CO_2 Density (kg/m^3)	Experimental Deviation (%)	Uncertainty (S.E)	Simulated Deviation (%)	Uncertainty (S.E)
169.39	54.6	6.3	-4.7	4.9
215.69	54.1	5.5	-5.0	8.4
252.41	61.6	5.3	7.5	12.8
280.83	66.7	5.2	-3.6	12.6
283.84	81.4	5.6	3.7	3.2
290.00	89.4	6.6	-22.7	14.0
362.73	135.6	5.4	-7.4	12.4
534.80	281.0	6.7	-24.7	17.4
655.70	290.3	7.1	-15.5	26.2

Table 5.16. Comparison of experimental and simulated xenon partition coefficients in terms of deviation from published values. Uncertainty is quoted as standard error. All values are given to 1 decimal place.

Simulated values of xenon indicated the same trends as observed for all other noble gas experimental simulations. A good correlation with published partition coefficients was observed at all densities with deviations ranging between -24.7% and 7.5% and an average value of -8.1% ± 12.4. No observable gradient could be discerned within the simulated values. This therefore placed the simulation results in opposition with the observed experimental trends which indicated a high positive deviation as a function of increasing density. Consequentially it was determined that for xenon, like all noble gases, a poor agreement between simulation and experiment was reached for this iteration of the model.

5.4.6 Summary of dense CO_2 simulations

Experimentally derived noble gas partition coefficients within highly dense CO_2-water systems were poorly reproduced by all simulations. No density derived deviation is observed within any simulations; instead partition coefficients remain in good agreement with low pressure published coefficients at all densities. However the experimental aspect of this project has proved significant deviations from published coefficients are to be expected at high densities. The inability of the model to currently replicate this therefore is a key issue requiring attention.

The good agreement between simulation and published values for the experimental range however indicates that the model is able to reasonably simulate CO_2-water while assuming near-ideal noble gas behaviour. Therefore it is concluded that non-ideality is presently not being adequately accounted for within the simulations. Consequentially the model in its current iteration is unsuitable for calculating partition coefficients for any noble gases within non-ideal (i.e. high density) systems. Therefore further work is required before it can be applied to predicting noble gas behaviour within CCS environments.

5.4.7 Model evaluation

Applying the model to CCS environments is not currently possible due to its inability to replicate trends seen within the experimental data set at high density. In order to address this outstanding issue the underlying cause(s) must first be identified. The aim of this section therefore is to discuss why the model poorly predicts partitioning at elevated densities. Possible causal mechanisms were; limitations of the simulation program, issues with the chemical potential approach, issues with unlike molecular interactions and selection of models. These are now discussed.

When a simulation approach does not adequately predict experimental trends the legitimacy of the program and the technique must be re-evaluated. This is required to ensure the discrepancy is not a product of the limitations of the simulation itself. However in addition to the testing here, given the proven track record of Towhee at accurately simulating binary phase systems (e.g. Houndonougbo *et al.*, 2007; Dai *et al.*, 2011; Vlcek *et al.*, 2011) the program itself was not considered to be the issue. Similarly as the applied chemical potential approach had a sound thermodynamic basis (Martin & Siepmann, 1998; Frenkel & Smit, 2002) and had satisfactorily reproduced partitioning at low pressure this too was assumed accurate. The most likely candidates therefore were poor unlike molecular interactions and/or a poor selection of models.

For this process molecules of water, CO_2 and each noble gas were individually selected and assessed for their accuracy in predicting key thermodynamic phase properties. All were proven to replicate experimental values both in the literature and by the verification of simulations run for this project. Therefore although the models are simplifications of existing physical molecules they are also not believed to be the primary source of the erroneous values. The only remaining factor yet to be considered therefore is the unlike intermolecular interactions between molecules.

Prior to this study the CO_2-water unlike interactions for the EPM2 and SPC/E molecules had been optimised to reproduce experimental binary phase behaviour between 323.15 – 348.15 K and 100 – 400 bar (Vlcek *et al.*, 2011). Given that the greatest partition coefficient deviations were observed within this range this unlike interaction can be reasonably ruled out. The noble gas-water interactions were similarly optimised in this study to generate better predictions of noble gas solubilities at low pressures. At higher pressures it is currently assumed interactions within the water phase remain essentially unchanged (4.10.1). Additionally the incorporation of aqueous CO_2 is not expected to affect noble gas solubility to a large degree (4.10.1). Thus it is reasonable to infer at this stage noble gas-water interactions will remain the same regardless of pressure. It is recognised though that this assumption will require future experimental verification.

This therefore leaves only the noble gas-CO_2 interactions. After being calculated by the Lorentz-Berthelot mixing rules no further optimisation process was implemented for these unlike interactions. For the chemical potential-derived partition coefficients at low pressure a good agreement was observed with the pure phase partitioning. This was used to infer that all molecular interactions were reasonably approximated prior to simulating experimental conditions. However at low pressures, where density is low, conditions are close to ideality. Under these conditions intermolecular interactions within the gas phase will only have a minor effect on partition coefficients. Therefore inaccuracies or oversimplifications in the noble gas-CO_2 potentials will not be immediately apparent. At higher densities though this unlike interaction will affect partition coefficients to a much greater extent.

From the experimental aspect it was considered that it was this progressive non-ideality as a function of density which promoted progressive deviation from expected partition coefficients. Under these extremely non-ideal conditions CO_2 is expected to act as a polar solvent with the solvation power increasing as a function of density. As solvation power increases so too does the ability to induce polarisation in non-polar atoms. Thus noble gas solubility in the CO_2 phase is affected in accordance with the ability to induce polarisation. This is based on the respective polarisabilities of each noble gas. Thus xenon is the most polarisable followed by krypton, argon, neon and lastly helium, which is poorly polarisable. This therefore resulted in xenon possessing the greatest enhanced solubility within the CO_2 phase as a function of density while the relative solubility of helium actually decreased.

In its current iteration however, no provision has been made for inducing polarisation to the noble gases within the CO_2 phase. As a consequence approximately ideal noble gas-CO_2 behaviour is being simulated within this obviously non-ideal environment. It is perfectly reasonable therefore that simulated partition coefficients replicate published coefficients even at high densities. This is because neither is presently able to satisfactorily incorporate deviations from ideal partitioning due to CO_2 density-based deviations.

Thus it is concluded that the noble gas-CO_2 unlike interactions are the reason the model poorly predicts partitioning under non-ideal conditions. This therefore requires immediate attention.

5.4.8 Reconciling the model with the experimental data

Clearly additional work is required to reconcile the simulated results with their experimental counterparts. From the preceding section it is clear that the reason for the discrepancy is due to a poor pair potential describing the noble gas-CO_2 interactions. At low pressures the interaction is sufficiently accurate to approximate behaviour observed in previous studies for other low pressure systems (Crovetto *et al.*, 1982; Smith, 1985). However at higher system densities the limitation of this simplified interaction becomes apparent; partitioning continues to be predicted according to their low pressure analogues. This study has categorically disproved the validity of this previous held assumption. Thus although the simulation replicates published values it poorly reproduces actual partitioning at high densities. Therefore further adaptations to the noble gas-CO_2 potential are required to create a simulation which successfully replicates its experimental counterparts.

It has been previously determined that the driving force of deviations is due to the carbon dioxide acting as a polar solvent with a progressively higher solvation power as density increases (4.10.3). This polar solvent is able to solvate noble gases due to their polarisable nature. Therefore an induced polarisation term should be included in the future for the noble gas-CO_2 interactions. Towhee already has the ability to include such a term and so the process of implementation and optimisation should be relatively straightforward. This additional level of complexity to the noble gas-CO_2 interaction should allow the density of the CO_2 phase to enhance noble gas solubility within this phase where appropriate. Consequentially a much better agreement between simulation and experimental partition coefficients should be achieved. Therefore by including a CO_2-noble gas induced polarisation term for each noble gas it is expected that the model will be in a position for legitimate application to CCS environments.

It is accepted that this additional level of complexity will result in the model becoming computationally more expensive although the magnitude of this cost is presently unknown. Without this though the model will be unable to acceptably replicate experimental values for high density systems. It is likely therefore that further refinements to the model will be required to increase efficiency so results can continue to be generated within an acceptable timeframe. Such improvements may include downsizing of the system and/or running the system on parallel processors.

By implementing this polarisation term it is fully expected that the simulation values can be fully reconciled with their experimental counterparts. Once this is achieved the model can be applied with confidence to predicting noble gas behaviour within CCS environments.

5.5 Summary

The aim of the modelling aspect of this project was to iteratively develop a simulation-based approach which could be used to predict partition coefficients of noble gases within CCS environments. Before this study no methodology existed which was capable of generating any noble gas partition coefficients within CO_2-water environments. Therefore although the final goal was not fully realised within the time constraints of this project significant milestones have been reached. It has been proven that by modelling a pure noble gas-water binary phase system reasonable partition coefficients can be obtained. This revealed the inaccuracies in using the Lorentz-Berthelot mixing rules to calculate noble gas-water interactions. Consequentially each interaction has been iteratively improved to provide significantly improved noble gas-water interactions for each noble gas except xenon. These improved potentials can be applied to other scenarios involving noble gas-water interactions which will improve the simulation quality.

Another key advancement was the adaptation of the chemical potential approach to generate partition coefficients for each noble gas within a CO_2-water binary phase system. These partitioning coefficients had a good agreement with the previous published values. Therefore an alternative approach was confirmed which could investigate noble gas partitioning at infinite dilution in low pressure systems i.e. no noble gas-noble gas interactions. Additionally this approach allowed partition coefficients for all noble gases to be determined at the same time which reduced the required number of simulations by 80%. Lastly the simulation was able to generate high density partition coefficients for experimental comparison which, although poorly reproduced experimental results, agreed well with the published values. Clearly insufficient provision was made in the model for non-ideal interactions between CO_2 and the noble gases. Therefore the agreement between the model and previously published values, both of which assumed reasonably ideal gas behaviour, is promising.

By modifying the noble gas-CO_2 interactions to incorporate an optimised polarisation potential this remaining issue of simulating non-ideality is expected to be fully resolved. Thus progressive non-ideality as a function of density for highly dense CO_2-water systems will be factored into the model. This will therefore allow full application of the model in predicting partition coefficients of noble gases under pressures and temperatures expected within CCS environments.

Chapter Six

Conclusions and future work

6.1 Conclusions

Partition coefficients for helium, argon, krypton and xenon were determined for pressures and temperatures ranging between 322.85 – 377.15 K and 89.4 – 134.26 bar. When these values were compared to the low pressure partition coefficients typically used to interpret these systems significant deviations were observed. As the density of the supercritical CO_2 phase increased a greater relative proportion of argon, krypton and xenon remained within the CO_2 phase compared to expectations i.e. partition coefficients were higher. Helium partition coefficients were lower, however, indicating a greater preference for the water phase. These density-derived deviations were a result of extreme non-ideality within the CO_2 phase. At high density the supercritical CO_2 phase acts as a polar solvent which induces polarisation in the noble gases. As the ability to induce polarisation increases as a function of atomic radius, xenon solubility within this phase is most enhanced followed by krypton and then argon. Helium, however, has poor polarisability and so solubility within this phase is lower at high density due to enhanced repulsive forces associated with a dense polar solvent.

These density-derived deviations from low pressure partition coefficient values have been quantified for helium, argon, krypton and xenon for CO_2 phase densities between 0 - 656 kg/m^3. By applying a second order polynomial fit to these deviations can be numerically determined for a given density. Using this approach revised partition coefficients which now accurately take into account non-ideality can now be applied to supercritical CO_2-water binary phase systems.

This experimental system was duplicated using a chemical potential-based GEMC simulation. The model in its present iteration is unable to accurately replicate experimental partition coefficients for supercritical CO_2-water binary phase systems. This is due to deficiencies in the current noble gas-CO_2 parameters which could not be resolved within the timeframe of this project. Despite this present limitation the model accurately predicts noble gas partitioning at low pressures. To accomplish this an optimisation process for all noble gas-water unlike ε_{ij} terms was implemented. The improved parameters for these interactions are presented in Table 5.6. By implementing an improved set of noble gas-CO_2 interaction terms, able to take into account polarisation, it is fully expected that partitioning coefficients for all noble gases derived using approach will replicate their experimental counterparts.

6.2 Future experimental work

As with all projects determining the scope for future work is an essential requirement. This future work can either be aimed at improving the existing methodology or expanding the original dataset beyond that of the initial remit. Existing limitations and areas of improvement have already been indicated where appropriate in this thesis. However the most important of these are summarised here. These have been subdivided into improvements to the experimental and the modelling procedures respectively.

It was not possible to generate experimental partition coefficients for neon within this project. Although it is possible to infer some probable characteristics from the behaviour of other noble gases an absolute quantification remains outstanding. This therefore represents a key area which requires focus as a matter of priority. Possible ways to resolve this would either be to increase the initial ^{21}Ne spike or to analyse the samples on a mass spectrometer with a higher resolution. A higher resolution machine would allow for separation of more abundant isotopes of neon from interference peaks.

One of the major sources of uncertainty derived from the experimental aspect was the issue of calculating density when sampling the CO_2 phase. It was known that the sampling density of the CO_2 phase was significantly higher than the experimental density. Sampling density was calculated based on the assumption that the samples were collected at room temperature and experimental pressure. However the validity of this assumption remains outstanding. As the resultant calculated difference in density served as the basis for one of the primary correction factors (density correction factor) an accurate value for this is essential. Therefore the accuracy of this approach for determining sampling density must be assessed. If no discrepancy is found then the legitimacy of this approach is proven. Alternatively if an observable difference is discovered then it can be quantified and this correction factor can be improved and applied to both existing and future data.

Currently density of the CO_2 phase is considered the driving force affecting deviations from partitioning. The trends observed for both pressure and temperature regimes are therefore believed to be purely symptomatic of changing densities. Under this assumption the infinite variations of pressure-temperature combinations which result in a specific density therefore are considered to all produce the same deviation of partition coefficients. While this hypothesis is observationally valid for pressures and temperatures within the range of interest presented here it may not necessarily be true for all pressure and temperature combinations. Therefore it is recognised that this also requires future work to ensure that deviations from published values can be reasonably assumed to be solely density-derived under all conditions.

Similarly the assumption is made here that density of the CO_2 phase is the predominant driving force for partition coefficient deviations. It is maintained therefore that CO_2 within the water phase will continue to only have a marginal effect on noble gas partitioning values, regardless of thermodynamic conditions. Under conditions where a greater proportion of CO_2 exists within the water phase than encountered here this assumption may also prove to be an oversimplification. Therefore this is something which may require consideration when expanding the current dataset. Additionally, although it is hypothesised here that salinity will produce the same effect on noble gas partitioning within supercritical CO_2-water systems (4.10.7), this assumption will also require validation.

Lastly, it is recognised that a paucity of data still exists. The nine new data points presented here have begun to demonstrate how noble gases partition between a CO_2 phase and a water phase at high pressures. Trends have been identified and quantified. However the thermodynamic range over which they have been determined is quite low. Although these are reasonable predictions of partition coefficients at lower densities, the same cannot be said for higher densities. As such the trend lines applied to the data cannot be extrapolated beyond the maximum experimental density. The only way to rectify this is to generate more partitioning data across a much wider pressure and temperature range. Only then can the trends be fully quantified and noble gas partitioning be fully documented for all environments encountered within CCS projects and related fields.

6.3 Future improvements to the model

Although progress has been made in constructing a model to compliment the experimental aspect it is still very much a work in progress. Most importantly the CO_2-noble gas interactions need a polarisation term in order to replicate experimental partitioning at high densities. Once these have been applied and optimised the model is expected to be able to replicate non-ideality encountered within experimental systems to generate partition coefficients in good agreement with the experimental values.

Additionally, although an optimisation process was applied to the noble gases, the uncertainty for each data point served as the limiting factor to how close the simulated values replicated published partitioning. Therefore, in order to improve upon these optimised potentials, further methods reducing the uncertainty require investigation. These may include running the simulations for longer, using larger systems and possibly running multiple identical simulations to increase the existing dataset. Xenon would most benefit from this as the extreme sensitivity when changing the ε_{ij} value coupled with the high uncertainty prevented this noble gas from being optimised. Also, although steps were taken to optimise helium-water ε_{ij} value at low pressure, full reconciliation was not attained. Therefore helium partition coefficients remained consistently lower than published values by a small degree. Given the lack of response to changing ε_{ij} values alone future optimisation may involve changing σ_{ij} as well for helium water-interactions to reconcile simulation and experimental partition coefficients.

Final Comments

It is clear that at trace levels the behaviour of noble gases is highly dependent on the environment in which they occupy. Where partitioning is concerned therefore the legitimacy of simply assuming near-ideal behaviour derived from pure phase low pressure analogues has been categorically disproved by this study. Therefore all systems of interest to the noble gas community where this supposition is maintained must be re-evaluated and redefined. The significance of molecular interactions at high densities can no longer be ignored on either an experimental or simulation level. Given the significant effect non-ideality can produce, to continue to assume blanket ideal behaviour in any environment is not ideal by any means!

Appendix I

Worked partition coefficient examples

AI.1 Partition coefficient & uncertainty for paired samples

As an aid to the reader the process of uncertainty propagation (2.6.7) is now applied to an example. For this example the partitioning of helium and its associated uncertainty are calculated from samplers A2 & W2 from an experiment at 322.85 K and 134.12 bar. The specific details of this run are now presented:

Factor	Symbol	Calculated Value	Units
Helium in CO_2 phase	C_{He}	1.29×10^{-11}	bar
Helium in CO_2 phase uncertainty	ΔC_{He}	1.99×10^{-13}	bar
Helium in H_2O phase	W_{He}	1.23×10^{-11}	bar
Helium in H_2O phase uncertainty	ΔW_{He}	2.29×10^{-13}	bar
Volume of CO_2 sampler A2	C_A	0.982	cm^3
Volume of CO_2 sampler A2 uncertainty	ΔC_A	0.00332	cm^3
Volume of H_2O sampler W2	W_A	1.442	cm^3
Volume of H_2O sampler W2 uncertainty	ΔW_A	0.00359	cm^3
Aliquot correction factor	F	37.732	N/A
Aliquot correction factor uncertainty	ΔF	0.1275	N/A
Density correction factor for CO_2 sample	ρ_c	1.375048	N/A
Density correction factor for H_2O sample	ρ_w	1.010758	N/A
Pressure	P	134.12	bar
Pressure uncertainty	ΔP	1	bar
Experimental temperature	T_{exp}	49.70	°C
Sampling temperature	T_{samp}	19.24	°C
Uncertainty in temperature	ΔT	0.2	°C

Table AI.1. Details of helium from paired sample chosen as example for calculating partitioning and associated uncertainty. Temperature is given in original units (Celsius) to ensure correct relative uncertainty.

First the corrections to each phase are applied (2.6). Sample volume correction is first applied to each phase:

$$\mathrm{C_{He}} = \frac{\mathrm{C_{He}}}{\mathrm{C_A}} = \frac{1.29\times10^{-11}}{0.982} = 1.31\times10^{-11} \tag{AI.1}$$

$$\mathrm{W_{He}} = \frac{\mathrm{W_{He}}}{\mathrm{W_A}} = \frac{1.23\times10^{-11}}{1.442} = 8.52\times10^{-12} \tag{AI.2}$$

Next the aliquot correction factor is applied to the CO_2 value:

$$\mathrm{C_{He}} = \mathrm{F}\times1.31\times10^{-11} = 37.732\ \times1.31\times10^{-11} = 4.95\times10^{-10} \tag{AI.3}$$

The density correction is now applied to each phase:

$$\mathrm{C_{He}} = \frac{4.95\times10^{-10}}{\rho_\mathrm{C}} = \frac{4.95\times10^{-10}}{1.375} = 3.60\times10^{-10} \tag{AI.4}$$

$$\mathrm{W_{He}} = \frac{8.52\times10^{-12}}{\rho_\mathrm{W}} = \frac{8.52\times10^{-12}}{1.010758} = 8.43\times10^{-12} \tag{AI.5}$$

Now all corrections have been applied the partition coefficient can be determined:

$$\mathrm{D_{He}} = \frac{\mathrm{C_{He}}}{\mathrm{W_{He}}} = \frac{3.60\times10^{-10}}{8.43\times10^{-12}} = 42.706 \tag{AI.6}$$

Now the associated uncertainty for this coefficient will be calculated. The first step is to calculate all relative uncertainties. These are presented in tabular form:

Relative uncertainty	Symbol	Calculated Value (3sf)	Rel. uncertainty^2 (3sf)
Helium in CO_2 phase	$\frac{\Delta C_{He}}{C_{He}}$	0.0154	2.37E-04
Helium in H_2O phase	$\frac{\Delta W_{He}}{W_{He}}$	0.0187	3.48E-04
Volume of CO_2 sampler A2	$\frac{\Delta C_A}{C_A}$	0.00338	1.14E-05
Volume of H_2O sampler W2	$\frac{\Delta W_A}{W_A}$	0.00249	6.20E-06
Aliquot correction factor	$\frac{\Delta F}{F}$	0.00338	1.14E-05
Experimental Pressure	$\frac{\Delta P_{\exp}}{P_{\exp}}$	0.00746	5.56E-05
Sampling Pressure	$\frac{\Delta P_{Samp}}{P_{Samp}}$	0.00746	5.56E-05
Experimental Temperature	$\frac{\Delta T_{\exp}}{T_{\exp}}$	0.00402	1.62E-05
Sampling Temperature	$\frac{\Delta T_{Samp}}{T_{Samp}}$	0.0104	0.000108
Total density uncertainty for both phases	$\frac{\Delta \rho_{Tot}}{\rho_{Tot}}$	0.0217	0.000471

Table AI.2. Relative uncertainties for error propagation example. Also calculated are the relative uncertainties squared as required for adding in quadrature.

The squared relative uncertainties from Table AI.2 can now be inserted into Equation 2.24:

$$\frac{\Delta \mathrm{D}_{\mathrm{He}}}{\mathrm{D}_{\mathrm{He}}} = \sqrt{2.37\times10^{-4} + 3.48\times10^{-4} + 1.14\times10^{-5} + 6.15\times10^{-6} + 1.14\times10^{-5} + 4.71\times10^{-4}} \qquad \text{(AI.7)}$$

$$\frac{\Delta \mathrm{D}_{\mathrm{He}}}{\mathrm{D}_{\mathrm{He}}} = \sqrt{1.08\times10^{-3}} \qquad \text{(AI.8)}$$

$$\frac{\Delta \mathrm{D}_{\mathrm{He}}}{\mathrm{D}_{\mathrm{He}}} = 0.0330 \qquad \text{(AI.9)}$$

From this a simple insertion of the generated partition coefficient from Equation AI.6 and a rearrangement of Equation AI.9 gives the uncertainty:

$$\Delta \mathrm{D}_{\mathrm{He}} = 0.0330\mathrm{D}_{\mathrm{He}} = 0.0330\times42.706 = 1.408 \qquad \text{(AI.10)}$$

AI.2 Calculating the procedural reproducibility uncertainty

A worked example calculating the procedural reproducibility uncertainty (2.6.8) for the entire helium dataset is now given.

From each set of samples an average value is calculated. This is presented in Table AI.3.

Sample date	^{4}He value (data point 1)	^{4}He value (data point 2)	^{4}He value (data point 3)	Average ^{4}He value
7.3.13	65.2	N/A	46.5	55.8
21.2.13	70.4	70.5	67.4	69.4
10.7.12	74.0	94.8	97.4	88.7
11.6.12	90.2	79.0	96.2	88.5
8.2.13	76.9	70.8	N/A	73.8
29.4.13	64.4	65.4	60.6	63.5
15.1.13	88.7	76.9	78.0	81.2
2.4.13	76.2	76.6	N/A	76.4
20.3.13	47.6	42.7	N/A	45.1

Table AI.3. ^{4}He partitioning values for each sample. Average values calculated via arithmetic mean as discussed in 2.6.7. N/A indicates a viable partition coefficient was not obtained. All values presented are given to 1 decimal place.

From this the absolute modular deviation of each data point from the average value could be calculated.

Sample date	Average ^{4}He value	Deviation (data point 1)	Deviation (data point 2)	Deviation (data point 3)
7.3.13	55.8	9.3	N/A	-9.3
21.2.13	69.4	1.0	1.0	-2.1
10.7.12	88.7	-14.7	6.0	8.7
11.6.12	88.5	1.7	-9.5	7.7
8.2.13	73.8	3.1	-3.1	N/A
29.4.13	63.5	1.0	1.9	-2.9
15.1.13	81.2	7.5	-4.3	-3.2
2.4.13	76.4	-0.2	0.2	N/A
20.3.13	45.1	2.4	-2.4	N/A

Table AI.4. Deviation of ^{4}He partitioning values from mean for each sample. N/A indicates a viable partition coefficient was not obtained. All values presented are given to 1 decimal place

These values could then be divided by their respective average partitioning values to give the relative deviation from the mean values.

Sample date	R.D. (data point 1)	R.D.^{2}	R.D. (data point 2)	R.D.^{2}	R.D. (data point 3)	R.D.^{2}
7.3.13	0.1671	0.0279	N/A	N/A	0.1671	0.0279
21.2.13	0.0145	0.0002	0.0151	0.0002	0.0296	0.0009
10.7.12	0.1655	0.0274	0.0679	0.0046	0.0976	0.0095
11.6.12	0.0196	0.0004	0.1070	0.0115	0.0874	0.0076
8.2.13	0.0414	0.0017	0.0414	0.0017	N/A	N/A
29.4.13	0.0152	0.0002	0.0301	0.0009	0.0453	0.0021
15.1.13	0.0920	0.0085	0.0527	0.0028	0.0393	0.0015
2.4.13	0.0026	0.0000	0.0026	0.0000	N/A	N/A
20.3.13	0.0540	0.0029	0.0540	0.0029	N/A	N/A

Table AI.5. Relative deviation of ^{4}He partitioning values from mean for each sample. Also given are the relative deviations squared (R.D.^{2}) which are summed in the next calculation. All values are given to 4 decimal places.

These relative deviations are subsequently squared and then summed to give the total average deviation squared. This gives us the $\sum_{1}^{n_{tot}}\left(\frac{(\overline{D}_{i(\mathrm{P,T})}-D_{i(\mathrm{P,T})})}{\overline{D}_{i(\mathrm{P,T})}}\right)^2$ term in Equation 2.28.

For the worked example this value is 0.143 (3sf). We then divide this by the total number of data points (n_{tot}):

$$\frac{\sum_{1}^{\mathrm{n_{tot}}}\left(\frac{(\overline{\mathrm{D}}_{\mathrm{i(P,T)}}-\mathrm{D}_{\mathrm{i(P,T)}})}{\overline{\mathrm{D}}_{\mathrm{i(P,T)}}}\right)^2}{\mathrm{n_{tot}}}=\frac{0.143}{23}=0.00624 \tag{AI.11}$$

Lastly this value is square rooted to give the average procedural reproducibility uncertainty at each experiment for helium (Equation 2.28).

$$\frac{\Delta \mathrm{D}_{\mathrm{HeProc(P,T)}}}{\overline{\mathrm{D}}_{\mathrm{HeProc(P,T)}}}=\sqrt{0.00624}$$
$$\frac{\Delta \mathrm{D}_{\mathrm{HeProc(P,T)}}}{\overline{\mathrm{D}}_{\mathrm{HeProc(P,T)}}}=0.078=7.8\% \tag{AI.12}$$

Thus the relative procedural uncertainty for helium is obtained. For each experiment this is combined with the respective average experimental uncertainty (Equation 2.27) via Equation 2.26 to give the uncertainty for each data point.

Appendix II

Pure noble gas-water simulation data tables

Noble Gas	ε scale factor	293.15K (MPa)	S.E. (MPa)	303.15K (MPa)	S.E. (MPa)	313.15K (MPa)	S.E. (MPa)	323.15K (MPa)	S.E. (MPa)	333.15K (MPa)	S.E. (MPa)	343.15K (MPa)	S.E. (MPa)	353.15K (MPa)	S.E. (MPa)
Helium	Exp	14425.6		14712.7		14723.2		14494.7		14070.5		13495.0		12810.2	
	0.5	13339.3	879.0	13381.5	483.8	12420.3	1164.7	11203.6	299.2	11446.6	258.2	11488.1	285.2	11627.8	264.7
	0.85	15822.1	1086.9	14084.7	1013.9	12858.5	208.2	13531.7	531.1	12518.5	737.7	12602.6	672.0	12774.2	285.2
	0.91	14291.3	509.3	15569.3	526.5	13417.0	1331.4	14533.1	737.8	13674.1	612.0	13499.2	808.6	12832.4	651.0
	0.95	12599.5	603.4	13067.4	858.6	13224.4	501.8	12506.2	632.5	13674.1	818.9	12332.6	833.8	13381.5	436.6
	1	14405.0	431.7	13325.2	433.5	14368.3	447.0	12689.4	491.3	12461.6	384.8	13111.4	216.1	11676.1	261.5
	2	6448.9	915.1	8394.8	484.0	7291.7	500.4	7135.6	227.8	7952.0	265.0	7243.7	350.3	9199.7	612.6

Table AII.1. Absolute Henry's coefficients for scaled helium ε_{ij} values at 1.01325 bar. Exp denotes experimental partition coefficients for the same temperature (Crovetto *et al.*, 1982; Smith, 1985). Uncertainty is quoted as standard error. All values given to 1 decimal place.

Noble Gas	ε scale factor	293.15K (MPa)	S.E. (MPa)	303.15K (MPa)	S.E. (MPa)	313.15K (MPa)	S.E. (MPa)	323.15K (MPa)	S.E. (MPa)	333.15K (MPa)	S.E. (MPa)	343.15K (MPa)	S.E. (MPa)	353.15K (MPa)	S.E. (MPa)
Helium	Exp	14425.6		14712.7		14723.2		14494.7		14070.5		13495.0		12810.2	
	0.5	12620.5	487.5	12744.0	416.1	11465.2	340.2	11745.1	730.1	9868.2	643.5	10380.0	513.9	9474.9	314.7
	0.85	14063.2	752.9	11909.9	493.4	14071.4	928.8	11809.4	804.2	12892.9	439.8	12036.1	398.2	10172.2	172.4
	0.91	15118.6	1090.4	13121.6	679.5	13639.9	768.5	12049.9	540.7	12178.8	392.0	11757.4	790.8	10816.5	199.1
	0.95	15168.4	1324.3	13506.4	735.6	12620.5	709.5	12466.2	724.4	11083.0	346.7	11348.4	374.7	10727.9	340.4
	1	13069.3	556.9	12706.0	595.6	13999.0	656.9	12241.2	478.1	11260.8	250.0	12298.1	365.2	11082.5	332.0
	2	7851.0	736.0	8090.2	689.4	7351.4	607.1	7896.2	292.4	7869.3	180.9	6818.3	384.2	6895.7	169.8

Table AII.2. Absolute Henry's coefficients for scaled helium ε_{ij} values at 10.1325 bar. Exp denotes experimental partition coefficients for the same temperature (Crovetto *et al.*, 1982; Smith, 1985). Uncertainty is quoted as standard error. All values given to 1 decimal place.

Noble Gas	ε scale factor	293.15K (%)	S.E. (%)	303.15K (%)	S.E. (%)	313.15K (%)	S.E. (%)	323.15K (%)	S.E. (%)	333.15K (%)	S.E. (%)	343.15K (%)	S.E. (%)	353.15K (%)	S.E. (%)	**Ave (%)**	**S.E. (%)**
Helium	0.5	-7.5	6.6	-9.0	3.6	-15.6	9.4	-22.7	2.7	-18.6	2.3	-14.9	2.5	-9.2	2.3	**-14.0**	**4.2**
	0.85	9.7	6.9	-4.3	7.2	-12.7	1.6	-6.6	3.9	-11.0	5.9	-6.6	5.3	-0.3	2.2	**-4.5**	**4.7**
	0.91	-0.9	3.6	5.8	3.4	-8.9	9.9	0.3	5.1	-2.8	4.5	0.0	6.0	0.2	5.1	**-0.9**	**5.4**
	0.95	-12.7	4.8	-11.2	6.6	-10.2	3.8	-13.7	5.1	-2.8	6.0	-8.6	6.8	4.5	3.3	**-7.8**	**5.2**
	1	-0.1	3.0	-9.4	3.3	-2.4	3.1	-12.5	3.9	-11.4	3.1	-2.8	1.6	-8.9	2.2	**-6.8**	**2.9**
	2	-55.3	14.2	-42.9	5.8	-50.5	6.9	-50.8	3.2	-43.5	3.3	-46.3	4.8	-28.2	6.7	**-45.4**	**6.4**

Table AII.3. Deviations of helium simulations for scaled ε_{ij} values at 1.01325 bar. Values given as percentage deviations from published partition coefficients at low pressure (Crovetto *et al.*, 1982; Smith, 1985). Averages are presented in bold. Uncertainty is quoted as standard error. All values given to 1 decimal place.

Noble Gas	ε scale factor	293.15K (%)	S.E. (%)	303.15K (%)	S.E. (%)	313.15K (%)	S.E. (%)	323.15K (%)	S.E. (%)	333.15K (%)	S.E. (%)	343.15K (%)	S.E. (%)	353.15K (%)	S.E. (%)	**Ave (%)**	**S.E. (%)**
Helium	0.5	-12.5	3.9	-13.4	3.3	-22.1	3.0	-19.0	6.2	-29.9	6.5	-23.1	5.0	-26.0	3.3	**-20.9**	**4.4**
	0.85	-2.5	5.4	-19.0	4.1	-4.4	6.6	-18.5	6.8	-8.4	3.4	-10.8	3.3	-20.6	1.7	**-12.0**	**4.5**
	0.91	4.8	7.2	-10.8	5.2	-7.4	5.6	-16.9	4.5	-13.4	3.2	-12.9	6.7	-15.6	1.8	**-10.3**	**4.9**
	0.95	5.1	8.7	-8.2	5.4	-14.3	5.6	-14.0	5.8	-21.2	3.1	-15.9	3.3	-16.3	3.2	**-12.1**	**5.0**
	1	-9.4	4.3	-13.6	4.7	-4.9	4.7	-15.5	3.9	-20.0	2.2	-8.9	3.0	-13.5	3.0	**-12.3**	**3.7**
	2	-45.6	9.4	-45.0	8.5	-50.1	8.3	-45.5	3.7	-44.1	2.3	-49.5	5.6	-46.2	2.5	**-46.6**	**5.8**

Table AII.4. Deviations of helium simulations for scaled ε_{ij} values at 10.1325 bar. Values given as percentage deviations from published partition coefficients at low pressure (Crovetto *et al.*, 1982; Smith, 1985). Averages are presented in bold. Uncertainty is quoted as standard error. All values given to 1 decimal place.

Noble Gas	ε scale factor	293.15K (MPa)	S.E (MPa)	303.15K (MPa)	S.E. (MPa)	313.15K (MPa)	S.E. (MPa)	323.15K (MPa)	S.E. (MPa)	333.15K (MPa)	S.E. (MPa)	343.15K (MPa)	S.E. (MPa)	353.15K (MPa)	S.E. (MPa)
Neon	Exp	12134.1		12851.2		13299.0		13495.2		13468.8		13254.9		12890.2	
	0.75	15464.7	1141.2	12076.9	1164.8	14263.1	1067.7	15310.5	1075.5	13941.2	1126.5	15997.0	779.0	14413.2	1065.6
	0.8	15329.0	1134.2	14405.0	1078.0	12019.6	1144.1	14450.2	1570.7	13703.7	374.8	11697.6	409.6	13929.7	638.5
	0.85	10822.4	1172.8	13165.9	568.4	10519.6	367.2	12549.5	907.7	13064.1	265.4	13084.3	587.6	12891.2	438.4
	0.9	15046.8	1194.6	11673.4	515.8	12411.2	1093.4	13311.2	1239.3	12435.6	551.1	13047.3	892.8	12777.4	427.3
	0.95	11657.3	1433.5	10216.3	1061.6	11614.5	1061.9	10733.6	1201.2	8894.4	323.9	11762.8	715.2	12438.6	572.1
	1	10899.8	509.2	12155.1	553.0	10868.3	522.2	11192.4	407.5	9830.7	396.7	10948.1	406.3	11446.6	466.3

Table AII.5. Absolute Henry's coefficients for scaled neon ε_{ij} values at 1.01325 bar. Exp denotes experimental partition coefficients for the same temperature (Crovetto *et al.*, 1982; Smith, 1985). Uncertainty is quoted as standard error. All values given to 1 decimal place.

Noble Gas	ε scale factor	293.15K (MPa)	S.E. (MPa)	303.15K (MPa)	S.E. (MPa)	313.15K (MPa)	S.E. (MPa)	323.15K (MPa)	S.E. (MPa)	333.15K (MPa)	S.E. (MPa)	343.15K (MPa)	S.E. (MPa)	353.15K (MPa)	S.E. (MPa)
Neon	Exp	12134.1		12851.2		13299.0		13495.2		13468.8		13254.9		12890.2	
	0.75	15753.8	2547.8	14550.2	1617.2	13753.2	1110.9	15738.1	1033.9	13285.0	1210.8	12232.9	753.4	10717.5	556.8
	0.8	14549.0	1679.7	16556.9	825.3	13135.2	706.4	11735.6	977.7	12865.0	769.4	12611.4	934.7	12548.0	747.3
	0.85	12739.5	1204.5	12983.1	514.9	12875.8	1039.8	13393.9	543.7	12585.7	600.4	11430.0	408.5	10628.4	481.9
	0.9	11475.9	1512.1	11573.1	1201.0	11119.2	947.8	11453.6	697.0	11371.5	541.5	10930.9	677.0	9954.5	465.1
	0.95	14047.9	1564.8	9870.2	684.7	11604.7	898.4	10284.7	598.5	9466.8	666.3	9972.9	139.2	9164.2	459.6
	1	10973.3	765.1	11385.1	879.6	10051.2	1044.3	10264.3	282.8	9784.7	328.4	9305.0	307.3	9793.2	309.9

Table AII.6. Absolute Henry's coefficients for scaled neon ε_{ij} values at 10.1325 bar. Exp denotes experimental partition coefficients for the same temperature (Crovetto *et al.*, 1982; Smith, 1985). Uncertainty is quoted as standard error. All values given to 1 decimal place.

Noble Gas	ε scale factor	293.15K (%)	S.E. (%)	303.15K (%)	S.E. (%)	313.15K (%)	S.E. (%)	323.15K (%)	S.E. (%)	333.15K (%)	S.E. (%)	343.15K (%)	S.E. (%)	353.15K (%)	S.E. (%)	**Ave (%)**	**S.E. (%)**
Neon	0.75	27.4	7.4	-6.0	9.6	7.2	7.5	13.5	7.0	3.5	8.1	20.7	4.9	11.8	7.4	**11.2**	**7.4**
	0.8	26.3	7.4	12.1	7.5	-9.6	9.5	7.1	10.9	1.7	2.7	-11.7	3.5	8.1	4.6	**4.8**	**6.6**
	0.85	-10.8	10.8	2.4	4.3	-20.9	3.5	-7.0	7.2	-3.0	2.0	-1.3	4.5	0.0	3.4	**-5.8**	**5.1**
	0.9	24.0	7.9	-9.2	4.4	-6.7	8.8	-1.4	9.3	-7.7	4.4	-1.6	6.8	-0.9	3.3	**-0.5**	**6.4**
	0.95	-3.9	12.3	-20.5	10.4	-12.7	9.1	-20.5	11.2	-34.0	3.6	-11.3	6.1	-3.5	4.6	**-15.2**	**8.2**
	1	-10.2	4.7	-5.4	4.5	-18.3	4.8	-17.1	3.6	-27.0	4.0	-17.4	3.7	-11.2	4.1	**-15.2**	**4.2**

Table AII.7. Deviations of neon simulations for scaled ε_{ij} values at 1.01325 bar. Values given as percentage deviations from published partition coefficients at low pressure (Crovetto *et al.*, 1982; Smith, 1985). Averages are presented in bold. Uncertainty is quoted as standard error. All values given to 1 decimal place.

Noble Gas	ε scale factor	293.15K (%)	S.E. (%)	303.15K (%)	S.E. (%)	313.15K (%)	S.E. (%)	323.15K (%)	S.E. (%)	333.15K (%)	S.E. (%)	343.15K (%)	S.E. (%)	353.15K (%)	S.E. (%)	**Ave (%)**	**S.E. (%)**
Neon	0.75	29.8	16.2	13.2	11.1	3.4	8.1	16.6	6.6	-1.4	9.1	-7.7	6.2	-16.9	5.2	**5.3**	**8.9**
	0.8	19.9	11.5	28.8	5.0	-1.2	5.4	-13.0	8.3	-4.5	6.0	-4.9	7.4	-2.7	6.0	**3.2**	**7.1**
	0.85	5.0	9.5	1.0	4.0	-3.2	8.1	-0.8	4.1	-6.6	4.8	-13.8	3.6	-17.5	4.5	**-5.1**	**5.5**
	0.9	-5.4	13.2	-9.9	10.4	-16.4	8.5	-15.1	6.1	-15.6	4.8	-17.5	6.2	-22.8	4.7	**-14.7**	**7.7**
	0.95	15.8	11.1	-23.2	6.9	-12.7	7.7	-23.8	5.8	-29.7	7.0	-24.8	1.4	-28.9	5.0	**-18.2**	**6.4**
	1	-9.6	7.0	-11.4	7.7	-24.4	10.4	-23.9	2.8	-27.4	3.4	-29.8	3.3	-24.0	3.2	**-21.5**	**5.4**

Table AII.8. Deviations of neon simulations for scaled ε_{ij} values at 10.1325 bar. Values given as percentage deviations from published partition coefficients at low pressure (Crovetto *et al.*, 1982; Smith, 1985). Averages are presented in bold. Uncertainty is quoted as standard error. All values given to 1 decimal place.

Noble Gas	ε scale factor	293.15K (MPa)	S.E. (MPa)	303.15K (MPa)	S.E. (MPa)	313.15K (MPa)	S.E. (MPa)	323.15K (MPa)	S.E. (MPa)	333.15K (MPa)	S.E. (MPa)	343.15K (MPa)	S.E. (MPa)	353.15K (MPa)	S.E. (MPa)
Argon	Exp	3707.1		4405.6		5037.1		5572.0		5991.9		6289.2		6465.5	
	1	4761.1	966.5	7548.6	1304.5	7985.3	1226.2	8418.5	975.1	9861.3	963.1	9369.8	883.9	9700.8	785.4
	1.05	6673.1	4120.6	5535.1	1522.5	8018.8	1620.3	4739.2	1049.9	8185.9	1109.5	6786.7	1154.8	9194.6	1485.7
	1.1	4721.1	798.5	3380.7	159.2	4471.9	1407.6	4955.7	1092.4	6313.1	58.0	6210.9	1078.2	6755.0	901.9
	1.15	3171.0	439.3	4043.3	467.9	2939.0	647.9	4371.6	732.4	4764.6	816.0	4581.1	485.5	5834.0	416.9

Table AII.9. Absolute Henry's coefficients for scaled argon ε_{ij} values at 1.01325 bar. Exp denotes experimental partition coefficients for the same temperature (Crovetto *et al.*, 1982; Smith, 1985). Uncertainty is quoted as standard error. All values given to 1 decimal place.

Noble Gas	ε scale factor	293.15K (MPa)	S.E. (MPa)	303.15K (MPa)	S.E. (MPa)	313.15K (MPa)	S.E. (MPa)	323.15K (MPa)	S.E. (MPa)	333.15K (MPa)	S.E. (MPa)	343.15K (MPa)	S.E. (MPa)	353.15K (MPa)	S.E. (MPa)
Argon	Exp	3707.1		4405.6		5037.1		5572.0		5991.9		6289.2		6465.5	
	1	8554.7	1635.0	9120.2	1050.5	7196.0	1112.9	8035.8	691.1	8595.1	545.3	8141.9	478.5	7661.5	547.3
	1.05	3804.7	1340.7	9620.5	1018.7	6203.6	729.5	6807.8	1555.4	8070.1	1767.1	5634.2	625.1	7315.6	900.8
	1.1	4388.4	729.8	4368.9	1826.7	4188.0	799.1	6295.4	2686.9	5604.7	900.3	4796.6	770.7	5114.9	426.6
	1.15	1511.0	230.3	2901.9	911.5	3209.9	1288.0	3311.6	147.5	4248.0	592.2	4234.1	614.9	5671.5	505.3

Table AII.10. Absolute Henry's coefficients for scaled argon ε_{ij} values at 10.1325 bar. Exp denotes experimental partition coefficients for the same temperature (Crovetto *et al.*, 1982; Smith, 1985). Uncertainty is quoted as standard error. All values given to 1 decimal place.

Noble Gas	ε scale factor	293.15K (%)	S.E. (%)	303.15K (%)	S.E. (%)	313.15K (%)	S.E. (%)	323.15K (%)	S.E. (%)	333.15K (%)	S.E. (%)	343.15K (%)	S.E. (%)	353.15K (%)	S.E. (%)	**Ave (%)**	**S.E. (%)**
Argon	1	28.4	20.3	71.3	17.3	58.5	15.4	51.1	11.6	64.6	9.8	49.0	9.4	50.0	8.1	**53.3**	**13.1**
	1.05	80.0	61.7	25.6	27.5	59.2	20.2	-14.9	22.2	36.6	13.6	7.9	17.0	42.2	16.2	**33.8**	**25.5**
	1.1	27.4	16.9	-23.3	4.7	-11.2	31.5	-11.1	22.0	5.4	0.9	-1.2	17.4	4.5	13.4	**-1.4**	**15.3**
	1.15	-14.5	13.9	-8.2	11.6	-41.7	22.0	-21.5	16.8	-20.5	17.1	-27.2	10.6	-9.8	7.1	**-20.5**	**14.2**

Table AII.11. Deviations of argon simulations for scaled ε_{ij} values at 1.01325 bar. Values given as percentage deviations from published partition coefficients at low pressure (Crovetto *et al.*, 1982; Smith, 1985). Averages are presented in bold. Uncertainty is quoted as standard error. All values given to 1 decimal place.

Noble Gas	ε scale factor	293.15K (%)	S.E. (%)	303.15K (%)	S.E. (%)	313.15K (%)	S.E. (%)	323.15K (%)	S.E. (%)	333.15K (%)	S.E. (%)	343.15K (%)	S.E. (%)	353.15K (%)	S.E. (%)	**Ave (%)**	**S.E. (%)**
Argon	1	130.8	19.1	107.0	11.5	42.9	15.5	44.2	8.6	43.4	6.3	29.5	5.9	18.5	7.1	**59.5**	**10.6**
	1.05	2.6	35.2	118.4	10.6	23.2	11.8	22.2	22.8	34.7	21.9	-10.4	11.1	13.1	12.3	**29.1**	**18.0**
	1.1	18.4	16.6	-0.8	41.8	-16.9	19.1	13.0	42.7	-6.5	16.1	-23.7	16.1	-20.9	8.3	**-5.3**	**23.0**
	1.15	-59.2	15.2	-34.1	31.4	-36.3	40.1	-40.6	4.5	-29.1	13.9	-32.7	14.5	-12.3	8.9	**-34.9**	**18.4**

Table AII.12. Deviations of argon simulations for scaled ε_{ij} values at 10.1325 bar. Values given as percentage deviations from published partition coefficients at low pressure (Crovetto *et al.*, 1982; Smith, 1985). Averages are presented in bold. Uncertainty is quoted as standard error. All values given to 1 decimal place.

Noble Gas	ε scale factor	293.15K (MPa)	S.E. (MPa)	303.15K (MPa)	S.E. (MPa)	313.15K (MPa)	S.E. (MPa)	323.15K (MPa)	S.E. (MPa)	333.15K (MPa)	S.E. (MPa)	343.15K (MPa)	S.E. (MPa)	353.15K (MPa)	S.E. (MPa)
Krypton	Exp	2012.6		2490.7		2948.3		3362.6		3717.0		4001.9		4213.7	
	1	4123.3	759.6	3332.3	555.4	6662.6	980.6	4725.1	755.9	5328.4	374.1	5075.6	876.3	6403.2	418.8
	1.05	2199.2	709.6	2342.4	375.8	3218.1	729.7	5409.2	972.9	3682.4	735.9	3663.2	715.6	5375.9	312.6
	1.1	N/A	N/A	1330.5	252.6	1516.6	286.9	1959.4	647.5	2013.0	350.7	2397.1	118.0	2776.0	396.9

Table AII.13. Absolute Henry's coefficients for scaled krypton ε_{ij} values at 1.01325 bar. Exp denotes experimental partition coefficients for the same temperature (Crovetto *et al.*, 1982; Smith, 1985). Uncertainty is quoted as standard error. N/A indicates no Henry's constants were obtained for that temperature. All values given to 1 decimal place.

Noble Gas	ε scale factor	293.15K (MPa)	S.E. (MPa)	303.15K (MPa)	S.E. (MPa)	313.15K (MPa)	S.E. (MPa)	323.15K (MPa)	S.E. (MPa)	333.15K (MPa)	S.E. (MPa)	343.15K (MPa)	S.E. (MPa)	353.15K (MPa)	S.E. (MPa)
Krypton	Exp	2012.6		2490.7		2948.3		3362.6		3717.0		4001.9		4213.7	
	1	3967.2	681.2	3744.6	760.7	5094.3	579.9	5293.4	698.0	6538.8	834.8	5428.6	472.8	4497.4	421.8
	1.05	1465.7	475.9	2976.4	862.7	3246.3	1230.4	3285.3	715.6	2981.3	556.5	3302.4	376.8	4446.1	417.5
	1.1	967.5	373.0	954.8	285.7	1183.4	214.7	1880.1	519.7	2313.9	375.5	1931.8	113.7	2147.6	343.0

Table AII.14. Absolute Henry's coefficients for scaled krypton ε_{ij} values at 10.1325 bar. Exp denotes experimental partition coefficients for the same temperature (Crovetto *et al.*, 1982; Smith, 1985). Uncertainty is quoted as standard error. N/A indicates no Henry's constants were obtained for that temperature. All values given to 1 decimal place.

Noble Gas	ε scale factor	293.15K (%)	S.E. (%)	303.15K (%)	S.E. (%)	313.15K (%)	S.E. (%)	323.15K (%)	S.E. (%)	333.15K (%)	S.E. (%)	343.15K (%)	S.E. (%)	353.15K (%)	S.E. (%)	**Ave (%)**	**S.E. (%)**
Krypton	1	104.9	18.4	33.8	16.7	126.0	14.7	40.5	16.0	43.4	7.0	26.8	17.3	52.0	6.5	**61.0**	**13.8**
	1.05	9.3	32.3	-6.0	16.0	9.1	22.7	60.9	18.0	-0.9	20.0	-8.5	19.5	27.6	5.8	**13.1**	**19.2**
	1.1	N/A	N/A	-46.6	19.0	-48.6	18.9	-41.7	33.0	-45.8	17.4	-40.1	4.9	-34.1	14.3	**-36.7**	**15.4**

Table AII.15. Deviations of krypton simulations for scaled ε_{ij} values at 1.01325 bar. Values given as percentage deviations from published partition coefficients at low pressure (Crovetto *et al.*, 1982; Smith, 1985). Averages are presented in bold. Uncertainty is quoted as standard error. All values given to 1 decimal place.

Noble Gas	ε scale factor	293.15K (%)	S.E. (%)	303.15K (%)	S.E. (%)	313.15K (%)	S.E. (%)	323.15K (%)	S.E. (%)	333.15K (%)	S.E. (%)	343.15K (%)	S.E. (%)	353.15K (%)	S.E. (%)	**Ave (%)**	**S.E. (%)**
Krypton	1	97.1	17.2	50.3	20.3	72.8	11.4	57.4	13.2	75.9	12.8	35.7	8.7	6.7	9.4	**56.6**	**13.3**
	1.05	-27.2	32.5	19.5	29.0	10.1	37.9	-2.3	21.8	-19.8	18.7	-17.5	11.4	5.5	9.4	**-4.5**	**22.9**
	1.1	-51.9	38.6	-61.7	29.9	-59.9	18.1	-44.1	27.6	-37.7	16.2	-51.7	5.9	-49.0	16.0	**-50.9**	**21.8**

Table AII.16. Deviations of krypton simulations for scaled ε_{ij} values at 10.1325 bar. Values given as percentage deviations from published partition coefficients at low pressure (Crovetto *et al.*, 1982; Smith, 1985). Averages are presented in bold. Uncertainty is quoted as standard error. All values given to 1 decimal place.

Noble Gas	ε scale factor	293.15K (MPa)	S.E. (MPa)	303.15K (MPa)	S.E. (MPa)	313.15K (MPa)	S.E. (MPa)	323.15K (MPa)	S.E. (MPa)	333.15K (MPa)	S.E. (MPa)	343.15K (MPa)	S.E. (MPa)	353.15K (MPa)	S.E. (MPa)
Xenon	Exp	1151.0		1513.4		1876.1		2216.2		2516.1		2764.6		2956.7	
	0.5	234548.6	57315.2	151231.3	51802.3	123567.1	25639.7	155884.6	27459.4	168875.0	63978.4	163956.3	31884.8	169439.8	28325.9
	1	772.0	263.2	1806.0	739.3	2456.1	820.2	2132.8	526.4	2872.9	339.0	3530.9	697.8	3566.9	558.0
	1.02	866.4	544.3	617.4	310.6	2713.1	1515.9	2006.2	563.8	3060.6	1753.3	1672.3	79.2	2346.0	429.0
	1.05	67.0	63.2	72.8	62.5	138.6	115.6	221.9	180.9	270.7	219.0	807.6	432.0	1294.4	597.4
	1.1	31.7	27.8	88.0	78.1	88.0	78.1	88.0	78.1	88.0	78.1	88.0	78.1	764.7	175.3
	2	2.0	0.2	2.1	0.1	1.6	0.1	1.3	0.0	1.5	0.1	1.5	0.0	2.0	0.1

Table AII.17. Absolute Henry's coefficients for scaled xenon ε_{ij} values at 1.01325 bar. Exp denotes experimental partition coefficients for the same temperature (Crovetto *et al.*, 1982; Smith, 1985). Uncertainty is quoted as standard error. All values given to 1 decimal place.

Noble Gas	ε scale factor	293.15K (MPa)	S.E. (MPa)	303.15K (MPa)	S.E. (MPa)	313.15K (MPa)	S.E. (MPa)	323.15K (MPa)	S.E. (MPa)	333.15K (MPa)	S.E. (MPa)	343.15K (MPa)	S.E. (MPa)	353.15K (MPa)	S.E. (MPa)
Xenon	Exp	1151.0		1513.4		1876.1		2216.2		2516.1		2764.6		2956.7	
	0.5	670138.9	251655.5	165347.6	59631.9	235311.2	102693.8	213585.6	58873.1	317235.4	45072.6	135064.0	11881.3	117138.7	14688.0
	1	1900.5	665.2	760.5	140.8	1714.1	335.6	1818.9	557.8	2065.2	341.7	2562.5	482.6	2447.8	317.9
	1.02	798.6	322.6	1152.4	442.1	1417.0	460.8	2128.0	539.0	1613.9	309.2	2455.4	485.8	2638.8	606.8
	1.05	106.3	69.0	123.1	68.3	198.3	131.9	304.6	282.5	304.6	199.7	566.4	436.4	800.1	591.9
	1.1	60.0	27.6	83.6	51.7	117.4	83.6	146.1	115.3	219.0	149.3	318.7	191.7	463.2	210.4
	2	17.4	0.8	14.4	0.7	13.6	0.5	9.5	0.4	8.4	0.3	8.6	0.3	8.6	0.2

Table AII.18. Absolute Henry's coefficients for scaled xenon ε_{ij} values at 10.1325 bar. Exp denotes experimental partition coefficients for the same temperature (Crovetto *et al.*, 1982; Smith, 1985). Uncertainty is quoted as standard error. All values given to 1 decimal place.

Noble Gas	ε scale factor	293.15K (%)	S.E. (%)	303.15K (%)	S.E. (%)	313.15K (%)	S.E. (%)	323.15K (%)	S.E. (%)	333.15K (%)	S.E. (%)	343.15K (%)	S.E. (%)	353.15K (%)	S.E. (%)	**Ave (%)**	**S.E. (%)**
Xenon	0.5	20277.5	24.4	9893.1	34.3	6486.5	20.7	6934.0	17.6	6611.9	37.9	5830.6	19.4	5630.8	16.7	**8809.2**	**24.4**
	1	-32.9	34.1	19.3	40.9	30.9	33.4	-3.8	24.7	14.2	11.8	27.7	19.8	20.6	15.6	**10.9**	**25.8**
	1.02	-24.7	62.8	-59.2	50.3	44.6	55.9	-9.5	28.1	21.6	57.3	-39.5	4.7	-20.7	18.3	**-12.5**	**39.6**
	1.05	-94.2	94.4	-95.2	85.9	-92.6	83.4	-90.0	81.5	-89.2	80.9	-70.8	53.5	-56.2	46.2	**-84.0**	**75.1**
	1.1	-97.2	87.6	-94.2	88.8	-95.3	88.8	-96.0	88.8	-96.5	88.8	-96.8	88.8	-74.1	22.9	**-92.9**	**79.2**
	2	-99.8	7.8	-99.9	5.5	-99.9	3.9	-99.9	3.3	-99.9	3.6	-99.9	2.2	-99.9	2.6	**-99.9**	**4.1**

Table AII.19. Deviations of xenon simulations for scaled ε_{ij} values at 1.01325 bar. Values given as percentage deviations from published partition coefficients at low pressure (Crovetto *et al.*, 1982; Smith, 1985). Averages are presented in bold. Uncertainty is quoted as standard error. All values given to 1 decimal place.

Noble Gas	ε scale factor	293.15K (%)	S.E. (%)	303.15K (%)	S.E. (%)	313.15K (%)	S.E. (%)	323.15K (%)	S.E. (%)	333.15K (%)	S.E. (%)	343.15K (%)	S.E. (%)	353.15K (%)	S.E. (%)	**Ave (%)**	**S.E. (%)**
Xenon	0.5	58121.4	37.6	10825.8	36.1	12442.8	43.6	9537.6	27.6	12508.4	14.2	4785.5	8.8	3861.8	12.5	**16011.9**	**25.8**
	1	65.1	35.0	-49.7	18.5	-8.6	19.6	-17.9	30.7	-17.9	16.5	-7.3	18.8	-17.2	13.0	**-7.7**	**21.7**
	1.02	-30.6	40.4	-23.8	38.4	-24.5	32.5	-4.0	25.3	-35.9	19.2	-11.2	19.8	-10.8	23.0	**-20.1**	**28.4**
	1.05	-90.8	64.9	-91.9	55.5	-89.4	66.5	-86.3	92.7	-87.9	65.6	-79.5	77.1	-72.9	74.0	**-85.5**	**70.9**
	1.1	-94.8	46.0	-94.5	61.8	-93.7	71.2	-93.4	78.9	-91.3	68.2	-88.5	60.1	-84.3	45.4	**-91.5**	**61.6**
	2	-98.5	4.5	-99.0	5.0	-99.3	3.5	-99.6	4.0	-99.7	3.1	-99.7	4.0	-99.7	2.4	**-99.3**	**3.8**

Table AII.20. Deviations of xenon simulations for scaled ε_{ij} values at 10.1325 bar. Values given as percentage deviations from published partition coefficients at low pressure (Crovetto *et al.*, 1982; Smith, 1985). Averages are presented in bold. Uncertainty is quoted as standard error. All values given to 1 decimal place.

Appendix III

Low pressure CO_2-water simulation data tables

Noble Gas	ε scale factor	293.15K (MPa)	S.E. (MPa)	303.15K (MPa)	S.E. (MPa)	313.15K (MPa)	S.E. (MPa)	323.15K (MPa)	S.E. (MPa)	333.15K (MPa)	S.E. (MPa)	343.15K (MPa)	S.E. (MPa)	353.15K (MPa)	S.E. (MPa)
Helium	Exp	14425.6		14712.7		14723.2		14494.7		14070.5		13495.0		12810.2	14425.6
	0.91	13231.5	41.5	13382.0	682.0	11955.5	539.5	13735.0	1209.0	12603.5	405.5	11210.5	71.5	9939.0	13231.5
	1	12988.0	416.0	14294.0	1239.0	12684.5	274.5	12297.0	61.0	11815.5	65.5	11685.5	231.5	10203.9	12988.0
Neon	Exp	12134.1		12851.2		13299.0		13495.2		13468.8		13254.9		12890.2	12134.1
	0.8	12623.0	168.0	13227.0	1035.0	11993.5	681.5	14704.5	1415.5	13490.0	515.0	11981.5	87.5	10611.2	12623.0
	1	9342.2	766.8	11224.0	1095.0	9688.7	454.3	9931.3	51.4	9783.7	126.2	10021.8	167.3	8719.6	9342.2
Argon	Exp	3707.1		4405.6		5037.1		5572.0		5991.9		6289.2		6465.5	3707.1
	1.1	2170.6	350.0	3327.3	1179.8	3148.6	177.8	5311.4	459.4	5297.1	288.7	4605.0	100.9	4286.0	2170.6
	1	6046.2	2107.8	9365.1	952.0	6309.9	1226.5	8479.2	63.3	8687.4	485.3	8483.0	255.9	7002.3	6046.2
Krypton	Exp	2012.6		2490.7		2948.3		3362.6		3717.0		4001.9		4213.7	2012.6
	1.05	1214.2	354.1	2084.4	1005.9	2086.9	108.1	3740.5	223.2	3905.1	417.7	3218.9	214.1	2999.5	1214.2
	1	4555.4	2735.9	6588.9	1398.4	3815.7	872.3	5781.2	427.2	6325.4	885.9	5265.8	224.7	4281.2	4555.4
Xenon	Exp	1151.0		1513.4		1876.1		2216.2		2516.1		2764.6		2956.7	1151.0
	1	726.5	390.8	930.9	592.4	1020.0	28.3	2067.9	362.6	2540.4	821.5	1637.0	242.2	1850.8	726.5

Table AIII.1. Absolute Henry's coefficients for experimental, optimised and unoptimised values of ε_{ij} at 1.01325 bar. Absolute simulation values and uncertainties calculated using methods outlined in 3.7.2 and 3.8. Experimental values taken from Crovetto *et al.*, and Smith (Crovetto *et al.*, 1982; Smith, 1985). Uncertainty is quoted as standard error. Averages are presented in bold. All values given to 1 decimal place.

Noble Gas	ε scale factor	293.15K (MPa)	S.E. (MPa)	303.15K (MPa)	S.E. (MPa)	313.15K (MPa)	S.E. (MPa)	323.15K (MPa)	S.E. (MPa)	333.15K (MPa)	S.E. (MPa)	343.15K (MPa)	S.E. (MPa)	353.15K (MPa)	S.E. (MPa)
Helium	Exp	14425.6		14712.7		14723.2		14494.7		14070.5		13495.0		12810.2	
	0.91	14145.0	486.0	14316.5	1437.5	13396.0	414.0	12440.5	111.5	12283.0	491.0	12401.5	134.5	10810.5	232.5
	1	13474.0	1252.0	13121.5	11.5	13882.0	270.0	11772.5	260.5	12616.5	544.5	11310.5	58.5	10605.4	783.7
Neon	Exp	12134.1		12851.2		13299.0		13495.2		13468.8		13254.9		12890.2	
	0.8	13713.0	328.0	14443.0	2027.0	14011.5	490.5	12888.5	99.5	12961.0	498.0	13576.0	26.0	11733.0	420.0
	1	9580.9	942.1	9719.5	39.3	10876.5	358.5	9420.8	192.1	10646.0	531.0	9665.7	51.6	9350.3	846.8
Argon	Exp	3707.1		4405.6		5037.1		5572.0		5991.9		6289.2		6465.5	
	1.1	3397.5	230.5	3947.8	1631.8	4921.9	198.3	4915.3	442.5	5165.2	345.2	6738.9	67.0	5376.6	4.7
	1	5227.4	625.2	4935.1	17.9	7656.7	415.0	6401.1	227.7	9018.4	322.1	9138.6	192.1	8777.0	1802.0
Krypton	Exp	2012.6		2490.7		2948.3		3362.6		3717.0		4001.9		4213.7	
	1.05	1879.5	282.2	2392.3	980.6	3777.8	371.6	3648.1	366.2	3759.8	35.4	5459.7	262.5	4457.4	309.1
	1	2461.8	472.8	2497.1	197.1	4960.8	635.6	3428.8	53.1	6152.9	25.8	6774.0	754.5	6572.7	1923.3
Xenon	Exp	1151.0		1513.4		1876.1		2216.2		2516.1		2764.6		2956.7	
	1	1715.6	546.9	674.0	102.8	3313.1	875.1	2502.2	248.3	2368.1	34.4	3840.2	806.9	3472.6	801.8

Table AIII.2. Absolute Henry’s coefficients for experimental, optimised and unoptimised values of ε_{ij} at 10.1325 bar. Absolute simulation values and uncertainties calculated using methods outlined in 3.7.2 and 3.8. Experimental values taken from Crovetto *et al.*, and Smith (Crovetto *et al.*, 1982; Smith, 1985). Uncertainty is quoted as standard error. All values given to 1 decimal place.

Noble Gas	ε scale factor	293.15K (%)	S.E. (%)	303.15K (%)	S.E. (%)	313.15K (%)	S.E. (%)	323.15K (%)	S.E. (%)	333.15K (%)	S.E. (%)	343.15K (%)	S.E. (%)	353.15K (%)	S.E. (%)	**Ave (%)**	**S.E. (%)**
Helium	0.91	-8.3	0.3	-9.0	5.1	-18.8	4.5	-5.2	8.8	-10.4	3.2	-16.9	0.6	-22.4	5.3	**-13.0**	**4.0**
	1	-10.0	3.2	-2.8	8.7	-13.8	2.2	-15.2	0.5	-16.0	0.6	-13.4	2.0	-20.3	5.4	**-13.1**	**3.2**
Neon	0.8	4.0	1.3	2.9	7.8	-9.8	5.7	9.0	9.6	0.2	3.8	-9.6	0.7	-17.7	6.8	**-3.0**	**5.1**
	1	-23.0	8.2	-12.7	9.8	-27.1	4.7	-26.4	0.5	-27.4	1.3	-24.4	1.7	-32.4	7.7	**-24.8**	**4.8**
Argon	1.1	-41.4	16.1	-24.5	35.5	-37.5	5.6	-4.7	8.6	-11.6	5.5	-26.8	2.2	-33.7	8.7	**-25.7**	**11.7**
	1	63.1	34.9	112.6	10.2	25.3	19.4	52.2	0.7	45.0	5.6	34.9	3.0	8.3	19.5	**48.8**	**13.3**
Krypton	1.05	-39.7	29.2	-16.3	48.3	-29.2	5.2	11.2	6.0	5.1	10.7	-19.6	6.6	-28.8	14.2	**-16.8**	**17.2**
	1	126.3	60.1	164.5	21.2	29.4	22.9	71.9	7.4	70.2	14.0	31.6	4.3	1.6	18.8	**70.8**	**21.2**
Xenon	1	-36.9	53.8	-38.5	63.6	-45.6	2.8	-6.7	17.5	1.0	32.3	-40.8	14.8	-37.4	38.2	**-29.3**	**31.9**

Table AIII.3. Deviations of chemical potential simulations for optimised and unoptimised values of ε_{ij} at 1.01325 bar. Values given as percentage deviations from published partition coefficients at low pressure (Crovetto *et al.*, 1982; Smith, 1985). Uncertainty is quoted as standard error. Averages are presented in bold. All values given to 1 decimal place.

Noble Gas	ε scale factor	293.15K (%)	S.E. (%)	303.15K (%)	S.E. (%)	313.15K (%)	S.E. (%)	323.15K (%)	S.E. (%)	333.15K (%)	S.E. (%)	343.15K (%)	S.E. (%)	353.15K (%)	S.E. (%)	**Ave (%)**	**S.E. (%)**
Helium	0.91	-1.9	3.4	-2.7	10.0	-9.0	3.1	-14.2	0.9	-12.7	4.0	-8.1	1.1	-15.6	2.2	**-9.2**	**3.5**
	1	-6.6	9.3	-10.8	0.1	-5.7	1.9	-18.8	2.2	-10.3	4.3	-16.2	0.5	-17.2	7.4	**-12.2**	**3.7**
Neon	0.8	13.0	2.4	12.4	14.0	5.4	3.5	-4.5	0.8	-3.8	3.8	2.4	0.2	-9.0	3.6	**2.3**	**4.0**
	1	-21.0	9.8	-24.4	0.4	-18.2	3.3	-30.2	2.0	-21.0	5.0	-27.1	0.5	-27.5	9.1	**-24.2**	**4.3**
Argon	1.1	-8.4	6.8	-10.4	41.3	-2.3	4.0	-11.8	9.0	-13.8	6.7	7.1	1.0	-16.8	0.1	**-8.0**	**9.8**
	1	41.0	12.0	12.0	0.4	52.0	5.4	14.9	3.6	50.5	3.6	45.3	2.1	35.8	20.5	**35.9**	**6.8**
Krypton	1.05	-6.6	15.0	-3.9	41.0	28.1	9.8	8.5	10.0	1.2	0.9	36.4	4.8	5.8	6.9	**9.9**	**12.7**
	1	22.3	19.2	0.3	7.9	68.3	12.8	2.0	1.5	65.5	0.4	69.3	11.1	56.0	29.3	**40.5**	**11.8**
Xenon	1	49.1	31.9	-55.5	15.2	76.6	26.4	12.9	9.9	-5.9	1.5	38.9	21.0	17.4	23.1	**19.1**	**18.4**

Table AIII.4. Deviations of chemical potential simulations for optimised and unoptimised values of ε_{ij} at 10.1325 bar. Values given as percentage deviations from published partition coefficients at low pressure (Crovetto *et al.*, 1982; Smith, 1985). Averages are presented in bold. Uncertainty is quoted as standard error. All values given to 1 decimal place.

Appendix IV

High pressure CO_2-water simulation data tables

Experiment		Helium	S.E.	Neon	S.E.	Argon	S.E.	Krypton	S.E.	Xenon	S.E.
1	Pub.	97.2		90.5		37.4		22.5		14.9	
	Sim.	89.0	3.4	92.1	4.6	33.7	2.4	24.2	2.0	14.4	1.8
2	Pub.	97.2		90.5		37.4		22.5		14.9	
	Sim.	86.9	4.3	88.8	5.9	32.0	3.5	20.5	2.7	11.2	2.0
3	Pub.	97.2		90.5		37.4		22.5		14.9	
	Sim.	85.2	5.7	86.7	7.7	32.4	4.7	22.3	3.9	12.6	3.3
4	Pub.	89.8		86.6		39.3		24.5		16.7	
	Sim.	81.5	1.0	86.5	1.4	37.3	1.5	27.8	1.8	17.9	2.3
5	Pub.	82.2		81.6		39.8		25.6		17.8	
	Sim.	67.4	3.0	71.0	4.0	30.9	2.6	22.6	2.2	13.8	1.9
6	Pub.	81.9		81.5		39.8		25.6		17.8	
	Sim.	70.7	2.3	75.6	3.2	33.9	2.4	26.3	2.5	16.5	2.1
7	Pub.	65.4		68.8		37.7		25.7		18.4	
	Sim.	52.8	0.7	57.4	1.0	30.7	1.0	24.6	0.9	17.5	0.9
8	Pub.	62.2		66.1		36.9		25.5		18.3	
	Sim.	52.8	1.1	58.0	1.1	31.5	1.2	25.2	1.3	17.4	1.5
9	Pub.	65.4		68.8		37.7		25.7		18.4	
	Sim.	56.3	0.4	61.7	0.6	33.6	0.5	27.1	0.6	19.1	0.6

Table AIV.1. Simulated partition coefficients for experimental conditions. Sim. and pub. denote simulation and published values respectively. Published values are taken from Crovetto *et al.*, and smith (Crovetto *et al.*, 1982; Smith, 1985) and are presented as unitless ratios between the CO_2 and water phase. Uncertainty is quoted as standard error. All values given to 1 decimal place.

Temp. (K)	Press. (bar)	y_{H_2O} (x10^3) (Sim.)	y_{H_2O} (x10^3) (Pub.)	Dev (%)	x_{CO_2} (x10^2) (Sim.)	x_{CO_2} (x10^2) (Pub.)	Dev (%)
323.07	89.40	0.8 ±0.03	3.91	-79.65	2.04 ±0.1	1.91	7.22
322.85	112.70	0.79 ±0.03	5.09	-84.45	2.53 ±0.18	2.11	20.05
322.85	134.12	0.84 ±0.03	5.85	-85.69	2.79 ±0.23	2.14	30.42
335.96	95.55	1.42 ±0.03	4.79	-70.29	1.69 ±0.07	1.82	-7.02
347.77	113.46	2.11 ±0.06	6.97	-69.79	2.05 ±0.14	1.92	7.13
348.22	129.30	2.08 ±0.05	8.04	-74.06	2.02 ±0.12	1.92	4.80
374.15	92.64	6.69 ±0.11	26.18	-74.45	1.36 ±0.04	1.31	4.24
377.15	112.84	6.73 ±0.13	26.71	-74.81	1.49 ±0.04	1.49	-0.30
373.14	134.26	5.38 ±0.11	27.27	-80.28	1.64 ±0.04	1.66	-0.77

Table AIV.2. Simulated mutual solubilities of CO_2 and water for experimental conditions. Sim. and pub. denote simulation and published values respectively. Dev. is the deviation of simulation values from their published counterparts. Published values are taken from Spycher *et al.*, (and references therein) (Spycher *et al.*, 2003). Uncertainty is quoted as standard error. All values given to 2 decimal places.

Chapter Seven

References

Allegre, C. J., Staudacher, T. & Sarda, P. (1987). Rare gas systematics: Formation of the atmosphere, evolution and structure of the Earth's mantle. *Earth and Planetary Science Letters* **81**(2-3): 127-150.

Allen, M. P. & Tildesley, D. J. (1987). *Computer simulation of liquids*, Clarendon Press.

Andersen, H. C. (1983). Rattle - a velocity version of the Shake algorithm for molecular dynamics calculations. *Journal of Computational Physics* **52**(1): 24-34.

Attard, P. (1993). Simulation of the chemical potential and the cavity free energy of dense hard sphere fluids. *Journal of Chemical Physics* **98**(3): 2225-2231.

Aubry, G., Sator, N. & Guillot, B. (2013). Vesicularity, bubble formation and noble gas fractionation during MORB degassing. *Chemical Geology* **343**: 85-98.

Bachu, S. (2003). Screening and ranking of sedimentary basins for sequestration of CO_2 in geological media in response to climate change. *Environmental Geology* **44**(3): 277-289.

Bachu, S., Bonijoly, D., Bradshaw, J., Burruss, R., Holloway, S., Christensen, N. P. & Mathiassen, O. M. (2007). CO_2 storage capacity estimation: Methodology and gaps. *International Journal of Greenhouse Gas Control* **1**(4): 430-443.

Baiker, A. (1999). Supercritical fluids in heterogeneous catalysis. *Chemical Reviews* **99**(2): 453-473.

Ballentine, C. J. (1997). Resolving the mantle He/Ne and crustal $^{21}Ne/^{22}Ne$ in well gases. *Earth and Planetary Science Letters* **152**(1-4): 233-249.

Ballentine, C. J., Brandenburg, J. P., van Keken, P. E. & Holland, G. (2007). Seawater recycling into the deep mantle - And the source of ^{3}He? *Geochimica Et Cosmochimica Acta* **71**(15): A56-A56.

Ballentine, C. J., Burgess, R. & Marty, B. (2002). Tracing fluid origin, transport and interaction in the crust *in* Porcelli, D., Ballentine, C. J., & Wieler, R. (Eds.). *Noble Gases in Geochemistry and Cosmochemistry. Reviews in Mineralogy and Geochemistry*, Mineralogical Society of America. **47:** 539-614.

Ballentine, C. J. & Burnard, P. G. (2002). Production, release and transport of noble gases in the continental crust *in* Porcelli, D., Ballentine, C. J., & Wieler, R. (Eds.). *Noble Gases in Geochemistry and Cosmochemistry. Reviews in Mineralogy and Geochemistry*, Mineralogical Society of America. **47:** 481-538.

Ballentine, C. J. & Holland, G. (2008). What CO_2 well gases tell us about the origin of noble gases in the mantle and their relationship to the atmosphere. *Philosophical Transactions of the Royal Society a-Mathematical Physical and Engineering Sciences* **366**(1883): 4183-4203.

Ballentine, C. J., Marty, B., Lollar, B. S. & Cassidy, M. (2005). Neon isotopes constrain convection and volatile origin in the Earth's mantle. *Nature* **433**(7021): 33-38.

Ballentine, C. J., ONions, R. K. & Coleman, M. L. (1996). A Magnus opus: Helium, neon, and argon isotopes in a North Sea oilfield. *Geochimica Et Cosmochimica Acta* **60**(5): 831-849.

Ballentine, C. J., Onions, R. K., Oxburgh, E. R., Horvath, F. & Deak, J. (1991). Rare gas constraints on hydrocarbon accumulation, crustal degassing and groundwater flow in the Pannonian Basin. *Earth and Planetary Science Letters* **105**(1-3): 229-246.

Ballentine, C. J., Schoell, M., Coleman, D. & Cain, B. A. (2001). 300 Myr old magmatic CO_2 in natural gas reservoirs of the West Texas Permian basin. *Nature* **409**(6818): 327-331.

Battani, A., Sarda, P. & Prinzhofer, A. (2000). Basin scale natural gas source, migration and trapping traced by noble gases and major elements: the Pakistan Indus basin. *Earth and Planetary Science Letters* **181**(1-2): 229-249.

Berendsen, H. J. C., Grigera, J. R. & Straatsma, T. P. (1987). The missing term in effective pair potentials. *Journal of Physical Chemistry* **91**(24): 6269-6271.

Berendsen, H. J. C., Postma, J. P. M., Van Gunsteren, W. F. & Hermans, J. (1981). Interaction models for water in relation to protein hydration in Pullman, B. (Ed.). *Intermolecular Forces*, Reidel, D.**:** 331-342.

Berendsen, H. J. C., Postma, J. P. M., Vangunsteren, W. F., Dinola, A. & Haak, J. R. (1984). Molecular dynamics with coupling to an external bath. *Journal of Chemical Physics* **81**(8): 3684-3690.

Bernardo, D. N., Ding, Y. B., Kroghjespersen, K. & Levy, R. M. (1994). An anisotropic polarizable water model: Incorporation of all-atom polarizabilities into molecular mechanics force fields. *Journal of Physical Chemistry* **98**(15): 4180-4187.

Bickle, M., Chadwick, A., Huppert, H. E., Hallworth, M. & Lyle, S. (2007). Modelling carbon dioxide accumulation at Sleipner: Implications for underground carbon storage. *Earth and Planetary Science Letters* **255**(1-2): 164-176.

Biggerstaff, D. R. & Wood, R. H. (1988). Apparent Molar Volumes of Aqueous Argon, Ethylene, and Xenon from 300-K to 716-K. *Journal of Physical Chemistry* **92**(7): 1988-1994.

Birkett, G. R. & Do, D. D. (2007). Simulation study of water adsorption on carbon black: The effect of graphite water interaction strength. *Journal of Physical Chemistry C* **111**(15): 5735-5742.

Black, H. (1996). Supercritical carbon dioxide: The "greener" solvent. *Environmental Science & Technology* **30**(3): A124-A127.

Blunt, M., Fayers, F. J. & Orr, F. M. (1993). Carbon dioxide in enhanced oil recovery. *Energy Conversion and Management* **34**(9-11): 1197-1204.

Boda, D. & Henderson, D. (2008). The effects of deviations from Lorentz-Berthelot rules on the properties of a simple mixture. *Molecular Physics* **106**(20): 2367-2370.

Botti, A., Bruni, F., Isopo, A., Modesti, G., Oliva, C., Ricci, M. A., Senesi, R. & Soper, A. K. (2003). Water structure in supercritical mixtures of water and rare gases. *Journal of Chemical Physics* **118**(1): 235-241.

Bourg, I. C. & Sposito, G. (2008). Isotopic fractionation of noble gases by diffusion in liquid water: Molecular dynamics simulations and hydrologic applications. *Geochimica Et Cosmochimica Acta* **72**(9): 2237-2247.

Brennwald, M. S., Vogel, N., Scheidegger, Y., Tomonaga, Y., Livingstone, D. M. & Kipfer, R. (2012). Noble gases as environmental tracers in sediment porewaters and in stalagmite fluid inclusions. *The Noble Gases as Geochemical Tracers*. P. Burnard, Springer**:** 123-154.

Brown, H. (1952). Rare gases and formation of the Earth's atmosphere. *The atmospheres of the Earth and Planets*. G. P. Kuiper. Chicago, University of Chicago Press**:** 258-266.

Burnard, P. G., Hu, R., Turner, G. & Bi, X. W. (1999). Mantle, crustal and atmospheric noble gases in Ailaoshan Gold deposits, Yunnan Province, China. *Geochimica Et Cosmochimica Acta* **63**(10): 1595-1604.

Caffee, M. W., Hudson, G. U., Velsko, C., Huss, G. R., Alexander, E. C. & Chivas, A. R. (1999). Primordial noble cases from Earth's mantle: Identification of a primitive volatile component. *Science* **285**(5436): 2115-2118.

Carlton, T. S. (1985). Relative atomic radii from scaling of repulsive interatomic force in noble gas Van der Waals molecules. *Journal of Chemical Physics* **82**(5): 2341-2345.

Carroll, M. R. & Draper, D. S. (1994). Noble gases as trace elements in magmatic processes. *Chemical Geology* **117**(1-4): 37-56.

Castro, M. C., Warrier, R. B., Hall, C. M. & Lohmann, K. C. (2012). A late Pleistocene-Mid-Holocene noble gas and stable isotope climate and subglacial record in southern Michigan. *Geophysical Research Letters* **39**.

Cey, B. D., Hudson, G. B., Moran, J. E. & Scanlon, B. R. (2009). Evaluation of noble gas recharge temperatures in a shallow unconfined aquifer. *Ground Water* **47**(5): 646-659.

Chatzis, G. & Samios, J. (2003). Binary mixtures of supercritical carbon dioxide with methanol. A molecular dynamics simulation study. *Chemical Physics Letters* **374**(1-2): 187-193.

Chun, M. S. (2003). A novel simulation architecture of configurational-bias Gibbs-Ensemble Monte Carlo for the conformation of polyelectrolytes partitioned in confined spaces. *Macromolecular Research* **11**(5): 393-397.

Cichowski, E. C., Schmidt, T. R. & Errington, J. R. (2005). Determination of Henry's law constants through transition matrix Monte Carlo simulation. *Fluid Phase Equilibria* **236**(1-2): 58-65.

Crovetto, R., Fernandez-Prini, R. & Japas, M. L. (1982). Solubilities of inert gases and methane in H_2O and in D_2O in the temperature range of 300 to 600 K. *Journal of Chemical Physics* **76**(76): 1077-1088.

Dai, J. X., Wang, L., Sun, Y. X., Wang, L. & Sun, H. A. (2011). Prediction of thermodynamic, transport and vapor-liquid equilibrium properties of binary mixtures of ethylene glycol and water. *Fluid Phase Equilibria* **301**(2): 137-144.

De Hoffmann, E. & Stroobant, V. (2007). *Mass Spectrometry: Principles and Applications*, Wiley-Blackwell.

Delhommelle, J. & Millie, P. (2001). Inadequacy of the Lorentz-Berthelot combining rules for accurate predictions of equilibrium properties by molecular simulation. *Molecular Physics* **99**(8): 619-625.

Diamond, L. W. & Akinfiev, N. N. (2003). Solubility of CO_2 in water from -1.5 to 100°C and from 0.1 to 100 MPa: Evaluation of literature data and thermodynamic modelling. *Fluid Phase Equilibria* **208**(1-2): 265-290.

Du, Z., Allan, N. L., Blundy, J. D., Purton, J. A. & Brooker, R. A. (2008). Atomistic simulation of the mechanisms of noble gas incorporation in minerals. *Geochimica Et Cosmochimica Acta* **72**(2): 554-573.

Dunai, T. J. & Porcelli, D. (2002). Storage and transport of noble gases in the subcontinental lithosphere in Porcelli, D., Ballentine, C. J., & Wieler, R. (Eds.). *Noble Gases in Geochemistry and Cosmochemistry. Reviews in Mineralogy and Geochemistry*, Mineralogical Society of America. **47:** 371-409.

Duxbury, A., White, D., Samson, C., Hall, S. A., Wookey, J. & Kendall, J. M. (2012). Fracture mapping using seismic amplitude variation with offset and azimuth analysis at the Weyburn CO_2 storage site. *Geophysics* **77**(6): B295-B306.

Dymond, J. H., Marsh, K. N., Wilhoit, R. C. & Wong, K. C. (2002). *Virial coefficients of pure gases and mixtures subvolume A: Virial coefficients of pure gases*, Springer-Verlag.

Enns, T., Scholand.Pf & Bradstre.Ed (1965). Effect of Hydrostatic Pressure on Gases Dissolved in Water. *Journal of Physical Chemistry* **69**(2): 389-&.

Errington, J. R. & Panagiotopoulos, A. Z. (1998). A fixed point charge model for water optimized to the vapor-liquid coexistence properties. *Journal of Physical Chemistry B* **102**(38): 7470-7475.

Even, W., Smith, J. & Roth, M. W. (2005). Molecular dynamics simulations of noble gases encapsulated in ^{60}C Fullerene. *Molecular Simulation* **31**(4): 207-213.

Ferrieri, R. A. (2003). Supercritical fluids in medical radioisotope processing and chemistry, Part II: Applications - real and demonstrated. *Journal of Labelled Compounds & Radiopharmaceuticals* **46**(10): 923-943.

Fincham, D. (1986). Choice of timestep in molecular dynamics simulation. *Computer Physics Communications* **40**(2-3): 263-269.

Forsman, J. & Woodward, C. E. (2010). Limitations of the Derjaguin Approximation and the Lorentz-Berthelot mixing rule. *Langmuir* **26**(7): 4555-4558.

Fotouh, K. & Shukla, K. (1997). Effect of quadrupole moment on excess properties of binary 2CLJQ mixtures from molecular dynamics simulation: model and real mixtures. *Fluid Phase Equilibria* **135**(1): 35-50.

Frenkel, D. & Smit, B. (2002). *Understanding Molecular Simulation: From Algorithms to Applications*, Elsevier.

Friedmann, S. J. (2007). Geological carbon dioxide sequestration. *Elements* **3**(3): 179-184.

Galliero, G., Boned, C., Baylaucq, A. & Montel, F. (2006). Molecular dynamics comparative study of Lennard-Jones alpha-6 and exponential alpha-6 potentials: Application to real simple fluids (viscosity and pressure). *Physical Review E* **73**(6).

Gerth, W. A. (1983). Effects of dissolved electrolytes on the solubility and partial molar volume of helium in water from 50 to 400 atmospheres at 25°C. *Journal of Solution Chemistry* **12**(9): 655-669.

Giddings, J. C., Myers, M. N., Mclaren, L. & Keller, R. A. (1968). High pressure gas chromatography of non-volatile species. *Science* **162**(3849): 67-73.

Gilfillan, S. M., Ballentine, C. J., Holland, G., Blagburn, D., Lollar, B. S., Stevens, S., Schoell, M. & Cassidy, M. (2008). The noble gas geochemistry of natural CO_2 gas reservoirs from the Colorado Plateau and Rocky Mountain provinces, USA. *Geochimica Et Cosmochimica Acta* **72**(4): 1174-1198.

Gilfillan, S. M. V., Lollar, B. S., Holland, G., Blagburn, D., Stevens, S., Schoell, M., Cassidy, M., Ding, Z. J., Zhou, Z., Lacrampe-Couloume, G. & Ballentine, C. J. (2009). Solubility trapping in formation water as dominant CO_2 sink in natural gas fields. *Nature* **458**(7238): 614-618.

Goldman, S., Joslin, C. & Wasserman, E. A. (1994). Theoretical calculation of the static dielectric constant of water at high temperatures and pressures. *Journal of Physical Chemistry* **98**(24): 6231-6233.

Graham, D. W. (2002). Noble gas isotope geochemistry of Mid-Ocean Ridge and Ocean Island Basalts: Characterization of mantle source reservoirs in Porcelli, D., Ballentine, C. J., & Wieler, R. (Eds.). *Noble Gases in Geochemistry and Cosmochemistry. Reviews in Mineralogy and Geochemistry*, Mineralogical Society of America. **47**.

Guillot, B. & Guissani, Y. (2001). How to build a better pair potential for water. *Journal of Chemical Physics* **114**(15): 6720-6733.

Guillot, B. & Sarda, P. (2006). The effect of compression on noble gas solubility in silicate melts and consequences for degassing at mid-ocean ridges. *Geochimica Et Cosmochimica Acta* **70**(5): 1215-1230.

Halliday, A. N. (2013). The origins of volatiles in the terrestrial planets. *Geochimica Et Cosmochimica Acta* **105**: 146-171.

Harris, J. G. & Yung, K. H. (1995). Carbon dioxide's liquid-vapor coexistence curve and critical properties as predicted by a simple molecular model. *Journal of Physical Chemistry* **99**(31): 12021-12024.

Heilweil, V. M., Healy, R. W. & Harris, R. N. (2012). Noble gases and coupled heat/fluid flow modeling for evaluating hydrogeologic conditions of volcanic island aquifers. *Journal of Hydrology* **464**: 309-327.

Higashi, H. & Tamura, K. (2010). Calculation of diffusion coefficient for supercritical carbon dioxide and carbon dioxide plus naphthalene system by molecular dynamics simulation using EPM2 model. *Molecular Simulation* **36**(10): 772-777.

Hilton, D. R. & Porcelli, D. (2003). Noble gases as mantle tracers *in* Carlson, R.W. Holland, H. & Turekian, K. (Eds.). *Treatise on Geochemistry*, Elsevier. **2:** 277-318.

Holland, G. & Ballentine, C. J. (2006). Seawater subduction controls the heavy noble gas composition of the mantle. *Nature* **441**(7090): 186-191.

Holland, G., Cassidy, M. & Ballentine, C. J. (2009). Meteorite Kr in Earth's mantle suggests a late accretionary source for the atmosphere. *Science* **326**(5959): 1522-1525.

Holland, G. & Gilfillan, S. (2012). Application of Noble Gases to the Viability of CO_2 storage in Burnard, P. (Ed.). *The Noble Gases as Geochemical Tracers*, Springer**:** 177-223.

Holloway, S. & Savage, D. (1993). The potential for aquifer disposal of carbon dioxide in the UK. *Energy Conversion and Management* **34**(9-11): 925-932.

Hoover, W. G. (1985). Canonical dynamics: Equilibrium phase-space distributions. *Physical Review A* **31**(3): 1695-1697.

Houndonougbo, Y., Kuczera, K., Subramaniam, B. & Laird, B. B. (2007). Prediction of phase equilibria and transport properties in carbon-dioxide expanded solvents by molecular simulation. *Molecular Simulation* **33**(9-10): 861-869.

Hu, R. Z., Bi, X. W., Jiang, G. H., Chen, H. W., Peng, J. T., Qi, Y. Q., Wu, L. Y. & Wei, W. F. (2012). Mantle-derived noble gases in ore-forming fluids of the granite-related Yaogangxian tungsten deposit, Southeastern China. *Mineralium Deposita* **47**(6): 623-632.

Hu, R. Z., Burnard, P. G., Bi, X. W., Zhou, M. F., Pen, J. T., Su, W. C. & Wu, K. X. (2004). Helium and argon isotope geochemistry of alkaline intrusion-associated gold and copper deposits along the Red River-Jinshajiang fault belt, SW China. *Chemical Geology* **203**(3-4): 305-317.

Huang, Y. L., Vrabec, J. & Hasse, H. (2009). Prediction of ternary vapor-liquid equilibria for 33 systems by molecular simulation. *Fluid Phase Equilibria* **287**(1): 62-69.

Hudson, G. H. & McCoubrey, J. C. (1960). Intermolecular forces between unlike molecules. A more complete form of the combining rules. *Transactions of the Faraday Society* **56**(6): 761-766.

IPCC (2005). *Carbon Dioxide Capture and Storage*, Cambridge University Press.

IPCC (2007). *Climate Change 2007: The Physical Science Basis*, Cambridge University Press.

Jahne, B., Heinz, G. & Dietrich, W. (1987). Measurement of the diffusion coefficients of sparingly soluble gases in water. *Journal of Geophysical Research Oceans* **92**(C10): 10767-10776.

Jambon, A., Weber, H. & Braun, O. (1986). Solubility of He, Ne, Ar, Kr and Xe in a basalt melt in the range 1250-1600°C. Geochemical Implications. *Geochimica Et Cosmochimica Acta* **50**(3): 401-408.

Jorgensen, W. L. (1981). Quantum and statistical mechanical studies of liquids .10. Transferable intermolecular potential functions for water, alcohols, and ethers. Application to liquid water. *Journal of the American Chemical Society* **103**(2): 335-340.

Jungwirth, P. & Tobias, D. J. (2002). Chloride anion on aqueous clusters, at the air-water interface, and in liquid water: Solvent effects on Cl- polarizability. *Journal of Physical Chemistry A* **106**(2): 379-383.

Kalinichev, A. G. (2001). Molecular simulations of liquid and supercritical water: Thermodynamics, structure, and hydrogen bonding. *Molecular Modelling Theory: Applications in the Geosciences*. R. T. Cygan and Kubicki, J. D., Minerealogical Society of America. **42:** 83-130.

Kamihira, M., Taniguchi, M. & Kobayashi, T. (1987). Removal of organic solvent from antibiotics with supercritical carbon dioxide. *Journal of Fermentation Technology* **65**(1): 71-75.

Katzer, J. (2007). *The Future of Coal. Options for a Carbon-Constrained World*, MIT.

Kauffman, J. F. (2001). Quadrupolar solvent effects on solvation and reactivity of solutes dissolved in supercritical CO_2. *Journal of Physical Chemistry A* **105**(14): 3433-3442.

Kendrick, M. A., Mark, G. & Phillips, D. (2007). Mid-crustal fluid mixing in a Proterozoic Fe oxide-Cu-Au deposit, Ernest Henry, Australia: Evidence from Ar, Kr, Xe, Cl, Br, and I. *Earth and Planetary Science Letters* **256**(3-4): 328-343.

Kennedy, B. M., Hiyagon, H. & Reynolds, J. H. (1990). Crustal neon: A striking uniformity. *Earth and Planetary Science Letters* **98**(3-4): 277-286.

Kennedy, B. M., Torgersen, T. & Van Soest, M. C. (2002). Multiple atmospheric noble gas components in hydrocarbon reservoirs: A study of the Northwest Shelf, Delaware Basin, SE New Mexico. *Geochimica Et Cosmochimica Acta* **66**(16): 2807-2822.

Kharaka, Y. K., Thordsen, J. J., Hovorka, S. D., Nance, H. S., Cole, D. R., Phelps, T. J. & Knauss, K. G. (2007). Subsurface monitoring of anthropogenic CO_2 injected in sedimentary basins: Results from the Frio-I brine test, Texas, USA. *Water-Rock Interaction, Vols 1 and 2, Proceedings*: 597-601.

Kim, W. J., Kim, J. D., Kim, J., Oh, S. G. & Lee, Y. W. (2008). Selective caffeine removal from green tea using supercritical carbon dioxide extraction. *Journal of Food Engineering* **89**(3): 303-309.

Kipfer, R., Aeschbach-Hertig, W., Peeters, F. & Stute, M. (2002). Noble gases in lakes and ground waters *in* Porcelli, D., Ballentine, C. J., & Wieler, R. (Eds.). *Noble Gases in Geochemistry and Cosmochemistry. Reviews in Mineralogy and Geochemistry*, Mineralogical Society of America. **47:** 615-700.

Klein, M. L., Aziz, R. A., Cohen, S. S. & Dubost, H. (1984). *Inert Gases - Potentials, Dynamics, and Energy Transfer in Doped Crystals*. Berlin, Springer-Verlag.

Kluge, T., Marx, T., Scholz, D., Niggemann, S., Mangini, A. & Aeschbach-Hertig, W. (2008). A new tool for palaeoclimate reconstruction: Noble gas temperatures from fluid inclusions in speleothems. *Earth and Planetary Science Letters* **269**(3-4): 407-414.

Klump, S., Grundl, T., Purtschert, R. & Kipfer, R. (2008). Groundwater and climate dynamics derived from noble gas, ^{14}C, and stable isotope data. *Geology* **36**(5): 395-398.

Klusman, R. W. (2011). Comparison of surface and near-surface geochemical methods for detection of gas microseepage from carbon dioxide sequestration. *International Journal of Greenhouse Gas Control* **5**(6): 1369-1392.

Kong, C. L. (1973). Combining rules for intermolecular potential parameters 2. Rules for Lennard-Jones (12-6) potential and morse potential. *Journal of Chemical Physics* **59**(5): 2464-2467.

Krause, D. & Benson, B. B. (1989). The solubility and isotopic fractionation of gases in dilute aqueous solution 2a. Solubilities of the noble-gases. *Journal of Solution Chemistry* **18**(9): 823-872.

Kulongoski, J. T. & Hilton, D. R. (2002). A quadrupole-based mass spectrometric system for the determination of noble gas abundances in fluids. *Geochemistry Geophysics Geosystems* **3**(6): U1-U10.

Leya, I. & Wieler, R. (1999). Nucleogenic production of Ne isotopes in Earth's crust and upper mantle induced by alpha particles from the decay of U and Th. *Journal of Geophysical Research-Solid Earth* **104**(B7): 15439-15450.

Li, H. P. & Maroncelli, M. (2006). Solvation and solvatochromism in CO_2-expanded liquids 1. Simulations of the solvent systems CO_2+cyclohexane, acetonitrile, and methanol. *Journal of Physical Chemistry B* **110**(42): 21189-21197.

Lippmann, J., Stute, M., Torgersen, T., Moser, D. P., Hall, J. A., Lin, L., Borcsik, M., Bellamy, R. E. S. & Onstott, T. C. (2003). Dating ultra-deep mine waters with noble gases and ^{36}Cl, Witwatersrand Basin, South Africa. *Geochimica Et Cosmochimica Acta* **67**(23): 4597-4619.

Lisal, M., William, W. R. S. & Nezbeda, I. (2001). Accurate vapour-liquid equilibrium calculations for complex systems using the reaction Gibbs-Ensemble Monte Carlo simulation method. *Fluid Phase Equilibria* **181**(1-2): 127-146.

Lithoxoos, G. P., Labropoulos, A., Peristeras, L. D., Kanellopoulos, N., Samios, J. & Economou, I. G. (2010). Adsorption of N_2, CH_4, CO and CO_2 gases in single walled carbon nanotubes: A combined experimental and Monte Carlo molecular simulation study. *Journal of Supercritical Fluids* **55**(2): 510-523.

Liu, C. T. & Lindsay, W. T. (1972). Thermodynamics of sodium chloride solutions at high temperatures. *Journal of Solution Chemistry* **1**(1): 45-69.

Lobaugh, J. & Voth, G. A. (1997). A quantum model for water: Equilibrium and dynamical properties. *Journal of Chemical Physics* **106**(6): 2400-2410.

Lopes, J. N. C. & Tildesley, D. J. (1997). Multiphase equilibria using the Gibbs-Ensemble Monte Carlo method. *Molecular Physics* **92**(2): 187-195.

Lopez-Rendon, R. & Alejandre, J. (2008). Molecular dynamics simulations of the aolubility of H_2S and CO_2 in water. *Journal of the Mexican Chemical Society* **52**(1): 88-92.

Lupton, J. E. & Craig, H. (1975). Excess ^{3}He in oceanic basalts - evidence for terrestrial primordial helium. *Earth and Planetary Science Letters* **26**(2): 133-139.

Mackintosh, S. J. & Ballentine, C. J. (2012). Using ^{3}He/^{4}He isotope ratios to identify the source of deep reservoir contributions to shallow fluids and soil gas. *Chemical Geology* **304**: 142-150.

Mahoney, M. W. & Jorgensen, W. L. (2000). A five-site model for liquid water and the reproduction of the density anomaly by rigid, nonpolarizable potential functions. *Journal of Chemical Physics* **112**(20): 8910-8922.

Martin, M. G. (2013). The Towhee Code. From http://towhee.sourceforge.net/.

Martin, M. G. & Siepmann, J. I. (1998). Calculating Gibbs free energies of transfer from Gibbs Ensemble Monte Carlo simulations. *Theoretical Chemistry Accounts* **99**(5): 347-350.

Martin, M. G. & Thompson, A. P. (2004). Industrial property prediction using Towhee and LAMMPS. *Fluid Phase Equilibria* **217**(1): 105-110.

Marty, B. (2012). The origins and concentrations of water, carbon, nitrogen and noble gases on Earth. *Earth and Planetary Science Letters* **313**: 56-66.

Marty, B., Dewonck, S. & France-Lanord, C. (2003). Geochemical evidence for efficient aquifer isolation over geological timeframes. *Nature* **425**(6953): 55-58.

Melchionna, S., Ciccotti, G. & Holian, B. L. (1993). Hoover NPT dynamics for systems varying in shape and size. *Molecular Physics* **78**(3): 533-544.

Metropolis, N., Rosenbluth, A. W., Rosenbluth, M. N., Teller, A. H. & Teller, E. (1953). Equation of State calculations by fast computing machines. *Journal of Chemical Physics* **21**(6): 1087-1092.

Min, B. J. (2005). Critically damped verlet algorithm for the study of the structural properties of condensed matter systems. *Journal of the Korean Physical Society* **46**(4): 872-874.

Mognetti, B. M., Yelash, L., Virnau, P., Paul, W., Binder, K., Muller, M. & MacDowell, L. G. (2008). Efficient prediction of thermodynamic properties of quadrupolar fluids from simulation of a coarse-grained model: The case of carbon dioxide. *Journal of Chemical Physics* **128**(10).

Mohamed, R. S., Saldana, M. D. A., Mazzafera, P., Zetzl, C. & Brunner, G. (2002). Extraction of caffeine, theobromine, and cocoa butter from Brazilian cocoa beans using supercritical CO_2 and ethane. *Industrial & Engineering Chemistry Research* **41**(26): 6751-6758.

Moore, J. C., Battino, R., Rettich, T. R., Handa, Y. P. & Wilhelm, E. (1982). Partial Molar Volumes of Gases at Infinite Dilution in Water at 298.15-K. *Journal of Chemical and Engineering Data* **27**(1): 22-24.

Moreira, M. A. & Kurz, M. D. (2012). Noble gases as tracers of mantle processes and magmatic degassing in Burnard, P. (Ed.). *The Noble Gases as Geochemical Tracers*, Springer**:** 371-391.

Morgenstern, D. A., LeLacheur, R. M., Morita, D. K., Borkowsky, S. L., Feng, S., Brown, G. H., Luan, L., Gross, M. F., Burk, M. J. & Tumas, W. (1996). Supercritical carbon dioxide as a substitute solvent for chemical synthesis and catalysis. *Green Chemistry* **626**: 132-151.

Mountain, R. D. (1995). Comparison of a fixed-charge and a polarizable water model. *Journal of Chemical Physics* **103**(8): 3084-3090.

Muller, P. (1994). Glossary of terms used in physical organic chemistry. *Pure and Applied Chemistry* **66**(5): 1077-1184.

Murthy, C. S., Singer, K. & Mcdonald, I. R. (1981). Interaction site models for carbon dioxide. *Molecular Physics* **44**(1): 135-143.

Niedermann, S. (2002). Cosmic-ray-produced noble gases in terrestrial rocks: Dating tools for surface processes *in* Porcelli, D., Ballentine, C. J., & Wieler, R. (Eds.). *Noble Gases in Geochemistry and Cosmochemistry. Reviews in Mineralogy and Geochemistry*, Mineralogical Society of America. **47:** 731-784.

Nielsen, L. C., Bourg, I. C. & Sposito, G. (2012). Predicting CO_2-water interfacial tension under pressure and temperature conditions of geologic CO_2 storage. *Geochimica Et Cosmochimica Acta* **81**: 28-38.

Nimz, G. J. & Hudson, G. B. (2005). The use of noble gas isotopes for monitoring leakage of geologically stored CO_2 *in* Thomas, D., Benson, S. (Eds.). *Carbon dioxide capture for storage in deep geologic formations* Elsevier Press. **2:** 1113–1130.

NIST. (2013). Thermophysical properties of fluid systems. From http://webbook.nist.gov/chemistry/fluid/.

Omelyan, I. P., Mryglod, I. M. & Folk, R. (2002). Optimized Verlet-like algorithms for molecular dynamics simulations. *Physical Review E* **65**(5).

Ozima, M. & Podosek, F. A. (2002). *Noble Gas Geochemistry*, Cambridge University Press.

Panagiotopoulos, A. Z. (1987). Direct determination of phase coexistence properties of fluids by Monte Carlo simulation in a new ensemble. *Molecular Physics* **61**(4): 813-826.

Paricaud, P., Predota, M., Chialvo, A. A. & Cummings, P. T. (2005). From dimer to condensed phases at extreme conditions: Accurate predictions of the properties of water by a Gaussian charge polarizable model. *Journal of Chemical Physics* **122**(24).

Pepin, R. O. & Porcelli, D. (2002). Origin of noble gases in the terrestrial planets *in* Porcelli, D., Ballentine, C. J., & Wieler, R. (Eds.). *Noble Gases in Geochemistry and Cosmochemistry. Reviews in Mineralogy and Geochemistry*, Mineralogical Society of America. **47:** 191-246.

Pinti, D. L., Castro, M. C., Shouakar-Stash, O., Tremblay, A., Garduno, V. H., Hall, C. M., Helie, J. F. & Ghaleb, B. (2013). Evolution of the geothermal fluids at Los Azufres, Mexico, as traced by noble gas isotopes, $\delta^{18}O$, δD, $\delta^{13}C$ and $^{87}Sr/^{86}Sr$. *Journal of Volcanology and Geothermal Research* **249**: 1-11.

Pinti, D. L. & Marty, B. (1995). Noble gases in crude oils from the Paris Basin, France: Implications for the origin of fluids and constraints on oil-water-gas interactions. *Geochimica Et Cosmochimica Acta* **59**(16): 3389-3404.

Podosek, F. A., Honda, M. & Ozima, M. (1980). Sedimentary noble gases. *Geochimica Et Cosmochimica Acta* **44**(11): 1875-1884.

Poling, B. E., Prausnitz, J. M., O'Connell, J. P. & Knovel (2001). *The properties of gases and liquids*. New York, McGraw-Hill.

Poole, P. H., Sciortino, F., Grande, T., Stanley, H. E. & Angell, C. A. (1994). Effect of hydrogen bonds on the thermodynamic behavior of liquid water. *Physical Review Letters* **73**(12): 1632-1635.

Porcelli, D. & Ballentine, C. J. (2002). Models for the distribution of terrestrial noble gases and evolution of the atmosphere *in* Porcelli, D., Ballentine, C. J., & Wieler, R.

(Eds.). *Noble Gases in Geochemistry and Cosmochemistry. Reviews in Mineralogy and Geochemistry,* Mineralogical Society of America. **47:** 411-480.

Porcelli, D., Ballentine, C. J. & Wieler, R. (2002). An overview of noble gas geochemistry and cosmochemistry in Porcelli, D., Ballentine, C. J., & Wieler, R. (Eds.). *Noble Gases in Geochemistry and Cosmochemistry. Reviews in Mineralogy and Geochemistry,* Mineralogical Society of America. **47:** 1-18.

Porcelli, D. & Halliday, A. N. (2001). The core as a possible source of mantle helium. *Earth and Planetary Science Letters* **192**(1): 45-56.

Potoff, J. J. & Siepmann, J. I. (2001). Vapor-liquid equilibria of mixtures containing alkanes, carbon dioxide, and nitrogen. *Aiche Journal* **47**(7): 1676-1682.

Price, L. C., W., B. C., Mac Gowan, D. & Wenger, L. (1981). Methane solubility in brines with application to the geopressured resource. Proceedings 5th Conference Geopressured Geothermal Energy, Baton Rouge, Louisiana.

Prini, R. F. & Crovetto, R. (1989). Evaluation of Data on Solubility of Simple Apolar Gases in Light and Heavy-Water at High-Temperature. *Journal of Physical and Chemical Reference Data* **18**(3): 1231-1243.

Prinzhofer, A., Dreyfus, S., Donard, O. & Dos Santos, E. V. (2007). Non-hydrocarbon compounds in oil and gas accumulations: Deep influx constrained by noble gases. *Geochimica Et Cosmochimica Acta* **71**(15): A811-A811.

Quigley, D. & Probert, M. I. J. (2004). Langevin dynamics in constant pressure extended systems. *Journal of Chemical Physics* **120**(24): 11432-11441.

Rane, K., S., Murali, S. & Errington, J. R. (2013). Monte Carlo simulation methods for computing liquid-vapor saturation properties of model systems. *Journal of Chemical Theory and Computation*.

Rapaport, D. C. (1983). Hydrogen bonds in water network organization and lifetimes. *Molecular Physics* **50**(5): 1151-1162.

Ravagnani, A. T. F. S. G., Ligero, E. L. & Suslick, S. B. (2009). CO_2 sequestration through enhanced oil recovery in a mature oil field. *Journal of Petroleum Science and Engineering* **65**(3-4): 129-138.

Raveendran, P., Ikushima, Y. & Wallen, S. L. (2005). Polar attributes of supercritical carbon dioxide. *Accounts of Chemical Research* **38**(6): 478-485.

Reverchon, E., Adami, R., Cardea, S. & Della Porta, G. (2009). Supercritical fluids processing of polymers for pharmaceutical and medical applications. *Journal of Supercritical Fluids* **47**(3): 484-492.

Reynolds, L., Gardecki, J. A., Frankland, S. J. V., Horng, M. L. & Maroncelli, M. (1996). Dipole solvation in nondipolar solvents: Experimental studies of reorganization energies and solvation dynamics. *Journal of Physical Chemistry* **100**(24): 10337-10354.

Rouessac, F. & Rouessac, A. (2007). *Chemical Analysis: Modern instrumentation methods and techniques,* Wiley-Blackwell.

Rudnick, R. L. & Fountain, D. M. (1995). Nature and composition of the continental crust: A lower-crustal perspective. *Reviews of Geophysics* **33**(3): 267-309.

Ryckaert, J. P., Ciccotti, G. & Berendsen, H. J. C. (1977). Numerical-integration of the cartesian equations of motion of a system with constraints: Molecular-dynamics of n-alkanes. *Journal of Computational Physics* **23**(3): 327-341.

Saharay, M. & Balasubramanian, S. (2004). *Ab initio* molecular-dynamics study of supercritical carbon dioxide. *Journal of Chemical Physics* **120**(20): 9694-9702.

Sala, J., Guardia, E. & Marti, J. (2010). Effects of concentration on structure, dielectric, and dynamic properties of aqueous NaCl solutions using a polarizable model. *Journal of Chemical Physics* **132**(21).

Sano, Y., Marty, B. & Burnard, P. (2012). Noble gases in the atmosphere *in* Burnard, P. (Ed.). *The Noble Gases as Geochemical Tracers,* Springer**:** 17-31.

Sano, Y. & Takahata, N. (2005). Measurement of noble gas solubility in seawater using a quadrupole mass spectrometer. *Journal of Oceanography* **61**(3): 465-473.

Sarda, P. & Guillot, B. (2005). Breaking of Henry's law for noble gas and CO_2 solubility in silicate melt under pressure. *Nature* **436**(7047): 95-98.

Seitz, M. G. & Hart, S. R. (1973). Uranium and boron distributions in some oceanic ultramafic rocks. *Earth and Planetary Science Letters* **21**(1): 97-107.

Sherwood-Lollar, B. & Ballentine, C. J. (2009). Insights into deep carbon derived from noble gases. *Nature Geoscience* **2**(8): 543-547.

Shibata, T., Takahashi, E. & Matsuda, J. (1998). Solubility of neon, argon, krypton, and xenon in binary and ternary silicate systems: A new view on noble gas solubility. *Geochimica Et Cosmochimica Acta* **62**(7): 1241-1253.

Sirk, T. W., Moore, S. & Brown, E. F. (2013). Characteristics of thermal conductivity in classical water models. *Journal of Chemical Physics* **138**(6).

Smith, D. E. & Dang, L. X. (1994). Computer simulations of NaCl association in polarizable water. *Journal of Chemical Physics* **100**(5): 3757-3766.

Smith, F. T. (1972). Atomic distortion and the combining rule for repulsive potentials. *Physical Review A* **5**(4): 1708-1713.

Smith, S. P. (1985). Noble gas solubility in water at high temperature. *Transactions - American Geophysical Union* **66**(66): 397-397.

Smith, S. P. & Kennedy, B. M. (1983). The solubility of noble gases in water and in NaCl brine. *Geochimica Et Cosmochimica Acta* **47**(3): 503-515.

Song, W., Rossky, P. J. & Maroncelli, M. (2003). Modeling alkane plus perfluoroalkane interactions using all-atom potentials: Failure of the usual combining rules. *Journal of Chemical Physics* **119**(17): 9145-9162.

Span, R. & Wagner, W. (1996). A new equation of state for carbon dioxide covering the fluid region from the triple-point temperature to 1100 K at pressures up to 800 MPa. *Journal of Physical and Chemical Reference Data* **25**(6): 1509-1596.

Sparks, R. S. J. (1978). The dynamics of bubble formation and growth in magmas: A review and analysis. *Journal of Volcanology and Geothermal Research* **3**(1-2): 1-37.

Spycher, N., Pruess, K. & Ennis-King, J. (2003). CO_2-H_2O mixtures in the geological sequestration of CO_2 I. Assessment and calculation of mutual solubilities from 12 to 100 °C and up to 600 bar. *Geochimica Et Cosmochimica Acta* **67**(16): 3015-3031.

Stalker, L., Boreham, C. & E., P. (2009). A review of tracers in monitoring CO_2 breakthrough: Properties, uses, case studies and novel tracers *in* Grobe, M., Pashin, J. C. & Dodge, R. L. (Eds.). *Carbon dioxide sequestration in geological media—State of the science: AAPG Studies in Geology*, The American Association of Petroleum Geologists. **59:** 595-608.

Stenhouse, M. J., Zhou, W. & Arthur, R. (2006). Assessment of the long-term fate of CO_2 injected into the Weyburn field: System-level modeling of CO_2 migration and potential impacts. *Advances in the Geological Storage of Carbon Dioxide: International Approaches to Reduce Anthropogenic Greenhouse Gas Emissions* **65**: 231-242.

Stute, M., Schlosser, P., Clark, J. F. & Broecker, W. S. (1992). Paleotemperatures in the Southwestern United-States derived from noble gases in groundwater. *Science* **256**(5059): 1000-1003.

Swope, W. C. & Andersen, H. C. (1984). A molecular dynamics method for calculating the solubility of gases in liquids and the hydrophobic hydration of inert-gas atoms in aqueous solution. *Journal of Physical Chemistry* **88**(26): 6548-6556.

Tang, K. T. & Toennies, J. P. (1986). New combining rules for well parameters and shapes of the Van der Waals potential of mixed rare gas systems. *Zeitschrift Fur Physik D-Atoms Molecules and Clusters* **1**(1): 91-101.

Thoma, M. J., McNamara, J. P., Gribb, M. M. & Benner, S. G. (2011). Seasonal recharge components in an urban/agricultural mountain front aquifer system using noble gas thermometry. *Journal of Hydrology* **409**(1-2): 118-127.

Tolstikhin, I. N. (1975). Helium isotopes in the Earth's interior and in the atmosphere: A degassing model of the Earth. *Earth and Planetary Science Letters* **26**(1): 88-96.

Torgersen, T. (1989). Terrestrial helium degassing fluxes and the atmospheric helium budget: Implications with respect to the degassing processes of continental crust. *Chemical Geology* **79**(1): 1-14.

Torgersen, T. & Kennedy, B. M. (1999). Air-Xe enrichments in Elk Hills oil field gases: Role of water in migration and storage. *Earth and Planetary Science Letters* **167**(3-4): 239-253.

Turner, G. (1989). The outgassing history of the Earth's atmosphere. *Journal of the Geological Society* **146**: 147-154.

Verlet, L. (1967). Computer experiments on classical fluids I. Thermodynamical properties of Lennard-Jones molecules. *Physical Review* **159**(1): 98-103.

Vinogradov, A. P. (1988). Regularities in distributions of chemical elements inside Earth's crust. *Selected Papers: Problems in Geochemistry and Cosmochemistry* **1**(1): 1-52.

Vlcek, L., Chialvo, A. A. & Cole, D. R. (2011). Optimized unlike-pair interactions for water-carbon dioxide mixtures described by the SPC/E and EPM2 models. *Journal of Physical Chemistry B* **115**(27): 8775-8784.

Vorholz, J., Harismiadis, V. I., Rumpf, B., Panagiotopoulos, A. Z. & Maurer, G. (2000). Vapor + liquid equilibrium of water, carbon dioxide, and the binary system, water + carbon dioxide, from molecular simulation. *Fluid Phase Equilibria* **170**(2): 203-234.

Wagner, W. & Pruss, A. (2002). The IAPWS formulation 1995 for the thermodynamic properties of ordinary water substance for general and scientific use. *Journal of Physical and Chemical Reference Data* **31**(2): 387-535.

Wallqvist, A. & Teleman, O. (1991). Properties of flexible water models. *Molecular Physics* **74**(3): 515-533.

Wang, B., Wu, X. Y. & Zhao, H. (2013). Novel improved multidimensional Stormer-Verlet formulas with applications to four aspects in scientific computation. *Mathematical and Computer Modelling* **57**(3-4): 857-872.

Weiss, R. F. (1971). Solubility of helium and neon in water and seawater. *Journal of Chemical and Engineering Data* **16**(2): 235-241.

Weiss, R. F. & Price, B. A. (1989). Dead Sea gas solubilities. *Earth and Planetary Science Letters* **92**(1): 7-10.

Wu, Y. J., Tepper, H. L. & Voth, G. A. (2006). Flexible simple point-charge water model with improved liquid-state properties. *Journal of Chemical Physics* **124**(2).

Yokochi, R. & Marty, B. (2004). A determination of the neon isotopic composition of the deep mantle. *Earth and Planetary Science Letters* **225**(1-2): 77-88.

Yonker, C. R., Frye, S. L., Kalkwarf, D. R. & Smith, R. D. (1986). Characterization of supercritical fluid solvents using solvatochromic shifts. *Journal of Physical Chemistry* **90**(13): 3022-3026.

Zartman, R. E., Reynolds, J. H. & Wasserburg, G. J. (1961). Helium argon, and carbon in some natural gases. *Journal of Geophysical Research* **66**(1): 277-306.

Zhang, H. Z., Huang, F., Gilbert, B. & Banfield, J. F. (2003). Molecular dynamics simulations, thermodynamic analysis, and experimental study of phase stability of zinc sulfide nanoparticles. *Journal of Physical Chemistry B* **107**(47): 13051-13060.

Zhang, Z. G. & Duan, Z. H. (2005a). An optimized molecular potential for carbon dioxide. *Journal of Chemical Physics* **122**(21): 1-15.

Zhang, Z. G. & Duan, Z. H. (2005b). Prediction of the PVT properties of water over wide range of temperatures and pressures from molecular dynamics simulation. *Physics of the Earth and Planetary Interiors* **149**(3-4): 335-354.

Zhou, Z., Ballentine, C. J., Schoell, M. & Stevens, S. H. (2012). Identifying and quantifying natural CO_2 sequestration processes over geological timescales: The Jackson Dome CO_2 Deposit, USA. *Geochimica Et Cosmochimica Acta* **86**: 257-275.

Zhou, Z., Bickle, M., Galy, A., Chapman, H., Kampman, N., Dubacq, B., M., W., Warr, O., Sirikitputtisak, T., Hannah, P. & Ballentine, C. J. (2011). Predicting CO_2 EOR and geological sequestration processes with artificial noble gas tracers. *Mineralogical Magazine* **75**(3).

Zhu, A. M., Zhang, X. B., Liu, Q. L. & Zhang, Q. G. (2009). A fully flexible potential model for carbon dioxide. *Chinese Journal of Chemical Engineering* **17**(2): 268-272.